A STUDY OF

TEFLON-BONDED COBALT OXIDE/GRAPHITE ELECTRODES

A thesis submitted for the Degree of Doctor of Philosophy

by

San-Ping Jiang

蒋　三　平

at

Chemical Energy Research Centre

The Chemistry Department

The City University

Northampton Square

London, EC1V OHB

This work was carried out under

the supervision of

Prof. A.C.C. Tseung

July 1987

ACKNOWLEDGEMENTS

I would like to express my sincere and grateful thanks to Prof. A.C.C. Tseung for his guidance and encouragement throughout the period of this work. I would also like to extend my gratitude to [redacted], for his helpful discussions at the initial stage of this work.

My thanks are also due to my colleagues in the Chemical Energy Research Centre, for many valuable help and discussions. I also wish to thank [redacted] and [redacted] of the Physics Department for their assistance in SEM and X-ray diffraction analyses. I am grateful to thank [redacted] and [redacted] for their valuable efforts to read and make this manuscript readable, and in particular for helpful advice given by [redacted] during preparation of this thesis.

I am most grateful to The State Education Commission of The People's Republic of China, for their financial support. I would also like to acknowledge the receipt of a Studentship from The British Council and The City University for carrying out the work reported in Chapter 9.

Finally, I would like to extend my sincere thanks to my parents for their understanding and encouragement over the past years.

ABSTRACT

The use of fuel cells as an energy supply in the space programme during the 1960's in the U.S.A. stimulated enormous interest in the investigation of electrocatalysts for oxygen reduction reaction, due to its vital importance in fuel cell research and development. However, despite the large research effort and extensive literature, the efficiency achieved in fuel cells is well below the theoretical value, and the kinetics and mechanism of oxygen reduction, particularly on gas diffusion electrodes, remain mostly a matter of speculation.

In this thesis extensive studies of the role of Co_3O_4 catalysts in oxygen reduction on Teflon-bonded Co_3O_4/graphite electrodes in alkaline solution were carried out both chemically and electrochemically. It was proposed that during oxygen reduction, the intermediate HO_2^- formed was homogeneously decomposed by dissolved Co^{2+} ions: Co_3O_4 is capable of being dissolved in concentrated alkaline solution. Impedance responses for O_2 reduction on Teflon-bonded graphite electrodes, Co_3O_4/graphite electrodes and semiconducting cobalt oxide electrodes, were, both experimentally and theoretically, studied. The accuracy and limitation of using a.c. impedance technique in gas diffusion electrodes were also discussed. In the final part of this thesis (Chapter 9) a novel deposition method to produce highly porous cobalt electrodes at room temperatures was reported. Preliminary experiments for the regeneration of air electrodes in situ were also carried out.

A high surface area Co_3O_4 (HSAC) was prepared by oxidizing and precipitating Co^{2+} ions in alkaline solution. The crystallographic structure of the prepared oxide was needle-shaped. The HSAC catalysts

were characterized by high surface area (89.88 m^2/g) and low electrical resistivity (1121.6 ohm·cm). It was shown that HSAC catalysts are highly active for both peroxide decomposition and oxygen reduction. When HSAC was coprecipitated with graphite to form a composite catalyst, a polarization potential of about 825 mV vs. DHE at 200 mA/cm^2 (25^oC, 5N KOH and under air) was obtained, and the electrode performance was quite stable.

The kinetics of the decomposition of hydrogen peroxide in the presence of 1 ppm Co^{2+} ions in 5N KOH solution were examined in Chapter 4. It was demonstrated that Co^{2+} ions in alkaline solutions are very active towards H_2O_2 decomposition. The decomposition reaction was found to be a 1.2 -order reaction.

A homogeneous decomposition mechanism involving the chain reactions was proposed. The peroxide decomposition was considered to be initiated by the formation of free radicals. The heterogeneous behaviour of cobalt oxide catalysts in alkaline solutions was explained by the termination processes of the free radical on Co^{3+} ions in the spinel lattice.

The equivalent circuit coupled with an adsorption process was employed to study the impedance responses in oxygen reduction on Teflon-bonded graphite electrodes. The characteristic exchange current density i_o' calculated from the charge transfer resistance R_{ct} was about 2 mA/cm^2, which is in good agreement with the data reported on pyrolytic graphite electrodes. The adsorption resistance R_a evaluated was found to be much higher that R_{ct} value, indicating again that the surface adsorption process of oxygen molecule is the rate determining step during O_2 reduction. The stability of graphite electrodes was examined

by measuring the apparent double layer capacitance. It was concluded that the instability of a graphite electrode is, mainly, caused by the attack of peroxide, formed during oxygen reduction, on the active sites of the graphite electrode.

In order to correlate the electrochemical activity of the electrodes and catalytic activity of the oxides incorporated, the impedance responses on Co_3O_4/graphite electrodes were analysed, using an analytical method for an electrode reaction coupled with a catalytic process. Results obtained showed that there is a close correlation between the catalytic parameters k_c and electroactive parameter i_o' values, both evaluated from the impedance measurements. The increasing i_o' values with the catalytic activities of Co_3O_4 were mainly due to the increase of recycling efficiency inside the pores of the electrodes. The dependence of k_c values on the measured potentials demonstrated, electrochemically, that HO_2^- formed during O_2 reduction on Co_3O_4/graphite electrodes is homogeneously decomposed by the dissolved Co^{2+} ions.

In Chapter 8, O_2 reduction reactions on HSAC and 3.1 at% Li-doped Co_3O_4 (LDC) electrodes were studied, using steady state polarization and impedance methods. An empirical impedance model, incorporating a surface oxide layer model and a modified Randles circuit, was developed. Though the theoretical background of this approach has not been established unanimously, it was shown clearly that the kinetics and mechanism of oxygen reduction are strongly dependent on the surface state of the semiconducting cobalt oxides, and the porous profile of the electrode has a more profound influence on the diffusion processes.

A novel reactive deposition method to prepare a highly porous cobalt electrode at room temperatures was described in Chapter 9. In this method, the cobalt was deposited electrochemically from cobalt salt solutions in the presence of bubbling oxygen. The porous cobalt electrodes prepared by the deposition method showed very fine grains (about 1 micron) and the pores are uniformly distributed. Significantly, the deposited cobalt electrodes showed very high electrical performance in alkaline solutions. The preliminary results of the regeneration of air electrodes in situ, based on the deposition of cobalt catalysts on the porous electrodes, was also reported. The potential application of such a reactive deposition method in the manufacture of storage batteries such as nickel-cobalt and silver-cobalt, and regeneration of air electrodes were discussed in Chapter 10.

CONTENTS

LIST OF TABLES

LIST OF FIGURES

NOTATION

a ..... Tafel slope, mV/decade

CPE ..... Constant phase element impedance

C_a ..... Adsorption capacitance, $\mu F/cm^2$

C_{dl} ..... Double layer capacitance, $\mu F/cm^2$

$C_{dl,app}$. Apparent double layer capacitance, $\mu F/cm^2$

C_{sl} ..... Capacitance of surface oxide layer, $\mu F/cm^2$

C_{wi} ..... Capacitance of Warburg diffusion impedance of species i, $\mu F/cm^2 \cdot s$

c_{si} ..... Surface concentration of species i

c^2_i ..... Perturbation of concentration of species i in solution

c^2_{si} .... Perturbation of surface concentration of species i

DHE ..... Dynamic hydrogen electrode

D_i ..... Diffusion coefficient of species i

F ..... Faraday constant, 96480 C/mole

F_r ..... Reliability factor

f_s ..... Surface factor

i ..... Current density, mA/cm^2

i_o ..... Exchange current density, mA/cm^2

i_o' ..... Characteristic exchange current density, mA/cm^2

j ..... Complex number, $(-1)^{\frac{1}{2}}$

k_a ..... Rate constant for adsorption process, 1/s

k_c ..... Rate constant for catalytic reaction, 1/s

k_f ..... First-order rate constant, 1/s

m ..... Fractional power of porous diffusion coefficient

n ..... Number of electrons

ocv ..... Open circuit voltage

R ..... Gas constant, 8.315 $J \cdot K^{-1}$/mole

R_a ..... Adsorption resistance, $\Omega \cdot cm^2$

R_{ct} ..... Charge transfer resistance, $\Omega \cdot cm^2$

R_{so} ..... Resistance of electrolyte, $\Omega \cdot cm^2$

R_{sl} ..... Resistance of surface oxide layer, $\Omega \cdot cm^2$

R_{wi} ..... Resistance of Warburg diffusion impedance of species i, $\Omega \cdot cm^2/s$

W ..... Warburg coefficient, $\Omega \cdot cm^2/s^{\frac{1}{2}}$

W_i ..... Warburg coefficient of species i, $\Omega \cdot cm^2/s^{\frac{1}{2}}$

W' ..... Porous diffusion coefficient, $\Omega\ cm^2/s^m$

Z ..... Complex impedance, $\Omega \cdot cm^2$

Z_f ..... Faradaic impedance, $\Omega \cdot cm^2$

Z_W ..... Warburg diffusion impedance, $\Omega \cdot cm^2$

Z_W' ..... Porous diffusion impedance

Y ..... Complex admittance, $\Omega^{-1} \cdot cm^{-2}$

Y_{cpe} .... Admittance of the constant phase element

Y_W ..... Warbury diffusion admittance

ϕ ..... Phase angle

α ..... Transfer coefficient for cathodic reaction

β ..... Transfer coefficient for anodic reaction

ω ..... Angular frequency

CHAPTER ONE

INTRODUCTION

1.1. General Background

The reduction and evolution of oxygen are of major importance to electrochemical energy conversion and storage. Oxygen cathodes are used in fuel cells[1] and metal-air batteries[2] and also are expected to find application in industrial electrolysis cells such as the chloralkali cells to replace the hydrogen evolution reaction, in the near future[3,4]. On the other hand, electroreduction of oxygen has been used for alternative methods of generating hydrogen peroxide in alkaline solutions at sufficient high overpotential[5], and of extracting oxygen from air coupled with oxygen evolution reaction[6]. The electrochemistry of oxygen has been extensively reviewed recently by Tarasevich, Sadkowski and Yeager[7], and by Schiffrin[8].

According to the number of electrons involved, the pathways of oxygen reduction can be classified into the following two overall pathways in alkaline solutions[9,10]:

A. Direct four-electron pathway

(1.1) $O_2 + 2H_2O + 4e = 4OH^-$;

$E_o = 0.401$ V

B. Intermediate two-electron pathway

(1.2) $O_2 + H_2O + 2e = HO_2^- + OH^-$;

$E_o = -0.0649$ V

followed by either the further reduction reaction

(1.3) $HO_2^- + H_2O + 2e = 3OH^-$;

$E_o = 0.867$ V

or the chemical decomposition reaction

(1.4) $2HO_2^- = 2OH^- + O_2$

where the potentials correspond to the standard state values vs. the normal hydrogen electrode (NHE) at 25°C. Note that in alkaline solutions the sum of reactions (1.2 + 1.3) or (1.2 + 1.4) is the equivalent of the overall four-electron reaction (1.1).

The extent to which each of these pathways takes place is strongly dependent on electrode material, surface states and electrolyte, as oxygen molecules are adsorbed on the cathode surface with dissociative adsorption. If the rate of electron transfer is greater than the rate of O_2 dissociation to adsorbed oxygen atoms, peroxide will be formed as a stable intermediate and O_2 is said to be reduced by a two-electron process. If, however, the rate of O_2 dissociation is greater than that of electron transfer, peroxide will not be an intermediate and O_2 is said to be reduced by a four-electron process. A good catalyst, then, for the reduction of O_2 must be not only a good electron catalyst but also a good peroxide decomposing catalyst.

In alkaline solutions the kinetics for the two-electron reaction (1.2) associated with the formation of intermediate peroxide are generally much faster than for reaction (1.1) when the comparison is at the same overpotential. However, the standard potential is so low compared with that of the corresponding four-electron process that the energy efficiency for the corresponding electrochemical systems is reduced. Applying the Nernst equation for reaction (1.2), it is obtained[11]

$$(1.5) \qquad E = E_o - \frac{RT}{2F} \ln \frac{(HO_2^-)(OH^-)}{(P_o)(H_2O)}$$

where the terms (i) correspond to the activities of species i and P_o is the pressure equivalent to the O_2 solution concentration. The

electrode potential could be increased by depressing the peroxide, HO_2^-, activity to a low value incorporating effective catalysts. Theoretically, if the activity of HO_2^- could be decreased to about 10^{-16}M, the electrode potential for reaction (1.2) will reach the thermodynamic value for the overall four-electron reduction reaction, assuming unit activities for OH^-, P_o and H_2O.

One of the challenging problems involving O_2 reduction is the marked irreversibility of the equilibrium potential for the four-electron reaction at moderate temperatures. The exchange current densities for reaction (1.1) are extremely small, typically in the range of 10^{-10} to 10^{-11} A/cm^2 of real surface for Pt and other noble metals at room temperatures. Bockris and Hug[12] obtained a reversible potential for the first time on a Pt electrode after long and careful purification of the electrolyte. Various workers[13,14] also reported the observations of the reversible potential on Pt electrodes in alkaline solutions. On semiconductor oxide electrodes, however, this reversible behavior for the O_2-H_2O couple was reported by Tseung and Bevan[15] on $La_{0.5}Sr_{0.5}CoO_3$ surface in KOH solution.

Various theories have been proposed to explain this poor attainability of the equilibrium potential for the four-electron process of O_2 reduction. One is the so-called oxide theory[16], which considers the rest potential, or open circuit voltage (ocv), as corresponding to the equilibrium potential of the metal-metal oxide reaction. The other is in favour of that the ocv is governed by two or more potentials[16,17].

1.2. Electrocatalysts for Oxygen Reduction

The electrocatalysts for oxygen reduction in aqueous solutions can be generally divided into four groups: carbon materials, metals, metal oxides and transition metal macrocyclic complexes. Used as catalysts and electrocatalysts for O_2 reduction these materials have very wide range of properties. In practice the maximum activity of an air electrode is often attained by incorporating two or more of these materials.

Beside the application of carbon materials as supports for catalysts, they are extensively employed in the battery industry and for power sources[18]. There are various forms of carbon or graphite depending on the processing conditions and original resources. Graphite and carbon after some activation treatments can be very active for O_2 reduction[19,20]. In alkaline solutions oxygen reduction proceeds principally through the formation of intermediate peroxide on carbon and graphite electrodes[11,21,22]. Unfortunately most of them are quite inert for the peroxide decomposition[18,23] and consequently the electrochemical activity is limited. In order to increase and sustain the electrochemical activity, the carbon and graphite electrodes are incorporated with peroxide decomposing catalysts, like platinum and metal oxides. The performances of these composite electrodes are greatly improved such as Co_3O_4/graphite[24] and Pt/graphite[25]. It was also reported that an activated coconut-shell charcoal electrode promoted with perovskite oxide catalysts could attain load current density as high as 1 A/cm^2[26]. In acid solutions a four-electron reaction without formation of intermediate H_2O_2 was detected on glassy carbon[27], but the activity was considerably reduced in acid

electrolytes.

The second group of electrocatalysts for O_2 reduction are metals like platinum, palladium, silver, gold etc.[12,28,29]. Among them platinum is probably the most important catalyst for oxygen reduction especially in acid solutions because of its extremely high activity towards O_2 reduction and peroxide decomposition and the high stability. From an energy efficiency point of view, an obvious advantage of platinum catalyst is that the oxygen reduction on a Pt electrode proceeds virtually through a four-electron reaction in both alkaline and acidic solutions at low overpotential, which has been proven by the rotating disk-ring technique[30,31,32]. The kinetics and mechanisms of oxygen reduction at platinum in acid and alkaline solutions have been recently re-examined by Sepa et al.[33,34]. Obviously, one of the disadvantages for the application of platinum in commercial O_2 reduction processes is its high cost.

Consequently, extended and intensified investigations have been carried out in an attempt to find effective and cheap substitutes. There are two major research directions, semiconducting oxides which have been extensively studied in the author's laboratory[23,24,35,36] and transition metal macrocyclic complexes[37,38,39]. The latter are synthesized by transition metal ions, mostly Co and Fe, and some organic complexes such as tetramethoxyphenylporphyrin (TMPP), phthalocyanines (Pc) and tetraazaannulene (TAA). The studies of O_2 reduction on these macrocyclics catalysts have usually been carried out on thin films of the macrocyclics adsorbed on a carbon, graphite or metal substrate[40,41]. Many of the transition metal macrocyclics have substantial catalytic activity for oxygen reduction and peroxide

decomposition in alkaline or acid solutions, depending on the ligand structure, central metal ion and electrolyte. Both the direct four-electron and peroxide processes are involved with macrocyclics catalysing reactions[42,43]. However, it is difficult to use them in practice because of the problem of the macrocyclics catalyst stability in aqueous electrolytes[44].

The macrocyclic catalyst stability could be increased by heating such macrocyclics, adsorbed or impregnated on a high surface area carbon or graphite, at temperatures of 450 to 900^{o}C in argon[37,45,46]. After heat treatment the macrocyclics structure is destroyed and Mossbauer spectra indicate the presence of cobaltous oxides with no evidence of Co-N_4 centers or any other form of cobalt[47]. X-ray diffraction only detects the existence of metallic cobalt[48]. There are arguments about the influences of pyrolysis on the catalytic activity of the transition metal macrocyclics[49]. It is recognized that the highly distributed cobalt ions in the heat treated Co-TMPP on carbon support could be responsible for the observed stability and the high electrochemical activity for O_2 reduction in alkaline solutions.

In contrast with the transition metal macrocyclic complexes, the metal oxides, typically spinel and perovskite oxides, are comparatively stable in alkaline solutions and active for both oxygen reduction and hydrogen peroxide decomposition. They are effective, cheap and easily available, which are especially important for industrial applications. High activity spinel catalysts can be prepared by a cryochemical method[50]. In some cases the activity of spinel oxides is in no way inferior to the activity of catalysts on a base of precious metals[51]. The electrochemical and chemical properties of spinel oxides were

reviewed by Tarasevich and Efremov[52]. The activity and role of spinel oxide catalysts in O_2 reduction will be discussed in more detail in following sections. Metal oxides with some other structures such as delafossite[53] and pyrochlore[54] were also studied as electrocatalysts for oxygen reduction in alkaline solutions.

1.3. Mechanisms of Oxygen Reduction

Sawyer and Seo[55] have proposed that the one-electron reduction of O_2 to superoxide ion, O_2^-, is reversible and independent of electrode materials and solution conditions.

$$(1.6) \qquad O_2 + e = O_2^- \qquad E^\circ = -0.284\text{V vs. NHE}$$

where the accepted standard potential is -0.284V vs. NHE at 25°C[56]. This reaction would be followed by some kind of interaction between the superoxide ions and protons. Sen et al.[57] have offered as evidence against such a mechanism on some particular surfaces. Studies of Morcos and Yeager[58] on O_2 reduction on a pyrolytic graphite electrode showed that oxygen reduction is inhibited on the basal plane relative to the edge surface. This marked dependence of the mechanism of O_2 reduction on the materials was also demonstrated on the carbon with different crystal structures[59]. Yeager and co-workers proposed the following mechanism for O_2 reduction on graphite and carbon[58,60]

$$(1.7) \qquad O_2 = O_{2(ads)}$$

$$(1.8) \qquad O_{2(ads)} + e = O_{2(ads)}^-$$

$$(1.9) \qquad O_{2(ads)}^- + H_2O + e = HO_2^- + OH^-$$

with the rate determining step (rds) of first electron transfer

reaction (1.8). The isotopic experiments have demonstrated that the oxygen bonds are modified rather than broken in the formation of peroxide[61]. But on glassy carbon the rds was suggested[62] to be a surface migration process of adsorbed O_2^- ions to accommodate an observed Tafel slope of 60 mV and a stoichiometric number of 1.

On spinel cobalt oxide Co_3O_4 the rotating disk-ring technique provides the evidence that the O_2 reduction proceeds principally through direct four-electron pathway in alkaline solutions, whereas on simple nickel oxides the final product of oxygen reduction is HO_2^-[63]. Similar to the mechanism for O_2 reduction on carbon, Efremov and Tarasevich[64] proposed a following mechanism

$$(1.10) \qquad M + O_2 = MO_2$$

$$(1.11) \qquad MO_2 + e = MO_2^-$$

$$(1.12) \qquad MO_2^- + H_2O = MHO_2 + OH^-$$

where M is the active site of Co_3O_4 or $NiCo_2O_4$. The reaction subsequently proceeds either with cleavage of O-O bonds or through the formation of HO_2^- ions. Such a mechanism could be associated with Pauling's mode[65] of interaction of oxygen with the catalyst surface. Under certain conditions the molecular oxygen, as pointed out by Tseung and co-workers[15,66] can be dissociatively adsorbed on the oxide surface in alkaline solutions. The electrochemical activity was found to be proportional to the partial pressure of oxygen on $NiCo_2O_4$ electrodes[67]. On the study of O_2 reduction on polycrystalline films of Co_3O_4 and Li-doped Co_3O_4 formed on a CoLi alloy in alkaline solutions, Savy[68] considered that a two-electron reaction is most likely to prevail on Co_3O_4.

It seems that mechanism for the reduction of oxygen is strongly influenced by the surface states of semiconducting oxides. Pirovano and Trasatti[69] determined the point of zero charge (pzc) of Co_3O_4 obtained by thermal decomposition of cobalt nitrate at various temperatures. They found that the pzc of Co_3O_4 exhibits a sharp rise as the calcination temperature is higher than about 500^oC. This is attributed to the initial surface decomposition of Co_3O_4 into CoO. The inner layer capacity which is related to the electrochemical surface area is also significantly decreased.

1.4. Role of Cobalt Catalyst in Oxygen Reduction on Cobalt Oxide/Graphite Electrodes

The role of spinel oxide catalysts was extensively studied on iron cobalt oxide/graphite[23] and nickel cobalt oxide/graphite[67] systems. It is shown that the intermediate peroxide formed electrochemically on the high surface area graphite by

$$(1.13) \qquad O_2 + H_2O + 2e = HO_2^- + OH^-$$

is catalytically decomposed on the cobaltite oxides,

$$(1.14) \qquad 2HO_2^- = O_2 + 2OH^-$$

where the cobaltite oxides were incorporated into the graphite electrodes. Recently, Lin and Tseung[70] investigated the catalytic activity of Co^{2+} for the H_2O_2 decomposition in alkaline solutions. It was shown that even at 1 ppm Co^{2+} in 5N KOH solution, there is considerable peroxide decomposition activity, which is much higher than that of 20 wt% Li-doped Co_3O_4 mixed with graphite.

On the other hand, only the electrochemical nature of spinel oxides is

considered as a role in the mechanism of O_2 reduction on Co_3O_4/graphite electrodes[71]. The promoting action of Co_3O_4 changes the mechanism of oxygen reduction and the reaction proceeds mainly to water. However, compared with high surface area graphite, the electrochemical activity of Co_3O_4 to reduce oxygen is very poor[23]. To understand further the role of spinel cobalt oxides during O_2 reduction on the composite oxide/graphite electrodes, it is necessary to consider the electrochemical and chemical properties of Co_3O_4 in alkaline solutions separately.

Co_3O_4[72] is a normal spinel type with Co^{2+} ions occupying the tetrahedral sites and Co^{3+} the octahedral sites. The ionic structure can be presented as follows.

$$(Co^{2+})_{tetra}(Co^{3+})_{2,octa}O_4$$

which means that Co^{3+} and Co^{2+} ions are located in isolated octahedral and tetrahedral voids respectively, which accounts for the very low electrical conductivity. Therefore, the electron transfer process between Co^{2+}/Co^{3+} couple is seriously restricted.

The H_2O_2 decomposition reaction is defined as an acceptor reaction[73], since it is catalysed by materials which can supply electrons to the H_2O_2 during the rate determining step which involves cyclic electron transfer between catalyst and H_2O_2 molecules. According to the relationship between the catalytic activity of the oxides and the redox potential of valence states of the oxide couples proposed by Roy[74], the possible active site is the metal ion with lower valence which can donate electrons. Goldstein and Tseung[75] studied the H_2O_2

decomposition catalysed by spinel type cobalt-iron oxides, $Co_xFe_{3-x}O_4$, and found that the maximum intrinsic activity for peroxide decomposition occurred at x = 1. They concluded that active centre for the catalytic decomposition of peroxide are divalent cobalt ions in the octahedral lattice sites, which can initiate a cyclic electron transfer scheme on the catalyst surface. An exception is the Co_3O_4 spinel which is very active to H_2O_2 decomposition, though all Co^{2+} ions occupy the tetrahedral sites. This implies that in alkaline solutions electron hopping may not be so seriously restricted in spinel lattice like octahedral sites in the case of Co_3O_4, as that between Fe^{2+}/Fe^{3+} couple in ferrite systems[76].

As far as the electroreduction of oxygen is concerned, the active sites in spinel oxides are complicated systems consisting probably of both divalent and trivalent cations with the electrolyte components coordinating them. Since chemisorption of oxygen is the first step in O_2 reduction, an active centre of the spinel oxide should be the one having strong bonding with molecular oxygen. The oxygen bonds with M^{3+} are more covalent than M^{2+} as a result of the shift of electron pairs to the trivalent cations in spinels. Consequently, the oxygen bonded with M^{3+} usually has a greater reactivity and the catalytic properties are primarily determined by M^{3+}.

There are questions raised regarding the mechanisms of cobaltite oxide catalysts in the decomposition of the peroxide during O_2 reduction on Co_3O_4/graphite electrodes. It is known from the Pourbaix diagram of cobalt[77], that Co^{2+} ions, existing as complex $HCoO_2^-$ ions, are thermodynamically stable in the range of O_2 reduction potentials in alkaline solutions. The question, therefore, is whether the dissolved

Co^{2+} ions have any influence on the stability and activity of cobalt oxides/graphite cathodes.

The stability of cobaltite oxides in alkaline solutions had been studied electrochemically and chemically. Tseung and Yeung[78] carried out cyclic voltammetry studies on $NiCo_2O_4$ and found the spinel to be stable only at potentials above 0.75 V vs. DHE. Efremov et al.[79,80] have shown that contact between Co_3O_4 and KOH solutions leads to the change of the spinel structure, forming simple cobalt oxides, CoO and Co_2O_3. The cobalt ions, Co^{3+} and Co^{2+} were detected in alkaline solutions. The spinel structure in alkaline solution is chemically unstable and this decomposition reaction of Co_3O_4 into simple cobalt oxides is obviously irreversible. However, it has been reported that Teflon-bonded Li-doped Co_3O_4/graphite electrodes[24] and $NiCo_2O_4$/graphite[78] electrodes were very active for the O_2 reduction, and such electrodes were quite stable in KOH solutions at room temperature under air.

On the basis of the studies of chemical and electrochemical activities of Co^{2+} ions in alkaline solution, Lin et al.[81] proposed that divalent cobalt ions act as a homogeneous catalyst for the peroxide decomposition during oxygen reduction at Co_3O_4/graphite electrodes.

$$(1.15) \qquad 6HCoO_2^- + 4HO_2^- = 2Co_3O_4 + O_2 + 10OH^-$$

$$(1.16) \qquad 4HCoO_2^- + 4HO_2^- = 2Co_2O_3 + O_2 + 8OH^-$$

Hence the concentration of Co^{2+} is always reduced to a very low level. It seems that there is a circulation of the spinel cobalt oxides and the dissolved Co^{2+} ions during O_2 reduction in the porous Co_3O_4/graphite electrodes. The cobalt oxides would be retained inside

the porous electrode structure. It is also realized that this homogeneous catalysis reaction of Co^{2+} could be localized in the region near the electrochemical active sites.

From the Nernst equation (1.5), it follows that if the catalyst is active enough to depress the HO_2^- activity to the equilibrium value for decomposition reaction (1.4), the electrode potential would be equal to the thermodynamic value for the overall four-electron reaction. It is noticed, however, that the equilibrium peroxide concentration (10^{-15}M in 10N KOH at 25^oC) is too low for HO_2^- ions to effectively diffuse to the active sites of heterogeneous catalysts. Because the active sites for electroreduction of oxygen differ from that for catalytic decomposition of peroxide, the heterogeneous catalysis of Co_3O_4 would be seriously limited, especially in the case of low activity of peroxide. It was found that the catalytic activity of cobalt oxide can be significantly increased by deposition of Co_3O_4 on high surface area carbon black. This was explained as a consequence of the better distribution of oxide catalysts[82]. Probably, the actual reason is that coprecipitation of cobalt oxide and carbon highly promotes the homogeneous catalytic effect of Co^{2+} as the heterophase decomposition rate of H_2O_2, if homogeneously catalysed, is enormously accelerated by the presence of interfaces[70].

From the above arguments, it becomes clear that there exists a homogeneous catalysis process in the peroxide decomposition during oxygen reduction. The dissolved Co^{2+} ions play an important role for the activity and stability of Co_3O_4/graphite cathode in alkaline solutions. The role of homogeneous catalytic activity of Co^{2+} ions would, however, strongly depend on the state of Co_3O_4 distribution on

the graphite support. During the decomposition of peroxide, the divalent cobalt ions in solution are themselves oxidized to Co^{3+} ions, which could be present in the lattice sites of cobalt oxide. Therefore the stability and activity of a graphite cathode promoted with cobalt catalysts are dependent on the relative rates of dissolution of Co^{2+} and production of HO_2^-. If the dissolved Co^{2+} ions exceed the amount required for the peroxide decomposition, cobalt ions will go into bulk solution and the stability and activity of the electrode is thus reduced. This would be expected to happen in the cases of nonuniform distribution of catalyst, especially in the cases where cobalt oxide catalysts are mechanically mixed with carbon or graphite supports. Any misunderstanding of the participation of the divalent cobalt ions in solution in the mechanisms of O_2 reduction would attribute to the discrepancies mentioned above. It is worth mentioning that the relatively high stability and activity of heated cobalt macrocyclic complexes could also be primarily due to the participation of Co^{2+}, which can dissolve from the cobaltous oxide.

1.5. Application of A.C. Impedance Technique to Teflon-Bonded Electrodes

Since Randles's[83] work on the rate constants of some simple electrode processes at the mercury electrode, impedance measurements have been extensively employed to investigate electrode reactions in various electrochemical systems such as the passive behaviour of metals[84,85], corrosion of steels[86], porous Raney-metal electrodes[87,88], semiconductor electrodes[89], batteries[90,91], oxygen electrodes[92,93,94], etc. Provided a suitable model for the electrode reaction is used, a set of kinetic parameters about the electrochemical reaction on the electrode/electrolyte interface can be evaluated from one impedance measurement. The theory of impedance in different electrode reactions has been well documented in literature[95,96,97].

In the field of oxygen electrochemistry reaction kinetics and mechanisms have been proposed, based mostly upon Tafel slopes[58,98] and stoichiometric numbers[99]. Other approaches to the mechanism were also made by the use of the potentiostatic pulse method[100], potential sweep[101], and rotating disk-ring electrodes[30,31]. However, literature about the application of the impedance method is relatively scarce, especially for the reduction of oxygen in gas diffusion porous electrodes. Iseki et al.[93,102] studied the oxygen evolution on noble metal electrodes and the impedance response showed rotated simple semicircles which could be described by the modified Randles equations. In alkaline solution, it was found[103] that the impedance responses of oxygen reduction at the dropping mercury electrode obey the Randles equivalent circuit. For oxygen reduction on porous carbon electrode, Drossbach[92] developed an equivalent circuit which incorporates

adsorption processes with the Randles circuit. This model was also used for O_2 reduction on Teflon-bonded Pt/C electrodes[104] under cathodic polarizations. The reliability of this model for catalyst/graphite electrodes where the catalytic decomposition of intermediate HO_2^- plays more important part with increase of polarization potentials is questionable. Obviously, there is a lack of information concerning both the experimental and theoretical treatments of impedance measurements of the reduction of oxygen on Teflon-bonded electrodes. The difficulties are due to the complex processes of oxygen reduction reaction. This complex situation can be schematically described by a general reaction diagram proposed by Bogotskii et al.[105,106] as shown in Fig. 1.1. Subscripts 'sol', 'sur' and 'ads' correspond to molecular O_2 or H_2O_2 in the bulk solution, in the solution adjacent to the electrode surface, and in the adsorbed state, respectively. The magnitudes of the reaction constants k_i are dependent on the electrode/electrolyte systems, and on the polarization potentials as well. Moreover, the lack in the understanding of electrochemical responses on gas diffusion porous electrodes makes it very difficult to apply the a.c. impedance techniques in this important field.

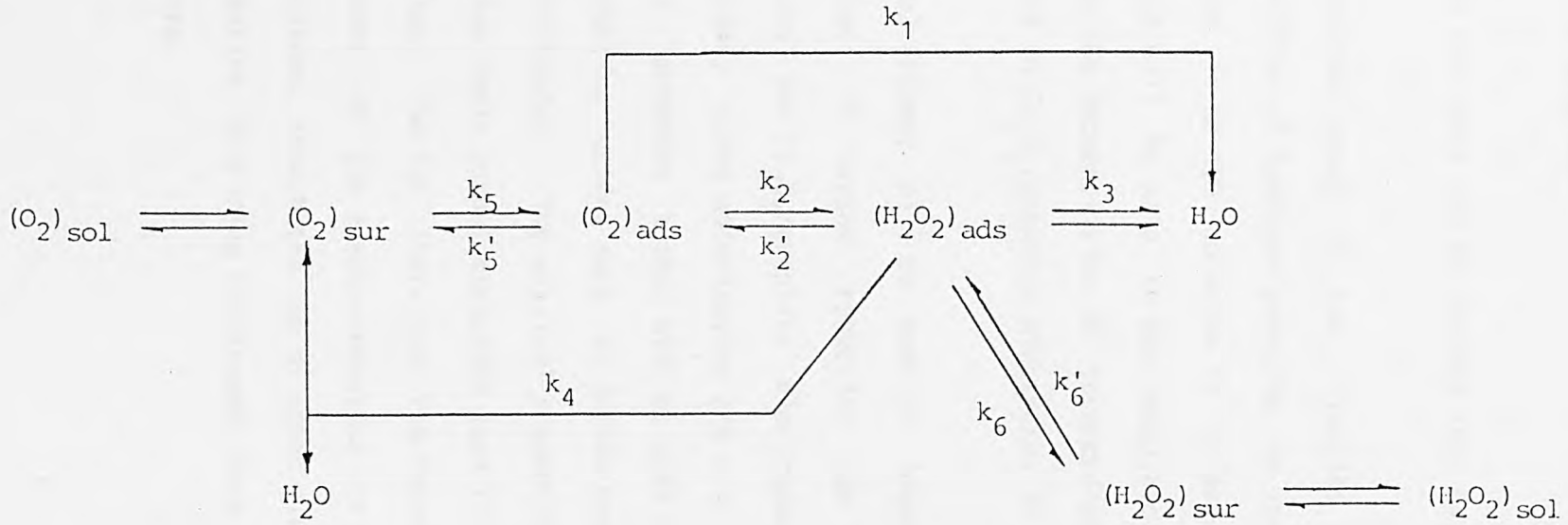

Fig. 1.1 A general reaction diagram for the oxygen and hydrogen peroxide reactions[105, 106].

1.6. Object of This Work

The object of this work can be divided into two main parts, as follows:

<1>. An extensive study of the kinetics and mechanisms of the decomposition of hydrogen peroxide on various Co_3O_4 catalysts and Co^{2+} ions in 5N KOH solution is to be carried out. Particular attention will be paid to the catalytic role of dissolved Co^{2+} ions for the decomposition of intermediate HO_2^-, formed during O_2 reduction on Co_3O_4/graphite electrodes in alkaline solutions.

<2>. A special attempt will be made to investigate the kinetics and mechanisms of oxygen reduction on Teflon-bonded graphite electrodes and Co_3O_4/graphite electrodes in alkaline solution, using steady state polarization and a.c. impedance methods. The same a.c. impedance method will be used to study O_2 reduction on semiconducting oxides such as Teflon-bonded Co_3O_4 and Li-doped Co_3O_4 electrodes. The physical properties of the semiconducting oxides and their porous structure lead to complicated O_2 reduction mechanisms. So far there are few reports about the impedance measurements of the electroreduction of oxygen on porous cobalt oxide systems, though the use of other electrochemical techniques, e.g. rotating disk-ring electrodes, have been well documented in literature.

CHAPTER TWO

EXPERIMENTAL PROCEDURES

The aim of this chapter is to outline the experimental methods used in the study of oxygen reduction systems.

2.1. Analytic Techniques

2.1.1. Gasometric Technique

As the decomposition of H_2O_2 in alkaline solutions is virtually a heterophase reaction, because of the oxygen gas evolved, a conventional gasometric technique was used for the investigation of the chemical kinetics of the decomposition reaction.

The gasometric apparatus used in this study is the improved version of the one devised by Cota et al.[107]. This apparatus was improved in the author's laboratory [23] and has been widely used[23,67]. The schematic diagram is shown in Fig. 2.1. The reaction vessel is a 250 ml 2-necked flask which is positioned directly above a magnetic stirrer. The temperature of the reaction vessel is controlled by the circulation of thermostatic water through a water pump. For the study of homogeneous catalysis of Co^{2+}, 50 ml of 5N KOH solution containing 1 ppm Co^{2+} was pipetted into the reaction vessel and then a 5 ml peroxide solution was injected into the vessel using a 5 ml syringe. The volume change due to the injection of peroxide solution was taken into account in the final calculation. In the case of cobalt oxide catalysts 50 mg catalyst was weighed and stirred in 50 ml of 5N KOH before injecting the peroxide solution.

The concentration of H_2O_2 was standardized by titrating against a standard $KMnO_4$ solution in an acidic medium[23]. It was necessary to

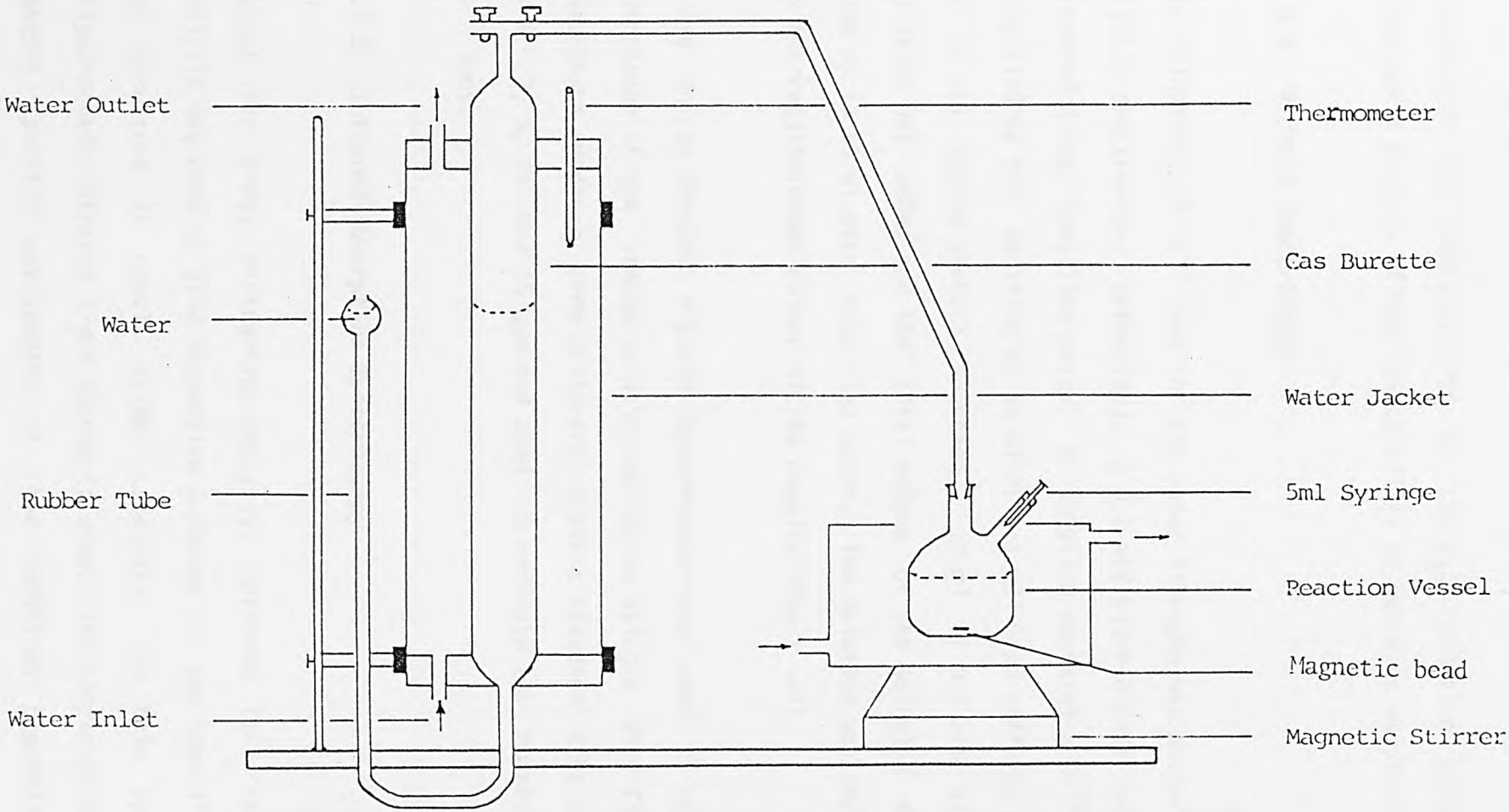

Fig. 2.1 Gasometric assembly: the hydrogen peroxide decomposition for kinetic studies.

standardize the concentration of the H_2O_2 solution prior to the experiments because of the low stability of peroxide solution.

2.1.2. Visible Spectroscopy

The solubility of Co^{2+} ions in KOH under nitrogen was measured using a visible spectroscopy method[90]. A 0.2 wt% nitro-R-salt solution was prepared using distilled water. A solution containing Co^{2+} ions was acidified by the addition of 10 ml of 1:1 HCl and buffered with 10 ml of 50 wt% sodium acetate solution. 10 ml of 0.2 wt% nitro-R-salt solution was added and the total volume of the solution was finally made up to 50 ml with distilled water. The solution was characterized by the reddish-brown colour of the complex cobalt salt.

A Pye Unicam SP6-250 visible spectrometer was used to measure the absorbance of the sample solution at 520 nm using a blue filter. The absorbance readings were calibrated against standard cobalt solutions of 0, 3, 5, 10 and 15 ppm and used to evaluate the concentration of Co^{2+} ions.

2.1.3. Infrared Absorption Spectroscopy

Except for X-ray diffraction analysis, infrared (IR) spectroscopy analysis was used to give supportive evidence for the identification of the structure of cobalt oxide catalysts. In this approach, a polychromatic infrared light source is used. The sample preferentially absorbs specific wavelengths of the radiation depending on the vibrational and rotational energies of the bonds in the molecule or compound. Therefore, IR absorption bands in a resultant spectrum are

characteristic of not only the function groups on a molecule, but also characteristic of the structure configuration of the molecule[108].

The IR spectroscopy measurements were carried out on a Perkin-Elmer 983G Infrared Spectrophotometer in the 4000-180 cm^{-1} region. The sample powders were ground with a KBr matrix (SpectrosoL). The ground fine powders were transferred to an evacuable die and pressed for about 2 minutes under vacuum. The determination of IR spectrum was immediately carried out on the sample disc prepared[109].

2.2. Electrochemical Techniques

2.2.1. Steady State Polarization

Polarization studies of oxygen reduction can be carried out by potentiostatic or galvanostatic techniques. Using the potentiostatic technique, the potential of the electrode is held at chosen values and the corresponding steady state current densities are measured, whereas in the galvanostatic mode the potential is recorded at each constant current density. The potentiostatic circuit and the galvanostatic circuit are schematically shown in Fig. 2.2. In the case of the cathodic reaction of oxygen on Teflon-bonded Co_3O_4/graphite electrodes in alkaline solutions, polarization measurements from both circuits will give the same results.

The floating cell technique[23,110] was used throughout the study of oxygen reduction reaction on Teflon-bonded air electrodes. The experimental setup is schematically presented in Fig. 2.3. The ohmic drop (or iR drop) in the solution between the tip of the Luggin

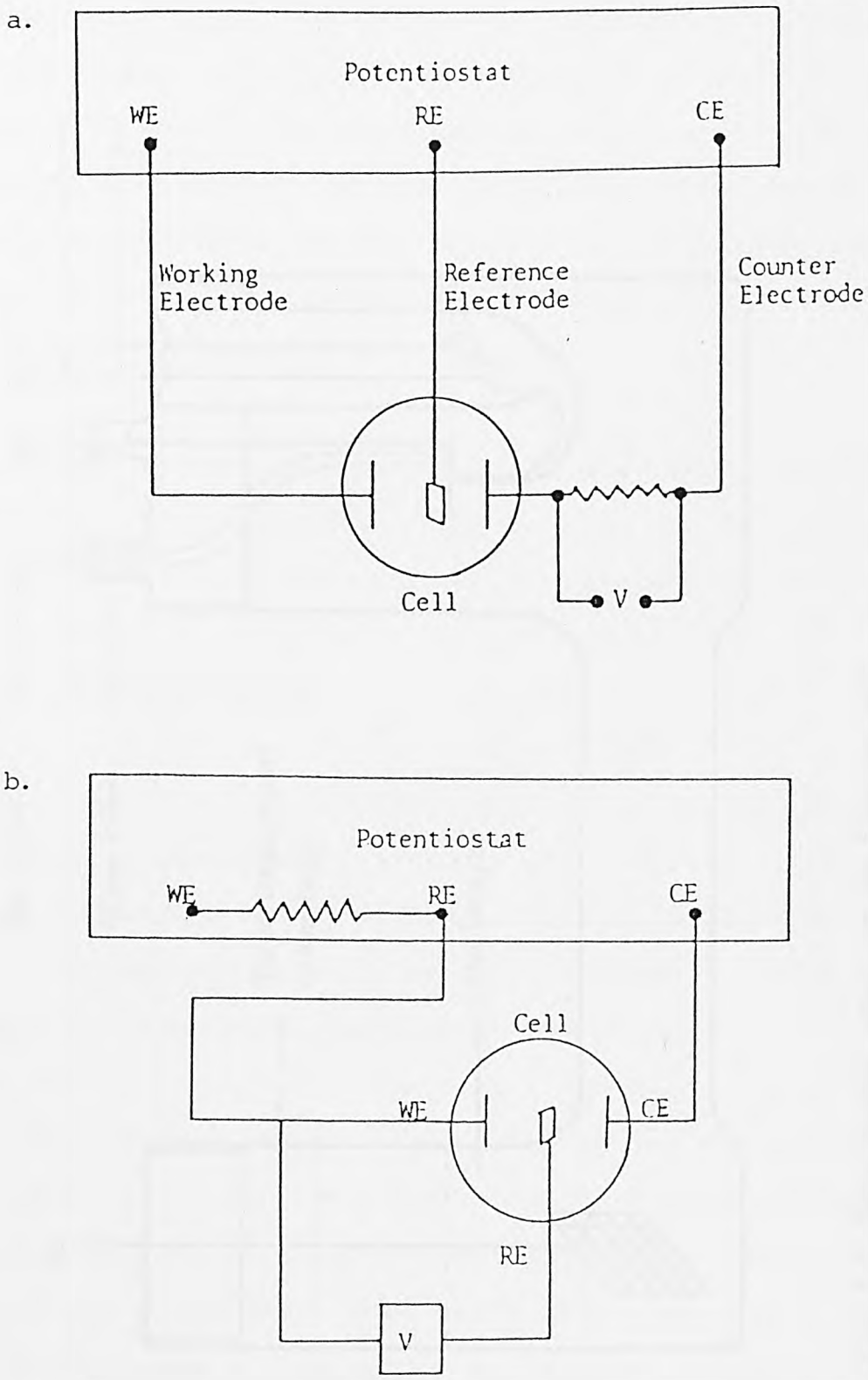

Fig. 2.2. Circuits for steady state polarization.

a. Potentiostatic mode; b. Galvanostatic mode.

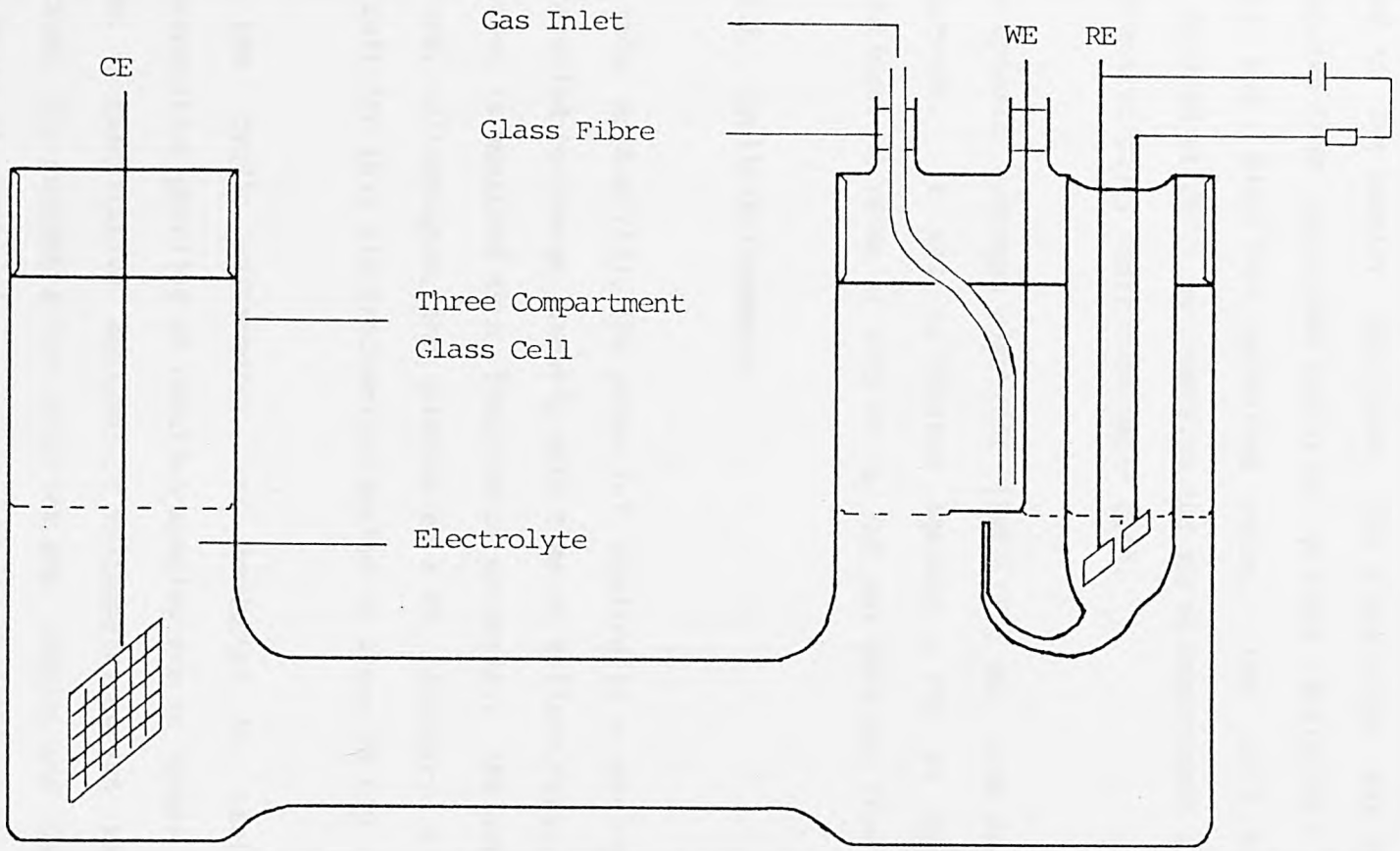

Fig. 2.3 Experimental setup for the floating cell.

capillary and the working electrode was conveniently determined using the interrupter method[111]. A large piece of 60 mesh Ni gauze was used as the counter electrode. The electrolyte was 5N KOH solution prepared from potassium hydroxide pellets (Analytical Reagent grade, BDH) and distilled deionised water. The cell temperature was maintained at 25^{o}C by immersing the three compartment glass cell in a thermostatically controlled water bath.

The dynamic hydrogen electrode (DHE)[112] was used as the reference electrode. It was calibrated against a RHE at 25^{o}C in 5N KOH solutions. A value of 34±3 mV vs. RHE was obtained from time to time.

2.2.2. Cyclic Voltammetry

In this method[113], the potential applied to a working electrode is controlled to change linearly with time at a fixed rate. The resultant current is measured as a function of potential. The potential/current curves, voltammogram, are plotted on a XY recorder. A potentiostatic circuit for this electrochemical method is shown in Fig. 2.4.

As the cyclic voltammetry was conducted in static solutions, concentration profiles of reaction species are no longer independent of time. A quantitative analysis of voltammetry curves may be difficult because the concentration profiles are complex and usually unknown. The shape of peaks also depends on the parameters such as sweep rate, the solution conditions, intermediates involved in the reaction and the geometric conditions of electrodes. However, cyclic voltammetry is very useful in the identification of steps and intermediates in the overall reactions.

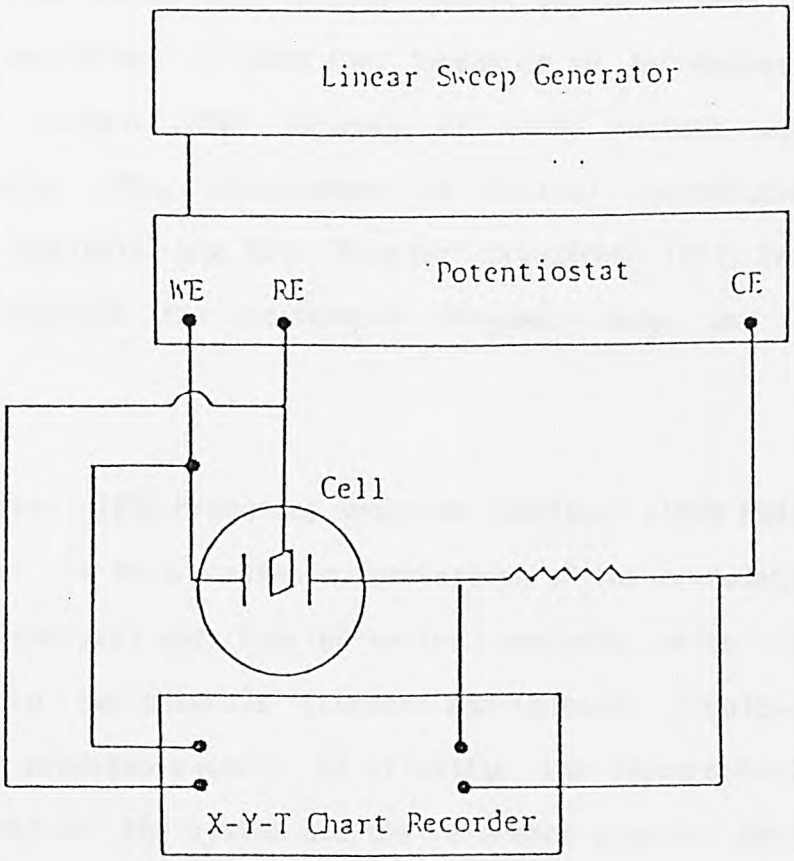

Fig. 2.4 Circuit for linear sweep voltammetry in potentiostatic mode.

2.2.3. A.C. Impedance[90,114]

In years past, the electrochemical impedance was measured by an a.c. bridge[115] which is limited to the frequency range of above 10 Hz. Other methods including Lissajous figures and phase sensitive detection (look-in amplifier) allowed the impedance to be measured over wider frequency ranges. The accuracy of these methods were, however, questionable. The development of digital correlation frequency response analysis and fast Fourier transform (FFT) techniques has greatly extended the measurable frequency range and improved the accuracy.

The Solartron 1250 Frequency Response Analyser (1250 FRA) is such an instrument. It incorporates a combination of the correlation frequency response analysis and Fourier series analysis, which is capable of measuring on two channels (current and voltage) simultaneously. The generator produces signals to stimulate the electrochemical system. The response of the system and the reference signals derived from the generator are multiplied and integrated over a whole number of cycles of the frequency by means of the correlation analysis. The real and imaginary (in phase and quadrature) components of the responses are evaluated based on the Fourier series analysis. The instrument was interfaced to an Apple IIe microcomputer via an IEEE 488 GPIB card. The complex plane plots were carried out using an EPSON FX-80 printer. A schematic diagram of the circuit for impedance measurement in potentiostatic mode is shown in Fig. 2.5. The data obtained from the impedance measurements were analysed to obtain faradaic impedance parameters, using an IBM microcomputer.

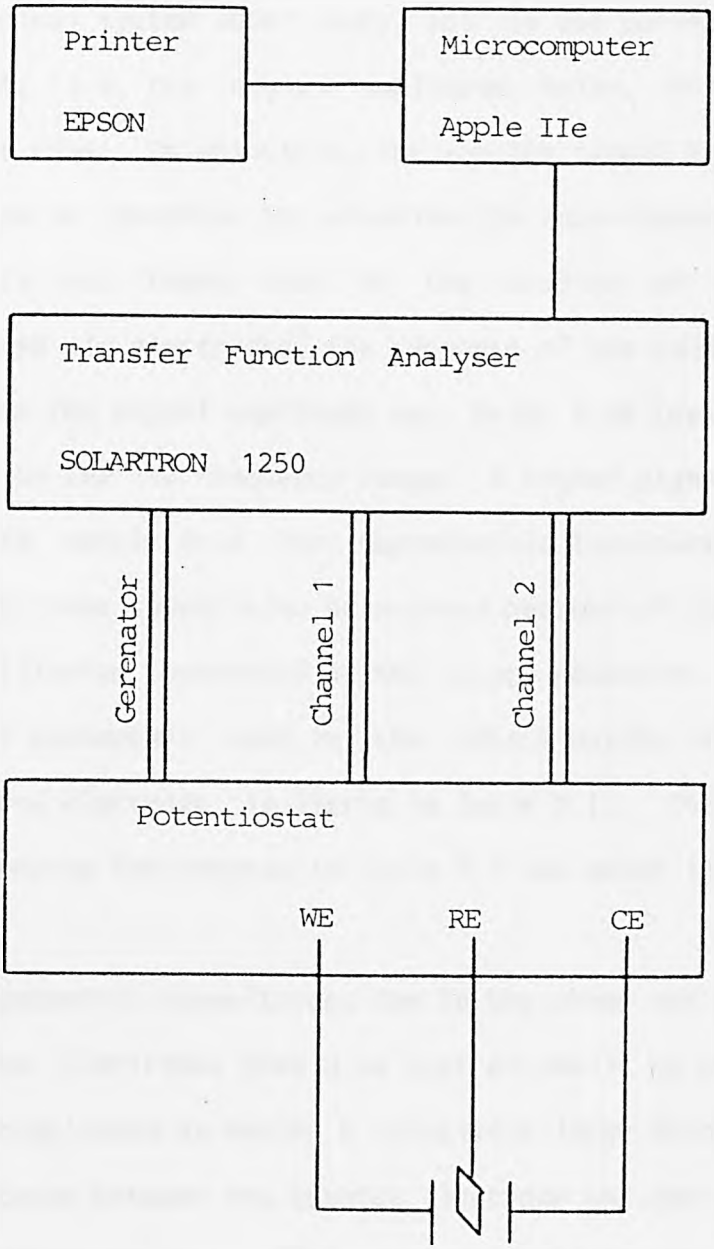

Fig. 2.5 Circuit for impedance measurement in potentiostatic mode.

The reproducibility and accuracy of the impedance measurements are by and large affected by the pretreatment and arrangement of the electrochemical system under study, and by the parameters used for the measurement; i.e. the signal amplitude, noise, frequency range and measurement time. In principle, the applied signal amplitude should be kept as low as possible to minimise the non-linear response of the system. It was found that in the studies of O_2 reduction on Teflon-bonded air electrodes, the response of the cell impedance became noisier when the signal amplitude was below 5 mV (peak to peak value), especially in the low frequency range. A higher signal amplitude (e.g. 10 mV) would result in a less reproducible impedance response. Long measurement times should also be avoided because of the poor attainment of the equilibrium potential of the oxygen reduction reaction. A set of typical parameters used in the determination of impedance of a Teflon-bonded electrode is listed in Table 2.1. The mean measurement time for running the program in Table 2.1 was about 11 minutes.

Also, the geometric capacitances due to the shape and relative position of the three electrodes should be kept as small as possible. This is usually accomplished by making a relatively large counter electrode, as the capacitance between the counter electrode and the working electrode can be represented as parallel with the cell impedance[116]. A full discussion about the causes of stray capacities and their effects on the measuring a.c. impedance is given by Gohr et al.[117]. In this present work a 60 mesh nickel screen with surface area of 30 cm^2 was used as the counter electrode and the stray capacities could be neglected if the impedance measurements are carried out in a concentrated electrolyte and at relatively low frequency (below about 10 KHz).

Table 2.1

A program setup for impedance measurement of a Teflon-bonded graphite electrode.

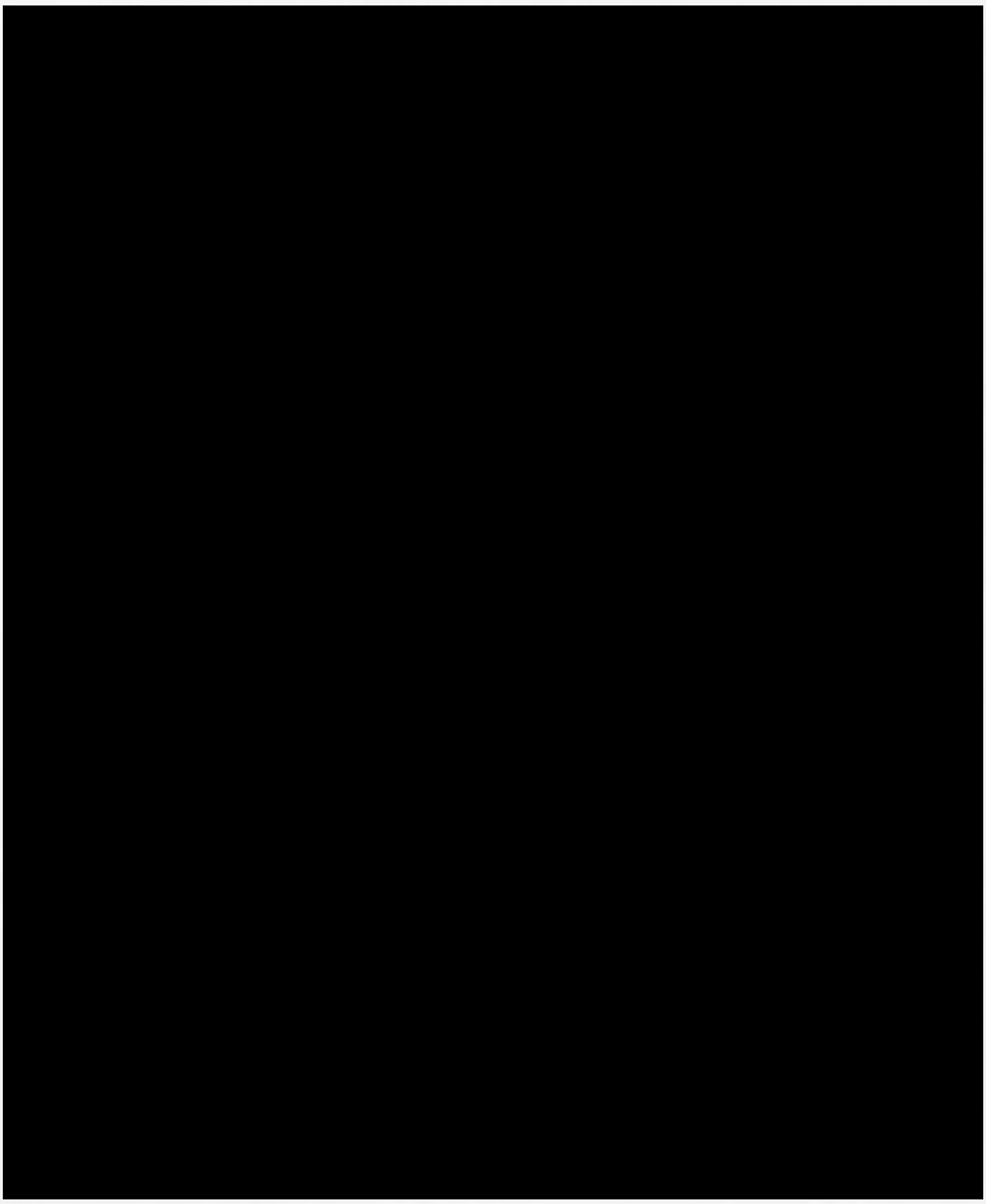

* These codes are taken from the Solartron 1096 Data Management System manual.

2.3. Fabrication of Teflon-Bonded Electrodes

2.3.1. Painting Method

In this method[118], FEP (copolymers of tetrafluoroethene and hexafluoropropene) was used as a binder to achieve an uniform mixture of electrocatalyst powder and FEP particles in aqueous dispersion. Weighed quantities of catalyst powder and a sufficient amount of FEP dispersion (60% of FEP by weight) were mixed in a beaker. The weight ratio of catalyst to the dispersion was found to be 2:1 which gave about 23 wt% of FEP in the catalyst layer. Distilled water was added and the beaker was placed in an ultrasonic bath for about 5 minutes in order to obtain a slurry which could be suitably moved. Using a fine brush, the slurry was then painted onto a $1cm^2$ 60 mesh Ni screen current collector which was previously degreased using acetone, and the electrode was dried by means of a hot air blower. The painting process was repeated until the desired loading and uniform distribution of catalyst on both sides of the Ni screen was obtained.

The electrode was heated at $300^{o}C$ for 1 hour in air to remove the wetting agent in the FEP dispersion. Electrochemical measurements were carried out immediately the electrode preparation was finished. In the case where it was not possible to do so, the electrodes fabricated were stored in a desiccator.

2.3.2. Rolling Method

The rolling method, for the fabrication of a Teflon-bonded electrode, is quite different from the painting method. The former mainly consists of the preparation of a separate catalyst layer and a separate hydrophobic layer[2].

In the case of the rolling method, PTFE (polytetrafluoroethene) aqueous suspension (GP-1, 60 wt% PTFE) was used as binder. A catalyst layer consisting of 10:3 catalyst phase to PTFE phase (i.e. approx. 77% catalyst and 23% PTFE) was prepared. 2 parts (weight) catalyst and 1 part PTFE dispersion were mixed and a few drops of water, enough to work into a dough, were added. The dough was rolled out often in different directions in order to create cross-linkages and improve mechanical strength. The final thickness of the catalyst layer was 0.3 mm. The finished layer was stored under water.

Similarly, a hydrophobic layer or gas diffusion layer containing much higher concentration of PTFE (about 60% PTFE) was also prepared. 2 parts (weight) acetylene black (Lampblack, Fisons) and 5 parts PTFE dispersion were mixed. The layer was rolled out in the same way as described for the catalyst layer. The layer was finally rolled to a 0.3 mm thickness and covered with a wet paper.

Fig. 2.6 shows a flow diagram of the electrode fabrication using the rolling method. The structure of the fabricated electrode is also shown in the figure. In order to increase contact between the catalyst and hydrophobic layers, both layers were rolled up to 0.5 mm before the final electrode assembly. A 60 mesh nickel gauze degreased by acetone

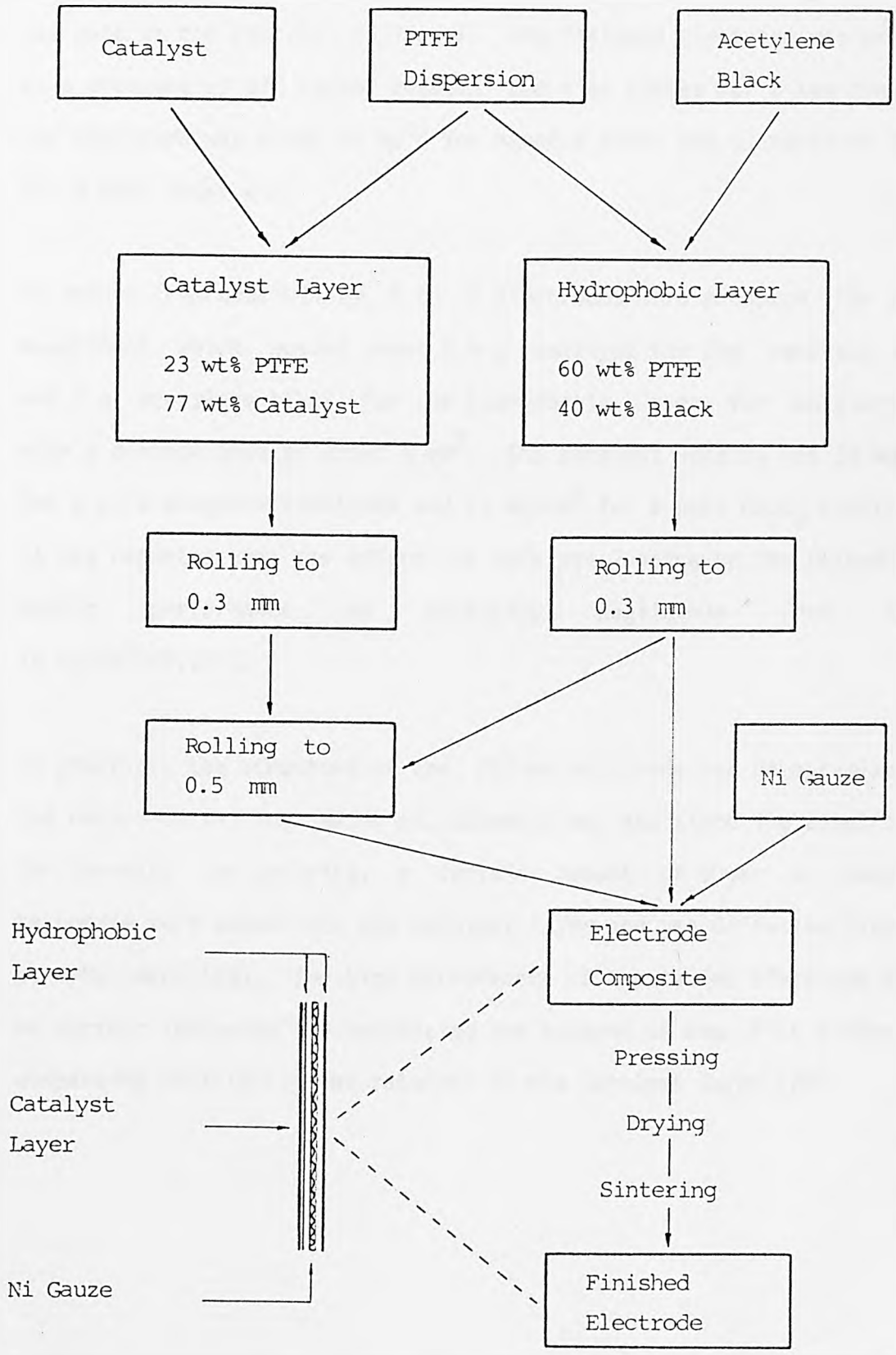

Fig. 2.6 A flow diagram of the electrode fabricated by the rolling method.

was used as the current collector. The finished electrode was pressed at a pressure of 670 Kg/cm^2 between two flat plates for a few minutes. The electrode was dried at 60^{o}C for about 5 hours and sintered at 300^{o}C for 1 hour under air.

To ensure reproducibility, 5 to 6 electrodes were produced for every experiment, which needed about 0.4 g catalyst for the catalyst layer and 1 g acetylene black for the hydrophobic layer, for an electrode with a surface area of about 1 cm^2. The catalyst loading was 18 mg/cm^2 for a pure graphite electrode and 21 mg/cm^2 for a pure Co_3O_4 electrode. It was reported that the effect of catalyst loading on the cathodic or anodic performance is virtually negligible from about 18 mg/cm^2[67,101].

In practice, the structure of the rolled electrode can be optimized by the choice of filling material, composition, and sintering conditions. To increase the porosity, a certain amount of sugar or ammonium carbonate were added into the catalyst layer and gas diffusion layer as pore-builders[119]. The high performance of the rolled electrode could be further increased by optimizing the content of the PTFE binder and dispersing efficiently the catalyst in the catalyst layer[120].

CHAPTER THREE

PREPARATION AND CHARACTERIZATION OF

COBALT OXIDE CATALYSTS

3.1. Introduction

Cobalt oxide catalysts, used in oxygen reduction, are generally prepared by low temperature decomposition of the corresponding metal hydroxide precipitates or metal salts. The sintering temperature is, usually, as low as 300 to 400^{o}C[121,122,123]. This preparation method is quite convenient and simple, and yields high surface area cobalt oxides. A relatively high surface area cobalt oxide can also be obtained by a cryochemical method (freeze-drying)[124,50]. To increase the activity of Co_3O_4/carbon air electrodes, Co_3O_4 catalysts may be coprecipitated onto a high surface area graphite support, to ensure an uniform distribution of the oxide catalysts[125].

The low temperature decomposition method, mentioned above, was employed as the catalyst preparation in this study. 300^{o}C has been found to be a desirable sintering temperature. At this temperature, both higher surface area and lower electrical resistance are optimized[122]. In addition to the low temperature decomposition method, a new catalyst preparation method[70] was used. This is described further in this chapter. The physical characteristics of the cobalt oxide and graphite powder samples are examined by BET surface area analysis, electrical resistivity measurement, transmission electron microscopy (TEM), infrared (IR) spectroscopy and X-ray diffraction analysis.

3.2. Preparation of High Surface Area Graphite

Graphite powders with high surface areas were produced by vacuum grinding using a vibrating ball mill[126,127]. Pure nickel shot was used as the grinder. Thirty five grammes of graphite (Foliac Graphite) was mixed with 3 Kg of nickel shot in a nickel chamber. Before the ball milling process began, the chamber was connected to a vacuum pump and evacuated for about 40 minutes. The pump was then turned off, and the milling was allowed to proceed for 8 to 15 hours under vacuum.

The ground graphite was sieved and collected. The fine powders were then carefully put into a glass tube and sintered at 900^{o}C for 1 hour, in a nitrogen gas atmosphere. This high temperature treatment in the absence of oxygen reduces the oxygen content of the graphite and increase the catalytic activity of graphite for oxygen reduction and peroxide decomposition[19].

After sintering, the graphite powder was stored in an airtight desiccator, to prevent CO_2 contamination, and labelled G.

3.3. Preparation of Cobalt Oxide Catalysts

3.3.1. Co_3O_4 by Precipitation Method

The conventional direct precipitation of cobalt chloride solution with KOH solution was one of the methods employed in the preparation of cobalt oxide catalysts. A solution of 300 ml of 10 wt% $CoCl_2$ (AnalaR) was added dropwise to a 200 ml solution of 15 wt% KOH whilst stirring. The initial blue colour of the precipitate rapidly turned pink. The precipitate was filtered and then washed thoroughly until it was completely free of alkali. The cobalt hydroxide precipitate was dried at 60°C for 5 hours and then sintered at 300°C for another 5 hours. The resulting Co_3O_4 catalyst powder was stored in an airtight container and labelled CP.

3.3.2. Li-Doped Co_3O_4 by Slurry Method

The slurry method is based on the one used by Teichner[128] for the preparation of Li-doped NiO. First, $Co(OH)_2$ was precipitated from mixed solution of $CoCl_2$ and KOH, as described previously, and washed free of alkali in a Buchner funnel connected to a water pump. The $Co(OH)_2$ precipitate was allowed to air-dry (ensuring that there are no cracks in the cake formed) and then 200 ml of a 6wt% solution of LiOH was evenly poured over the cake. The resulting slurry was air-dried again. The final precipitate, containing LiOH, was dried at 60°C for 5 hours and then sintered at 300°C for another 5 hours. The Li-doped Co_3O_4 prepared was then stored in an airtight container and labelled LDC.

The doping level of lithium in Co_3O_4 was determined by analysing the atomic contents of total lithium and free lithium; the difference is then taken as the amount of lithium incorporated into the spinel lattice[129]. The free Li was leached by 10 V% glacial acetic acid (AnalaR) at about 50°C and the total Li was dissolved by aqua regia. The concentration of lithium in both solutions was determined by atomic absorption spectroscopy. The result of atomic concentration of lithium ions is given as follows.

Total Li	Free Li	Li in Spinel
at%	at%	at%
18.09	14.99	3.10

The doping level of lithium in Co_3O_4 prepared by the slurry method was 3.10 at%, quite below the free lithium ions determined. Therefore, in this case, lithiation of the cobalt oxide is predominantly on the surface.

3.3.3. High Surface Area Co_3O_4

It is well known that cobalt hydroxide, $Co(OH)_2$, is soluble in concentrated alkali metal hydroxide solutions[130]. Lin and Tseung[70] developed a new method to obtain a high surface area Co_3O_4 by oxidizing and precipitating the dissolved $HCoO_2^-$ ions in alkaline solutions, using hydrogen peroxide solution as the oxidizing agent.

The apparatus used in the preparation of the high surface area Co_3O_4 is schematically shown in Fig. 3.1. A solution of 1500 ml of 50 wt% KOH solution was carefully introduced into a 2000 ml round-bottom flask.

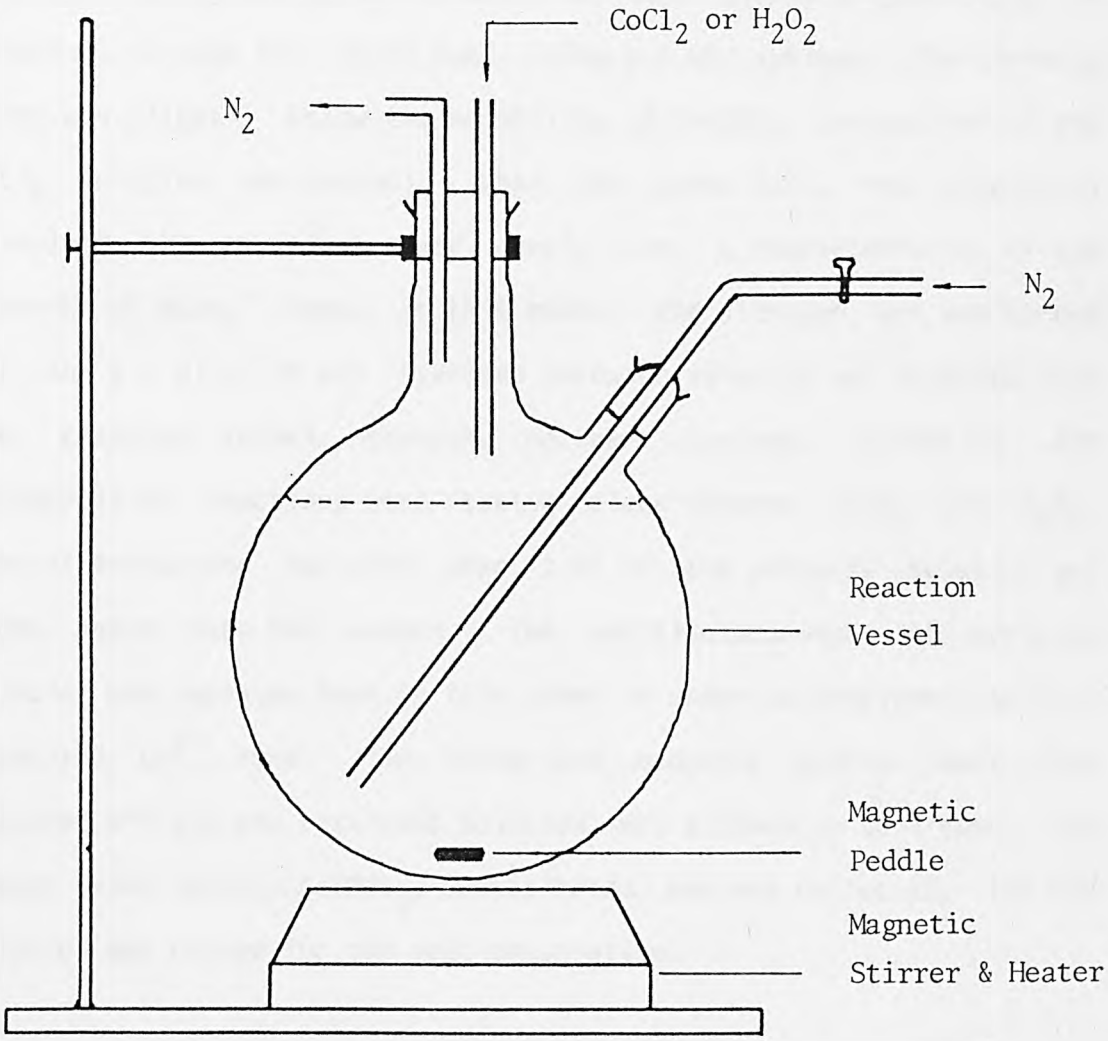

Fig. 3.1 Apparatus for preparation of high surface area cobalt oxide, HSAC.

The magnetic stirrer and the heater were switched on. In order to increase the solubility of cobalt, the solution was heated to about $60^{o}C$ and de-aerated by passing through a stream of oxygen-free nitrogen. A 10 wt% $CoCl_2$ solution was then slowly dripped into the solution, through the inlet tube, using a 5 ml syringe. The quantity added was slightly below the solubility of $Co(OH)_2$ (about 5 ml 10 wt% $CoCl_2$ solution was needed). When the added $CoCl_2$ was completely dissolved, the solution turned deeply blue; a characteristic of the presence of $HCoO_2^-$ ions. At this moment, the nitrogen gas was turned off, and a 1 ml of 20 wt% hydrogen peroxide solution was injected into the reaction vessel through another syringe. Oxidation and decomposition reactions were taking place between $HCoO_2^-$ and H_2O_2. When effervescence had died down, 1 ml of the peroxide solution was added again into the vessel. The addition procedure of peroxide solution was repeated four or five times in order to completely oxidize dissolved Co^{2+} ions. The heater and magnetic stirrer were then switched off and the resultant solution was allowed to cool down. The cobalt oxide (mainly $Co(OH)_3$) precipitated and was collected. The KOH solution was reused for the next preparation.

The precipitate was thoroughly washed with distilled water to ensure that it is completely free of alkaline solution. It was then dried at $60^{o}C$ for about 5 hours and sintered at $300^{o}C$ for 3 hours. The final product, very light and having fine dark-brown particles, was stored in an airtight container and labelled HSAC.

The following chemical reactions possibly occurred during preparation:

(3.1) $2KOH(excess) + CoCl_2 = Co(OH)_2 + 2KCl$

(3.2) $Co(OH)_2 + 2OH^- = HCoO_2^- + H_2O$

(3.3) $4HCoO_2^- + 4HO_2^- + 6H_2O = 4Co(OH)_3 + 8OH^- + O_2$

(3.4) $6HCoO_2^- + 4HO_2^- = 2Co_3O_4 + 10OH^- + O_2$

(3.5) $2HO_2^- \xrightarrow{\text{Cobalt Catalysts}} 2OH^- + O_2$

(3.6) $Co(OH)_3 \xrightarrow{\text{air, } 300^oC} Co_3O_4 + H_2O$

3.4. Preparation of Composite Co_3O_4/Graphite Catalyst

A cobalt oxide/graphite composite catalyst was prepared by coprecipitation of high surface area Co_3O_4 onto a high surface area graphite support. The method is basically similar to the one described above. A quantity of graphite was mixed with alkaline solution and introduced into the reaction vessel shown in Fig. 3.1. The mixture was rigorously stirred until the graphite powder was thoroughly wetted. The subsequent preparation procedure was exactly the same as previously described, for the preparation of high surface area Co_3O_4. On the addition of H_2O_2 solution, the dissolved cobaltous ions were oxidized and subsequently deposited onto the graphite particles suspended in solution. Consequently, a thorough dispersion of cobalt oxide catalyst particles into the graphite support was realised.

The coprecipitate of cobalt oxide and graphite was filtered and washed to neutral, dried at 60°C for 5 hours and then sintered at 300°C for 3 hours. The cobalt concentration was determined by atomic absorption spectroscopy, using aqua regia to dissolve deposited cobalt oxide.

The activity of the prepared composite catalyst, for oxygen reduction, was found to be strongly dependent on the concentration of the Co_3O_4 content. The surface area decreased significantly with increase in the cobalt oxide concentration. Optimizing the composition of the Co_3O_4/graphite composite, a Co_3O_4 concentration of 1.22 wt%, was found to be suitable. The composite catalyst was therefore prepared, as described earlier, comprising of a 1.22 wt% Co_3O_4 concentration. The catalyst so prepared was stored in an airtight container and labelled CG.

3.5. Characterization of Cobalt Oxide Catalysts

3.5.1. BET Surface Area and Electrical Resistivity

The specific surface areas of the catalysts were measured using a Micrometric Surface Area Analyser (Coulter Electronics, Luton), according to the BET model[131]. The electrical resistivity of cobalt oxide powder samples was determined using a Teflon cell similar to that employed by Goldstein[23] and Botejue[129]. The experimental procedures of measuring surface areas and electrical resistivity can be found in references 111 and 129.

Table 3.1 compares the surface areas and the electrical resistivities of the powder samples. The catalyst prepared by the oxidation of dissolved Co^{2+} ions in alkaline solution (HSAC) has much higher surface area than the one obtained by the conventional precipitation method (CP). Sintering of HSAC at 300^oC increased the surface area, which could be attributed to the dehydration of $Co(OH)_3$. Compared with high

Table 3.1

Specific surface area and electrical resistivity of cobalt oxide catalysts and graphite.

Powder Sample	Surface Area m^2/g	Resistivity ohm·cm
Graphite	294.78	0.3
CG	234.74	1.2
High surfacer area Co_3O_4, HSAC		
Dried	65.43	$4.0*10^6$
Sintered	89.88	1121.6
Co_3O_4, CP	52.19	8065.0
3.1 at% Li-doped Co_3O_4, LDC	27.48	58.3

surface area graphite, the surface area of the composite Co_3O_4/graphite catalyst, CG, appears to be slightly reduced. It is also observed that the doping of Li^+ into Co_3O_4 by the slurry method decreased, considerably, the surface area of the oxide. The possible reason may be that the presence of both alkaline ions and lithium ions accelerate the rate of sintering[129].

In a normal spinel cobalt oxide, the Co^{2+} and Co^{3+} ions are located in separate tetrahedral and octahedral positions respectively. The electrical resistivity of Co_3O_4 is in fact high at room temperature; typically about 10^{4+} ohm·cm[132]. As shown in Table 3.1, the measured resistivity of the cobalt oxide prepared by conventional precipitation (CP) is lower, about 8000 ohm·cm. However, the data given in the literature are for a single crystal product. In a high surface area form, the electrical resistivity for Co_3O_4 (HSAC) was considerably reduced. The difference between CP and HSAC depicts the nonstoichiometric composition of Co_3O_4 catalysts obtained by various methods, as well as possible structure defects due to the preparation procedure, e.g. dehydration of $Co(OH)_3$. The extremely high resistivity value for dried HSAC sample, shown in the table, indicates that the composition before sintering is not Co_3O_4.

3.5.2. Transmission Electron Microscopy Analysis

The crystallographic structures of the cobalt oxide and graphite powder samples were determined using the JEOL Analytical Electron Microscope (JEM 100B). A transmission mode at 60 KeV beam was used for all the powder samples.

Fig. 3.2 shows the transmission electron micrographs of cobalt oxide and graphite powder samples. The magnification used was 30000. Simple hexagonal structures were observed for both CP and LDC. In contrast, HSAC has a different and complicated crystal appearance. Most of them are needle-shaped crystals as shown in Fig. 3.2(c). It is thought that during preparation, the growth of perfect hexagonal crystals was interrupted by the oxidation of $HCoO_2^-$ and the decomposition of H_2O_2 on them. The irregular needle-like crystals that were formed could, therefore, be attributed to a complex interference between oxidation, decomposition, and precipitation reactions that were occurring; further decomposition of $Co(OH)_3$ also resulted in the formation of more needle-like crystals. In support of this point, the dried and sintered HSAC have the same crystal appearance, and in fact the specific surface area in the case of the latter was increased. From the micrographs, it was measured that the diameter of the hexagonal particles of CP and LDC is in the range of 200 nm to 400 nm, and for HSAC the needle-like particles are much smaller, about 80 nm diameter. It would be expected that there would be better contact and dispersion between cobalt oxide particles with a needle-shaped structure and high surface area graphite particles.

Coprecipitation of the HSAC catalyst onto the graphite support hardly changes the crystal appearance. Though cobalt oxide is denser than graphite particles, the Co_3O_4 particles are not revealed on the transmission electron micrographs, as shown in Figs. 3.2(e) and (f). This could be explained by the fact that the concentration of HSAC is very small (1.22 wt% Co_3O_4), and that the tiny needle-shaped particles are very uniformly distributed on the surface as well as in the internal pores of the high surface area graphite.

(a)

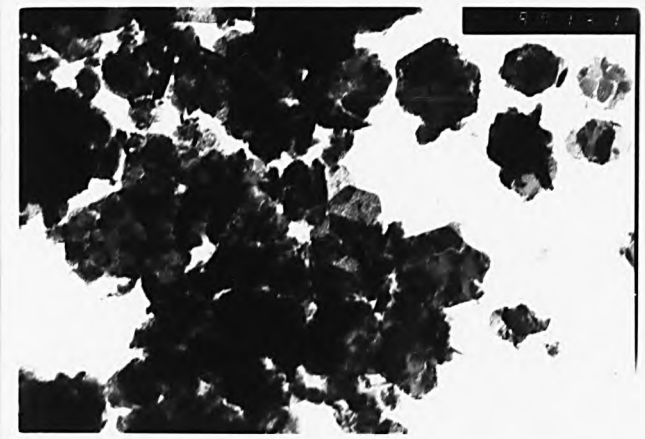

Co_3O_4, CP

(b)

Li-doped

Co_3O_4, LDC

(c)

High surface area

Co_3O_4, HSAC

Sintered

Fig. 3.2 Transmission electron micrographs of powder samples.

Magnification: 30,000 X.

(d)

High surface area Co_3O_4, HSAC Dried

(e)

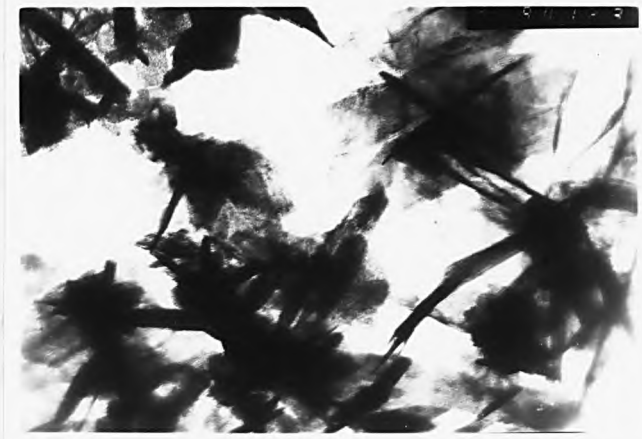

CG

(f)

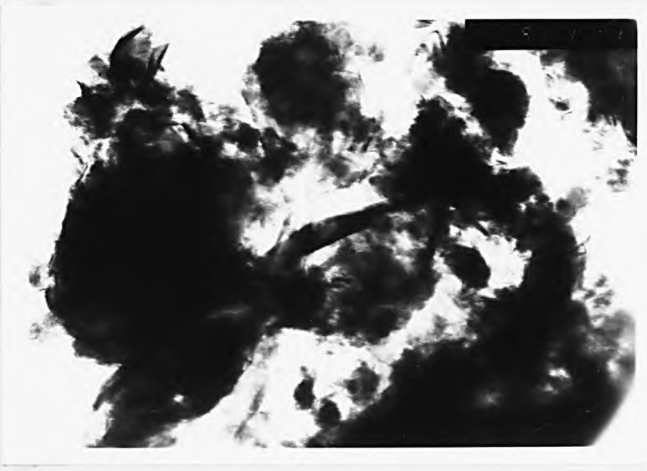

Graphite

Fig. 3.2 continued.

3.5.3. Infrared Spectroscopy and X-ray Analysis

The composition and formation of the crystal structure of cobalt oxide samples were examined by infrared (IR) spectroscopy (Perkin-Elmer, 983G) and X-ray diffraction (Phillips, PW 101c). The Debye-Scherrer powder technique was used for the X-ray diffraction analysis. For cobalt oxide, a molybdenum source with a wavelength of 7.10 nm was employed. The films were indexed by measurement of the line position using a standard Perspex ruler (Mo Kα, Enraf-Nonius Ltd.). The d-spacing values were directly read from the ruler.

Fig. 3.3 summarises the infrared spectra of various cobalt oxide catalysts measured in the wavelength range of 4000-180 cm^{-1}. The IR spectrum for Co_3O_4 has two characteristic absorption bands at 570 and 670 cm^{-1}[133] as shown in Fig. 3.3 for Co_3O_4 obtained by the different methods. These bands may be assigned to the Co^{3+}-O bonds and Co^{2+}-O bonds that vibrate in the octahedral and tetrahedral positions, respectively[79]. The absorption bands appearing at 1499, 1443, 1100, and 866 cm^{-1} for 3.1at% Li-doped Co_3O_4 (Fig. 3.3(b)) show the possible existence of lithium carbonate[133], which may be formed by the contact of free lithium ions on the oxide surface with air. Before sintering at 300°C, the IR spectrum of HSAC (Fig. 3.3(d)) shows the characteristic absorption behaviour of heterogenite or stainierite CoOOH[134].

The lattice d-spacing values of various cobalt oxide catalysts from X-ray diffraction analyses are given in Table 3.2. Compared with the ASTMA's data for spinel Co_3O_4[135], cobalt oxide prepared by the oxidation of dissolved Co^{2+} ions from KOH solution (HSAC) is the same

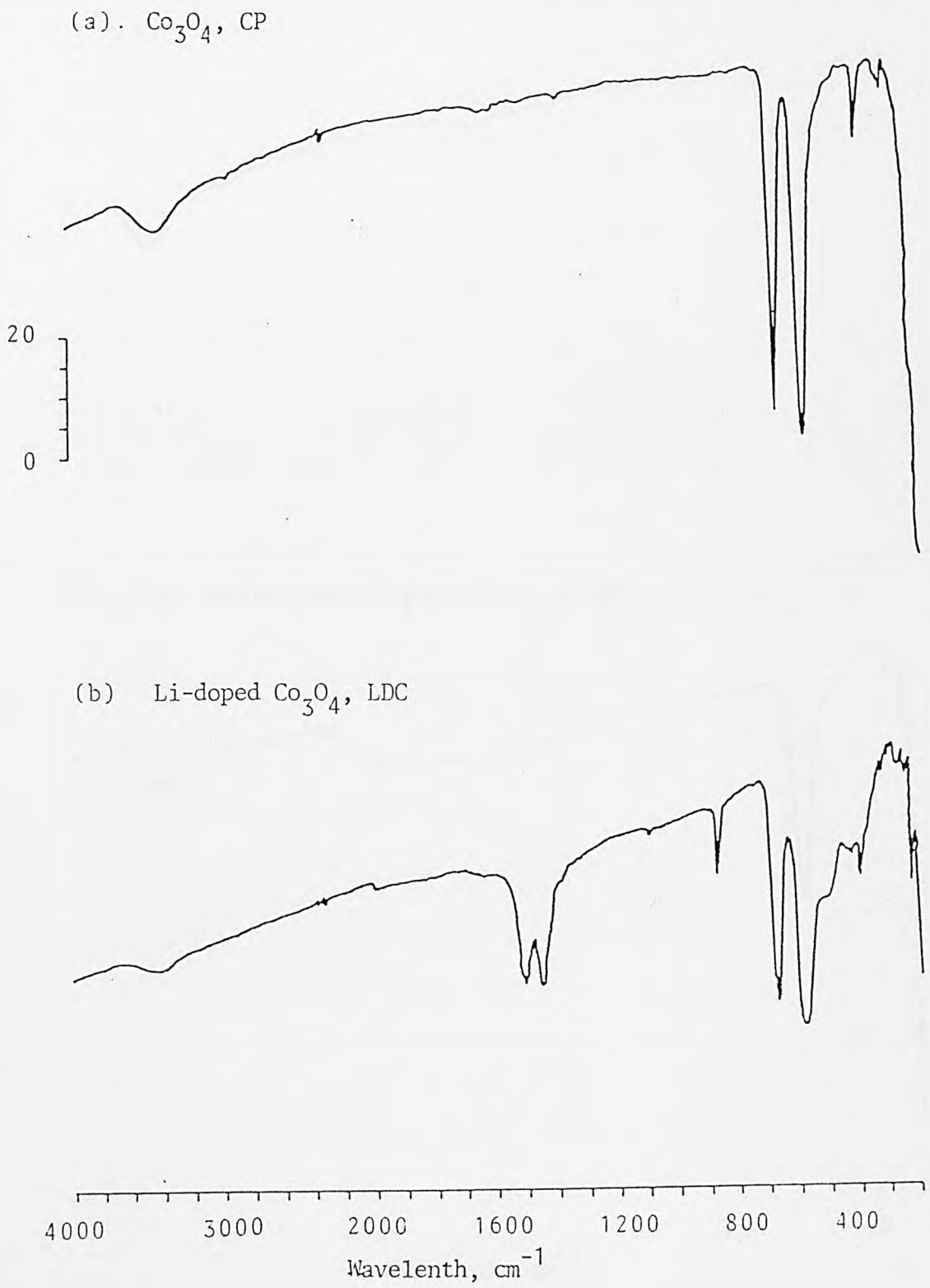

Fig. 3.3 Infrared spectra of cobalt oxide catalysts.

Matrix: KBr.

(c) High surface area Co_3O_4, HSAC - sintered

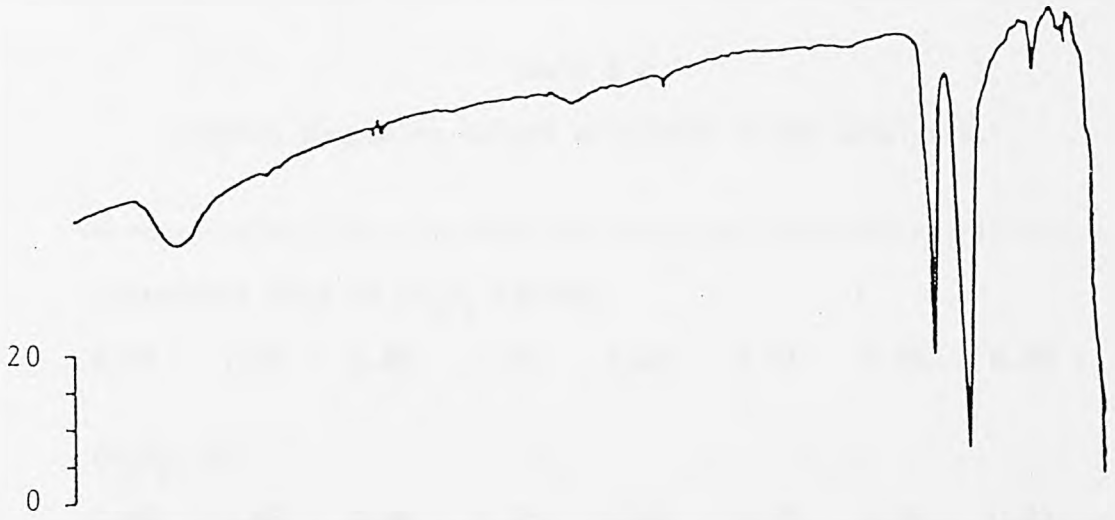

(d) High surface area Co_3O_4, HSAC - dried

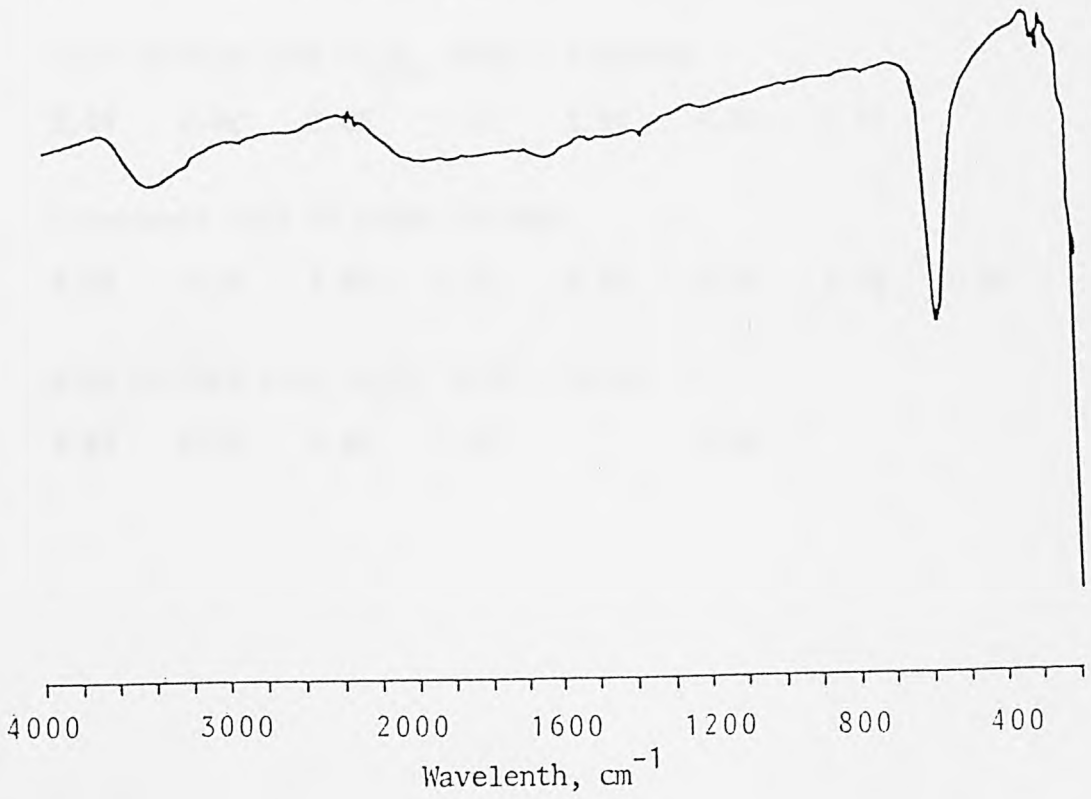

Fig. 3.3 continued.

Table 3.2

Lattice d-spacing values of cobalt oxide catalysts.

Literature data of Co_3O_4 (ASTMA)							
2.44	**1.43**	**2.86**	1.56	2.02	4.67	1.05	0.93
Co_3O_4, CP							
2.44	**1.43**	**2.86**	1.55	2.03	4.70	1.05	0.93
3.1 at% Li-doped Co_3O_4, LDC							
2.44	**1.43**	**2.86**	1.56	2.03	4.67	1.05	0.93
High surface area Co_3O_4, HSAC - sintered							
2.44	**1.42**	**2.86**	1.55	2.03	4.70	1.05	
Literature data of CoOOH (ASTMA)							
4.38	**2.31**	**1.80**	1.43	0.88	1.36	1.50	0.87
High surface area Co_3O_4, HSAC - dried							
4.40	**2.32**	**1.80**	1.43		1.36		

Co_3O_4 as that obtained by the conventional precipitation method (CP). However, the dried HSAC sample did not show the diffraction pattern of $Co(OH)_2$ or Co_3O_4. The diffraction lines associated with it indicate that the compound is mainly heterogenite cobalt oxide hydroxide, CoOOH.

CHAPTER FOUR

CHEMICAL KINETICS OF HYDROGEN PEROXIDE DECOMPOSITION IN THE PRESENCE OF COBALT OXIDE CATALYSTS

4.1. Introduction

Oxygen reduction on carbon, graphite and certain metal oxides is considered to proceed principally through the formation of intermediate peroxide in alkaline solutions. Since the electroreduction of H_2O_2 is unlikely to occur in normal operation potential, for the reaction to proceed further the intermediate peroxide is, predominantly, catalytically decomposed.

Chemically, H_2O_2 is highly unstable and decomposed into water and oxygen:

$$2H_2O_2 = 2H_2O + O_2 \qquad (4.1)$$

The reaction (4.1) is accompanied by a free energy change of -29.42 Kcal/mole at 25^oC[136]. However, absolutely pure H_2O_2 kept in inert containers does not decompose at ordinary temperatures because of the high activation energy of the decomposition reaction. Nevertheless, the reaction can be catalysed by a number of metals and metal oxides such as platinum group metals[137,138], manganese oxides[139], and spinel oxides like cobalt-iron oxides[75] and cobalt oxides[107]. Transition metal ions often act as homogeneous catalysts for the decomposition of H_2O_2 in acid or neutral solutions[140].

The decomposition of hydrogen peroxide has been proposed to be heterogeneously catalysed on the surface of cobalt oxide catalysts in alkaline solutions[75,141]. However, it has been argued in Chapter One that such heterogeneous mechanism of H_2O_2 decomposition cannot give a satisfactory answer for the disagreements of the chemical instability

and the electrochemical activity and stability of Co_3O_4 in alkaline solutions. More recently, Lin et al.[70] demonstrated that Co^{2+} ions in very low concentration are extremely active for the decomposition of H_2O_2 in alkaline solutions. It is, therefore, of importance to study in detail the chemical kinetics and mechanism of H_2O_2 decomposition catalysed by the cobalt catalysts, especially the dissolved Co^{2+} ions in alkaline solution.

The decomposition of hydrogen peroxide on the surface of cobalt oxide catalysts in alkaline solutions can be described by the first-order reaction law[75]. The rate of the decomposition reaction is proportional to the instantaneous concentration of H_2O_2, and can be expressed by a first-order equation[142].

$$dx/dt = k_f (a - x) \qquad (4.2)$$

where a is the initial concentration of H_2O_2 and x the concentration of H_2O_2 which has been decomposed after time t.

Separating the variables and integrating, we obtain

$$-\ln(a - x) = k_f t + c \qquad (4.3)$$

where c is a constant. The initial condition is that x = 0 at t = 0, whence c = -lna, and the integrated equation becomes

$$\ln[a/(a - x)] = k_f t \qquad (4.4)$$

As the volume of oxygen decomposed is the most convenient measurable

parameter in peroxide decomposition, it is better to use oxygen volume instead of peroxide concentration in the rate equation. According to reaction (4.1), there is a proportional relationship between the O_2 volume evolved, V, and the consumed concentration of H_2O_2 at time t, which can be written as

$$V = b\,x \tag{4.5}$$

where b is a proportionality constant. Using the condition that $V = V_{max}$ at $x = a$,

$$a = V_{max}/b \tag{4.6}$$

Substituting equation (4.6) into equation (4.4), the rate equation expressed in terms of oxygen volume decomposed, can be obtained:

$$\ln[V_{max}/(V_{max} - V)] = k_f\,t \tag{4.7}$$

If $\ln[V_{max}/(V_{max} - V)]$ is plotted against time t, a straight line passing through the origin is obtained for a first-order reaction; the slope of which is the first-order rate constant, k_f, 1/s.

4.2. Experimental

Co_3O_4 has a tendency to dissolve gradually in KOH, releasing Co^{2+} into the solution[143]. It is of interest to study the influence of temperature and molarity of KOH on the solubility of $Co(OH)_2$ and Co_3O_4. $CoCl_2$ or Co_3O_4 prepared by the precipitation method was added to KOH solution (5N and 10N respectively) thermostated at various temperatures, either under N_2 or in air. The solutions were kept for over 24 hours before they were filtered. The concentration of Co^{2+} was determined by atomic absorption spectroscopy and visible spectroscopy.

The decomposition reactions of H_2O_2 on different cobalt catalysts were carried out by the conventional gasometric technique as described in section 2.1.1. The electrolyte, 5N KOH, was made from potassium hydroxide pellets (Analar) and distilled water. The alkaline solution containing 1 ppm Co^{2+} was prepared by diluting cobalt standard solution (for atomic absorption spectroscopy) in 5N KOH solution. The experimental conditions, if there is no specific notation were generally kept as

Temperature	30 ^{o}C;
5N KOH	50 ml;
1.15M H_2O_2*	5 ml;
Catalyst	50 mg;
Stirring rate	Mark 5.

*The initial concentration of H_2O_2 is therefore 0.105M.

4.3. Results and Discussions

4.3.1. Solubility of Cobalt(II) in Alkaline Solutions

Table 4.1 shows the solubility of cobalt oxides and cobalt hydroxide in KOH solutions at various test conditions. It is recognized that $Co(OH)_2$ is rather soluble in concentrated KOH solutions under an atmosphere of nitrogen. The intense blue colour of the solution observed, was due to the presence of $Co(OH)_3(H_2O)^-$ or $HCoO_2^-$ ions[130]. In the case of cobalt spinel oxide (CP), the test conditions, i.e. the KOH concentration, the temperature and the atmosphere, have little effect on the solubility of Co_3O_4. This shows that the structure of the cobalt spinel oxide is relatively stable in alkaline solutions. As shown in the table, the solubility of 3.1 at% Li-doped Co_3O_4 is essentially the same as Co_3O_4. This indicates that in this lithium doping level, the spinel structure of cobalt oxide is hardly changed, which was also confirmed by the X-ray diffraction results. However, it is not surprising that the solubility of CoO (Analar, BDH) is comparably higher, especially at high temperatures.

4.3.2. Comparison of Catalytic Activity of Various Cobalt Catalysts

Fig. 4.1 compares the rates of the peroxide decomposition in the presence of various cobalt catalysts at an initial concentration of 0.18M H_2O_2. It is shown that Co^{2+} ions in alkaline solution were extremely active toward the decomposition of H_2O_2 even at the concentration of 1 ppm ($1.7 * 10^{-5}$M) in solution. On the addition of 50 mg high surface area graphite, the catalytic activity of cobalt ions

Table 4.1

Solubility of cobalt oxides at various temperatures in KOH solutions.

Cobalt Oxide	Solubility of Co^{2+}, ppm	
	Temperature	
	$25^{o}C$	$60^{o}C$
$Co(OH)_2$, 5N KOH, N_2	22.48	61.98
$Co(OH)_2$, 10N KOH, N_2	124.04	312.59
Co_3O_4(CP), 5N KOH, Air	1.30	1.75
Co_3O_4(CP), 10N KOH, Air	1.35	2.10
Co_3O_4(CP), 5N KOH, N_2	1.41	2.01
Co_3O_4(CP), 10N KOH, N_2	1.50	2.40
Li-Co_3O_4(LDC), 5N KOH, Air	0.80	1.80
Li-Co_3O_4(LDC), 10N KOH, Air	1.54	3.60
CoO, 5N KOH, Air	1.75	8.25
CoO, 10N KOH, Air	2.00	23.75

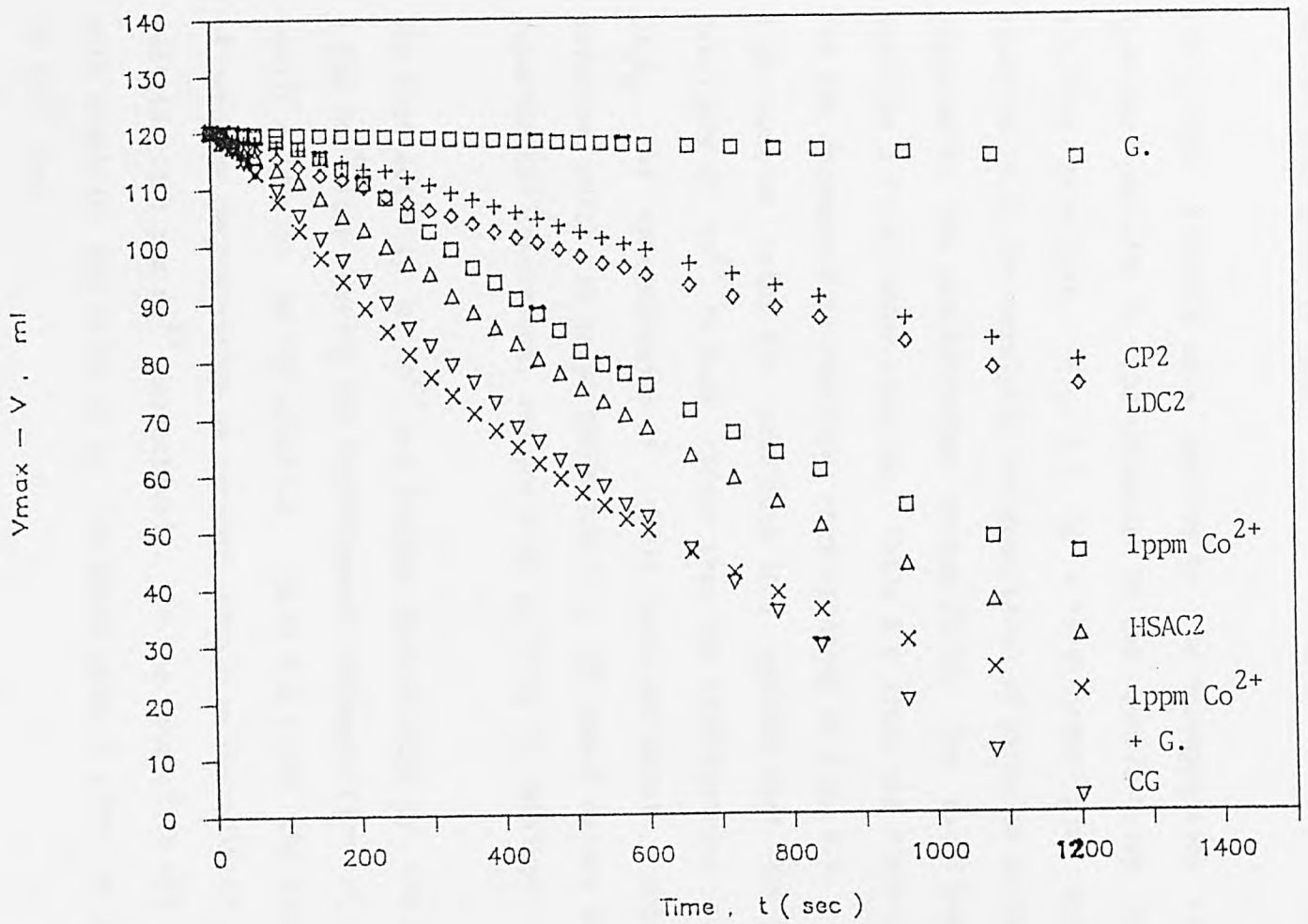

Fig. 4.1 Peroxide decomposition curves catalyzed by different cobalt catalysts. 30°C, 50ml 5N KOH and 5ml 2.0M H_2O_2.

was even higher than that of 20 wt% of high surface area Co_3O_4 mixed with graphite (HSAC2). The activity of Co^{2+} was comparable with that of the composite catalyst, 1.22 wt% HSAC coprecipitated with high surface area graphite (CG).

First-order kinetics were applied to the decomposition reactions of hydrogen peroxide in the presence of the cobalt oxide catalysts in alkaline solutions. Fig. 4.2 is a first-order plot according to equation (4.7) for catalytic decomposition of peroxide on 20 wt% Co_3O_4 prepared by the precipitation method (CP2). The excellent linearity confirms a first-order reaction. Table 4.2 lists the first-order rates for the decomposition reactions corresponding to Fig. 4.1. The evident high reaction rates for cobaltous ions confirm that the homogeneous catalysis of Co^{2+} is much faster than the heterogeneous catalysis of Co_3O_4. The concentration of cobalt ions was about 1 ppm in 5N KOH solution, which is below the solubility of cobalt oxides at the same experimental conditions, and yet high activity is obtained.

The high activity of Co^{2+} was further demonstrated by the addition of 1 ppm Co^{2+} ions during the heterogeneous decomposition of peroxide on cobalt oxides in 5N KOH solution. Table 4.3 gives the reaction rates of peroxide decomposition on various cobalt oxides with or without the addition of 1 ppm Co^{2+} respectively. In the case of 10 wt% Co_3O_4 mixed with graphite, the value of k_f increases about 5 times in the presence of Co^{2+} ions.

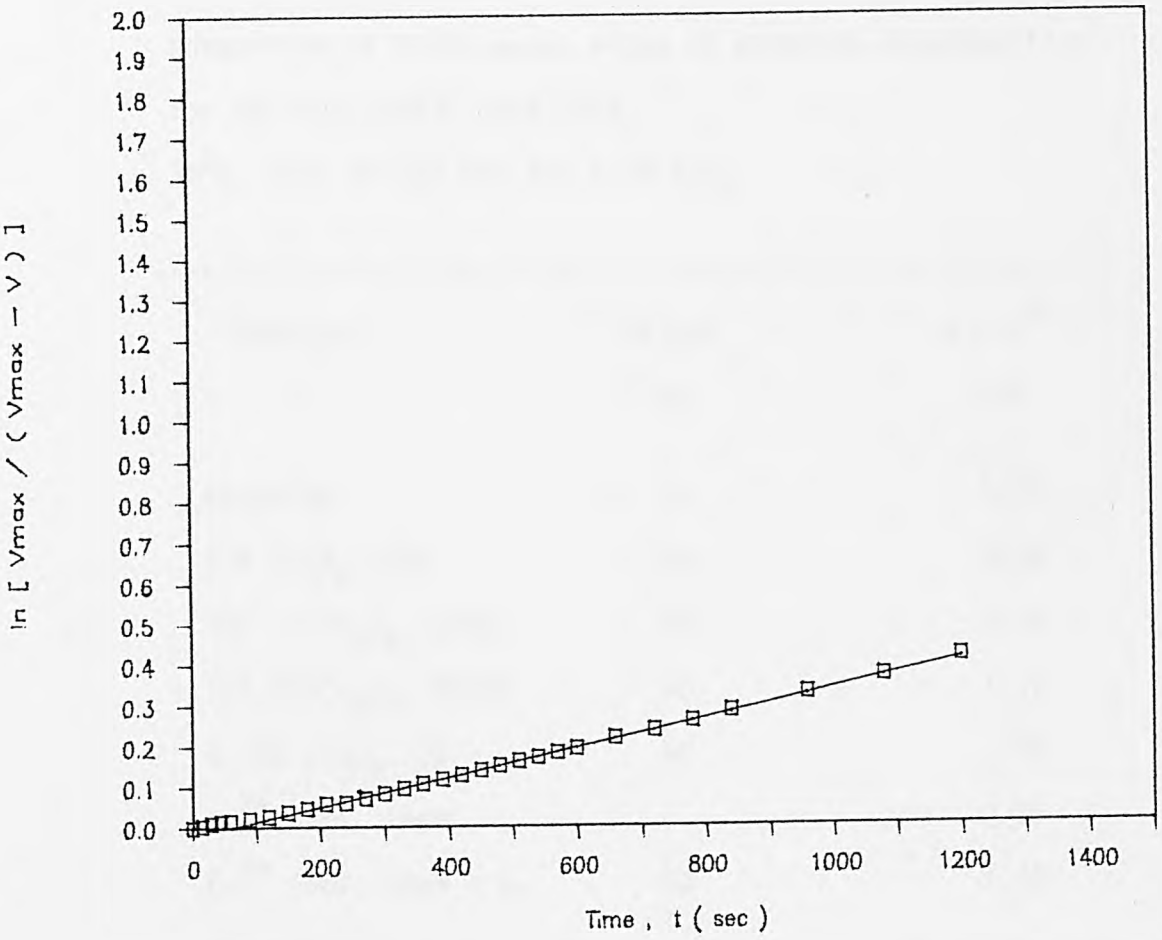

Fig. 4.2 First-order plot of peroxide decomposition by 20 wt% Co_3O_4 mixed with graphite, CP2.
$30^{\circ}C$, 50ml 5N KOH and 5ml 2.0M H_2O_2.

Table 4.2

Comparison of first-order rates of peroxide decomposition for various cobalt catalysts.

$30^{o}C$, 50ml 5N KOH and 5ml 2.0M H_2O_2.

Catalyst	Weight mg	k_f*10^3 1/s
Graphite	50	0.07
20% Co_3O_4, CP2	50	0.36
20% Li-Co_3O_4, LDC2	50	0.38
20% HSACo_3O_4, HSAC2	50	1.11
1.22% Co_3O_4, CG	50	1.60
Co^{2+} Ions, 1ppm		0.97
Co^{2+} Ions, 1ppm + G.	50	1.45

G. -- High surface area graphite.

Table 4.3

Comparison of first-order rates of peroxide decomposition with or without addition of 1 ppm Co^{2+}.

$30^{o}C$, 50ml 5N KOH and 5ml 1.15M H_2O_2.

Catalyst	Weight, mg	k_f*10^3, 1/s
Graphite	50	0.07
10% Co_3O_4	50	0.22
*10% Co_3O_4	50	1.08
20% Co_3O_4	50	0.50
*20% Co_3O_4	50	1.02
10% $HSACo_3O_4$	50	0.79
*10% $HSACo_3O_4$	50	1.51
20% $HSACo_3O_4$	50	2.00
*20% $HSACo_3O_4$	50	2.58
1.22% Co_3O_4, CG	50	2.03
Co^{2+} Ions, 1 ppm		0.71
Co^{2+} Ions, 1 ppm + G.	50	1.26

* With the addition of 1 ppm Co^{2+} ions.

G. -- High surface area graphite.

4.4. Characteristics of Homogeneous Catalysis by Co^{2+} Ions

4.4.1. Effect of Addition of Graphite

Fig. 4.3 shows the effect of the addition of high surface area graphite on the decomposition reaction of H_2O_2 catalysed by 1 ppm Co^{2+} at 30^oC in 5N KOH solution. The initial concentration of peroxide was 0.105M. From corresponding first-order rate plots, given in Fig. 4.4, the reaction rate of Co^{2+} was obviously increased by the presence of high surface area graphite, though the graphite is practically inert to the peroxide decomposition[21,23]. In the decomposition reactions of H_2O_2, in the presence of Co^{2+} homogeneous catalysts, the decomposition reaction undergoes an induction period. This induction period can be said to be greatly reduced on the addition of graphite and by the increase of temperatures.

There are two possible reasons responsible for the existence of the induction period. One is that peroxide decomposition is virtually a heterophase reaction. Because the energy required for the creation of a new phase is less in the region of some kinds of interphase, than inside a bulk solution, the homogeneous decomposition of H_2O_2 in solution mainly takes place in the region of these interphases: e.g. reaction vessel and oxygen bubbles evolved. The decomposition is, therefore, initially inhibited due to the lack of interphases. As such, the addition of high surface area graphite creates a large number of interphases and thus reduces the induction period.

The other reason is the possible participation of free radicals in the peroxide decomposition[144]. It has been shown that the initial rate

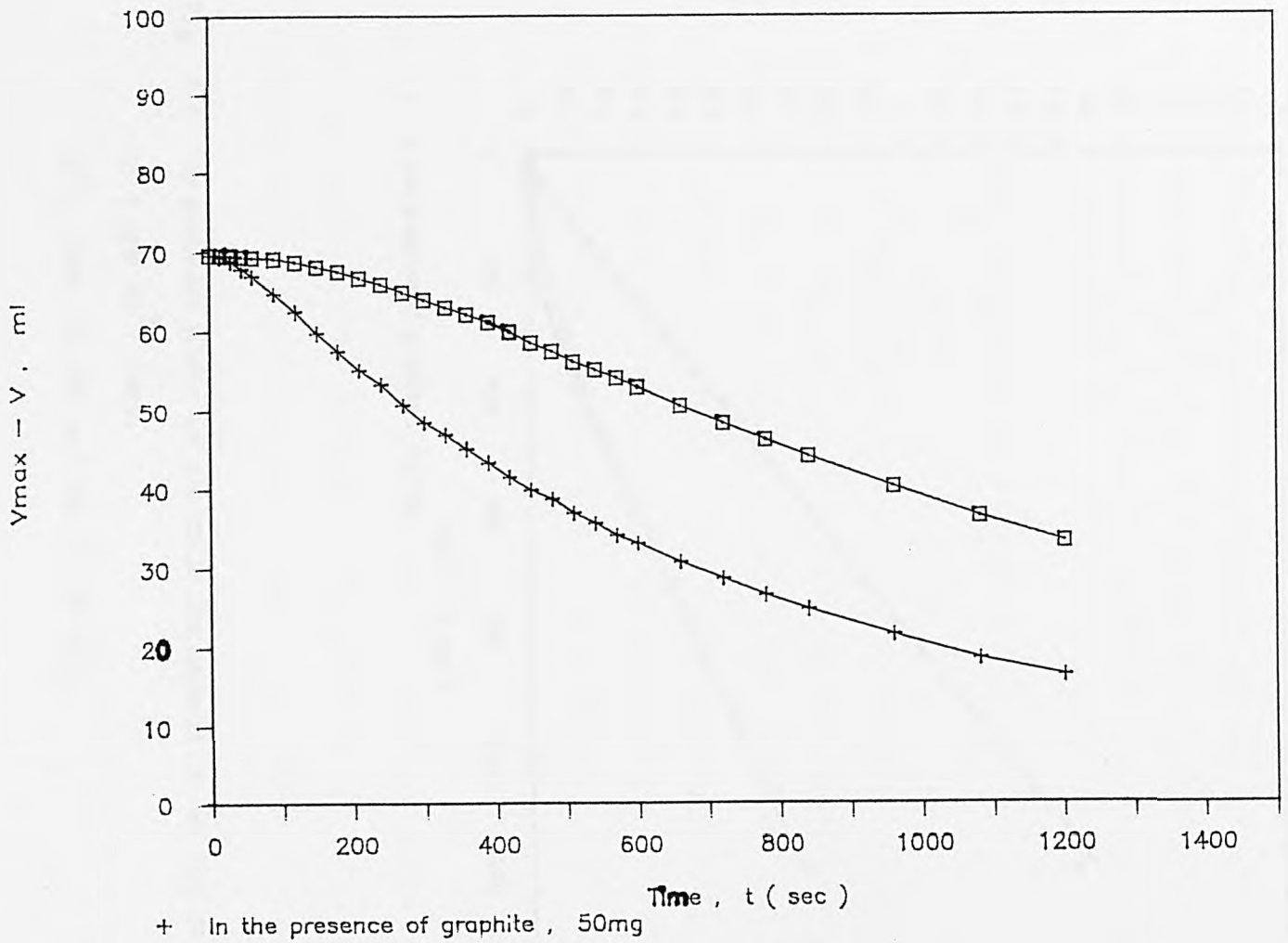

Fig. 4.3 Peroxide decomposition curves in the presence of 1 ppm Co^{2+} ions. 30°C, 50ml 5N KOH and 5ml 1.15M H_2O_2.

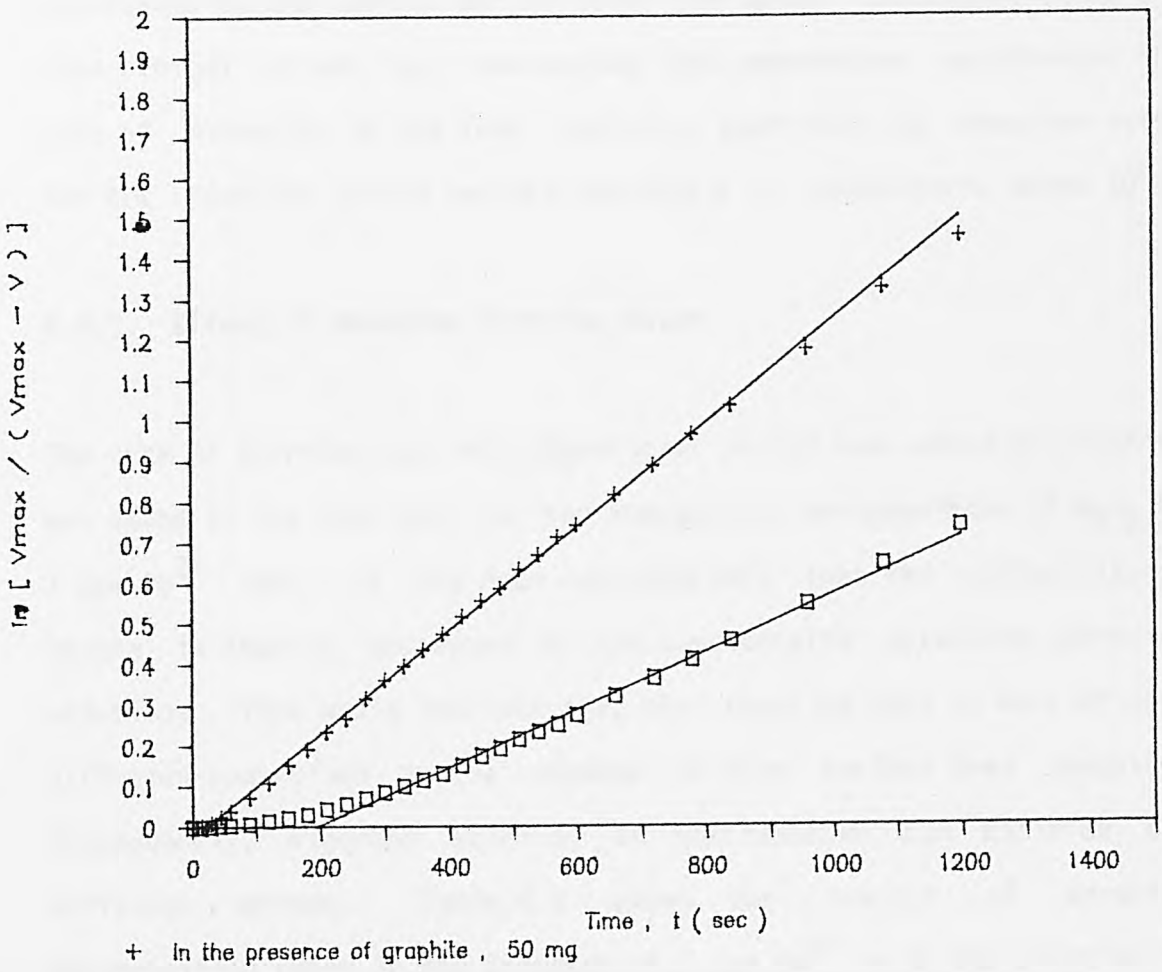

Fig. 4.4 First-order plots of peroxide decomposition in the presence of 1 ppm Co^{2+} ions.
$30^{0}C$, 50ml 5N KOH and 5ml 1.15M H_2O_2.

of the formation of superoxide radical is influenced by the temperature and the concentration of H_2O_2[144]. In the presence of graphite particles, the short period at the start of the reaction would correspond to the period during which the steady concentration of the free radical is set up. Increasing the temperature accelerates the rate of formation of the free radicals, such that the reaction rate, and the induction period becomes negligible at temperatures above 40^oC.

4.4.2. Effect of Reaction Stirring Rates

The rate of stirring was only significant in the case where no graphite was added to the catalyst, in the homogeneous decomposition of H_2O_2 by 1 ppm Co^{2+} ions. It has been reported[145] that the diffusivity of oxygen is sharply decreased in the concentrated potassium hydroxide solutions. This would indicate that the reaction rate is more or less diffusion-controlled in the absence of high surface area graphite. Consequently, vigorous stirring of the reaction can minimize the diffusion effect. Table 4.4 shows the results of peroxide decomposition rates in the presence of 1 ppm Co^{2+} in 5N KOH solution at 30^oC, at various stirring rates. The mechanical stirring rates were expressed by the speed indicator knob on the mechanical stirrer. The higher the position number, the faster the stirring speed. As expected, the reaction rate was truly independent of the stirring rates if the high surface area graphite was added in the reaction solution.

Table 4.4

Effect of reaction stirring rates on the peroxide decomposition reaction in the presence of 1 ppm Co^{2+}. $30^{o}C$, 50ml 5N KOH and 5ml 1.15M H_2O_2.

Stirring Rate	$k_f * 10^4$, 1/s	
	In absence of graphite	In presence of graphite, 50mg
0	4.54	12.39
1	6.75	11.16
5	7.11	12.56

Table 4.5

Activation energy of the peroxide decomposition in the presence of 1 ppm Co^{2+} ions.
50ml 5N KOH and 5ml 1.15M H_2O_2.

	E_a, KJ/mol	A
In absence of graphite	64.15	$1.22*10^8$
In presence of graphite, 50mg	59.15	$0.65*10^8$

4.4.3. Effect of Temperature

The effect of temperature on reaction rate is described by the famous Arrhenius equation which can be written as follows.

$$(4.8) \qquad d\ln k_f/dT = E_a/RT^2$$

If E_a, the Arrhenius activation energy, is a constant with respect to temperature, integration results in

$$(4.9) \qquad \ln k_f = -E_a/RT + \ln A$$

or

$$(4.10) \qquad k_f = A \cdot \exp(-E_a/RT)$$

where A is a 'frequency factor' and T the absolute temperature.

The rates of homogeneous decomposition of H_2O_2 in the presence of 1 ppm Co^{2+} were determined at various temperatures. The initial concentration of peroxide was kept as 0.105M. Fig. 4.5 shows the logarithmic plots of the first-order rate constants against the reciprocal of absolute temperature. The apparent activation energies for peroxide decomposition catalysed by 1 ppm Co^{2+} were calculated from the value of the slopes obtained, using equation (4.9). The results are shown in Table 4.5.

The addition of high surface area graphite to the Co^{2+} ions does not show any remarkable effect on activation energy, as can be seen in Table 4.5. This result could indicate that the peroxide decomposition is initiated by the radical in the presence of Co^{2+} in solution. It

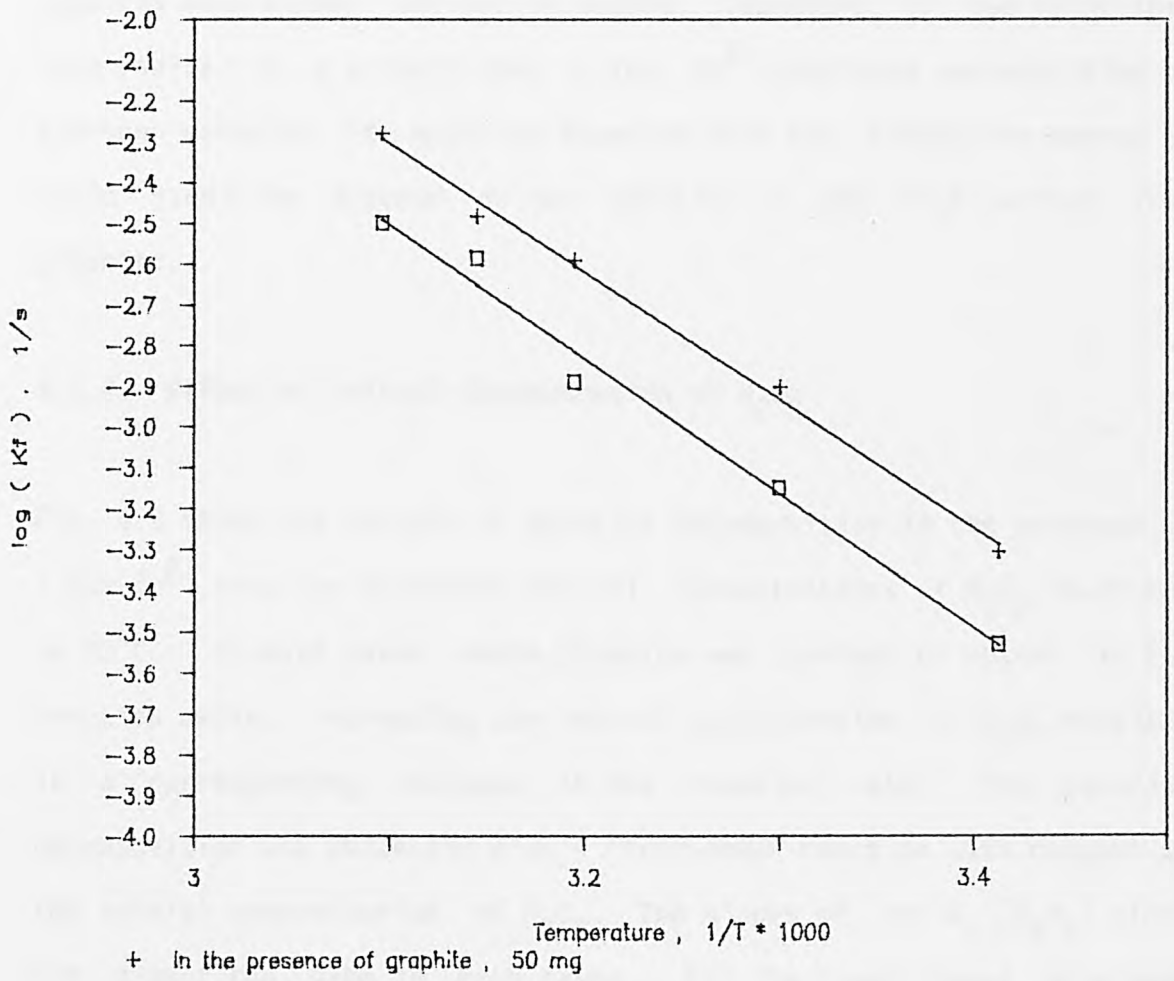

Fig. 4.5 Activation energy plots for peroxide decomposition in the presence of 1 ppm Co^{2+} ions.
50ml 5N KOH and 5ml 1.15M H_2O_2.

can, therefore, be said that addition of graphite would not increase the rate of the formation of free radical, which in itself is physically unreasonable. The formation of free radicals generally requires much higher activation energy. Therefore, if the split into free radical is a primary step in the Co^{2+}-catalysed decomposition of hydrogen peroxide, it would be expected that the activation energy E_a could hardly be altered on the addition of the high surface area graphite.

4.4.4. Effect of Initial Concentration of H_2O_2

Fig. 4.6 shows the results of peroxide decomposition in the presence of 1 ppm Co^{2+} ions for different initial concentrations of H_2O_2 in 5N KOH at 30^oC. In both cases where graphite was present or absent in the reaction media, increasing the initial concentration of H_2O_2 resulted in a corresponding increase in the reaction rate. The peroxide decomposition was evidently also a first-order reaction with respect to the initial concentration of H_2O_2. The slopes of the k_f-$[H_2O_2]$ plots are almost the same in both cases. For the same reason as stated earlier, this first-order relationship between the decomposition rate and the initial H_2O_2 concentration is also independent of the presence of high surface area graphite.

From the collision theory[146], the reaction rate is dependent on the number of effective collisions which have sufficient energy of the right kind for reaction. With vigorous stirring it is suggested that decomposition of H_2O_2 in solution is not controlled by the diffusion process. By direct e.s.r. (electron spin resonance) spectroscopy, Nagy et al.[147] showed that initial rate of superoxide formation was

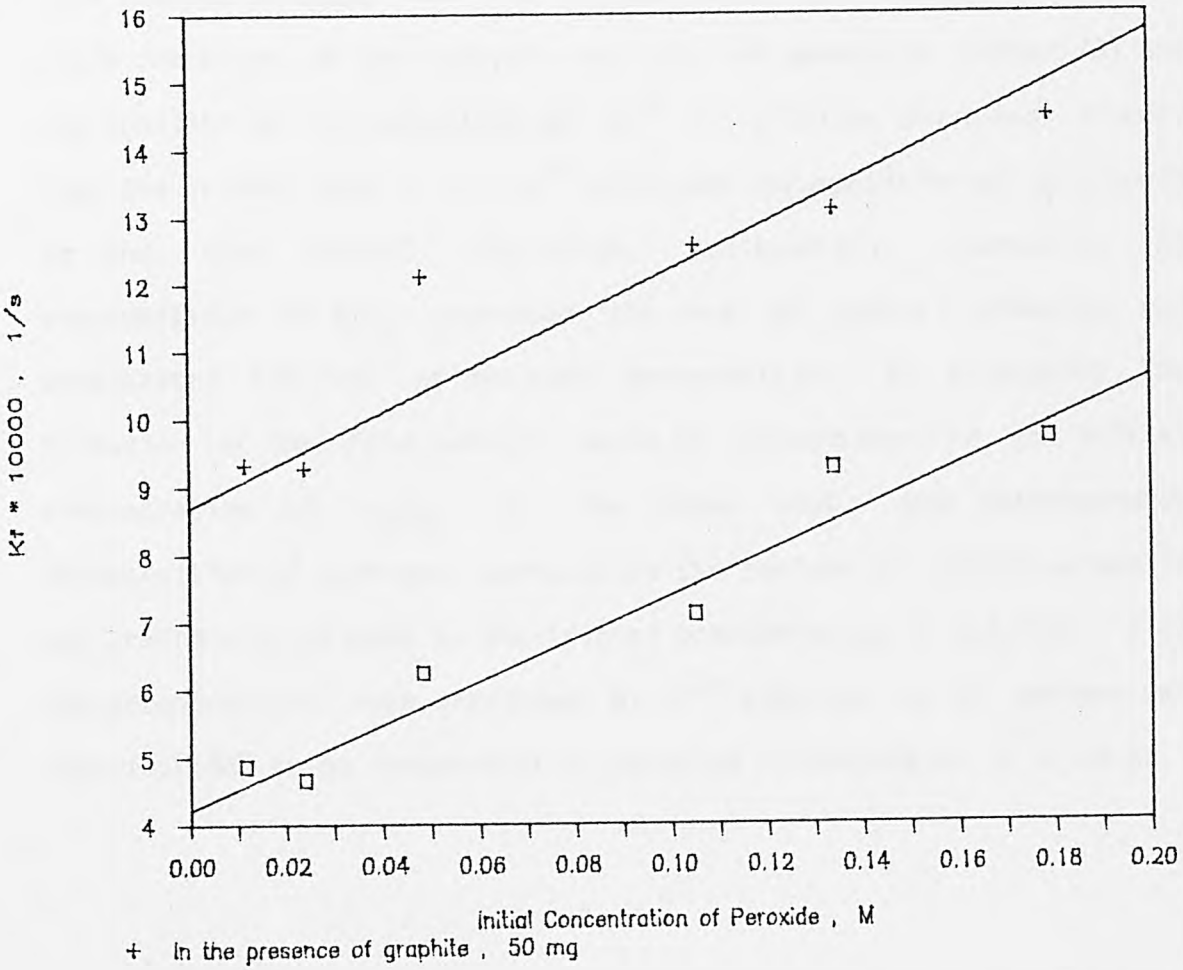

Fig. 4.6 Dependence of first-order rate k_f on the initial concentration of hydrogen peroxide in the presence of 1 ppm Co^{2+} ions. 30°C and 50ml 5N KOH.

proportional to the 0.6 power of the concentration of hydrogen peroxide in the OsO_4-catalysed reaction. In aqueous solutions the hydroxyl radicals are generated by the reaction between hydrogen peroxide and some transition metal ions like ferrous ions[140]. Because the further chain reactions of the radical and H_2O_2 are generally faster[73] and the equilibrium concentration of Co^{2+} in alkaline solutions is very low, the primary step in the Co^{2+}-catalysed decomposition of H_2O_2 would be the free radical initiation. Consequently, increasing the concentration of H_2O_2 increased the rate of radical formation and accelerated the rate of peroxide decomposition. At this point the formation of the free radical would be proportional to the initial concentration of H_2O_2. On the other hand, the heterogeneous decomposition of hydrogen peroxide on the surface of cobalt oxides is not practically related to the initial concentration of H_2O_2[23]. Also the decomposition rate catalysed by Cr^{3+} adsorbed on Al surface was reported[148] to be independent of peroxide concentration in solution.

4.5. Qualitative Estimation of HO_2^- Concentration during Oxygen Reduction

As shown in Fig. 4.6, the homogeneous catalytic activity of Co^{2+} in KOH is proportional to the initial concentration of H_2O_2. It is therefore necessary to examine the changes of concentration of intermediate peroxide during oxygen reduction in an applied system.

Theoretically, this can be done by means of cyclic voltammetry technique. Under conditions of a single reversible electrode process and semi-infinite linear diffusion to a planar electrode of constant area, the peak current I_p at 25^oC is given by the Randles-Sevcik equation[149]

$$(4.11) \qquad I_p = 2.69*10^5 n^{3/2} A c_b D^{\frac{1}{2}} v^{\frac{1}{2}}$$

where c_b is the concentration in solution, A the surface area of the electrode and v the sweep rate. The peak current density is directly proportional to the bulk concentration of diffusion species. However, since the applied system studied here is a gas diffusion graphite electrode with a porous structure, coupled with the complex pathways of oxygen reduction (see Fig. 1.1), this equation could only be qualitatively applied.

A cyclic voltammogram of O_2 reduction on a Teflon-bonded graphite electrode in KOH was recorded between the potentials of 1000 to 600 mV vs. DHE at a sweep rate of 10 mV/s. This is shown as Fig. 4.7. The anodic part of the curve corresponds to the reaction of the intermediate peroxide[150]. Thus the accumulation of peroxide at the

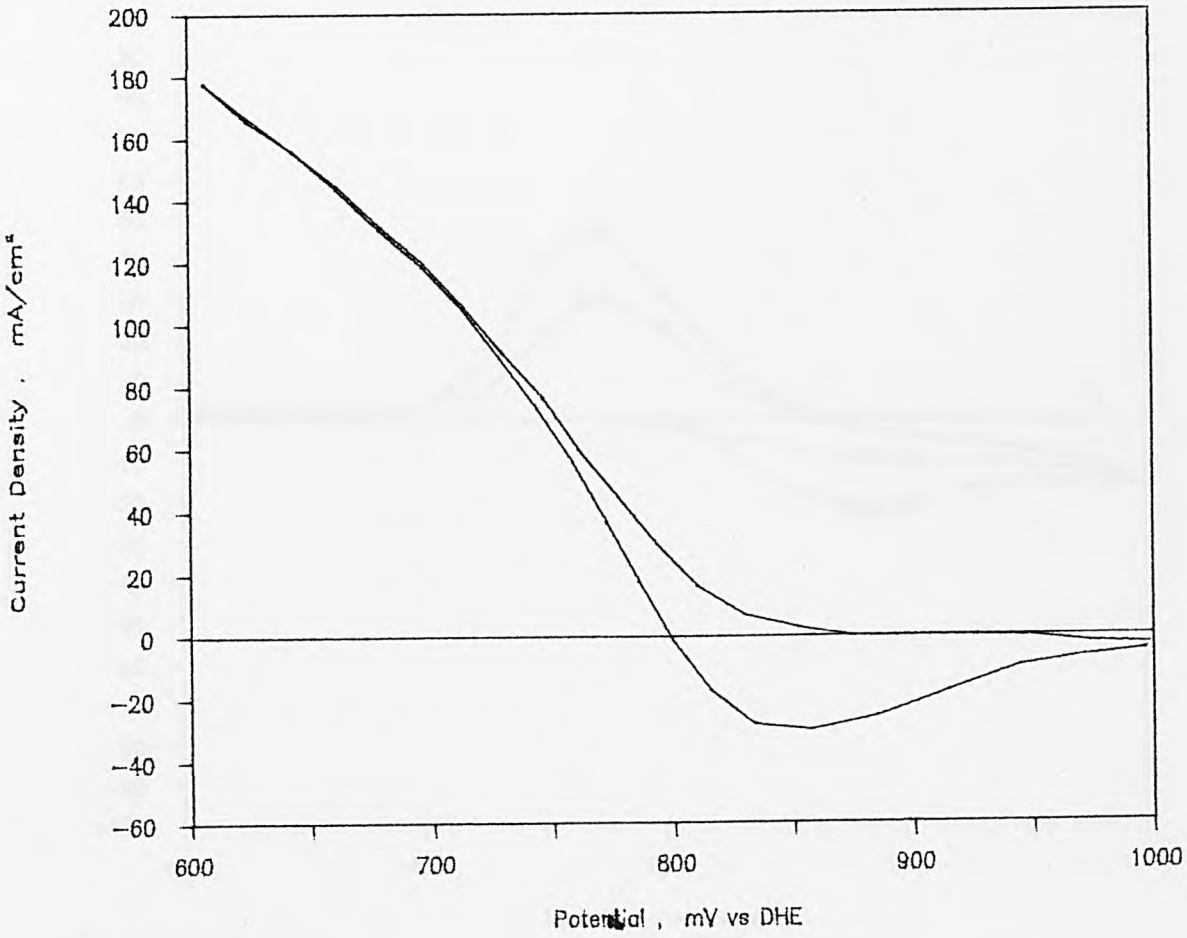

Fig. 4.7 Voltammetric curve recorded for a floating Teflon-bonded graphite electrode at sweep rate of 10 mV/sec. 25°C, 5N KOH and using air as feed gas.

PAGE MISSING IN ORIGINAL

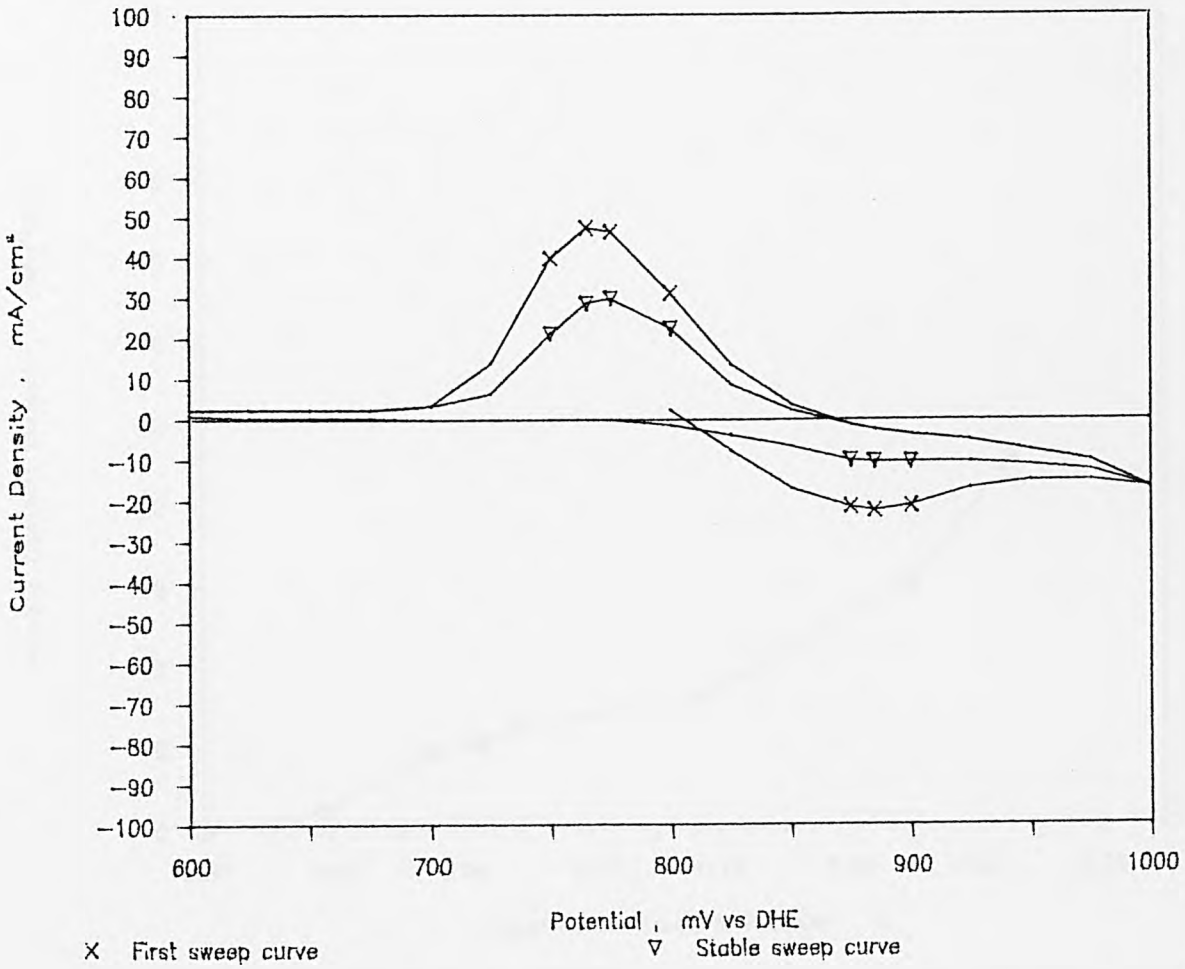

Fig. 4.8 Voltammetric curves recorded for an immersed Teflon-bonded graphite electrode in the absence of dissolved O_2 at sweep rate of 10 mV/sec.
$25^{0}C$, 5N KOH and 0.069M H_2O_2.

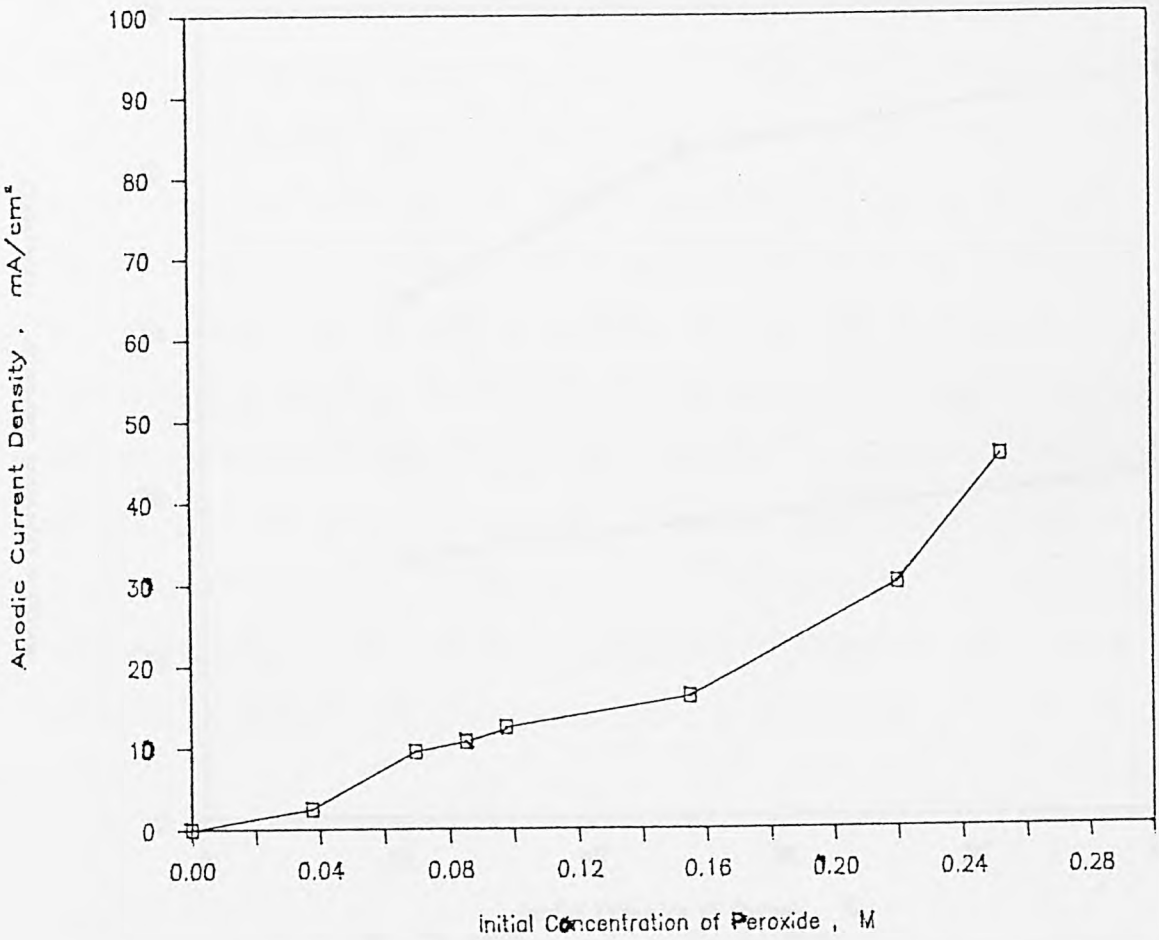

Fig. 4.9 Relationship between the anodic peak current density and the initial concentration of H_2O_2 in the voltammetric measurement on an immersed Teflon-bonded graphite electrode at sweep rate of 10 mV/sec.
25°C and 5N KOH.

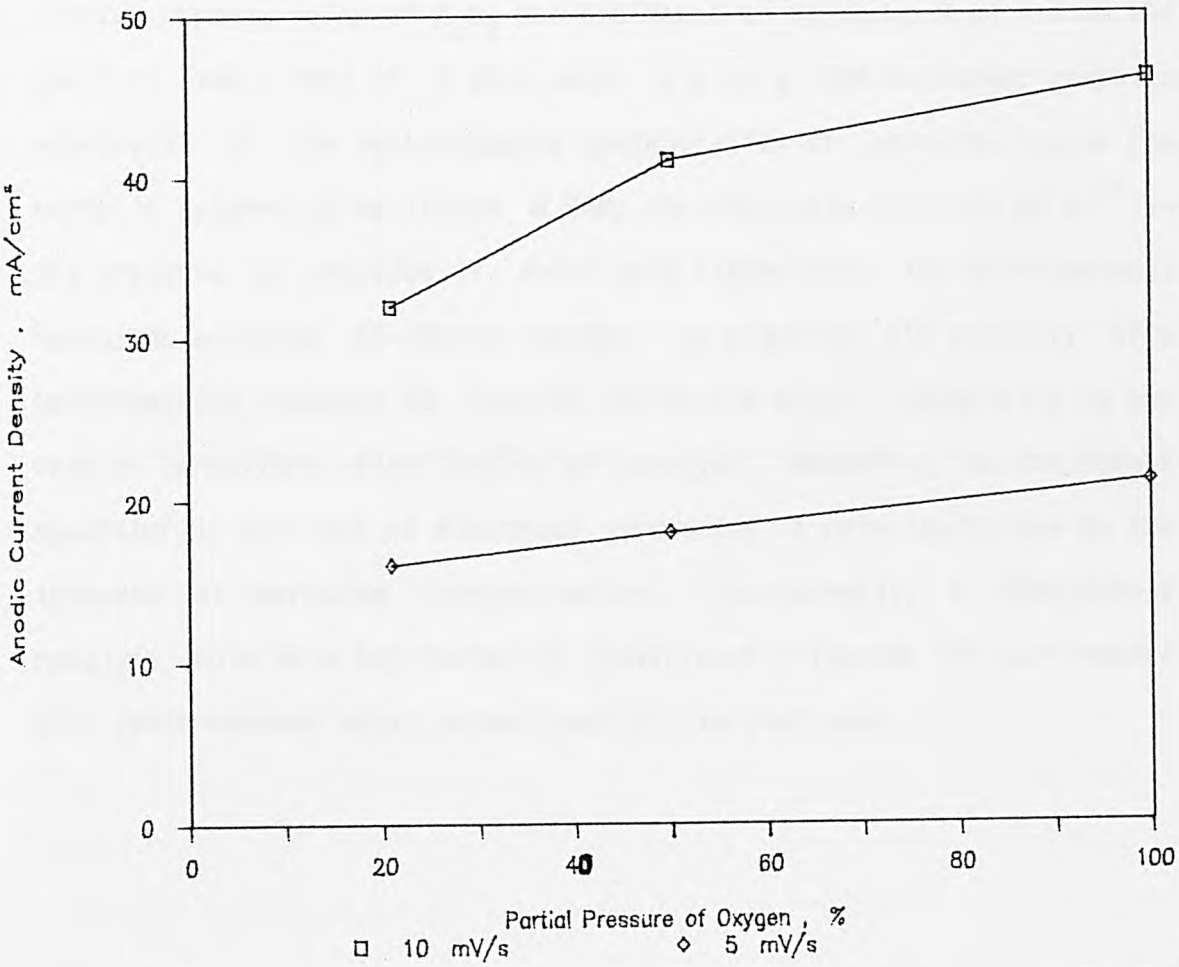

Fig. 4.10 Relationship between the anodic peak current density and the partial pressure of oxygen in the voltammetric measurement on a floating Teflon-bonded graphite electrode.
25°C and 5N KOH.

The results of the linear potential sweep indicates that the surface concentration of HO_2^- formed in the reduction of oxygen on a porous graphite electrode is very high. Qualitatively, the magnitude of surface concentration of H_2O_2 was estimated to be about 0.1M inside the pores at sweep rate of 5 mV/s under air on a Teflon-bonded graphite electrode. If the instantaneous concentration of peroxide inside the pores is assumed to be around 0.08M, the catalytic activity of Co^{2+} in the presence of graphite is still much higher than the heterogeneous catalytic activity of cobalt oxides. In practice the activity of a heterogeneous catalyst is limited inside the pores, especially in the case of nonuniform distribution of catalyst. According to the Nernst equation[11] the loss of electrode potential is principally due to the increase of peroxide concentration. Consequently, a homogeneous catalyst could be a key factor to significantly improve the performance of a Teflon-bonded metal oxide/graphite air electrode.

After discussion with [redacted] it was agreed that an alternative hypothesis of the hydrogen peroxide decomposition mechanism should be considered. Taking into account the processes involved, the homogeneous-heterogeneous mechanism as outlined earlier was considered, and the results of this analysis is given in Appendix B, which suggest that it is more appropriate than the one given in p. 81-87.

4.6. Concluding Remarks

Various mechanisms have been proposed for the decomposition of H_2O_2 over a variety of heterogeneous and homogeneous catalysts. Most of them are based on the pioneering work of Haber and Weiss[73,152] who first invoked a chain mechanism involving free radicals for the decomposition of H_2O_2 by Fe^{2+} ions. According to the classical Haber-Weiss mechanism, the dissociation of H_2O_2 was believed to occur as a result of electron donation from the metal substrate to the solution and the formation of the perhydroxyl radical, $HO_2^{\cdot}$, could also occur due to electron transfer to the metal[153].

Experimentally, the participation of free radicals in the decomposition of H_2O_2 by homogeneous catalysis can be verified by using fast-flow technique coupled with e.s.r. spectroscopy. It was reported that the free radical, $HO_2^{\cdot}$, was detected on the $VOSO_4$ - H_2O_2 system[154] and $TiCl_3$ - H_2O_2 system[155] in acid solutions. It has been shown[144,147] that the hydroxyl radical, $OH^{\cdot}$, and superoxide radical, O_2^{-}, are formed in the OsO_4-catalysed decomposition of H_2O_2 in weakly alkaline solution. On the other hand, the superoxide radicals were also spectroscopically observed in the aqueous phase in the decomposition of H_2O_2 on some metals[156] and metal oxides[157] as well.

In the Co^{2+}-catalysed decomposition of H_2O_2 in alkaline solutions, the first step could be electron donation by the catalyst to yield an $OH^{\cdot}$ radical as follows:

$$(4.12) \qquad Co^{2+} + H_2O_2 \rightarrow Co^{3+} + OH^{-} + OH^{\cdot}$$

On the other hand if the cobalt catalyst accepts an electron (the possible active site will be Co^{3+} ion) a $HO_2^{\cdot}$ radical would be produced according to the following equation:

$$(4.13) \qquad Co^{3+} + H_2O_2 \dashrightarrow Co^{2+} + H^+ + HO_2^{\cdot}$$

The relative rate of the reactions (4.12) and (4.13) may depend on the redox potential of the catalyst in the pH of the medium[74]. However, it has been proved[75,141] that the active centre in the cobaltite oxide catalysts for peroxide decomposition is the divalent cobalt ions. In alkaline medium the activity of Co^{3+} is much lower than that of Co^{2+} because the former is hardly dissolved in the solution. Therefore, the radical is initiated primarily by the reaction (4.12). The hydroxyl radical produced induces the further chain reactions. Reaction steps may be written as follows:

$$(4.12) \qquad Co^{2+} + H_2O_2 \xrightarrow{k_1} Co^{3+} + OH^- + OH^{\cdot}$$

$$(4.14) \qquad OH^{\cdot} + H_2O_2 \xrightarrow{k_2} H_2O + HO_2^{\cdot}$$

$$(4.15) \qquad HO_2^{\cdot} + H_2O_2 \xrightarrow{k_3} H_2O + OH^{\cdot} + O_2$$

$$(4.16) \qquad HO_2^{\cdot} \overset{k_4}{=\!=} H^+ + O_2^-$$

$$(4.17) \qquad Co^{3+} + O_2^- \xrightarrow{k_5} Co^{2+} + O_2$$

where k_4 is the dissociation constant of $HO_2^{\cdot}$ adsorbed on the Co^{3+} ions. To derive the kinetic law for the decomposition reaction, the steady-state approximation[152,158] could be applied to the reaction radical. This approximation assumes that during all, or almost all, of the reaction the concentration of the free radical in the system

remains essentially constant. In the Co^{2+}-catalysed decomposition of H_2O_2, this assumption would be valid if the free radicals are present in very low concentration[159]. Compared with the Fe^{2+}-H_2O_2 reaction in acidic solutions[140], the concentration of the hydroxyl radical in this system is much lower mainly due to the low solubility of Co^{2+} in alkaline solution. It therefore follows that

$$(4.18) \qquad \frac{d[OH^{\cdot}]}{dt} = 0$$

$$= k_1(Co^{2+})(H_2O_2) - k_2[OH^{\cdot}](H_2O_2) + k_3[HO_2^{\cdot}](H_2O_2)$$

where the parenthesis [] denotes the concentration of species in steady state. The decomposition rate of H_2O_2 can then be expressed as

$$(4.19) \qquad r = - d(H_2O_2)/dt$$

$$= k_1(Co^{2+})(H_2O_2) + k_2[OH^{\cdot}](H_2O_2) + k_3[HO_2^{\cdot}](H_2O_2)$$

Equations (4.18) and (4.19) are solved for the rate equation, giving

$$(4.20) \qquad - d(H_2O_2)/dt = 2k_2[OH^{\cdot}](H_2O_2)$$

Compared with the first-order equation (4.2), it is obvious that the first-order constant could be written as

$$(4.21) \qquad k_f = 2k_2[OH^{\cdot}]$$

It has been demonstrated that the k_f is proportional to the initial concentration of hydrogen peroxide. Consequently, this equation means

that the steady state concentration of $OH^{\cdot}$ is proportional to the initial concentration of H_2O_2. This relationship could be expressed by an empirical expression:

$$(4.22) \qquad [OH^{\cdot}] = a[H_2O_2]_i^{x}$$

where $[H_2O_2]_i$ is the initial concentration of peroxide, a is a constant and x is in the range of 0 to 1. Introducing a new kinetic first-order constant, k, the first-order constant k_f is related to $[H_2O_2]_i$ as follows:

$$(4.23) \qquad k_f = k\,[H_2O_2]_i^{x}$$

Therefore, the value of x should satisfy the condition that the kinetic first-order rate constant k is independent of the initial concentration of H_2O_2. The relationship between k and $[H_2O_2]_i$ is shown in Fig. 4.11 with x value of 0.32. The value of k_f is corresponding to that in Fig. 4.6. It seems that the initiation of the free radical is principally dependent on the initial concentration of peroxide. Consequently, the decomposition of hydrogen peroxide in the presence of 1 ppm Co^{2+} in alkaline solutions is a first-order reaction with respect to the concentration of H_2O_2 and is also proportional to the 0.32 power of the initial concentration.

In the heterogeneous decomposition of peroxide on cobalt-iron oxide system, the apparent activation energy is reported in the range of 37.68 to 46 KJ/mol in alkaline solutions[23]. Compared with the heterogeneous catalytic systems, the apparent activation energy E_a in the Co^{2+}-catalysed decomposition of H_2O_2 is relatively higher as shown

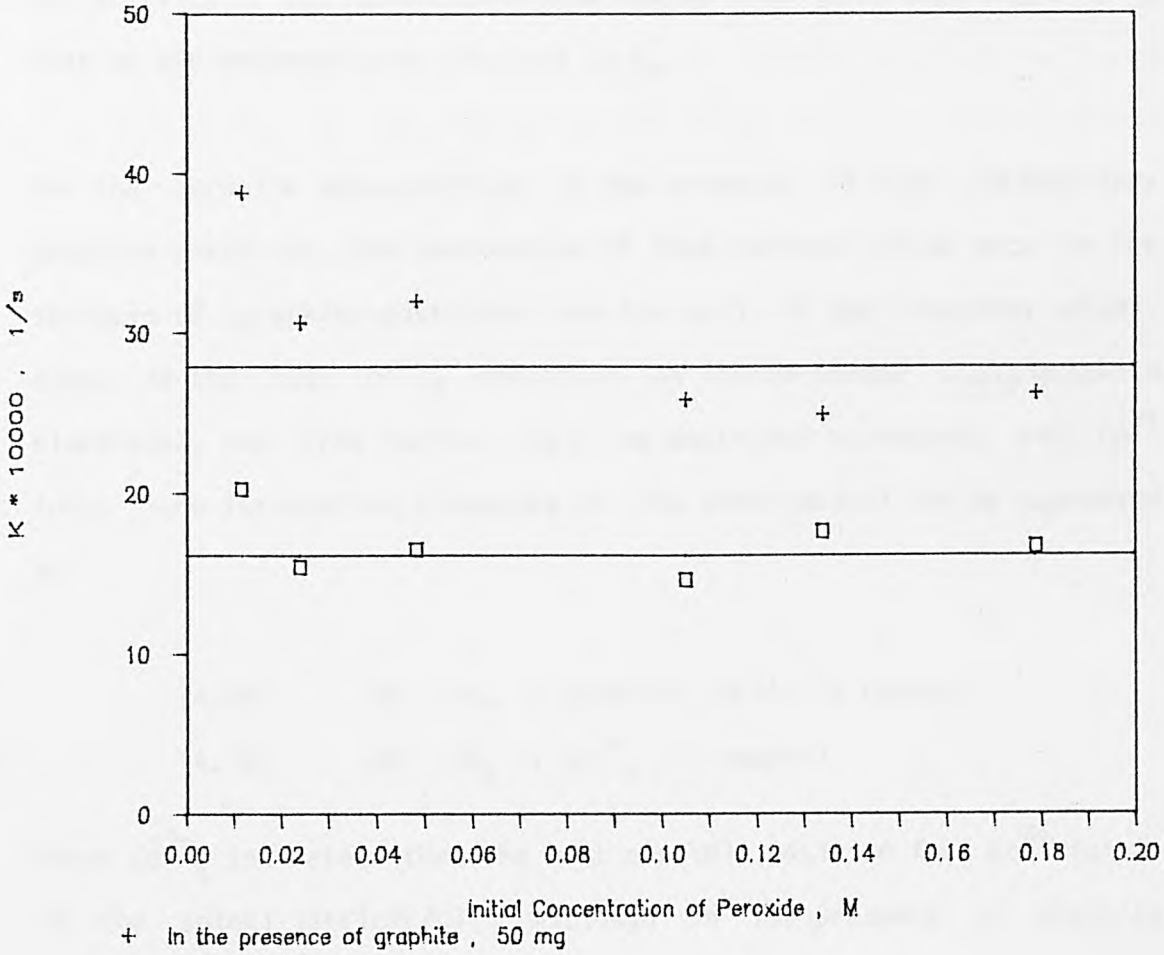

Fig. 4.11 Dependence of kinetic first-order rate k on the initial concentration of hydrogen peroxide in the presence of 1 ppm Co^{2+} ions with x value of 0.32.
30^0C and 50ml 5N KOH.

in Table 4.5. The reason could be that the split of H_2O_2 into free radicals in the first step usually requires high activation energy. Because of the low activation energy of the subsequent chain reaction, the activity of the homogeneous catalyst Co^{2+} is still much higher than that of the heterogeneous catalyst Co_3O_4.

For the peroxide decomposition in the presence of high surface area graphite particles, the termination of free radicals could occur on the surfaces of graphite particles and the wall of the reaction vessel. Also, in the case of O_2 reduction on Teflon-bonded Co_3O_4/graphite electrodes, the free radical could be destroyed on contact with Co^{3+} ions. Such termination processes of the free radical can be expressed as

(4.24) $OH^{\cdot}$, $OH_2^{\cdot}$ + graphite, wall --> removal

(4.25) $OH^{\cdot}$, $OH_2^{\cdot}$ + $Co^{3+}{}_s$ --> removal

where $Co^{3+}{}_s$ indicates that the most possible position for Co^{3+} ion is in the spinel lattice[70]. Although in the presence of graphite appreciable deviations occurred, the kinetic first-order constant k is generally independent on the $[H_2O_2]_i$ as shown in Fig. 4.11. This fact could indicate that the radicals are destroyed to a negligible extent by the effect of graphite.

However, in the Co^{2+}-catalysed decomposition of intermediate H_2O_2 during oxygen reduction on Teflon-bonded Co_3O_4/graphite electrodes, the termination of the free radicals on the Co^{3+} ions could be very significant. In this particular case the assumption of steady state conditions cannot be applied. Nevertheless, the primary step could still be the free radical initiation, with the subsequent chain

reactions interrupted. It is emphasized that the homogeneous decomposition of intermediate peroxide is rather localized at the regions near the electrochemical active sites inside the pores. Due to the effect of Co^{3+} as an inhibitor, the decomposition of peroxide on cobalt oxide catalysts behaves like a first-order reaction and is in fact independent of the initial concentration of peroxide as reported in literature. This marked characteristic of the Co^{2+}-catalysed decomposition of peroxide indicates that the catalytic activity of cobalt oxides is strongly affected by the distribution of the catalysts.

CHAPTER FIVE

A.C. IMPEDANCE -- THEORETICAL CONSIDERATIONS

5.1. Introduction

The principle of a.c. impedance is basically dependent on the fact that current-overpotential relations are virtually linear at low overpotentials[96,115,160]. When an electrochemical system is subjected to a small alternating signal (usually sinusoidal), the response, as an impedance, corresponding to the frequency of the signal is determined. In representing and analysing the a.c. impedance, the phasor concept is used in which voltages and currents are thought of as rotating vectors and are represented in the complex plane.

Hence in a linear system, if the signal is sinusoidal, e.g. an a.c. current,

$$(5.1) \qquad I = I_m \sin\omega t$$

where ω is the angular frequency, I the instantaneous value of current (representing alternating value only) and I_m the amplitude; then the voltage response of the system must also be sinusoidal and of the same angular frequency ω, but different in amplitude and phase from the current. This can be represented as

$$(5.2) \qquad V = V_m \sin(\omega t + \phi)$$

where ϕ is the phase angle. The complex impedance Z is defined as the relation between the phasors, V and I

$$(5.3) \qquad Z = V/I$$

or can be separated into a real part of resistive component, ReZ, and an imaginary part of capacitive component, ImZ, in complex plane by introducing a complex rotation j, j being $(-1)^{\frac{1}{2}}$:

$$Z = ReZ - jImZ \tag{5.4}$$

For a parallel connection of impedances it is convenient to use the complex admittance Y which is defined as the reciprocal impedance:

$$\begin{aligned} Y &= 1/Z \\ &= ReY + jImY \end{aligned} \tag{5.5}$$

where ReY and ImY are the real component and imaginary component of the complex admittance as well.

5.2. A.C. Impedance for a Simple Electrode Reaction

Consider a simple electrode reaction:

$$O + ne = R \tag{5.6}$$

where there are no other interfacial processes such as adsorption, chemical catalytic reaction, etc. involved. The complex impedance of such an electrode reaction can be represented by the well-known Randles equivalent circuit[83] shown in Fig. 5.1. In the circuit R_{so} is the ohmic resistance of solution, C_{dl} the double layer capacity, R_{ct} the charge transfer resistance and Z_w the Warburg impedance representing the impedance due to the diffusion of reactant and product. In this case the complex impedance is usually broken up into non-faradaic

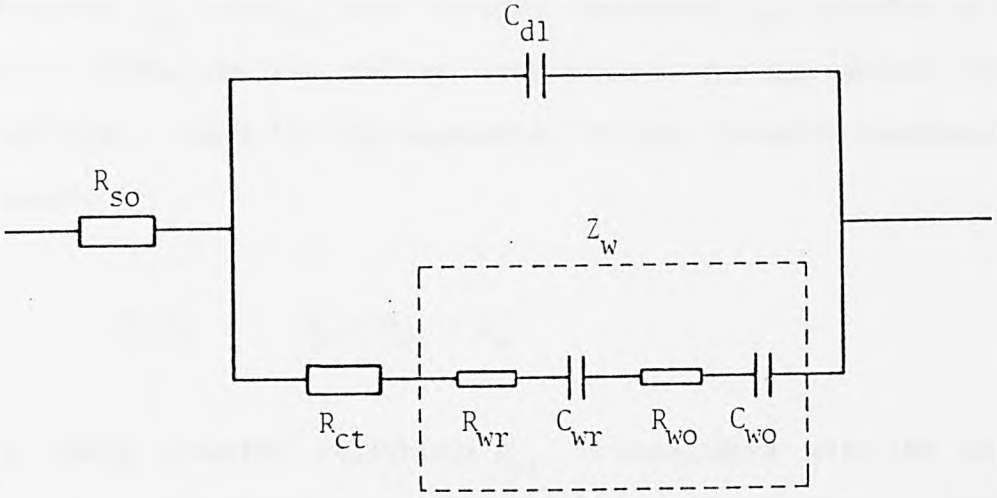

Fig. 5.1 Randles equivalent circuit for a simple electrode reaction.

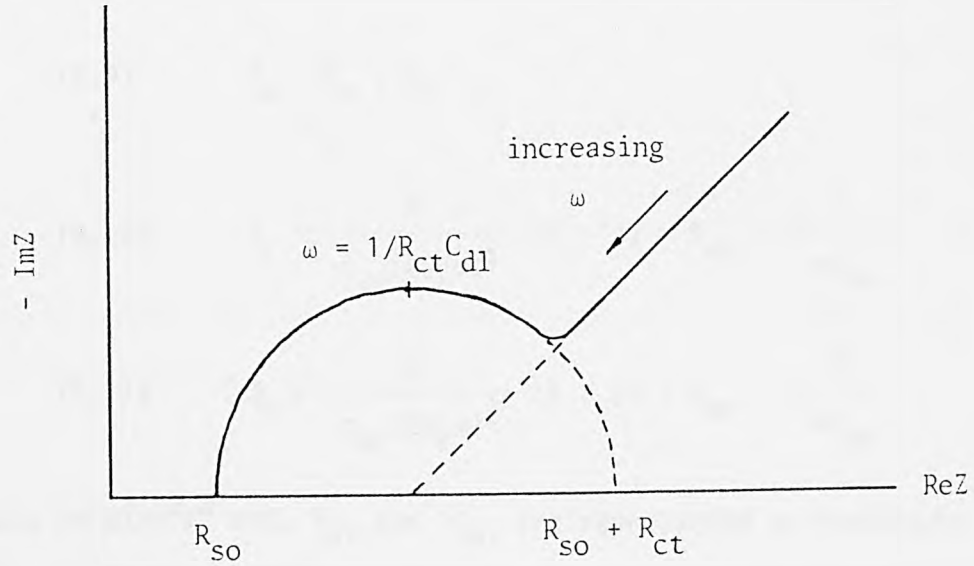

Fig. 5.2 Complex impedance plot for the circuit of Fig. 5.1.

impedance, C_{dl} and R_{so}, and faradaic impedance, Z_f. Solution of Fick's second diffusion law, taking into account the appropriate boundary conditions, leads to the expression of the faradaic impedance (see Appendix A):

$$Z_f = R_{ct} + Z_w \tag{5.7}$$

The charge transfer resistance R_{ct} is associated with the exchange current density i_o for a planar diffusion field by the following equation,

$$R_{ct} = \frac{RT}{nF} * \frac{1}{i_o} \tag{5.8}$$

The Warburg impedance Z_w, however, comprises of diffusion impedance of reactant and product

$$Z_w = Z_o + Z_r \tag{5.9}$$

where

$$Z_o = \frac{g}{c_{so}(2D_o\omega)^{\frac{1}{2}}}(1 - j) = R_{wo} - j\frac{1}{\omega C_{wo}} \tag{5.10}$$

$$Z_r = \frac{g}{c_{sr}(2D_r\omega)^{\frac{1}{2}}}(1 - j) = R_{wr} - j\frac{1}{\omega C_{wr}} \tag{5.11}$$

g equals to RT/n^2F^2 and, R_{wi} and C_{wi} are represented as resistance and capacitance components of the Warburg impedance for species i respectively.

$$R_{wi} = \frac{1}{\omega C_{wi}} = \frac{g}{c_{si}(2D_i\omega)^{\frac{1}{2}}} \tag{5.12}$$

where c_{si} is the surface concentration of species i. It is obvious that both C_{wi} and R_{wi} are not independent of frequency, which is distinct from the normal concept of capacitance and resistance.

Introducing the Warburg coefficient, W as

$$(5.13) \qquad W = W_o + W_r = \frac{g}{c_{so}(2D_o)^{\frac{1}{2}}} + \frac{g}{c_{sr}(2D_r)^{\frac{1}{2}}}$$

where W_o and W_r are Warburg coefficients of reactant and product respectively. Consequently, the faradaic impedance of equation (5.7) can also be expressed as

$$(5.14) \qquad Z_f = R_{ct} + W\omega^{-\frac{1}{2}}(1 - j)$$

Therefore, from Fig. 5.1 it follows that the complex impedance is

$$(5.15) \qquad Z = R_{so} + \frac{1}{j\omega C_{dl} + \frac{1}{R_{ct} + W\omega^{-\frac{1}{2}} - jW\omega^{-\frac{1}{2}}}}$$

A graphical method to analyse impedance parameters has been given by Sluyters and co-workers[161,162,163].

At very high frequency, the Warburg impedance becomes unimportant in relation to charge transfer resistance R_{ct}, and equation (5.15) can be simplified and separated into real and imaginary parts.

$$(5.16) \qquad Z = R_{so} + \frac{R_{ct}}{1+\omega^2 C_{dl}^2 R_{ct}^2} - j\frac{\omega C_{dl} R_{ct}^2}{1+\omega^2 C_{dl}^2 R_{ct}^2}$$

A plot of the real component of this impedance against its imaginary component is a single semicircle as depicted in Fig. 5.2. The charge transfer resistance R_{ct} can be directly obtained from the diameter of the semicircle and the angular frequency which corresponds to the maximum of the semicircle is thus related to the double layer capacity C_{dl} and R_{ct}.

$$\omega_{max} = 1/C_{dl}R_{ct} \qquad (5.17)$$

At low frequency, where the diffusion process often predominates, the complex impedance reduces to

$$Z = R_{so} + R_{ct} + W\omega^{-\frac{1}{2}} - j(W\omega^{-\frac{1}{2}} + 2W^2C_{dl}) \qquad (5.18)$$

According to this equation, the complex plot is a straight line with a slope of 45^{o}. Therefore, an impedance plot in the whole frequency region has the form shown in Fig. 5.2. In a real system the shapes obtained in the complex impedance plane depend on the relative magnitudes of R_{ct}, W and C_{dl}.

5.3. Analytical Methods

Information about the kinetics and mechanism of an electrochemical reaction mainly comes from the faradaic impedance, which is generally assumed to be separable from non-faradaic impedance, i.e. double layer charging process. This prior separation of double layer capacity from the cell impedance is based on the assumption[163] that the charging process is frequency independent and the faradaic impedance is generally dependent on the frequency. However, Delahay[164] pointed out that this prior separation is not justified theoretically for the non-steady state conditions. A complicated expression[165] for the total interfacial impedance can be derived in spite of introducing a set of double layer parameters. Epelboin and Keddam[166] approached this problem by studying electrode reaction of extreme cases, pure diffusion and pure reaction control processes. It was shown that the distinguishing between the double layer capacity and faradaic impedance is favourable in the presence of a supporting electrolyte and in the absence of specific adsorption of reactant and product. At present it is still convenient to accept that this prior separation of the double layer capacitance (C_{dl}) is applicable to oxygen reduction in air electrodes.

5.3.1. Separation of Solution Resistance, R_{so}

As shown in equation (5.16), the solution resistance R_{so} can always be determined by the impedance of the cell at sufficient high frequencies. The validity of the value of R_{so} obtained can be checked with measurements at different potentials in the presence of supporting electrolyte. In Table 5.1 the solution resistance of a Teflon-bonded

Table 5.1

R_{so} and $C_{dl,app}$ values of a Teflon-bonded graphite electrode measured at various potentials.

$25^{o}C$, 5N KOH and using air as feed gas.

Potential mV vs DHE	R_{so} $Ohm \cdot cm^2$	$C_{dl,app}$ $\mu F/cm^2$
ocv	0.296	1865
925	0.296	1941
900	0.296	1989
850	0.299	2284
825	0.289	1993
800	0.300	2217

graphite electrode was determined at different potentials, at 25°C in 5N KOH solution under air, in the frequency range of 6-10 KHz. It is shown that the values of R_{so} were almost constant.

Vectorial subtraction of R_{so} from the complex impedance Z yields the electrode impedance Z_e.

5.3.2. Separation of Double Layer Capacitance, C_{dl}

Admittance representation can be, appropriately, used to separate the double layer capacity and the faradaic impedance[167]. The electrode admittance of Fig. 5.1 is given by

$$Y_e = j\omega C_{dl} + 1/Z_f \qquad (5.19)$$

Assuming C_{dl} is independent of frequency, dividing above equation by the angular frequency results in

$$Y_e/\omega = jC_{dl} + 1/\omega Z_f \qquad (5.20)$$

Consequently, extrapolation of Y_e/ω, or the equivalent of the parallel capacitive component of the electrode impedance C_p[168], to infinite frequency should result in the value of C_{dl}. Such an extrapolation procedure is given in Fig. 5.3 for a Teflon-bonded graphite electrode at open circuit under air. The values of apparent double layer capacitance $C_{dl,app}$ determined at different polarization potentials are also given in Table 5.1.

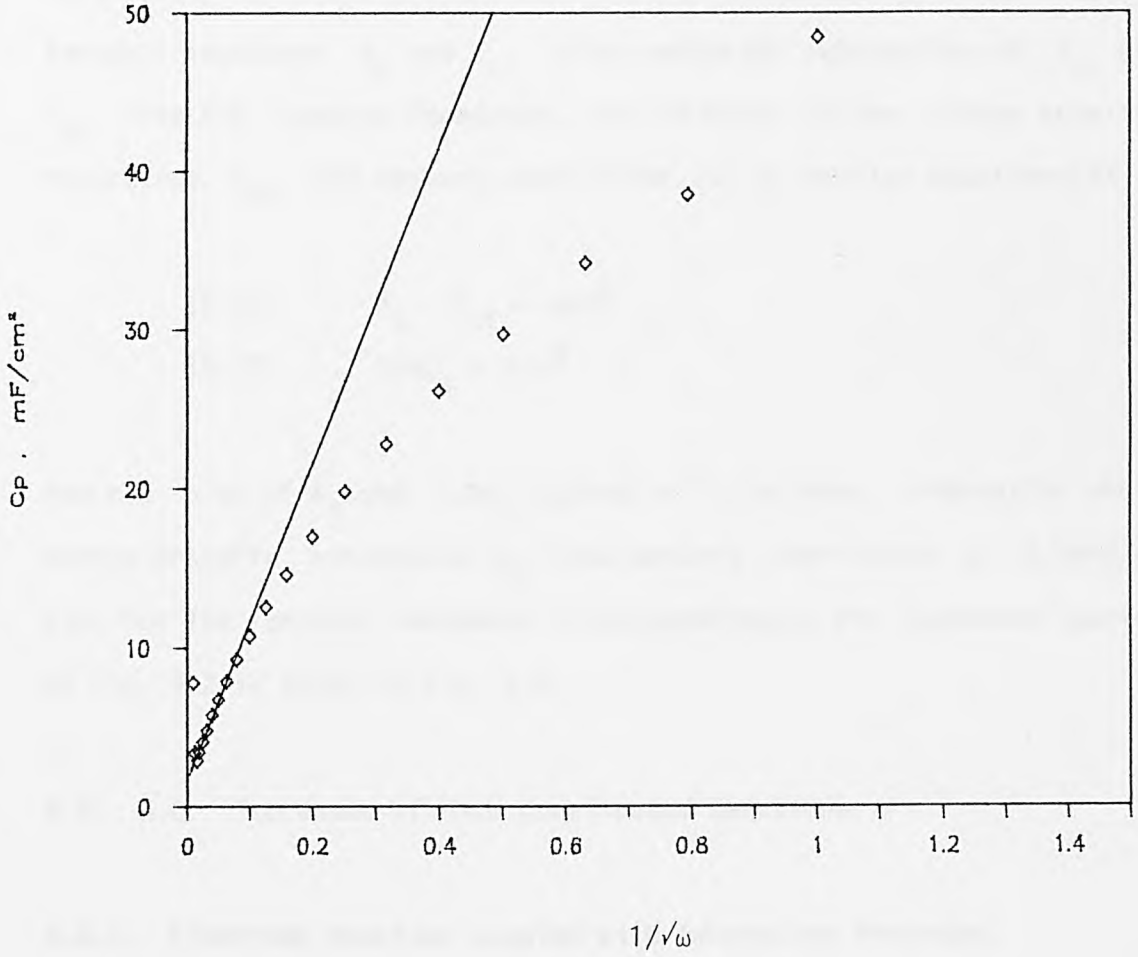

Fig. 5.3 Determination of apparent double layer capacity, $C_{dl,app}$, of a graphite electrode by extrapolation of C_p at high frequency at ocv. The intercept gave $C_{dl,app}$ value of 1.87 mF/cm^2.

25^{0}C, 5N KOH and using air as feed gas.

5.3.3. Determination of R_{ct} and W

The determination of kinetic parameters R_{ct} and W from faradaic impedances is based on Randles method. The serial components of faradaic impedance R_s and C_s, after vectorial subtraction of R_{so} and C_{dl} from the complex impedance, are related to the charge transfer resistance, R_{ct}, and Warburg coefficient, W, by Randles equations[83].

$$R_s = R_{ct} + W/\omega^{\frac{1}{2}} \qquad (5.21)$$

$$1/\omega C_s = W/\omega^{\frac{1}{2}} \qquad (5.22)$$

Hence a plot of R_s and $1/\omega C_s$ against $\omega^{-\frac{1}{2}}$ discloses information about charge transfer resistance R_{ct} and Warburg coefficient W. A Randles plot for the faradaic impedance corresponding to the impedance spectra of Fig. 5.2 is shown in Fig. 5.4.

5.4. A.C. Impedance of More Complicated Reactions

5.4.1. Electrode Reaction Coupled with Adsorption Processes

When an electrode reaction is complicated by adsorption of intermediate[169,170] and of reactants, the impedance responses deviate from the classical Randles behaviour. The first attempt to account for reactant adsorption in impedance theory was made by Laitinen and Randles[171], by assuming two pathways for charge transfer, viz. via the adsorbed species and via the non-adsorbed species. However, the treatment of impedance of an electrode reaction coupled with adsorption of reactant or product is usually dependent on the degree of adsorption. For the case of very weak adsorption, the adsorption

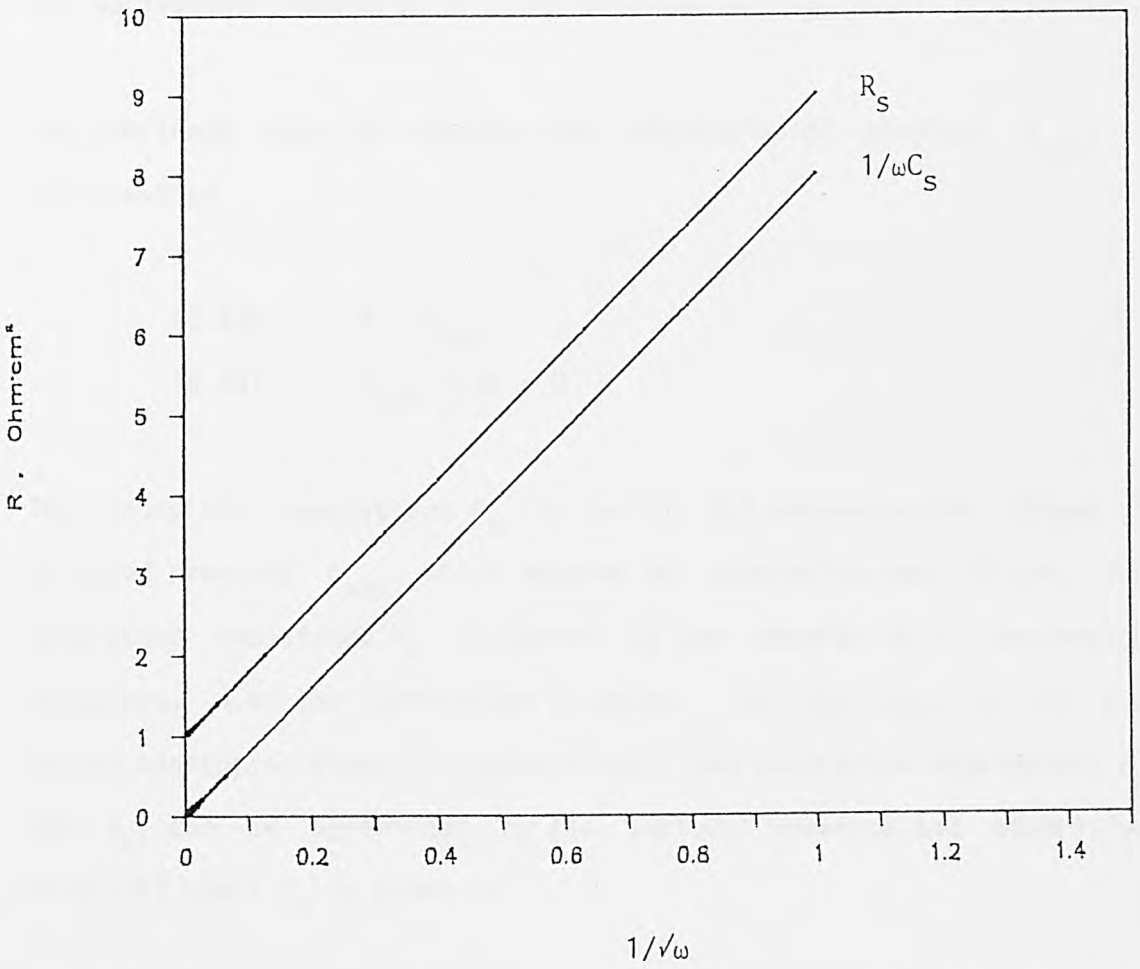

Fig. 5.4 Theoretical Randles plots for a simple electrode reaction. R_{ct} = 1 ohm·cm^2; $W_r = W_o$ = 4 ohm·cm^2/s$^{\frac{1}{2}}$.

impedance can be simplified to a capacity parallel to the double layer capacity[172]. Generally, the adsorption impedance can be represented by an additional frequency-independent capacitance and resistance in the equivalent circuit[92,173,174] as shown in Fig. 5.5.

The electrode reaction coupled with adsorption of reactant, O_{ads}, is expressed as

$$(5.23) \qquad O = O_{ads}$$

$$(5.24) \qquad O_{ads} + ne = R$$

The adsorption capacitance C_a is due to the concentration change of adsorbed reactant O_{ads}, which depends on adsorption equilibrium. The adsorption resistance R_a is caused by the adsorption or desorption processes, i.e. the adsorption kinetics. In the cases of not too strong adsorption (specific adsorption), the adsorption impedances, C_a and R_a, can be determined by the surface coverage and adsorption rate[174] where C_a is given by

$$(5.25) \qquad C_a = n^2F^2c_o{}^s/RT$$

and R_a by

$$(5.26) \qquad R_a = RT/n^2F^2c_o{}^sk$$

where $c_o{}^s$ is the surface coverage of species O_{ads} and k is the rate constant of the adsorption reaction. From the equivalent circuit of Fig. 5.5, the faradaic impedance is written as

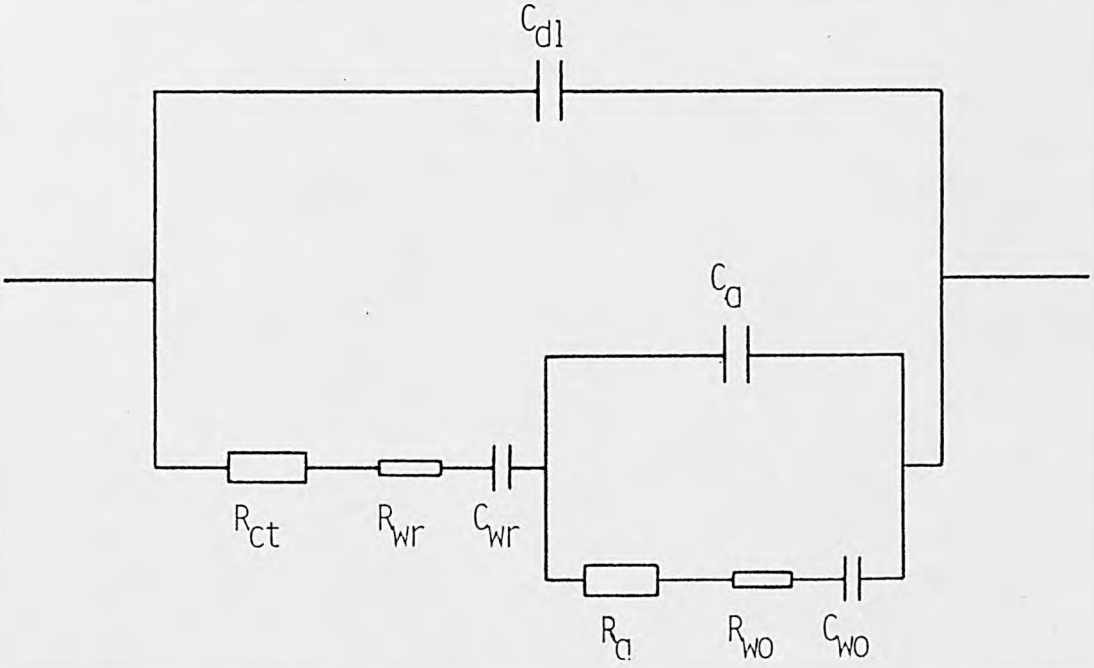

Fig. 5.5 Equivalent circuit for an electrode reaction coupled with adsorption processes.

$$(5.27) \qquad Z_f = R_{ct} + W_r\omega^{-\frac{1}{2}}(1-j) + \frac{1}{j\omega C_a + \dfrac{1}{R_a + W_o\omega^{-\frac{1}{2}}(1-j)}}$$

A theoretical Randles response of the faradaic impedance for the electrode reaction coupled with the adsorbed reactant O_{ads} was calculated with a set of parameters as shown in Fig. 5.6. Two distinct linear regions are observed at high frequencies and at low frequencies respectively. It is also noted that the capacity component of the faradaic impedance lies above the resistant component as frequency increases. These characteristics could be used to distinguish adsorption process from other chemical interfacial reactions.

5.4.2. Electrode Reaction Coupled with a Catalytic Reaction

Consider an electrode reaction coupled with a catalytic reaction

$$(5.5) \qquad O + ne = R$$

$$(5.28) \qquad R + Z \underset{k_2}{\overset{k_1}{=\!=}} O + Y$$

where k_1 and k_2 are forward and backward reaction rate constants respectively. The catalytic reaction is assumed to be a first-order reaction. The differential equations are similar to the case of electrode reaction coupled with a chemical reaction[175], expressing as

$$(5.29) \qquad \frac{\partial c_r}{\partial t} = D_r \frac{\partial^2 c_r}{\partial x^2} - k_1 c_r + k_2 c_o$$

$$(5.30) \qquad \frac{\partial c_o}{\partial t} = D_o \frac{\partial^2 c_o}{\partial x^2} + k_1 c_r - k_2 c_o$$

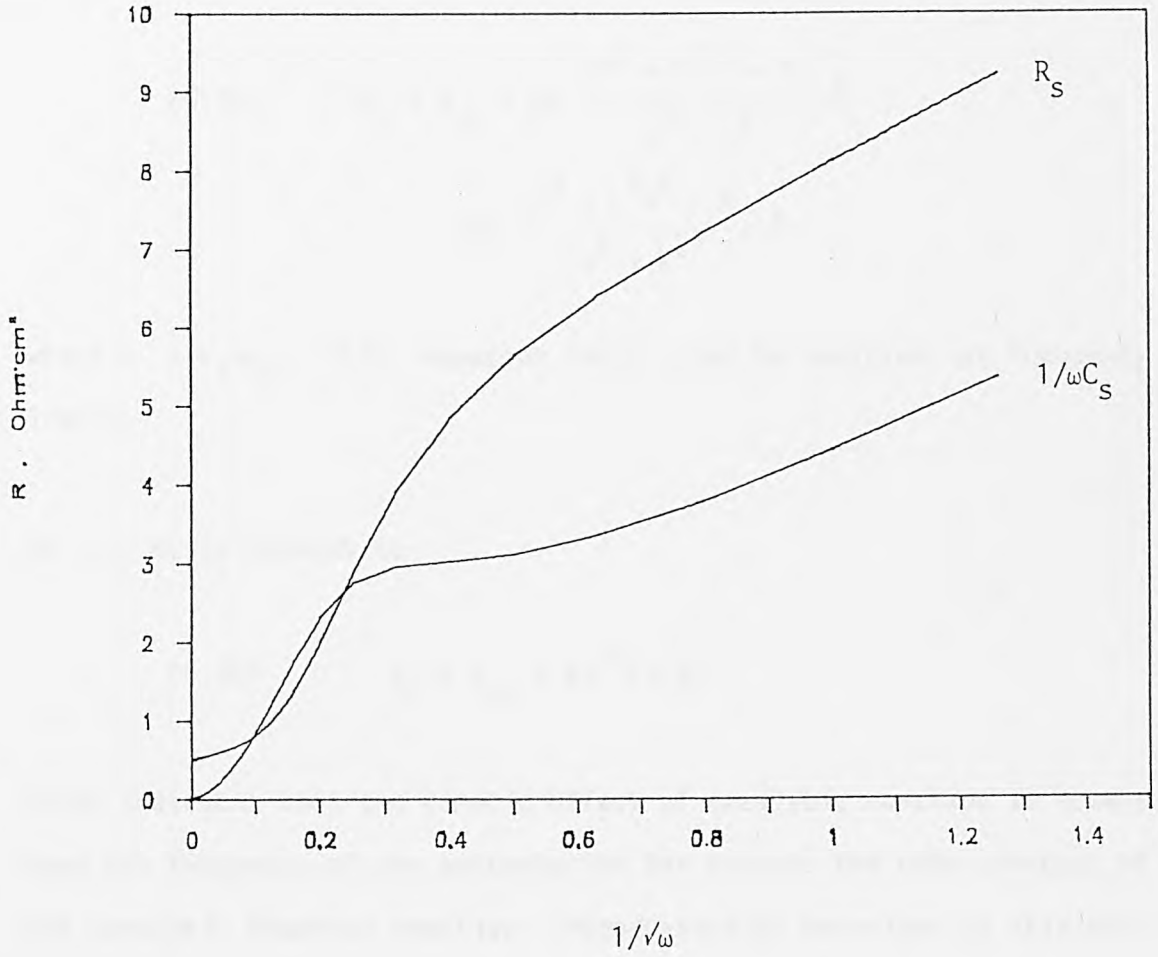

Fig. 5.6 Theoretical Randles plots for an electrode reaction coupled with an adsorption process.

R_{ct} = 0.5 ohm.cm^2; $W_r = W_o$ = 2 ohm.cm^2/s$^{1/2}$;
C_a = 0.015 F/cm^2; R_a = 4 ohm.cm^2.

The derivation is started with a set of boundary conditions and the expression of faradaic impedance is given by[176,177]

$$(5.31) \qquad Z_f = R_{ct} + W\left(\frac{(\omega^2 + k^2)^{\frac{1}{2}} + k}{\omega^2 + k^2}\right)^{\frac{1}{2}} - jW\left(\frac{(\omega^2 + k^2)^{\frac{1}{2}} - k}{\omega^2 + k^2}\right)^{\frac{1}{2}}$$

where $k = k_1 + k_2$. This equation could also be analysed at frequency limits.

At $\omega >> k$, Z_f reduces to

$$(5.32) \qquad Z_f = R_{ct} + W\omega^{-\frac{1}{2}}(1-j)$$

which indicates that the kinetic effect of catalytic reaction is absent when the frequency of the perturbation far exceeds the rate constant of the catalytic chemical reaction. Pseudo-Randles behaviour is attained. Therefore, previous analytical procedures can be applied to obtain information about the faradaic impedance at high frequency region.

If $\omega << k$, then the imaginary component of Z_f vanishes and the real component becomes frequency independent.

$$(5.33) \qquad Z_f = R_{ct} + W(2/k)^{\frac{1}{2}}$$

The slope of Randles plots at low frequencies approaches zero. Fig. 5.7 shows theoretical Randles plots for the faradaic impedance of an electrode reaction followed by chemical catalytic reaction. The faradaic impedance of an electrode reaction coupled with catalytic

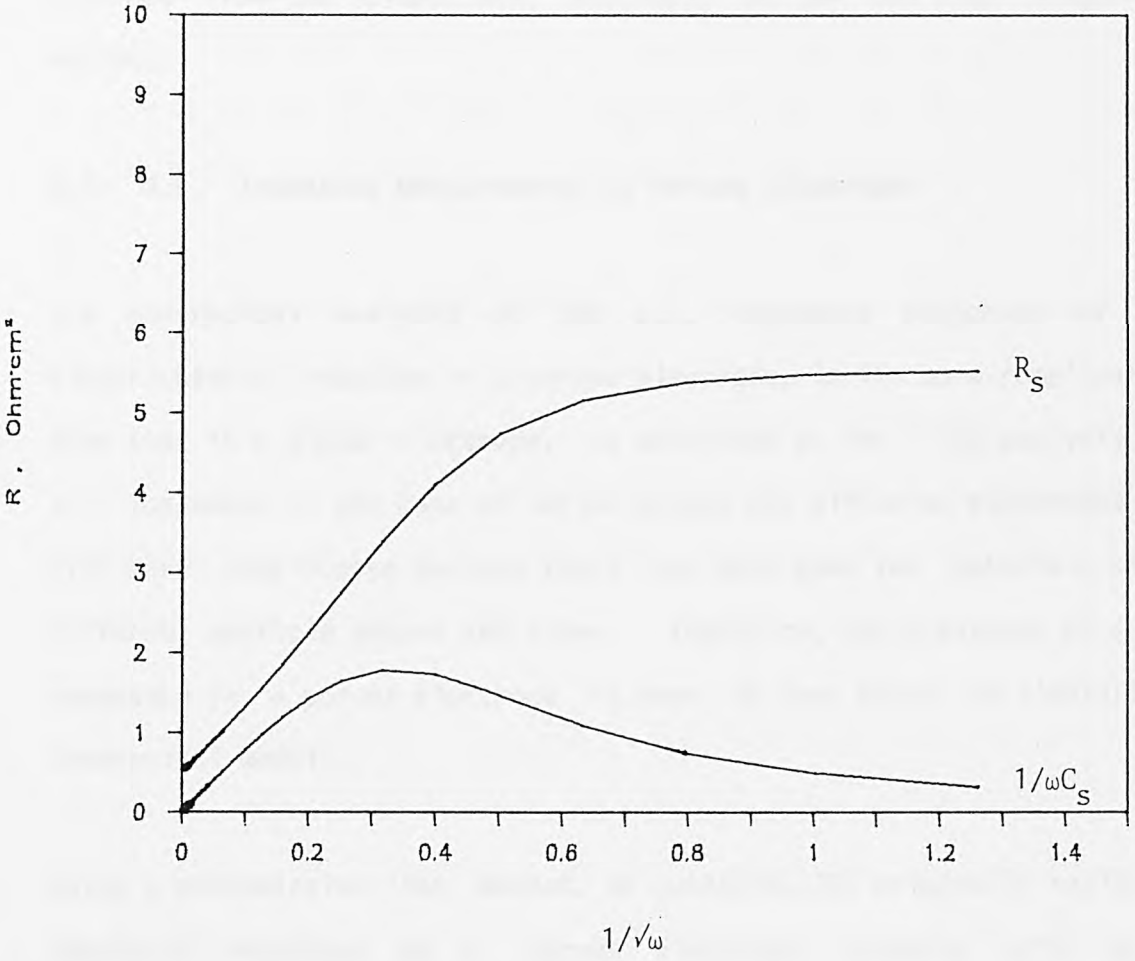

Fig. 5.7 Theoretical Randles plots for an electrode reaction coupled with a catalytic reaction.

R_{ct} = 0.5 ohm·cm^2; $W_r = W_o$ = 4 ohm·cm^2/s$^{\frac{1}{2}}$; K_c = 5 1/s.

reaction is obviously characterized by a pure resistance component at low frequencies, which is distinguishable from an adsorption process. The parameters of faradaic impedance and catalytic reaction could be obtained from the slopes and intercepts at low and high frequency regions.

5.5. A.C. Impedance Measurements in Porous Electrodes

The theoretical analysis of the a.c. impedance responses of an electrochemical reaction in a porous electrode, is far more complicated than that in a planar electrode, as described so far. The analysis of a.c. impedance in the case of Teflon-bonded gas diffusion electrodes is even more complicated because there are more than two materials with different particle shapes and sizes. Therefore, the treatment of a.c. impedance in a porous electrode is more or less based on simplified theoretical models.

Using a transmission line method, de Levie[95,178] originally analysed impedance responses on a porous electrode, assuming pores with essentially cylindrical channels of uniform diameter and semi-infinite length. The absolute magnitude of the impedance in this case is proportional to the square root of that of the equivalent planar electrode. For shallow pores with depth l, the impedance of a single pore Z_p is described as[95]

$$Z_p = (ZR)^{\frac{1}{2}} \coth l R_{so}/(ZR)^{\frac{1}{2}} \qquad (5.34)$$

where Z is the complex impedance per unit length of the planar electrode. Further analysis[179] showed that effect of pore profile on

the impedance measurement is much more significant at low frequency region. The pores are actually unable to follow the variations in potential or current quickly at sufficiently high frequencies. The influence of pore profile on the impedance decreases with increase in frequency. At high frequencies the pore behaves as a semi-infinite pore, whereas at low frequencies, it behaves as a finite pore. For a cylindrical pore the penetration depth can be expressed by[95]

$$(5.35) \qquad l_x = \tfrac{1}{2}*(r/\omega R_{so} C_{dl})^{\frac{1}{2}}$$

where l_x is penetration depth, r the pore radius and R_{so} the resistivity of electrolyte inside the pore. When the penetration depth approaches the pore depth, the shape of the pore wall has little influence on the impedance[87].

So far quantitative a.c. impedance analyses have been found to be successful only in the cases of simple porous structures such as loosely packed metal powders. The porous structure can be approached by an equivalent semi-infinite cylindrical pore model[95,178], or finite cylindrical pore model[180]. Such examples can be found in sintered-plate cadmium electrodes[181], Raney gold electrodes[87], Raney-nickel[88], and carbon monofluoride electrodes[91]. For more complex structures (e.g. Teflon-bonded electrodes), an uniform cylindrical pore model cannot account for the influence of pores on electrochemical reactions because the porous structure of a Teflon-bonded electrode is networked by gas-filled pores and liquid-filled pores[182,183]. Besides, in de Levie's approach[95], the solution resistance in the flooded part of the pore was dismissed as compared with the resistance of the liquid film. This simplification

cannot be made when considering the a.c. impedance of gas diffusion electrode, and this limits the accuracy of the information that can be obtained. Hence, an analytical analysis is generally employed in the a.c. impedance interpretation of O_2 reduction on gas diffusion electrodes[104,184]. The drawback of this method is that it is impossible to obtain the porous structure parameters like pore size, pore distribution, etc. Nonetheless, the a.c. impedance technique can provide useful information concerning kinetics and mechanism of oxygen reduction on Teflon-bonded air electrodes and the electroactivity of the electrodes.

CHAPTER SIX

A.C. IMPEDANCE STUDY OF OXYGEN REDUCTION ON TEFLON-BONDED GRAPHITE ELECTRODE

6.1. Introduction

The mechanisms and kinetics of oxygen reduction on carbon and graphite materials in alkaline solutions, have been extensively studied. Oxygen is quantitatively reduced to peroxide by a two-electron process[21,60]:

$$(6.1) \qquad O_2 + H_2O + 2e = HO_2^- + OH^-$$

which occurs rapidly, but its standard reduction potential, -0.0649 V (NHE) at 25°C, lies very much below the potential for the ideal four-electron process. The further reduction of intermediate peroxide ions does not, usually, occur at an appreciable rate on such a surface without the addition of catalysts. Isotopic studies[61] with O^{18} have indicated that the reduction of O_2 to HO_2^- as well as the reverse anodic process do not involve the actual rupture of the O-O bond but rather the modification of the bond type.

Yeager et al.[60] carried out the kinetic study of oxygen-peroxide couple on various types of carbon and graphite using the rotating disk technique. On the basis of the observed cathodic Tafel slope (120 mV/decade) and the first order dependence of the kinetic reduction on dissolved O_2 concentration, the rate determining step (rds) for the O_2 reduction was suggested to be the first electron transfer process

$$(6.2) \qquad O_2 + e = O_{2(ads)}^-$$

with a transfer coefficient of 0.5. However, on a stationary pyrographite electrode, Tarasevich et al.[185] found two distinct slopes for O_2 reduction in alkaline solutions, 30 mV per decade at

relatively low polarization and about 90 to 100 mV per decade when the potential displaced toward the cathodic side. They concluded that in the case of stationary pyrographite electrodes, the equilibrium state of the O_2/HO_2^- couple should be taken into account at low polarization range. It was argued by Appleby and Marie[186] that the mechanism of oxygen reduction on carbon materials would also depend on the local electrode surface/electrolyte volume ratio in alkaline solution. In the case of high surface area carbon materials, the most probable rds was considered to be the second electron transfer process

$$(6.3) \qquad O_2^- + H_2O + e = HO_2^- + OH$$

The electrochemical activity was observed to be proportional to the surface area of the carbon and graphite materials studied.

It is almost impossible to unanimously determine the mechanisms of O_2 reduction on Teflon-bonded graphite electrode on the basis of polarization data, because of the high active surface area and the nature of the multi-electron process of the oxygen reduction. The a.c. impedance technique can be used, under appropriate conditions, to evaluate the important kinetic data of O_2 reduction on carbon and graphite electrodes and some information about the structure of the electrode. Drossbach and Schmittinger[187] applied the impedance method to study oxygen reduction on a porous carbon electrode, using an adsorption equivalent circuit. They indicated that the rate determining step depends on the polarization potential. In the case of Teflon-bonded electrodes, the electrochemical active area between the electrode and electrolyte can be obtained by measuring the double layer capacitance[188,189]. Unfortunately, there are very few reports about

the application and interpretation of a.c. impedance on oxygen reduction, especially on the Teflon-bonded gas diffusion electrodes. There is an urgent need, therefore, to extend the understanding of the impedance behaviour of O_2 reduction on Teflon-bonded graphite electrodes.

Discussion in literature gives two basic reasons for the performance deterioration of carbon air electrodes operating in alkaline solutions: carbonate formation in the electrolyte continuing to the precipitation of solid carbonates in the porous structure of the electrodes[190], and decomposition at the carbon surface of the H_2O_2 produced during electrode operation[191]. It is of interest to determine the possible reasons for performance deterioration of the graphite gas diffusion electrodes, and to find out the relationship between the performance and the electrochemical active surface area of the electrodes.

6.2. Steady State Polarization Performance

The steady state polarization performances for O_2 reduction on Teflon-bonded graphite electrodes were found to be poor and unstable, particularly under air. Fig. 6.1 compares the polarization curves for a graphite electrode (fabricated by the rolling method, see section 2.3.2.) at 25^oC in 5N KOH under air and oxygen. A limiting current density was observed (within the experimental range of current density) for the reduction of oxygen on the graphite electrode under air, indicating that the reaction is controlled by concentration and diffusion polarization at relatively lower current density. The corresponding Tafel plot for O_2 reduction on Teflon-bonded graphite electrode under air is given in Fig. 6.2. At low current density, the observed cathodic Tafel slope was 52.56 mV per decade and this value was doubled to 111.24 mV per decade as the current density increased. Using pure oxygen, as a feeding gas, the values of Tafel slope were slightly reduced to 48.23 mV/decade at the low polarization region and 99.07 mV/decade at the high polarization region respectively. This is shown in Fig. 6.3.

The doubling of the Tafel slope at high current density was predicted by various pore models[192,193]. With increasing polarization the reaction can become localized to the vicinity of the interface between gas and electrolyte, and this can cause a shift from one Tafel region to another, with the doubled Tafel slope compared to the first region. This has been confirmed experimentally for a Teflon-bonded gas diffusion electrode[194]. In the interfaces between the gas-filled pores and liquid-filled pores, the electrolyte forms menisci and thin films enveloping the pore walls[195]. The reactant O_2 dissolved in the

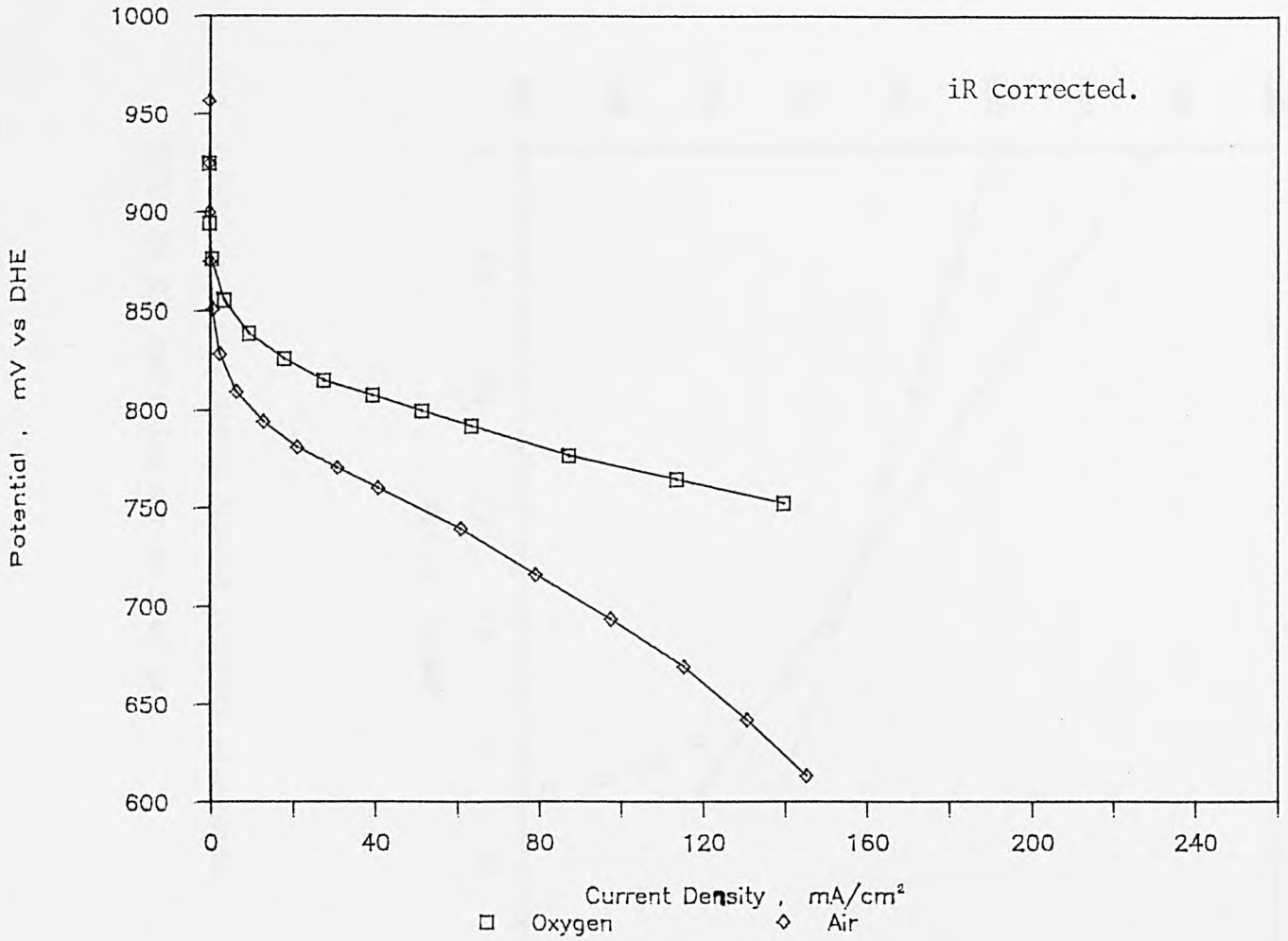

Fig. 6.1 Polarization curves of a Teflon-bonded graphite electrode.

$25^{0}C$, 5N KOH and using air and oxygen as feed gas.

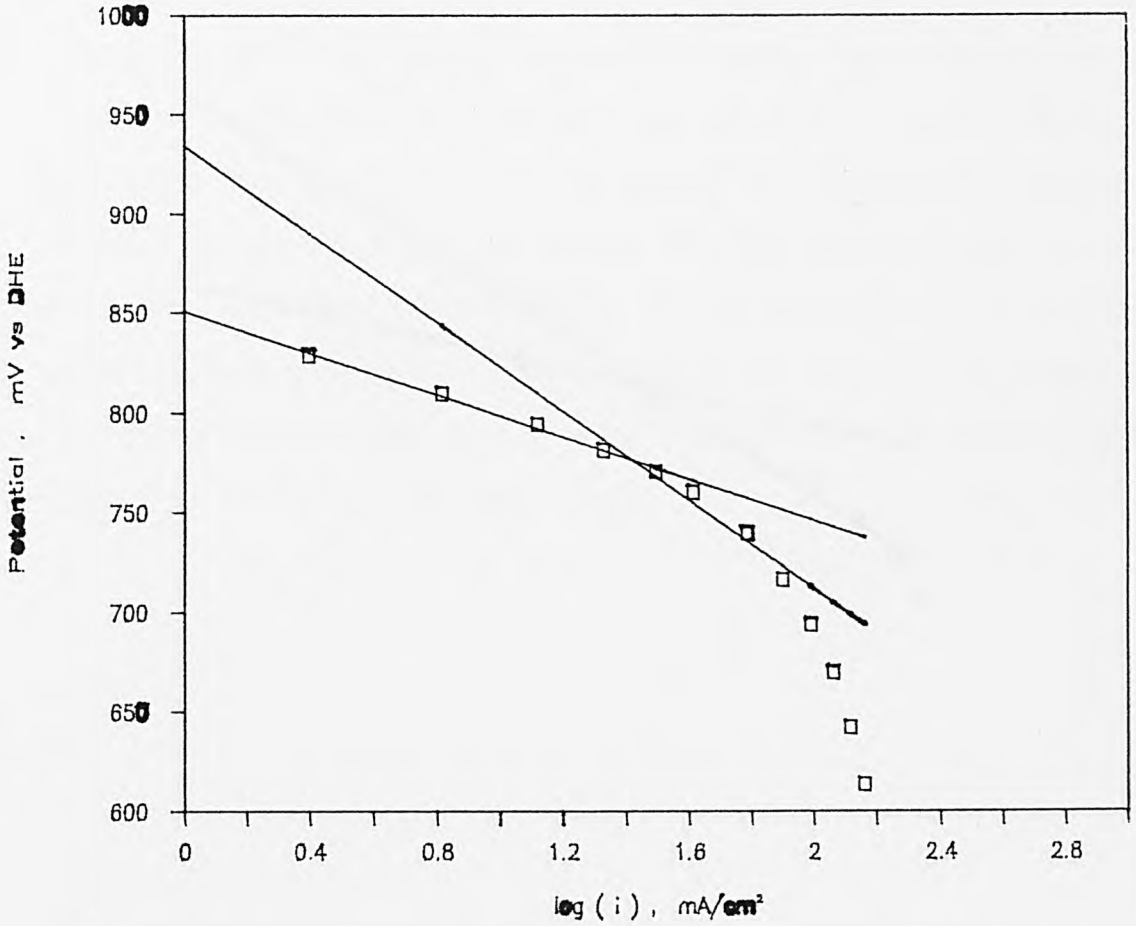

Fig. 6.2 Tafel plots of a Teflon-bonded graphite electrode. 25°C, 5N KOH and using air as feed gas.

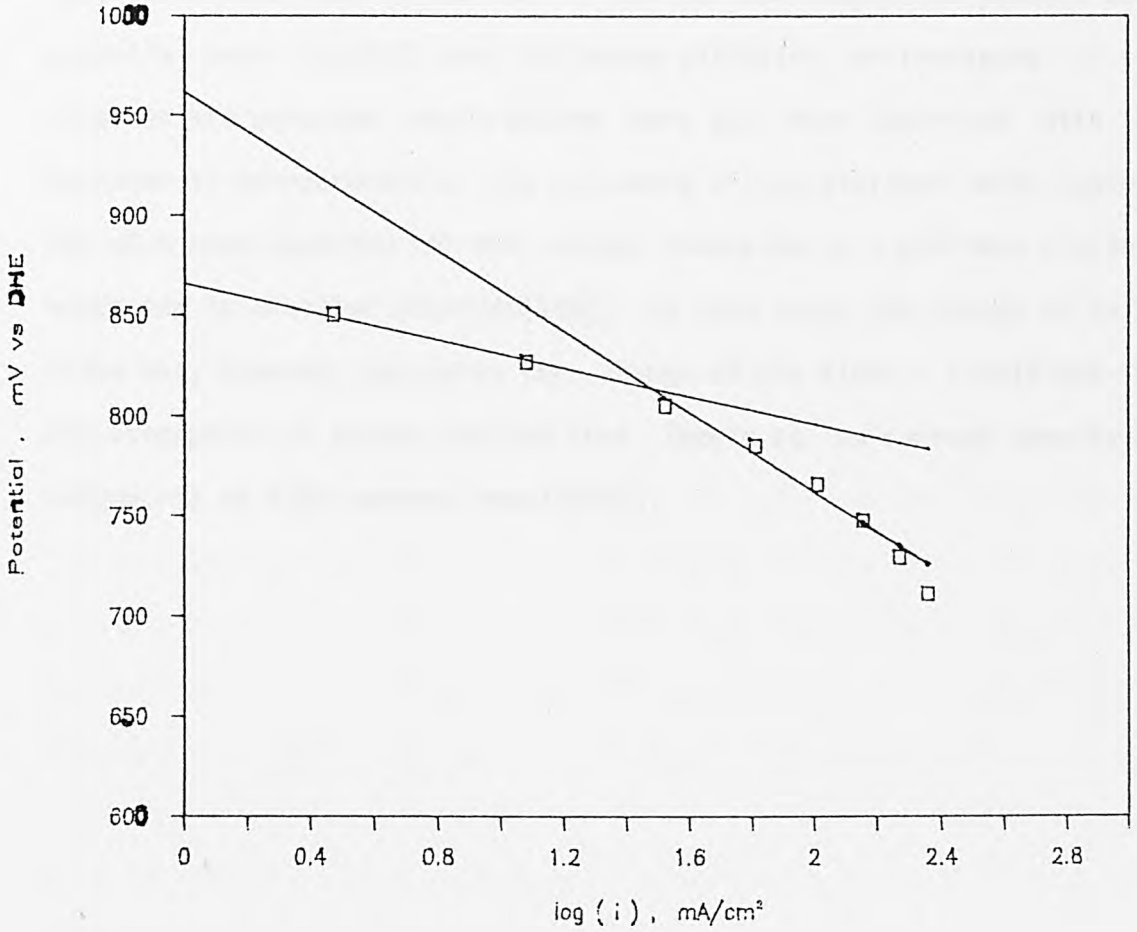

Fig. 6.3 Tafel plots of a Teflon-bonded graphite electrode.
25°C, 5N KOH and using oxygen as feed gas.

electrolyte film diffuses rather rapidly through this liquid and is reacted at the active sites. Relatively, the distance for the diffusion of intermediate peroxide into the bulk solution is increased. This could mean that if the rds is the surface adsorption process at a potential near ocv[60], the following diffusion or transport of the intermediate peroxide would become more and more important with the increase in overpotential. The existence of two distinct Tafel regions has also been observed for the oxygen reduction on a polished platinum electrode in alkaline solution[196]. In this case, the change of Tafel value was, however, caused by the change of the kinetic conditions for the adsorption of oxygen species from Temkin at low current density to Langmuiria at high current density[33].

6.3. A.C. Impedance Measurements

6.3.1. Experimental

A.C. impedance measurements have been carried out on Teflon-bonded graphite electrodes in 5N KOH solution at 25°C, using air or pure oxygen as feed gas. The measured potential was controlled at ocv, 900, 850 and 800 mV (DHE) respectively. The electrodes were made by the rolling method. The input parameters for the measurement have already been given in Chapter 2 (see Table 2.1). The graphite electrodes were polarized between potential 1000 to 750 mV (DHE) in 5N KOH at sweep rate of about 0.4 mV per minute before the a.c. impedance measurement. This pretreatment ensures that the electrodes are uniformly wetted. An adsorption equivalent circuit, which has been discussed in the previous chapter, was used to evaluate the kinetic parameters of O_2 reduction on the Teflon-bonded graphite electrodes. The calculated data was compared with the experimental ones for the electrodes. The result was a set of values for R_{ct}, C_a, R_a, etc., which not only gave the best fit over the whole frequency region but was also physically reasonable. The evaluated and the observed impedance responses were displayed on the Randles plane.

The activity and stability of Teflon-bonded graphite electrodes without the incorporation of catalysts were also studied using the a.c. impedance method. Impedance measurements were carried out at 25°C in 5N KOH, using air as feed gas. Apparent double layer capacitance $C_{dl,app}$ was determined as a function of polarization length, under a constant cathodic current density of 50 mA/cm^2. The activity and stability of the electrode was shown as a plot of values of $C_{dl,app}$

against the cathodic polarization time in hours.

6.3.2. Results and Discussions

6.3.2.1. Impedance Responses

Fig. 6.4 shows the complex impedance plots of O_2 reduction on a Teflon-bonded graphite electrode at various potentials under air. As a whole, the impedance responses were characterized by a distorted semicircle and a Warburg diffusion tail. A close view of the impedance spectrum measured at 850 mV (DHE) is given in Fig. 6.5. The slope for the diffusion tail was determined to be 43.72^{o}, which is very close to the 45^{o} for the Warburg diffusion process on a planar electrode.

It will be shown later by the results of faradaic analysis at high frequencies, that the charge transfer resistance R_{ct} is very small (10^{-2} ohm·cm^2) and remains relatively constant for varying polarization potentials. The size of the semicircle observed is, however, dependent on the potential. They became smaller as the polarization potential increased. It was quickly realized that the semicircles appearing at relatively low potentials were not due to the charge transfer processes for reaction (6.1). The values of R_{ct} were so small that the semicircle plot for the charge transfer reaction almost disappeared. Consequently, it became obvious that the observed semicircles were due to the coupled adsorption and desorption processes of the reactants during oxygen reduction. It was also noticed, immediately, that the impedance responses show fast rate of electron transfer reaction with respect to the coupled chemical reaction for the reduction of oxygen on Teflon-bonded graphite electrodes. Therefore, chemical reactions play

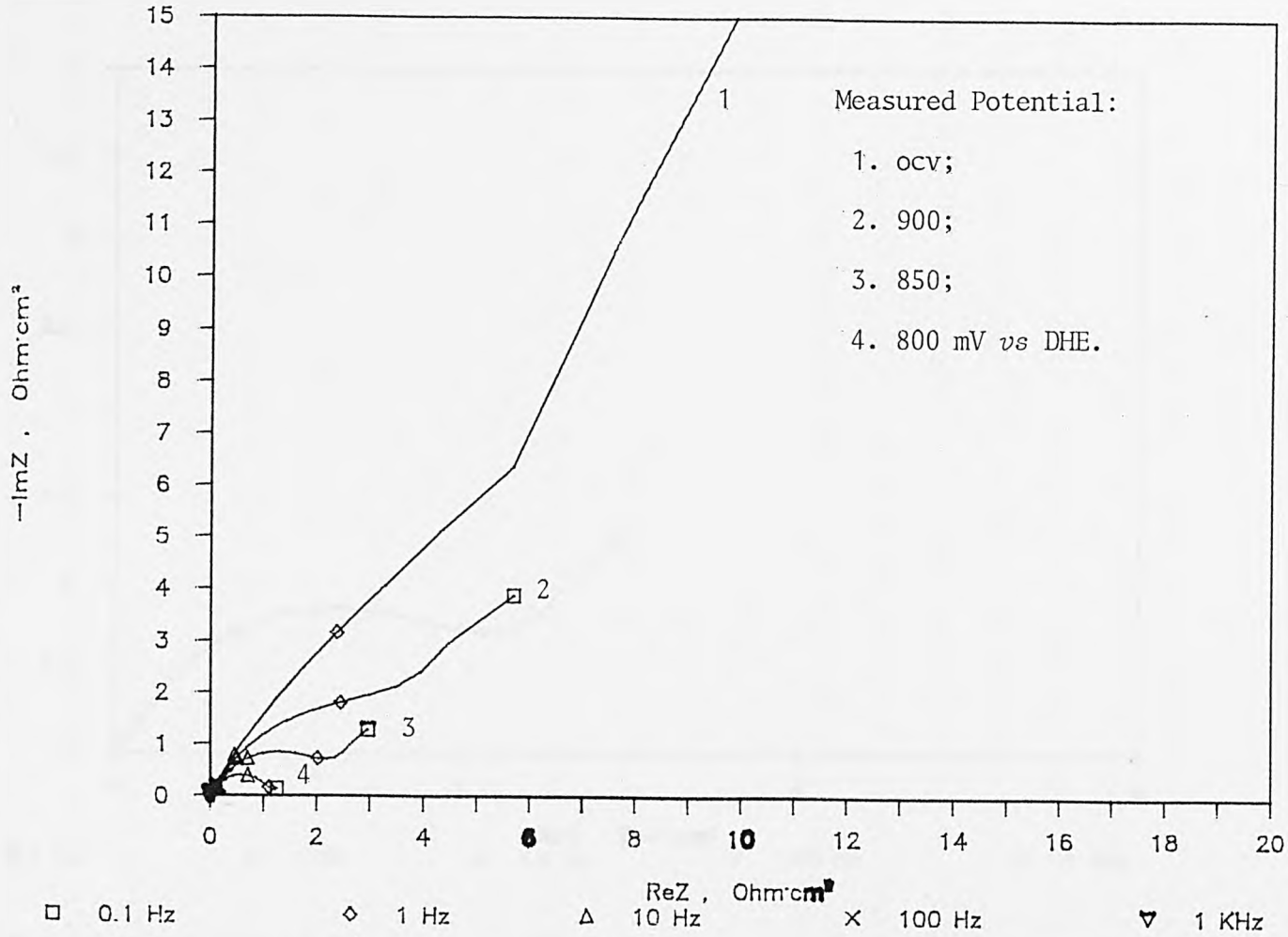

Fig. 6.4 Measured impedance responses of graphite electrode at various potentials. 25°C, 5N KOH and using air as feed gas.

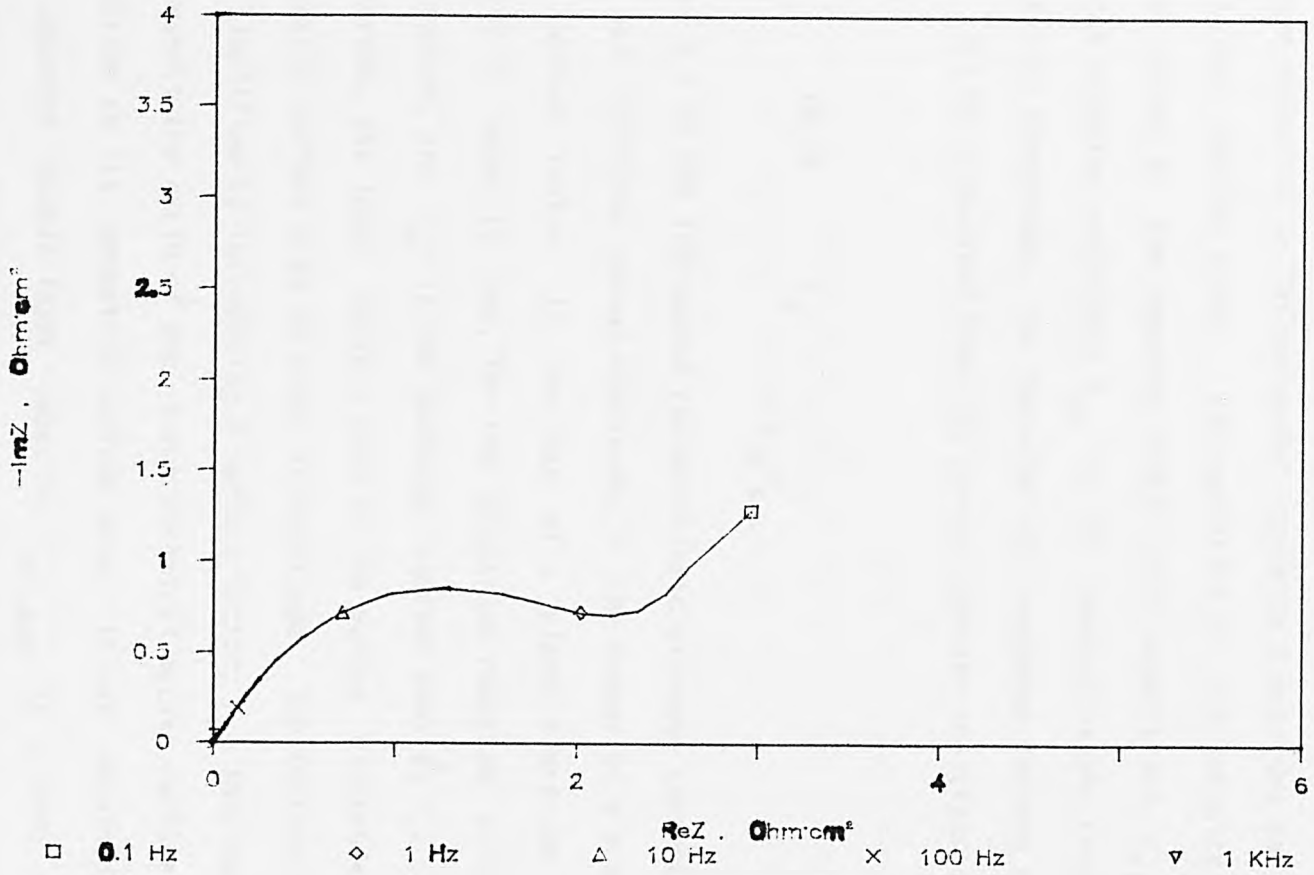

Fig. 6.5 A close view of the measured impedance response of graphite electrode at 850 mV. 25°C, 5N KOH and using air as feed gas.

a more dominant role in the O_2 reduction on Teflon-bonded graphite electrodes.

6.3.2.2. Adsorption Equivalent Circuit Analysis

Initially the evaluation procedure of impedance parameters for the oxygen reduction on Teflon-bonded graphite electrodes was started with classical Randles plots. Extrapolation at the infinite frequencies gives values of the apparent double layer capacitance $C_{dl,app}$ and the charge transfer resistance R_{ct}. In the case of oxygen reduction on gas diffusion electrodes, the characteristic exchange current density, i_o', can also be calculated from the charge transfer resistance, R_{ct}.

$$(6.4) \qquad i_o' = \frac{RT}{nFR_{ct}f_s}$$

where i_o' is the introduced characteristic exchange current density for the gas diffusion porous electrode, n the number of electrons and f_s the surface factor. In the case of a planar electrode the surface factor is equal to one, for the electrode reaction without specific adsorption, and i_o' is the exchange current density i_o. In a porous electrode, the inner surface area of the porous electrode exceeds the geometric surface area by order of magnitude. The texture of the pores was simplified by introducing a surface factor, f_s. This surface factor represents the ratio of the electrochemical active surface area of the electrode to its geometric surface area. It was obtained by dividing the apparent double layer capacity, $C_{dl,app}$, by a true double layer capacity value for a planar graphite electrode. However, the value of the true double layer capacity varies with the electrode materials as well as measuring conditions. Taking into account the variations of

C_{dl} values reported in literature, shown in Table 6.1, an assumed value of C_{dl} = 10 $\mu F/cm^2$ seems reasonable for calculating the surface factor.

The characteristic exchange current density i_o' calculated from equation (6.4) is about 2 mA/cm^2 for the oxygen reduction on Teflon-bonded graphite electrodes, as shown in Table 6.2. The calculated i_o' values from the charge transfer resistance are found to be in good agreement with the published i_o values for O_2 reduction on pyrolytic graphite in alkaline solutions[60]. This shows that the i_o' values are characterised by the electrochemical activities of O_2 reduction on gas diffusion porous electrodes. The assumption that the number of electrons is 2, used in equation (6.4) is thus justifiable. The magnitude of i_o' again verifies that the oxygen reduction on the surface of the Teflon-bonded graphite electrodes predominates by a two-electron pathway. For the direct four-electron pathway the exchange current density is much lower, the magnitude of which is in the range of about 10^{-8} mA/cm^2[17,196].

However, in the whole range of frequencies used, the Randles equation for a simple electrode reaction is too simple to apply to the O_2 reduction on porous graphite electrodes even at ocv. It has been confirmed that adsorption of oxygen molecules on the graphite surface is the first step and the subsequent faradaic adsorption process with one-electron transfer was proposed as the rate determining step[57,204]. Such an electrochemical system has been represented by an adsorption equivalent circuit[92] (shown in Fig. 5.5). The rate constant of the adsorption process can be derived from the resistance and capacitance of adsorption impedance (see equations 5.25 and 5.26) by

Table 6.1

A list of C_{dl} values for planar carbon and graphite electrodes.

Electrode	Electrolyte	C_{dl} $\mu F/cm^2$
Various carbons	KOH	10 [197]
Graphitized carbon black	0.01N NaCl	4.3[198]
XC-72, Cabot		8 [199]
Basal plane, stress annealed pyrographite	0.9M NaF	3 [200]
Basal plane, cleaved ordinary pyrographite	0.5M KCl	12 [201]
Basal plane, polished ordinary pyrographite	0.5M KCl	12 [201]
Glassy carbon	KCl	25 [202]
Basal plane, stress annealed pyrographite	Acetonitrile	3 [203]

$$k_a = \frac{1}{R_a C_a} \qquad (6.5)$$

where k_a is the rate constant of adsorption and R_a and C_a are the resistance and capacitance of adsorption impedance respectively.

The Randles plots for O_2 reduction on a Teflon-bonded graphite electrode, at ocv, under air are shown in Fig. 6.6. The symbols (□ for R_s and + for $1/\omega C_s$) express the experimental impedance data, and the solid lines are the estimated impedance responses corresponding to the adsorption equivalent circuit. The theoretical impedance data were calculated using equation (5.27) with a set of values for the kinetic parameters. Taking into account the influence of porosity, the agreement between the observed impedance response and the theoretical one are reasonably good; indicating the validity of the adsorption model for the O_2 reduction reactions on the Teflon-bonded electrode. Table 6.2 shows that the resistance of adsorption is much higher than the charge transfer resistance. Consequently, the rate of surface adsorption process of O_2 molecules is much slower than that of the electron transfer process. At equilibrium potential (ocv) the oxygen reduction on Teflon-bonded graphite electrodes is primarily controlled by the adsorption reaction of oxygen molecules on the active surface of the graphite. This synopsis is in accordance with the rotating disk-ring results on pyrolytic graphite[60]. As polarization potential decreases, two linear regions at low and high frequencies on the Randles plots are obtained. These are shown in Fig. 6.7 for the graphite electrode at 900 mV. The Randles plots still remain the characteristics of adsorption impedance model, i.e. the capacitive components of the impedance are higher than the resistance ones at high frequency region.

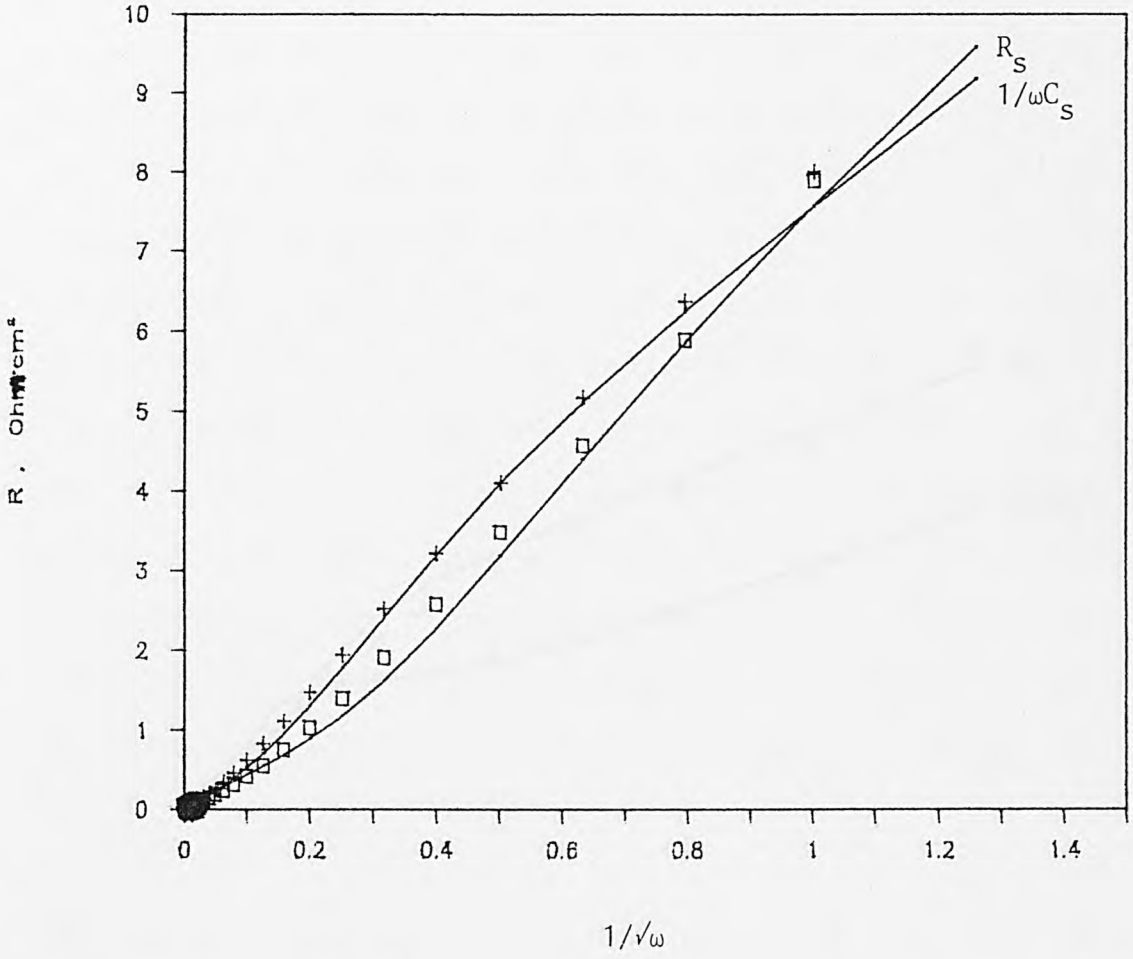

Fig. 6.6 Fitted Randles plots for graphite electrode at ocv. 25°C, 5N KOH and using air as feed gas.

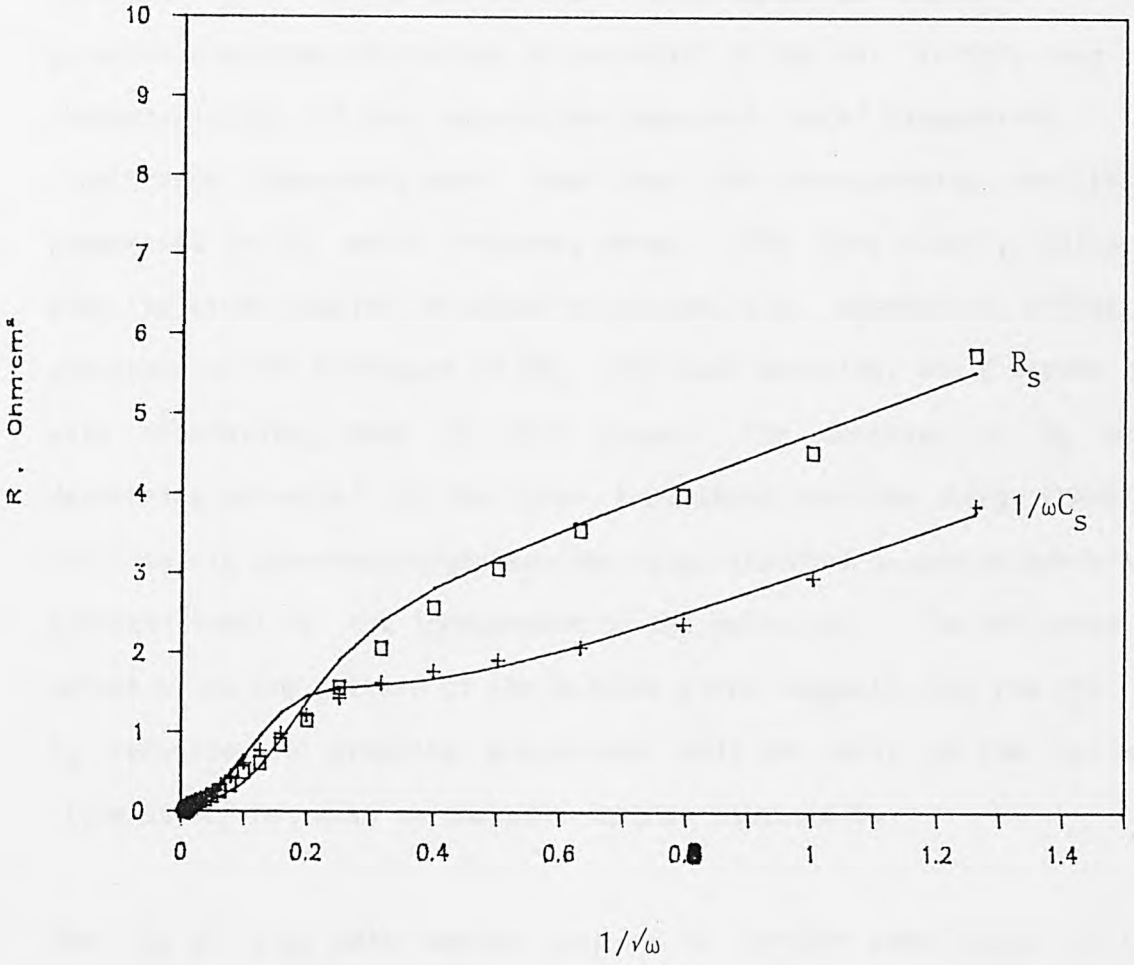

Fig. 6.7 Fitted Randles plots for graphite electrode at 900 mV. 25°C, 5N KOH and using air as feed gas.

It was found that the calculated impedance responses deviate significantly from the observed impedance responses, in the high frequency region, when the polarization was shifted further in the cathodic region. Fig. 6.8 is the fitted impedance responses for the graphite electrode determined at potential of 850 mV. In this case the characteristics of the adsorption impedance model disappeared. The capacitance components were lower than the corresponding resistance components in the whole frequency range. This fact clearly indicates that the other coupled chemical processes, e.g. adsorption, diffusion processes or the transport of HO_2^- into bulk solution, would become the rate determining step at this stage. The decrease of R_a with decreasing potential, on the other hand shows that the charge transfer reaction via adsorbed oxygen species (e.g. adsorbed oxygen molecule and hydroxyl ions) is not independent of the potential. The influence of potential on the pattern of the Randles plots suggests that the rds for O_2 reduction on graphite electrodes rely not only on the surface state[59,60] but also on the polarization potentials.

The rds at high polarization regions is further complicated by the possibility of the self-decomposition of the intermediate peroxide. It can be seen from the complex impedance plots in Fig. 6.4 that the Warburg tail has almost disappeared at 800 mV. The drop in adsorption capacitance C_a could be caused by another surface adsorption process; intermediate HO_2^- ions. Therefore, it is important to emphasize that the adsorption impedance equivalent circuit could only be applicable in O_2 reduction on Teflon-bonded graphite electrodes at potentials near ocv.

In gas diffusion electrodes, the electrochemical reactions mostly

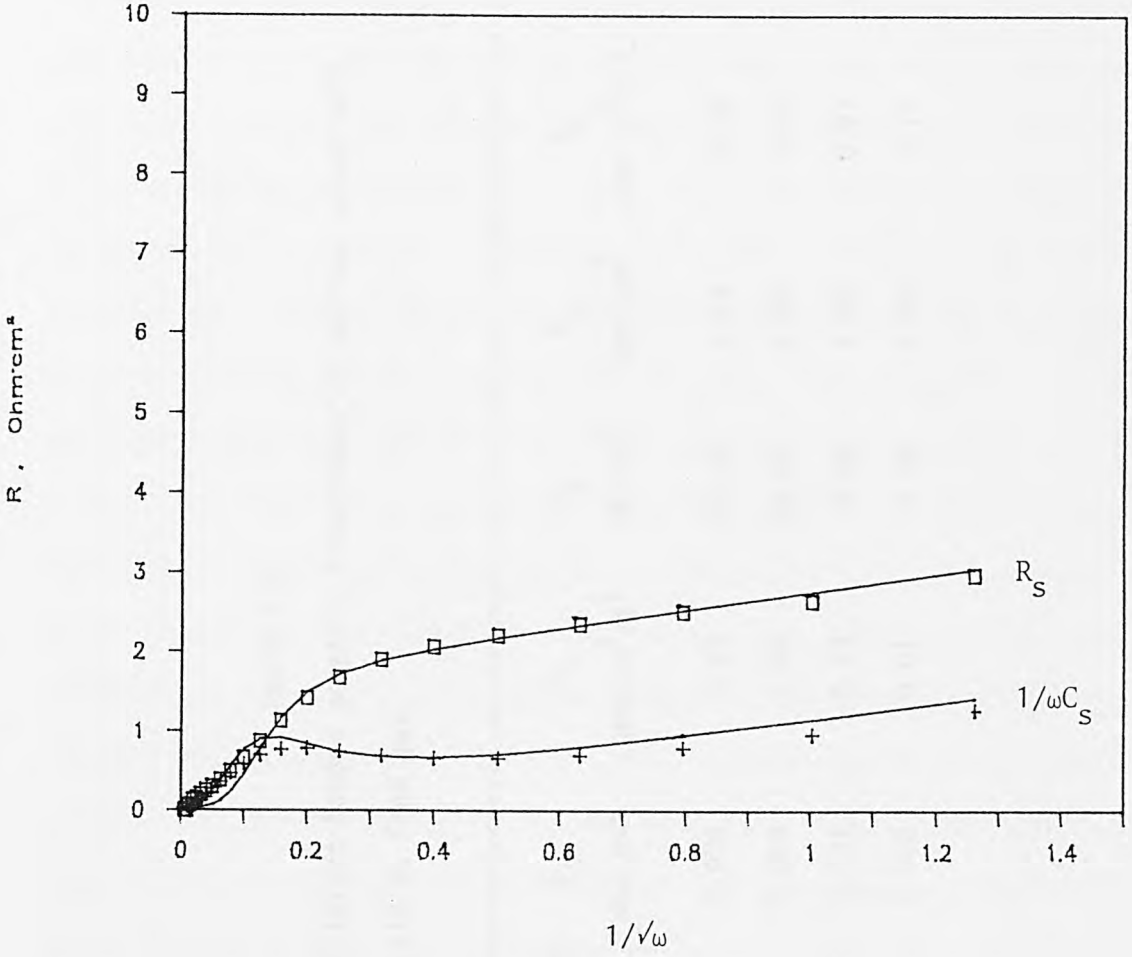

Fig. 6.8 Fitted Randles plots for graphite electrode at 850 mV. 25°C, 5N KOH and using air as feed gas.

Table 6.2

Impedance parameters of Teflon-bonded graphite electrodes at various potentials. $25^{o}C$, 5N KOH and using air as feed gas.

Potential mV vs DHE	$C_{dl,app}$ mF/cm^2	Surface Factor	R_{ct} $ohm \cdot cm^2$	W_r $ohm \cdot cm^2/s^{\frac{1}{2}}$	C_a mF/cm^2	R_a $ohm \cdot cm^2$	W_o $ohm \cdot cm^2/s^{\frac{1}{2}}$	i_o' mA/cm^2
ocv	1.870	187	0.034	3.91	75.00	3.24	2.76	2.02
900	1.989	199	0.029	2.06	19.60	1.92	0.85	2.23
850	2.284	228	0.031	0.13	9.85	1.69	0.97	1.81
800	2.217	222	0.028	0.01	8.34	1.04	0.15	2.07

proceed in the vicinity of the regions where gas-filled pores are in contact with liquid-filled ones. In graphite or graphite-supported electrodes, the ohmic potential gradients could be assumed negligible due to the conductivity of electrodes and electrolyte. Oxygen reduction takes place inside the pores as well as outside the pores, e.g. the area near the electrolyte-side surface of the electrode[104]. This consideration indicates that the influence of porous structure in Teflon-bonded electrodes on impedance responses could be approached by introducing a surface factor at low polarizations. It was, therefore, found that the observed impedance responses for the oxygen reduction on graphite electrode were fitted quite well with adsorption equivalent circuit at low polarizations, indicating the rds is the oxygen adsorption. With the increase of polarization, the oxygen reduction takes place preferentially in and around the gas and liquid pore interfaces. It would be expected that the diffusion processes would become rate controlling step due to the increase of the diffusion length. This conclusion coincides with the results of Kenjo and Kawatsu[25] concerning the variation of limiting current density with the thickness of both catalyst layer and the gas diffusion layer.

6.3.2.3. Active Surface Area of Teflon-bonded Graphite Electrode

In principle, the effective surface area between electrode and electrolyte can be assessed by measuring the apparent double layer capacities; provided that the double layer capacitance of the true electroactive component is known[188,205,206]. It is assumed that the measured $C_{dl,app}$ can be used as an indicative parameter of the electrochemical active surface area. It should be pointed out that this active surface area is different from the wetted interfacial area

between electrode and electrolyte. Therefore, a comparison of the wetted surface area and the electroactive surface area for a Teflon-bonded graphite electrode is important.

The geometric surface area of the graphite electrode studied was 1 cm^2. The depth of the reaction layer was approximately 0.25 mm. The porosity of the catalyst layer was about 29 %, determined from the weight differences between a dry electrode and an electrode soaked with electrolyte. Based on a simplified porous model, with cylindrical pores of 50 nm average diameter, it was calculated that the wettable surface area is about 0.26 m^2. Again assuming that the double layer capacitance C_{dl} for the true electroactive component is 10 $\mu F/cm^2$, the average electroactive surface area calculated from $C_{dl,app}$ values was about 250 cm^2 in the potential range studied. In this case about 10 % of the wetted surface area of the reaction layer is involved in the electrochemical reaction. According to Darby's[182,207] model for a hydrophilic gas fed porous electrode, the electrochemical reaction predominantly takes place in the gas-liquid interface (where a liquid pore intersects a gas pore). Consequently, only a small part of the wettable interfacial area is electrochemically active. The measured double layer capacity could be an indication of the magnitude of the gas-liquid-solid interfacial area, involved directly in the electrochemical reactions. It was found that this active surface area calculated from $C_{dl,app}$ values is almost independent on the polarization potentials and on the partial pressure of oxygen. Consequently, the $C_{dl,app}$ value obtained from a.c. impedance measurements is a structural parameter of a gas diffusion electrode.

6.3.2.4. Stability of Teflon-Bonded Graphite Electrodes

It has been confirmed, above, that the apparent double layer capacitance $C_{dl,app}$ is in fact an indicative parameter of the electrochemically active area of porous electrodes. Therefore, the activity and stability of Teflon-bonded graphite electrodes could be investigated through measuring the $C_{dl,app}$ values as a function of polarization length. The evaluated $C_{dl,app}$ value was plotted against the cathodic polarization time. This is shown in Fig. 6.9. The determination of $C_{dl,app}$ was also done on the same electrode under pure oxygen and only marginal differences were found. Therefore, it can be said that the decrease of $C_{dl,app}$ value in a Teflon-bonded graphite electrode is not due to the nitrogen blanking in the pores[189].

The $C_{dl,app}$ values have a tendency to decrease with increasing polarization time, as shown in Fig. 6.9. This indicates that the electrochemical active surface area reduces as oxygen reduction proceeds on the graphite air electrode. Generally, the polarization performance of a pure graphite electrode, without promoting catalytic effects, is unstable in alkaline solutions[23]. There is, therefore, a correlation between the $C_{dl,app}$ value and the stability properties of graphite electrodes. It can be pointed out that the performance deterioration of a graphite air electrodes is primarily caused by the loss of electrochemical active surface area. This loss could be attributed to the carbonate formation inside the pores[190], the peroxide decomposition at the graphite surface[191], or the loss of hydrophobicity[208]. The effects of carbonate formation of the electrolyte in the porous structure and of peroxide produced during O_2 reduction on the performance of carbon air electrodes were studied by

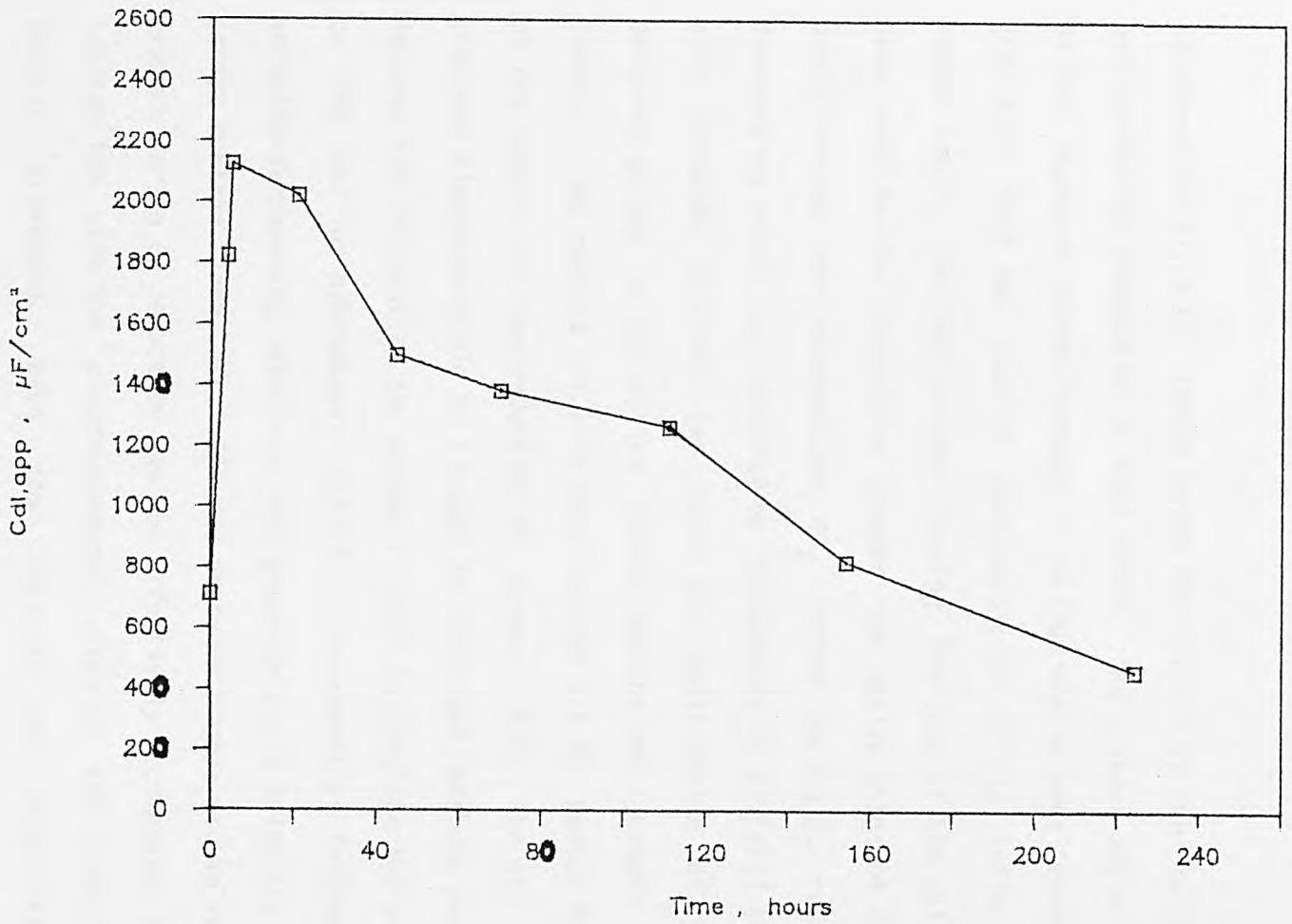

Fig. 6.9 Dependence of $C_{dl,app}$ value on polarization time for a graphite electrode at cathodic current density of 50 mA/cm^2.

$25^{\circ}C$, 5N KOH and using air as feed gas.

Gamburtsev[209] in alkaline solutions. He pointed out that the service life of the carbon electrodes deteriorates mainly because the hydrogen peroxide formed as an intermediate during oxygen reduction decomposes at the surface of the carbon.

Rotenberg et al.[210] investigated the effects of KOH solution on the hydrophobicity properties of PTFE sheet. The contact angle versus time of KOH exposure passes through a minimum and becomes constant. This indicated that the loss of hydrophobicity of the Teflon binder is rather small. The main process causing the loss of the active surface area could be the interaction between the active sites of the graphite particles and the intermediate HO_2^- formed during O_2 reduction. An interesting result was reported by Kukushkina et al.[211] that contact with peroxide solution can cause the modification of acidic and peroxide groups on the active carbon surface and increase the oxygen content. The results of this modification are to reduce the activity of the carbon for the reduction of oxygen. Also, the gas pores of a graphite electrode could be flooded in prolonged cathodic polarization, because the increase of the oxygen content in graphite and carbon leads to the loss of hydrophobicity[212]. Consequently, incorporation of peroxide-decomposing catalysts into graphite could delay the process of active surface area loss. If the peroxide formed as an intermediate product during O_2 reduction can be effectively decomposed, the further interaction with the electrochemical sites of the graphite can be largely prevented. Both the activity and stability of the catalyst/graphite electrodes would be improved.

CHAPTER SEVEN

KINETICS OF OXYGEN REDUCTION ON TEFLON-BONDED COBALT OXIDE/GRAPHITE ELECTRODES

7.1. Introduction

In nearly 30 years, a vast amount of research work has been extensively carried out on the electroreduction of oxygen on graphite and carbon electrodes, supported by semiconducting oxide catalysts. The main driving forces behind these researches are: (1) the search for cheaper and more efficient catalysts in place of the expensive noble metals, e.g. platinum group metals that were originally used as catalysts, and (2) the need for a deep understanding of oxygen electrochemistry through the mechanism studies of O_2 reduction on various oxide/carbon or oxide/graphite systems; in relation to their applications in fuel cells, industrial water electrolysers and metal-air batteries.

Oxygen reduction studies have been carried out on a limited number of oxide/carbon systems such as manganese oxide/carbon[213], perovskite oxide promoted carbon electrodes[15,26], spinel oxide/graphite[23,24], etc. Among the systems studied, the spinel type oxides, particularly Co_3O_4 and its cobaltites, play a crucial role in oxygen reduction in alkaline solutions. This is due to their particular spinel AB_2O_4-tpye structures, which are relatively stable in alkaline solutions and usually possess high activities towards oxygen reduction and peroxide decomposition[52,214]. The studies of O_2 reduction on carbon or graphite air electrodes incorporated with different cobaltites such as $NiCo_2O_4$[67,215], Li-doped Co_3O_4[24] Co_3O_4[71], and $MnCo_2O_4$[216] systems have been reported.

In general, the performances of the carbon and graphite electrodes are significantly improved on incorporating the cobalt oxide catalysts. The understanding of the mechanisms of oxygen reduction on such

composite electrodes are, however, far from complete. The effect of spinel cobalt oxides on promoted carbon electrodes was reported, by a group of Russian researchers[71,217] to be fully electrochemical. Oxygen reduction on Co_3O_4/carbon electrodes proceeds directly to water without intermediate formation of peroxide. They considered the possibility of a dissociative chemisorption of O_2 on a spinel Co_3O_4[64], but failed to explain the role of the electrochemical activity of carbon. According to the data on isotopic exchange[218], a dissociative adsorption of oxygen could occur on some transition metal oxides[15,218,219]. However, compared with these metal oxides, the activity of activated carbon and high surface area graphite for O_2 reduction in alkaline solutions is, in fact, much higher[19,220]. On lanthanum perovskite oxides, the formation of hydrogen peroxide has been observed at high overpotentials[221].

Tseung and co-workers[222,223] have been more concerned about the catalytic activity of cobalt oxides in the decomposition of the peroxide formed during O_2 reduction on graphite. Based on a theory about an electrochemical reaction followed by a regenerative heterogeneous catalytic reaction[224], Goldstein and Tseung[222] studied the relationship of the activity of electrocatalysts of cobaltite oxides and the kinetics of oxygen reduction. The intermediate peroxide is catalytically decomposed on the active sites of cobalt-iron oxides. They claimed that the maximum enhancement of cobalt-iron oxide/graphite electrodes is to double the pseudo-exchange current density value. For cathodic oxygen reduction on manganese oxides in alkaline solutions, the electrochemical activity is dependent on the catalytic activity of the manganese oxides for peroxide decomposition[158,213].

However, from the view of catalytic decomposition of H_2O_2, it has been confirmed experimentally, in this thesis, that divalent cobalt ions have a much higher activity than cobalt oxides. The proposed mechanisms of peroxide decomposition in the presence of Co^{2+} in alkaline solutions (see section 4.6) also indicated that the intermediate HO_2^-, obtained during O_2 reduction on the composite cobalt oxide/graphite electrodes, could be homogeneously decomposed by the dissolved Co^{2+} ions inside the pores; though the activity is dependent to a large extent on the distribution state of Co_3O_4. It is, thus, of importance to study the reduction of oxygen on Teflon-bonded graphite electrodes promoted by cobalt oxides on two aspects: (1) possible role of the Co_3O_4 catalysts in the mechanisms of O_2 reduction, and (2) relationship between the catalytic activity of the catalysts and the electrochemical activity and stability of the composite electrodes.

It was pointed out that the kinetic results of O_2 reduction on Teflon-bonded air electrodes, obtained by conventional methods (e.g. steady state polarization) could be distorted because of the internal ohmic resistance and the concentration overpotential associated with diffusion of O_2 across the pores[225]. The a.c. impedance technique, however, offers a useful tool to investigate the kinetics and mechanisms of oxygen reduction on Teflon-bonded air electrodes[104,226]. The limitations to the interpretation of impedance results are the complex porous structure of the Teflon-bonded electrodes and the complicated processes of O_2 reduction[195]. In this respect the application of the impedance method is not so successful as it has been proved in many other electrochemical systems.

This chapter reports investigations carried out on O_2 reduction on various Teflon-bonded Co_3O_4/graphite electrodes, using both steady state polarization and transition a.c. impedance methods. The results obtained are compared in order to increase further the understanding of the kinetics and mechanisms of oxygen reduction on Teflon-bonded Co_3O_4/graphite electrodes in alkaline solutions.

7.2. Steady State Polarization Measurements

7.2.1. Experimental

The steady state polarization of Co_3O_4/graphite electrodes was carried out, potentiostatically, on a floating model at 25^oC in 5N KOH solutions. Both air and pure oxygen were used respectively as feed gases. The electrode potentials were measured against a DHE reference electrode in the same solution. The electrodes were fabricated by the painting method and catalyst loading was in the range of 21 to 25 mg/cm^2. For the purpose of simplicity, the composite electrodes were coded as follows.

CG — Teflon-bonded electrode of 1.22 wt% high surface area Co_3O_4 coprecipitated with graphite;

HSAC2 — Teflon-bonded electrode of 20 wt% high surface area Co_3O_4 mixed with graphite;

LDC2 — Teflon-bonded electrode of 20 wt% 3.1 at% Li-doped Co_3O_4 mixed with graphite;

CP2 — Teflon-bonded electrode of 20 wt% Co_3O_4 mixed with graphite.

7.2.2. Results and Discussions

Fig. 7.1 shows the steady state polarization curves for oxygen reduction on various Teflon-bonded Co_3O_4/graphite electrodes in 5N KOH at 25°C in air. The potentials were measured against a DHE and were iR corrected. It can be seen in Fig. 7.1 that the activation polarization for oxygen reduction on electrode CP2 is larger but, conversely, is smaller on electrode CG. It can be noted that the performance of CG is even better than electrode HSAC2; a polarization potential of about 825 mV is observed at a current density of 200 mA/cm^2 on electrode CG. The concentration of Co_3O_4 dispersed among the high surface area graphite is only 1.22 wt% in the case of electrode CG. It is also observed that the polarization performance of Co_3O_4 is significantly improved by doping 3.1at% lithium into Co_3O_4 (electrode LDC2). The electrochemical activities of Teflon-bonded Co_3O_4/graphite electrodes are in general coincident with the sequence of catalytic activities of cobalt catalysts for the decomposition of hydrogen peroxide.

The corresponding Tafel plot indicates that the concentration overpotential for electrode CG is negligible up to 200 mA/cm^2, as shown in Fig. 7.2. For oxygen reduction on electrode CP2 there are two distinct Tafel slopes as can be seen in Fig. 7.3. The remarkable difference in the values of the Tafel slope obtained at higher polarization, could mainly be attributed to the increase of concentration overpotential caused by the lower catalytic activity of cobalt catalysts (In the case of Teflon-bonded electrodes prepared by the painting method, there essentially exists only one catalyst layer.), and, therefore, a lower coefficient of oxygen recycling. A comparison of Tafel parameters for O_2 reduction on the Teflon-bonded

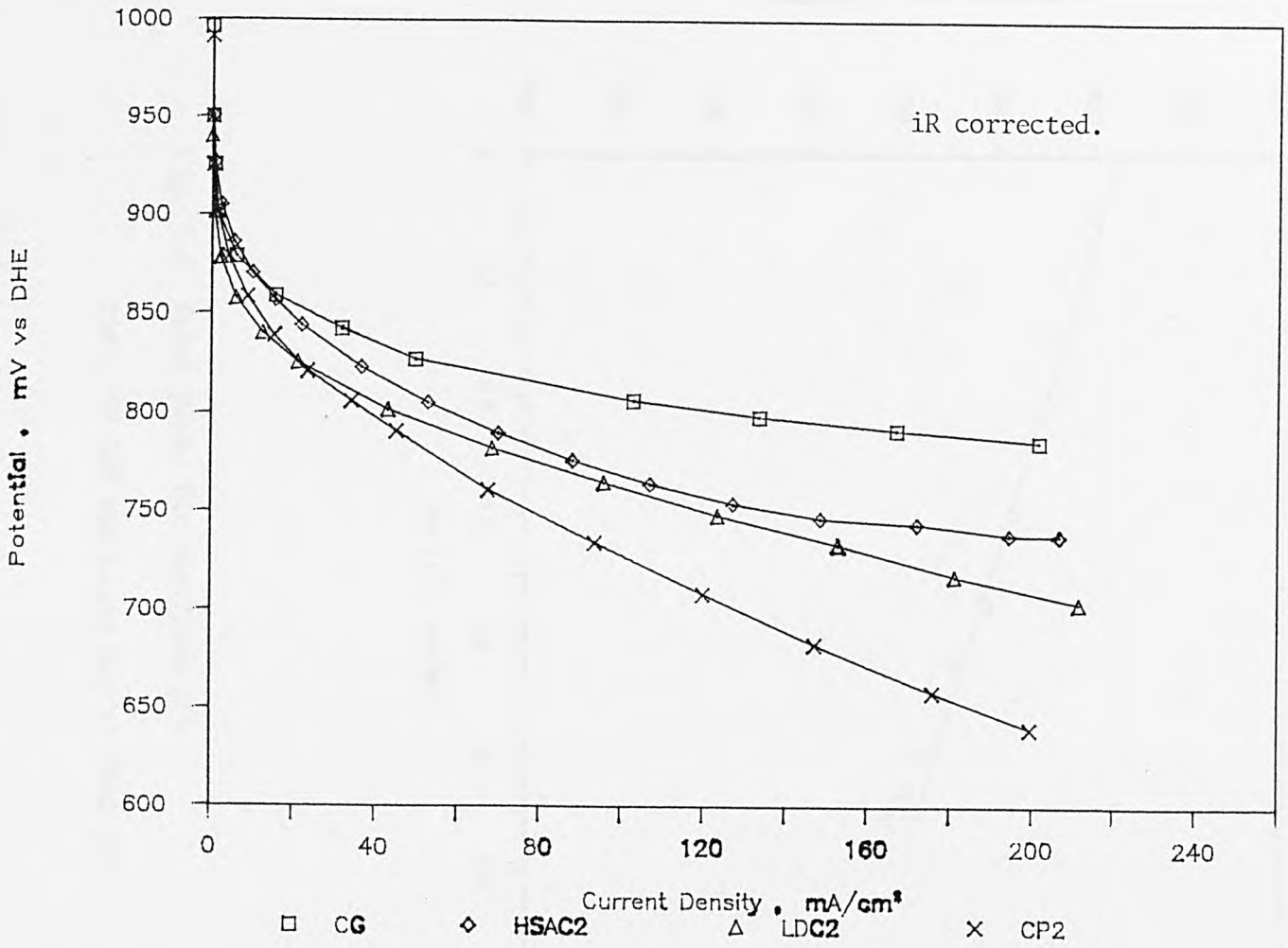

Fig. 7.1 Polarization curves of Teflon-bonded Co_3O_4/graphite electrodes. 25°C, 5N KOH and using air as feed gas.

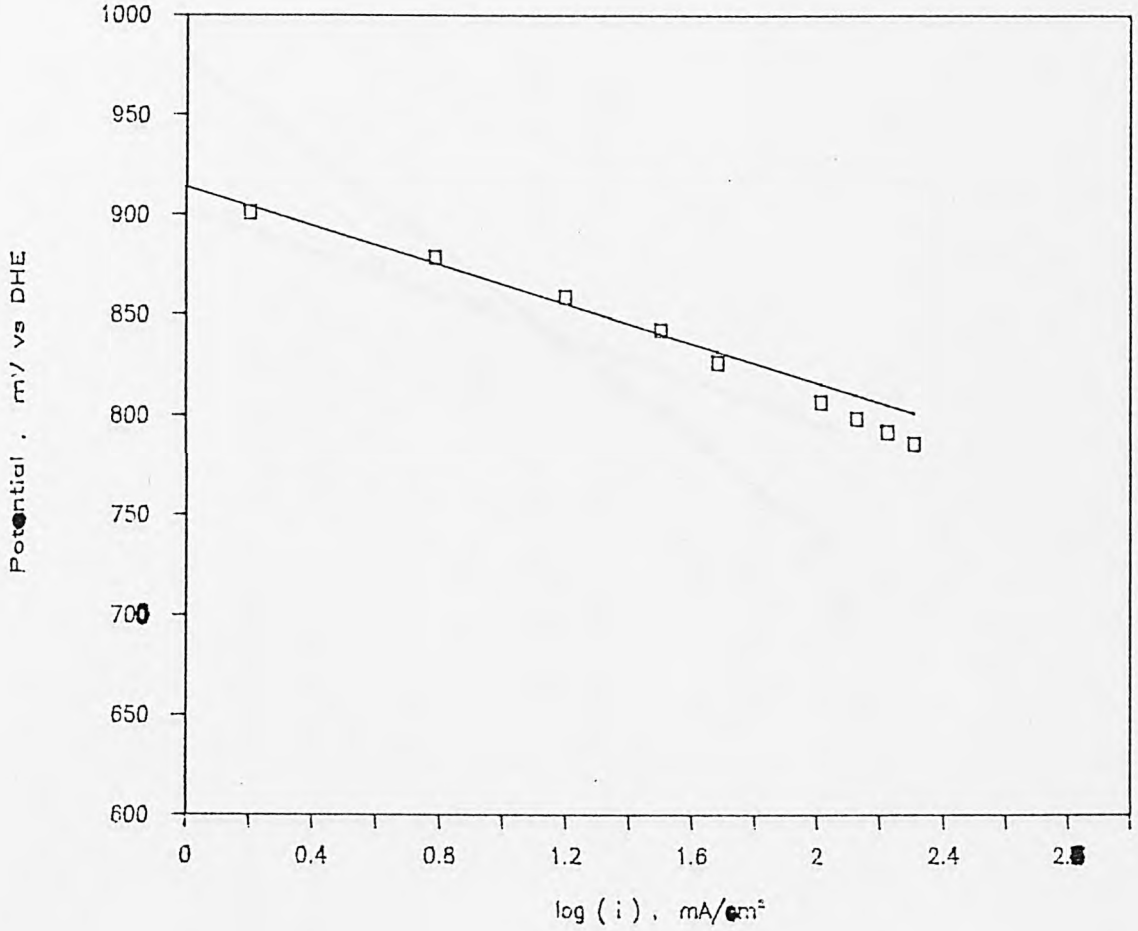

Fig. 7.2 Tafel plots for electrode CG.

25^{0}C, 5N KOH and using air as feed gas.

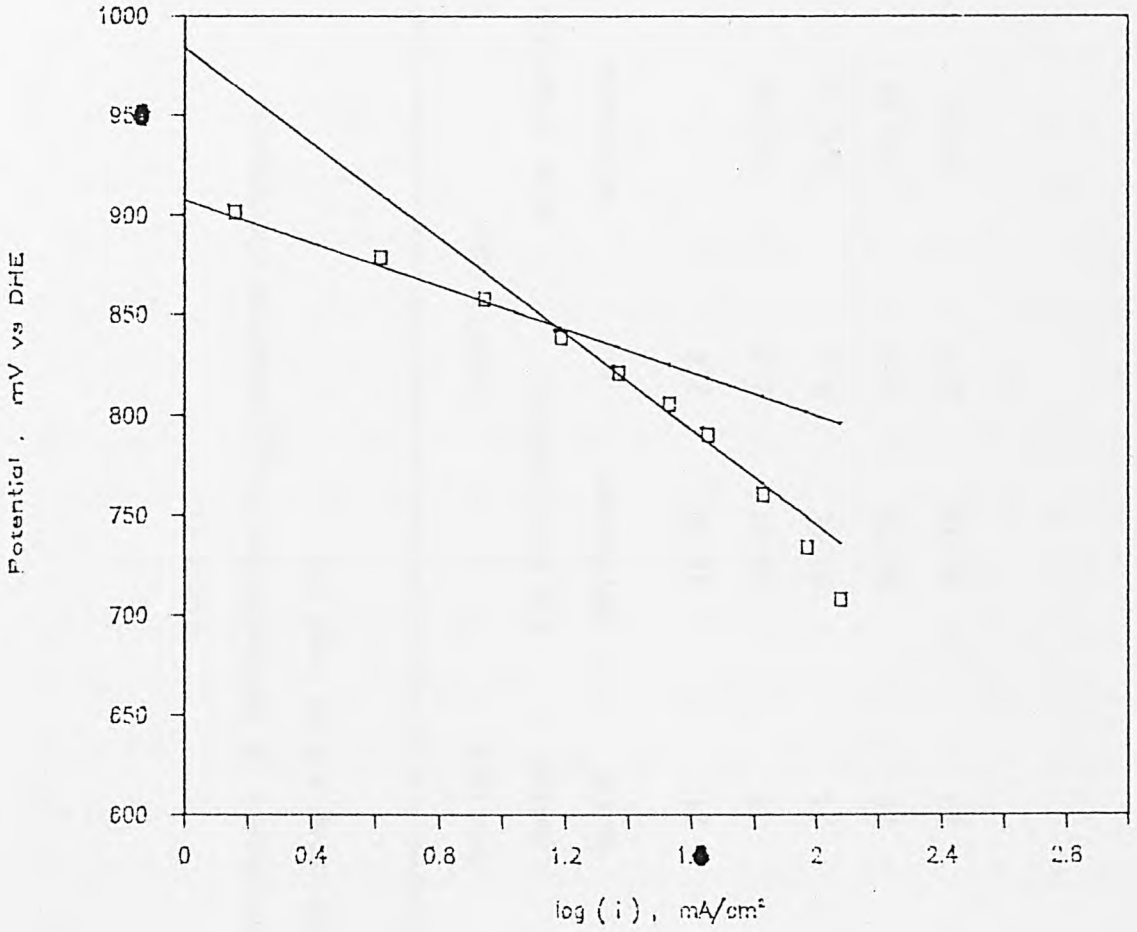

Fig. 7.3 Tafel plots for electrode CP2.

25^{0}C, 5N KOH and using air as feed gas.

Table 7.1

Polarization parameters of Teflon-bonded Co_3O_4/graphite electrodes.
25^oC, 5N KOH and using air as feed gas.

Electrode Code	Catalyst Loading mg/cm^2	Tafel slope			
		Low polarization		High polarization	
		mV/decade	n	mV/decade	n
CG, 1.22% HSACo_3O_4	21	48.78	2.4		
HSAC2, 20% HSACo_3O_4	25	54.91	2.2	112.99	1.0
LDC2, 20% Li-doped Co_3O_4	24	57.51	2.1	115.71	1.0
CP2, 20% Co_3O_4	23	53.70	2.2	119.22	1.0
Graphite	23	52.23	2.3	125.21	0.9

electrodes studied here is given in Table 7.1. The number of electrons participating in the O_2 reduction was calculated on the assumption that the transfer coefficient is 0.5.

It is possible to study the effect of mass transport on the electrochemical behaviour of porous electrodes on the basis of transport hindrance plots (plot of potential difference via current density)[192]. The $\Delta E/i$ curves were obtained by subtracting the potential values for an electrode operating in air, E_a, from the potential values obtained for the same electrode operating in pure oxygen, E_o; at the same current density. Fig. 7.4 is the polarization curves for the electrodes described in Fig. 7.1, using pure oxygen as feed gas. The potential differences ($\Delta E = E_o - E_a$) were calculated for a chosen constant current density, for each electrode. The results are shown in Fig. 7.5. Generally, the transport hindrance plots are characterized by three regions. The period of the first region is very short and the kinetics for oxygen reduction at such low current density could be described by the Nernst equation[21,192]. At relatively lower overpotentials, there are linear portions with small slopes for all four Teflon-bonded electrodes, indicating that the mass transport resistances are all relatively small and also insensitive to the activities of added cobalt oxide catalysts. The constant differing values of the potentials could also mean that the electrodes are operated in the Tafel region[227]. As cathodic polarization increases the potential difference values for CP2 and LDC2 increase, while for HSAC2 and CG the characteristics of the curves remain unchanged. Because there is no hydrophobic layer (supplying gas to the catalyst layer as in the rolling method) in any of the electrodes, the effect of the porous structure of the hydrophobic layer on the rate of mass

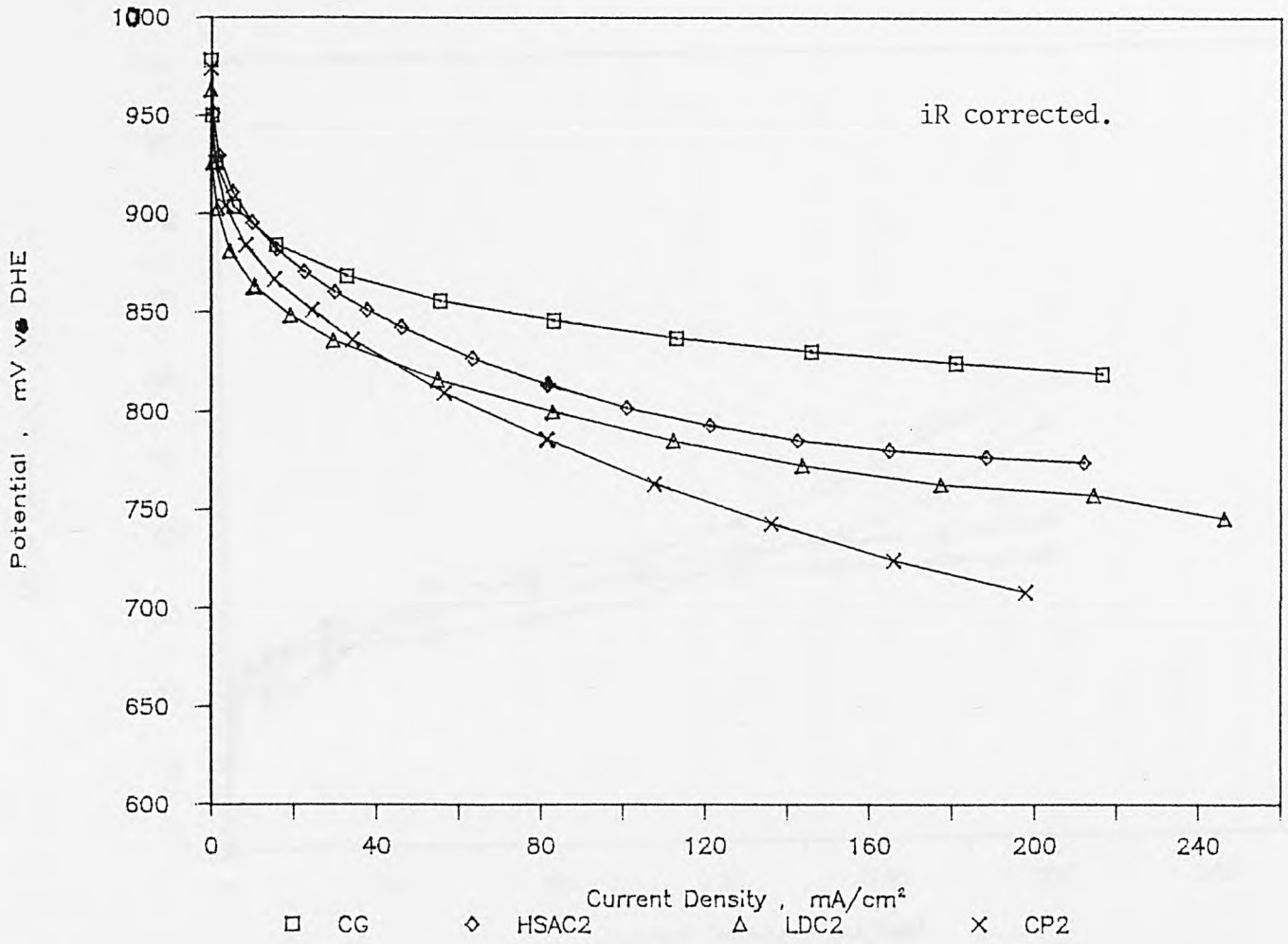

Fig. 7.4 Polarization curves of Teflon-bonded Co_3O_4/graphite electrodes.
25°C, 5N KOH and using oxygen as feed gas.

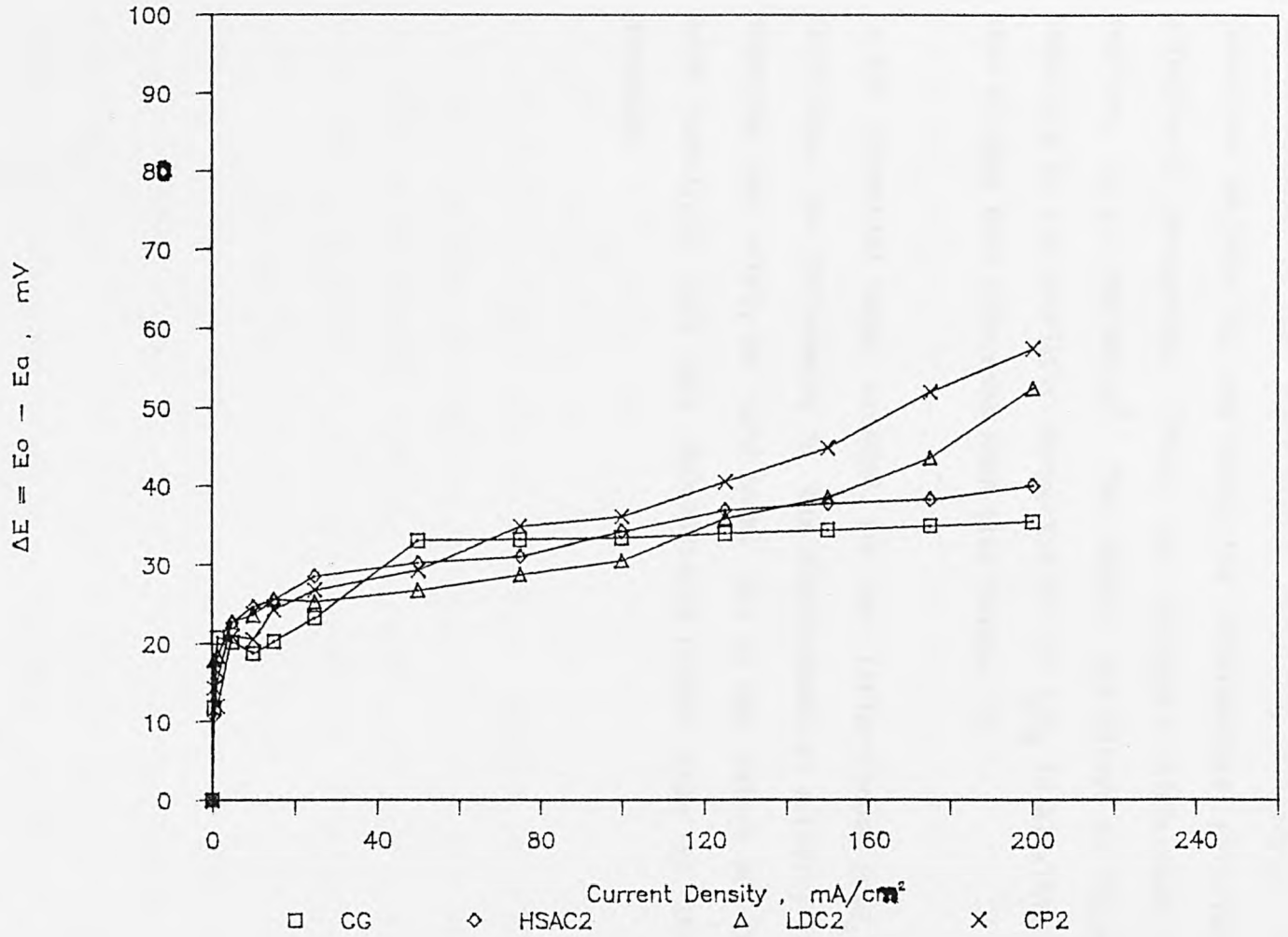

Fig. 7.5 Transport hindrance plots for O_2 reduction on Co_3O_4/graphite electrodes. 25°C and 5N KOH.

transport is eliminated[192]. Therefore, the increase shown in the mass transport hindrance plots is likely to be associated with increasing concentration overpotential of oxygen diffusion in the pores, because of the lower oxygen recycling efficiency. During O_2 reduction on both CG and HSAC2 the intermediate peroxide is more effectively decomposed. Thus, the transport hindrances are kept smaller, up to 200 mA/cm^2. The higher activities of CG and HSAC2 catalysts in the catalytic decomposition of H_2O_2 in alkaline solutions have already been expounded upon (see Chapter 4).

In the potential range studied, for the Teflon-bonded Co_3O_4/graphite electrodes, the differences in the electrochemical activity for oxygen reduction can safely be said to be due to the nature of the cobalt oxide catalysts that are incorporated rather than to the porous structure.

7.3. A.C. Impedance Measurements

7.3.1. Experimental

Test electrodes for a.c. impedance measurements were fabricated by the rolling method, with catalyst loadings of about 20 mg/cm^2. The experimental parameters for impedance measurements were the same as mentioned in the study of Teflon-bonded graphite electrodes (see section 6.3.1). The same precaution was also taken to polarize the electrodes between 1000 and 750 mV in 5N KOH before the impedance measurements were taken. The measurements were carried out at 25^{o}C in 5N KOH at various polarization potentials, i.e. ocv (open circuit voltage), 900, 850 and 800 mV. The potential readings were taken against a dynamic hydrogen electrode (DHE) and air was used as the feed gas.

The analytical method for an electrode reaction coupled with a catalytic reaction, described in section 5.4.2, was used to evaluate the kinetic parameters from the observed impedance data for O_2 reduction on graphite electrodes incorporated with various Co_3O_4 catalysts. It was found that for the impedance data obtained at a potential near the equilibrium potential, neither the equivalent circuit analysis (used for an electrode reaction coupled with an adsorption process) nor the analytical methods could successfully be used for the evaluation of faradaic impedance parameters. In these situations the coupled chemical reactions could involve both surface adsorption of reactants and catalytic decomposition of product HO_2^- but with comparable reaction rates. The results obtained from the impedance analysis of O_2 reduction on Teflon-bonded graphite electrodes

have revealed that surface adsorption could only be the rate determining step if the polarization potential is above about 850 mV. Therefore, it is possible to simplify the electrochemical system in study and to avoid the interferences of impurity or other surface reactions, by carrying out impedance measurements at relatively lower potentials. The measured potential for the theoretical impedance analysis was taken as 850 mV (DHE). The value of the catalytic reaction parameter k_c is estimated from the intercept values, extrapolated at higher and lower frequencies, and the slope at higher frequencies (see equation 5.33). It must be emphasized that it is not necessary for the catalytic reaction rate k_c to be exactly equal to the corresponding first-order reaction constant k_f obtained from the kinetic studies of peroxide decomposition. The initial conditions of the decomposition of hydrogen peroxide and the catalytic activity of Co_3O_4 catalysts would differ significantly in bulk cobalt oxides and for that distributed inside the porous electrodes during O_2 reduction. Nevertheless, the k_c values are mainly dependent on the chemical activity of the cobalt oxides for peroxide decomposition. In respect of the electrochemical activity of the electrodes this parameter k_c, calculated from the observed impedance responses, is considered to be more meaningful and important.

7.3.2. Results and Discussions

7.3.2.1. Impedance Responses

Fig. 7.6 shows the complex impedance plots of electrode CG measured at $25^{o}C$ in 5N KOH solution in air. Generally, the impedance spectra are shaped in the form of semicircles; they bend out with increasing cathodic potential. It has been confirmed in the previous chapter that for O_2 reduction on Teflon-bonded graphite electrodes, the semicircles obtained from the impedance measurements are not associated with the charge transfer reactions. However, the Warburg tail was not observed for the impedance responses in the present study, where the graphite electrodes were incorporated with Co_3O_4 catalysts. The disappearance of the diffusion tail in the low frequency region indicates the predominant role of the catalytic decomposition of peroxide, formed as an intermediate, during the oxygen reduction.

Theoretically, it is possible to exclude the influence of chemical reactions if the frequency of perturbation far exceeds the chemical reaction rates[228]. As a role the faradaic parameters, i.e. charge transfer resistance R_{ct} and the Warburg diffusion coefficient W, can be obtained in a sufficiently high frequency region using the Randles equation. Such Randles plots are shown in Fig. 7.7 for the electrode CG at ocv. A straight line was only observed in the high frequency region. The irregular behaviour of the measured impedance data at low frequencies shows the complex reactions of O_2 and the HO_2^- intermediate. The intercept obtained from the resistance components on the Randles plane gives the value of R_{ct} and the slope the value of W. It is impossible to distinguish between the contribution made by

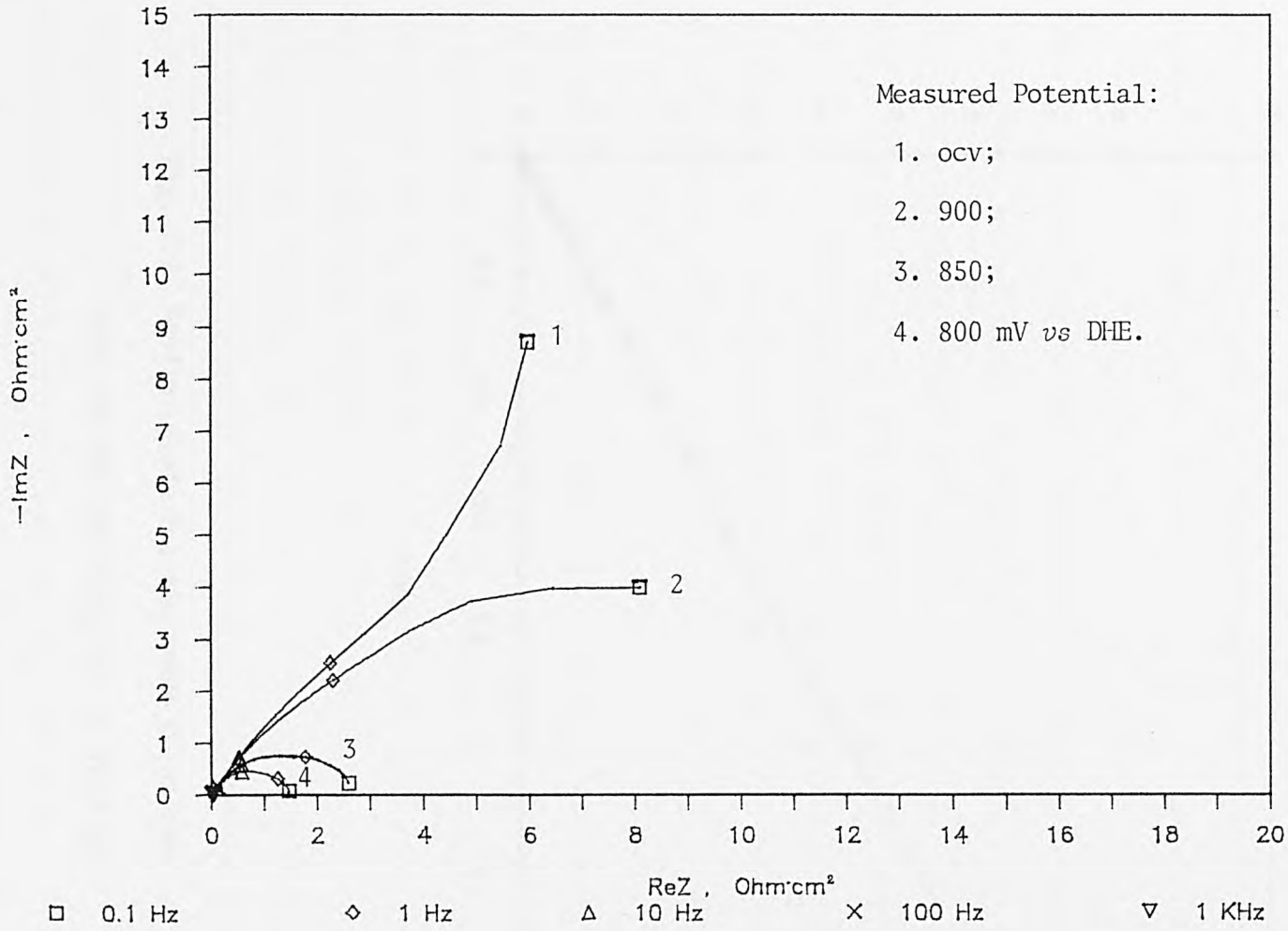

Fig. 7.6 Measured impedance responses of electrode CG at various potentials. 25°C, 5N KOH and using air as feed gas.

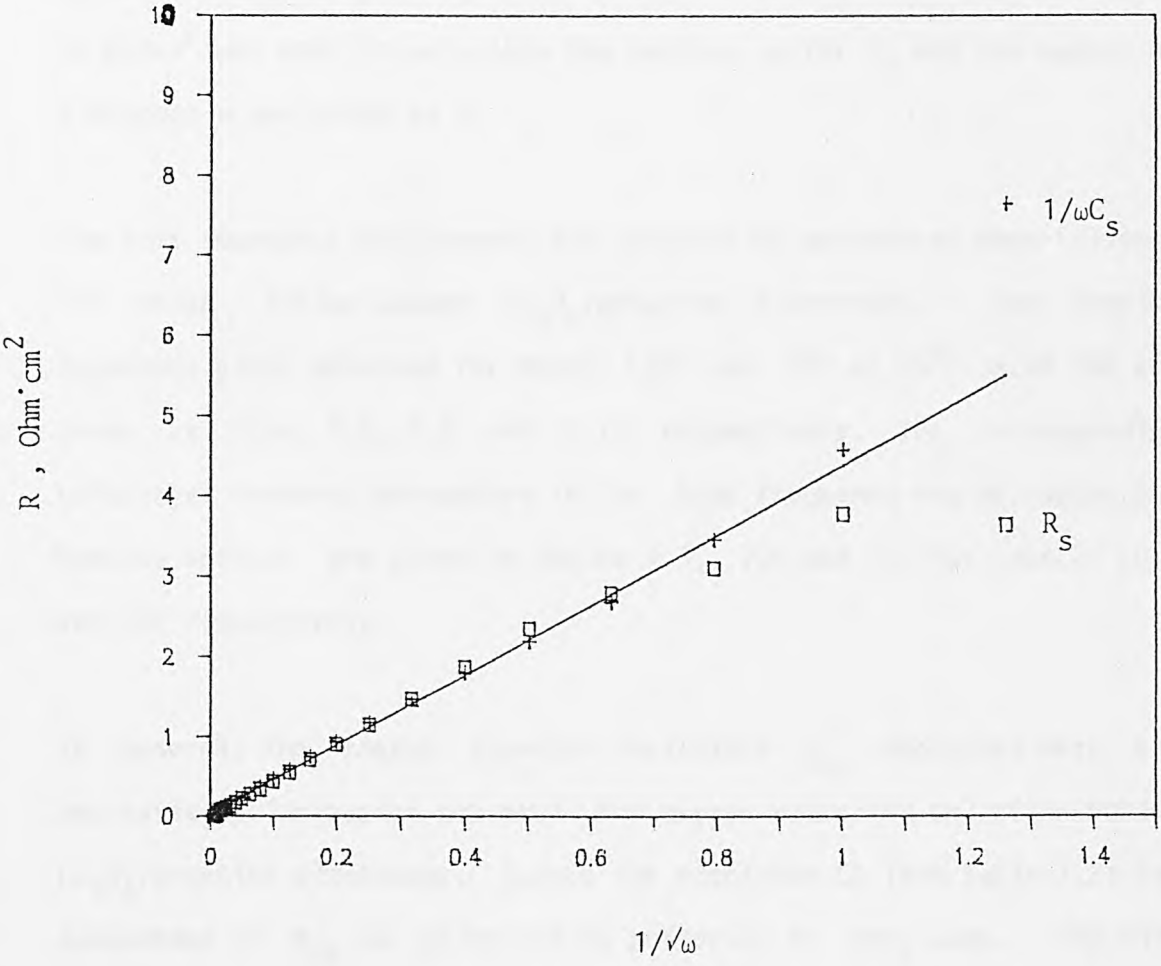

Fig. 7.7 Randles plots for electrode CG at ocv.

25°C, 5N KOH and using air as feed gas.

reactant oxygen and product peroxide to the Warburg diffusion impedance at this stage. Table 7.2 lists the measured faradaic parameters of the electrode CG. The characteristic exchange current density i_o' was calculated according to equation (6.4); the double layer capacitance of 10 $\mu F/cm^2$ was used to calculate the surface factor f_s and the number of electrons n was taken as 2.

The same impedance measurement and calculation procedures were followed for other Teflon-bonded Co_3O_4/graphite electrodes. The complex impedance plots obtained for HSAC2, LDC2 and CP2 at 25°C in 5N KOH are shown as Figs. 7.8, 7.9 and 7.10 respectively. The corresponding calculated faradaic parameters in the high frequency region, using the Randles methods are given in Tables 7.3, 7.4 and 7.5 for HSAC2, LDC2 and CP2 respectively.

In general, the charge transfer resistance R_{ct} decreases with the decreasing polarization potential for oxygen reduction on Teflon-bonded Co_3O_4/graphite electrodes. Except for electrode CG (see Table 7.2) the dependence of R_{ct} on polarization potential is very weak. The only physical difference between electrode CG and the rest is that the Co_3O_4/graphite catalyst was prepared by precipitating cobalt oxide catalysts onto the graphite carriers from alkaline solution. This could have resulted in promoting not only the homogeneous catalytic activity of Co^{2+} localized inside the pores, but also the electrochemical activity of Co_3O_4 for O_2 reduction. Because the intermediate peroxide is effectively decomposed inside the pores, in the case of electrode CG, the possible poisoning of the electrochemical active sites, mainly of graphite particles, due to the contact with HO_2^- ions can be avoided to a large extent. Therefore, the activity of

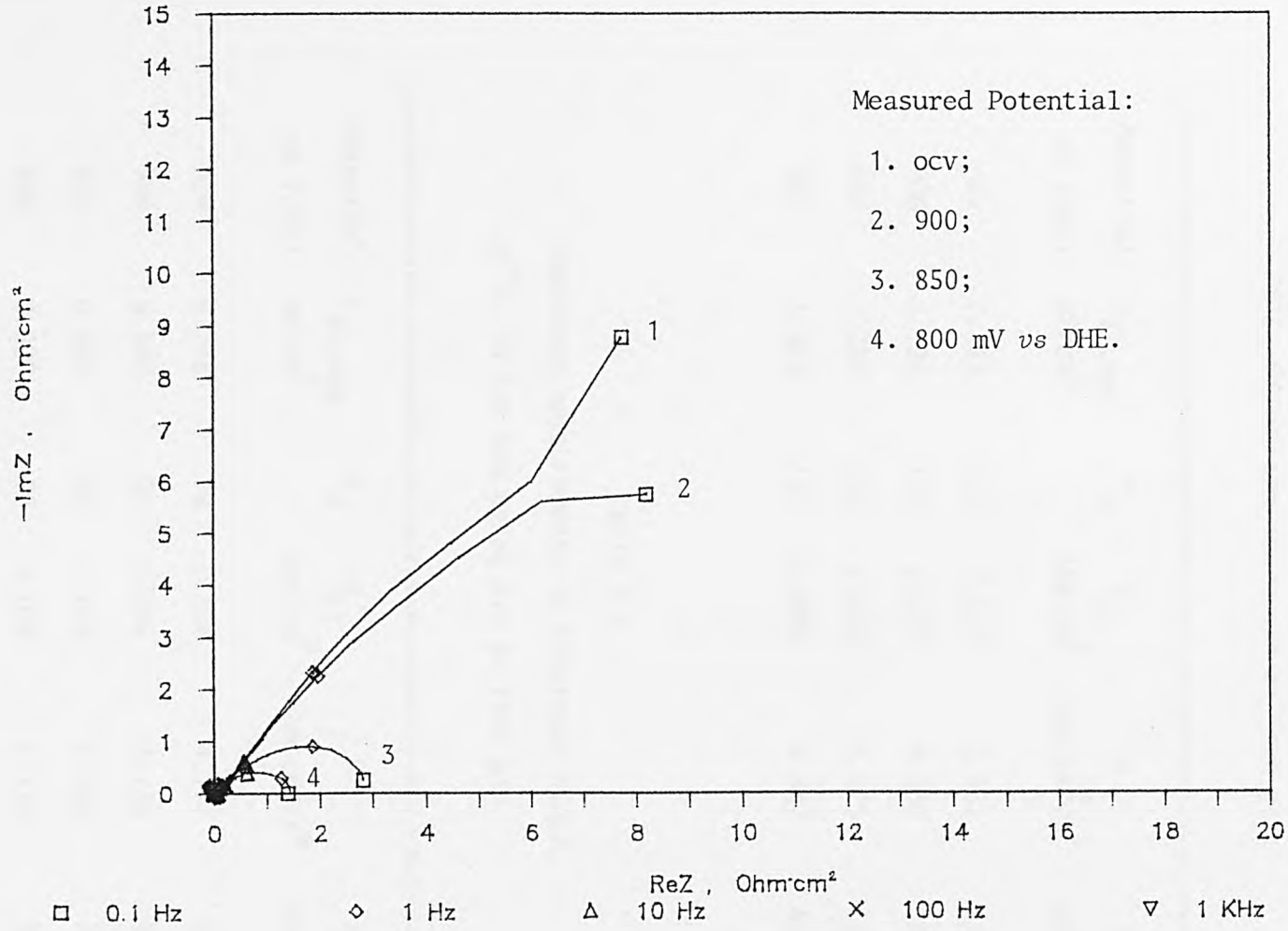

Fig. 7.8 Measured impedance responses of electrode HSAC2 at various potentials. 25°C, 5N KOH and using air as feed gas.

Table 7.2

Impedance measurements on electrode CG.

$25^{o}C$, 5N KOH and using air as feed gas.

Potential mV (DHE)	$C_{dl,app}$ mF/cm^2	f_s	R_{ct} $ohm \cdot cm^2$	W $ohm \cdot cm^2/s^{\frac{1}{2}}$	i_o' mA/cm^2
ocv	1.112	111	0.016	3.561	7.22
900	1.194	119	0.014	4.350	7.68
850	1.200	120	0.009	4.526	11.89
800	1.308	131	0.0024	4.327	40.90

Table 7.3

Impedance measurements on electrode HSAC2.

$25^{o}C$, 5N KOH and using air as feed gas.

Potential mV (DHE)	$C_{dl,app}$ mF/cm^2	f_s	R_{ct} $ohm \cdot cm^2$	W $ohm \cdot cm^2/s^{\frac{1}{2}}$	i_o' mA/cm^2
ocv	0.778	78	0.036	4.177	4.58
900	0.840	84	0.036	4.712	4.25
850	0.828	83	0.022	4.897	7.05
800	0.920	92	0.026	4.718	5.37

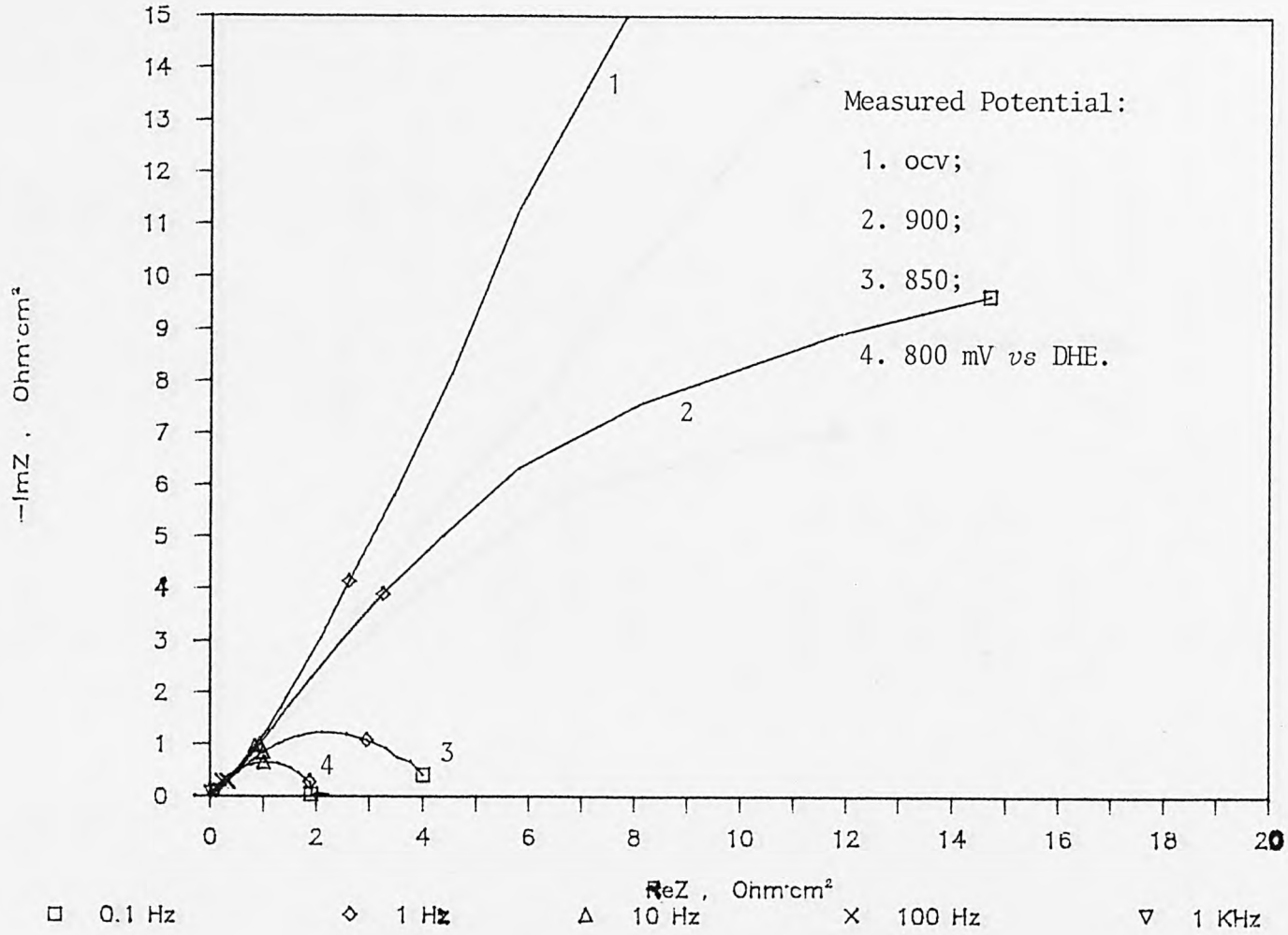

Fig. 7.9 Measured impedance responses of electrode LDC2 at various potentials. 25°C, 5N KOH and using air as feed gas.

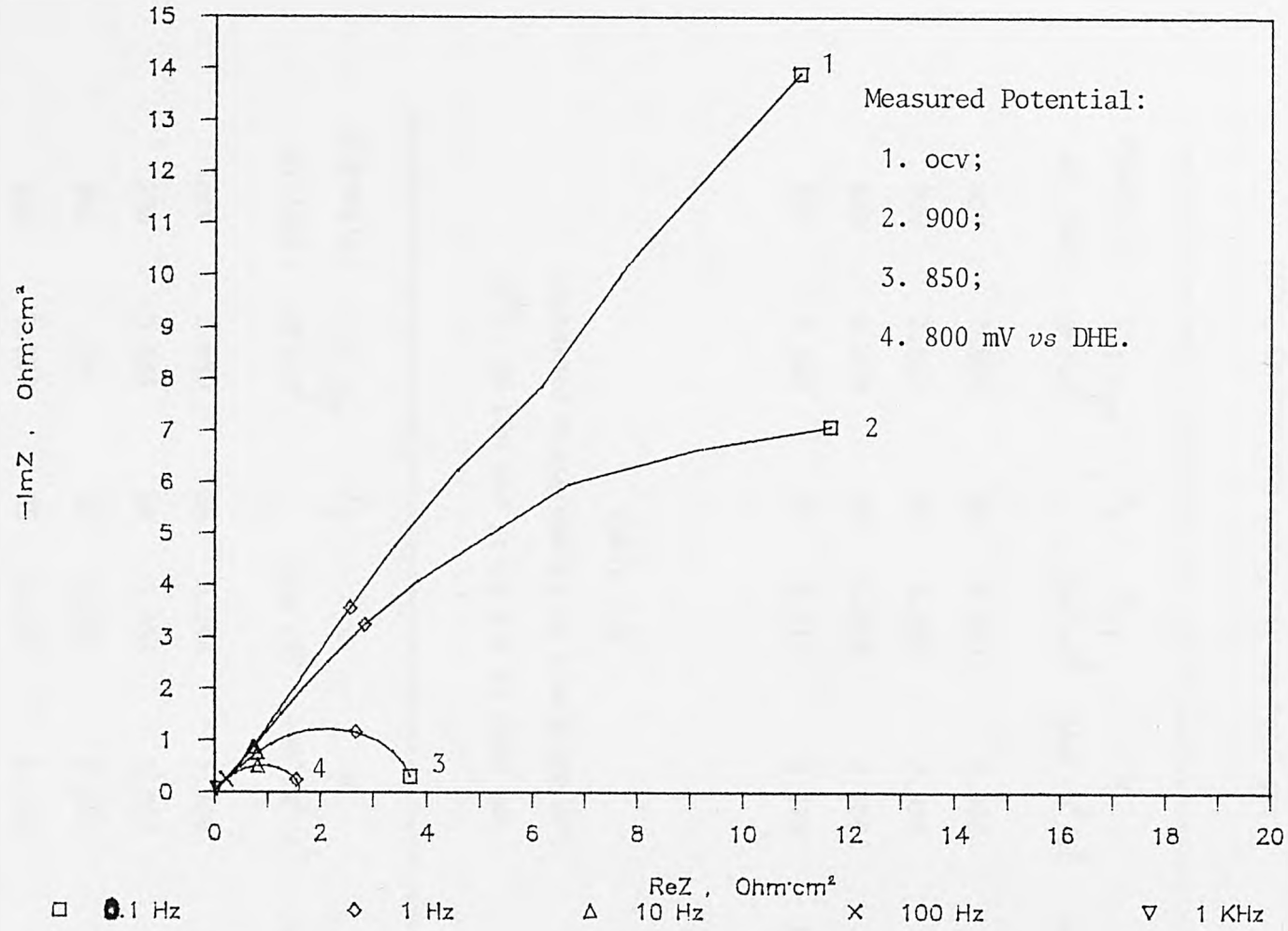

Fig. 7.10 Measured impedance responses of electrode CP2 at various potentials. 25°C, 5N KOH and using air as feed gas.

Table 7.4

Impedance measurements on electrode LDC2.

$25^{o}C$, 5N KOH and using air as feed gas.

Potential mV (DHE)	$C_{dl,app}$ mF/cm^2	f_s	R_{ct} $ohm \cdot cm^2$	W $ohm \cdot cm^2/s^{\frac{1}{2}}$	i_o' mA/cm^2
ocv	0.802	80	0.043	6.902	3.72
900	0.917	92	0.043	7.891	3.26
850	0.854	85	0.028	8.109	5.37
800	0.865	87	0.011	8.075	13.49

Table 7.5

Impedance measurements on electrode CP2.

$25^{o}C$, 5N KOH and using air as feed gas.

Potential mV (DHE)	$C_{dl,app}$ mF/cm^2	f_s	R_{ct} $ohm \cdot cm^2$	W $ohm \cdot cm^2/s^{\frac{1}{2}}$	i_o' mA/cm^2
ocv	0.880	88	0.044	5.908	3.32
900	0.838	84	0.035	5.932	4.38
850	0.798	80	0.032	6.674	5.03
800	0.853	85	0.037	6.120	4.07

CG is significantly increased. The irregular behaviour of the Warburg diffusion coefficient, with respect to potential, could be caused by the complex influence of the porous structure of a Teflon-bonded electrode on reactant diffusion processes. The almost constant values of Warburg coefficients in the measured potential range seem to indicate the relatively higher resistance to the transport of O_2 molecules through the gas-filled pores in the hydrophobic layer. So to optimize the electrochemical performance of such double-layer air electrodes, it is necessary to minimize the transport hindrance on the gas-side layers[25].

7.3.2.2. Comparison of Faradaic Impedance Parameters

The faradaic parameters for the various Co_3O_4/graphite electrodes, measured at 25^oC in 5N KOH solution at ocv, are summarized in Table 7.6; where the faradaic parameters for a Teflon-bonded graphite electrode is also given. With no exception, the i_o' values for the Teflon-bonded graphite electrode and the electrodes incorporating various cobalt oxide catalysts are all of the order of milliamperes (between 2-7 mA/cm^2). It can immediately be concluded that despite the incorporation of Co_3O_4 catalysts into the graphite electrode and despite the significant difference in the dispersion of cobalt oxide catalysts, the overall electron transfer reactions are hardly affected and O_2 reduction still proceeds through the two-electron pathway described for the graphite electrodes. The results from the impedance measurements are found to be in disagreement with the conclusions drawn from the work based on disk-ring techniques[71,217].

As would be expected from the kinetics of oxygen reduction on various

Table 7.6

Impedance parameters of Teflon-bonded Co_3O_4/graphite electrodes. 25°C, 5N KOH, air and ocv.

Electrode Code	$C_{dl,app}$ mF/cm^2	f_s	R_{ct} ohm·cm^2	W ohm·cm^2/s$^{\frac{1}{2}}$	i_o' mA/cm^2
CG	1.112	111	0.016	3.561	7.22
HSAC2	0.778	78	0.036	4.177	4.58
LDC2	0.802	80	0.043	6.902	3.72
CP2	0.880	88	0.044	5.908	3.32
Graphite	1.865	187	0.034	4.692	2.02

cobalt oxide/graphite electrodes, the higher the activity for the decomposition of H_2O_2, the higher the i_o' value. This experimental observation again confirmed that the i_o' value is characteristic of an electrochemical activity for a gas diffusion electrode. The strong dependence of characteristic exchange current density on catalytic activity means that the rate determining step is changed to the catalytic decomposition reaction of intermediate HO_2^- after the catalysts are incorporated into graphite electrodes. The best electrochemical activity for oxygen reduction was observed on the electrode CG. In this case the i_o' value increased more than three times, compared with that for the pure graphite electrode. It is interesting to point out that according to the heterogeneous catalytic mechanism for O_2 reduction on cobalt-iron oxide/graphite systems put forward by Goldstein[23], the maximum enhancement of the electrodes is only to double the pseudo-exchange current density value. The discrepancy could be explained by two reasons. One is that the direct application of the heterogeneous catalytic mechanism during O_2 reduction is not appreciable in the cobalt oxide catalyst systems because of the participation of dissolved Co^{2+} ions, and the other is that the kinetics of O_2 reduction evaluated solely on the steady state polarization data, in the case of gas diffusion electrodes, are less reliable.

It was also noticed that the double layer capacity was remarkably reduced when 20 wt% of cobalt oxides were incorporated in the graphite electrodes. Since the value of $C_{dl,app}$ is the measurement of the electrochemical active area for the porous electrodes, the reduction in double layer capacity means that more than 50% of the effective reaction area was lost in the case where the cobalt oxide catalyst was

mechanically mixed with high surface area graphite. This loss of reaction area after the incorporation of cobalt oxides was, certainly, not totally due to the relatively low surface area of the oxides. If it were so, only 17% of the reaction area of the graphite electrode could be lost with the addition of 20 wt% cobalt oxides, assuming the average surface area of cobalt oxides is about 50 m^2/g. A more reasonable explanation could come from the distribution of oxide catalysts among the high surface area graphite. The pore size analysis[120] of the reaction layer for a Teflon-bonded carbon electrode revealed that there are two distinctive pore distributions. The smaller pore, which is less than 0.1 micron, functions as a reaction area and the larger pore acts as a gas channel. The transmission electron microscopy analyses have indicated that most of the cobalt oxide particles precipitated are greater than 0.1 micron. As a result, most cobalt oxide particles are not accessible to the smaller pores and most likely are located inside the larger pores or near the mouth of the smaller pores. Consequently, the reaction areas are seriously blocked by the oxide particles. To ameliorate this, the oxide catalysts should be uniformly precipitated on the graphite or carbon and the amount of oxide catalysts should be kept minimal.

7.3.2.3. Theoretical Analysis of A.C. Impedance Responses

The impedance measurements were carried out potentiostatically at 850 mV. The experiments were carried out in 5N KOH solution at 25°C, in air. The observed impedance responses and the estimated impedance responses from equation (5.31) were displayed on the Randles plane as before.

Figs. 7.11, 7.12, 7.13 and 7.14 show the results of both the theoretical and experimental impedance responses of oxygen reduction on electrodes CG, HSAC2, LDC2 and CP2 respectively. The symbols represent the experimental impedance data after vectorial subtraction of the non-faradaic impedance R_{so} and $C_{dl,app}$. The solid lines represent the results of estimated impedance data according to the analytical procedure described in section 5.4.2. In all cases the fittings between the theoretical and the experimental impedance responses are reasonable, especially in high frequency regions. At low frequencies certain deviations were found between the theoretical and the observed impedance data. Most probably, in the low frequency region the structural effect of porous electrode is more profound. The impedance measurements are also influenced to some extent by other interfacial reactions such as the surface adsorption process. The theoretical impedance parameters referred from Figs. 7.11-14 are shown in Table 7.7. For comparison, the first-order rate constants k_f obtained from chemical kinetic studies of H_2O_2 decomposition are also given in the table.

Significantly, the correlation between the catalytic parameters k_c evaluated from impedance measurements and the electrochemical activity

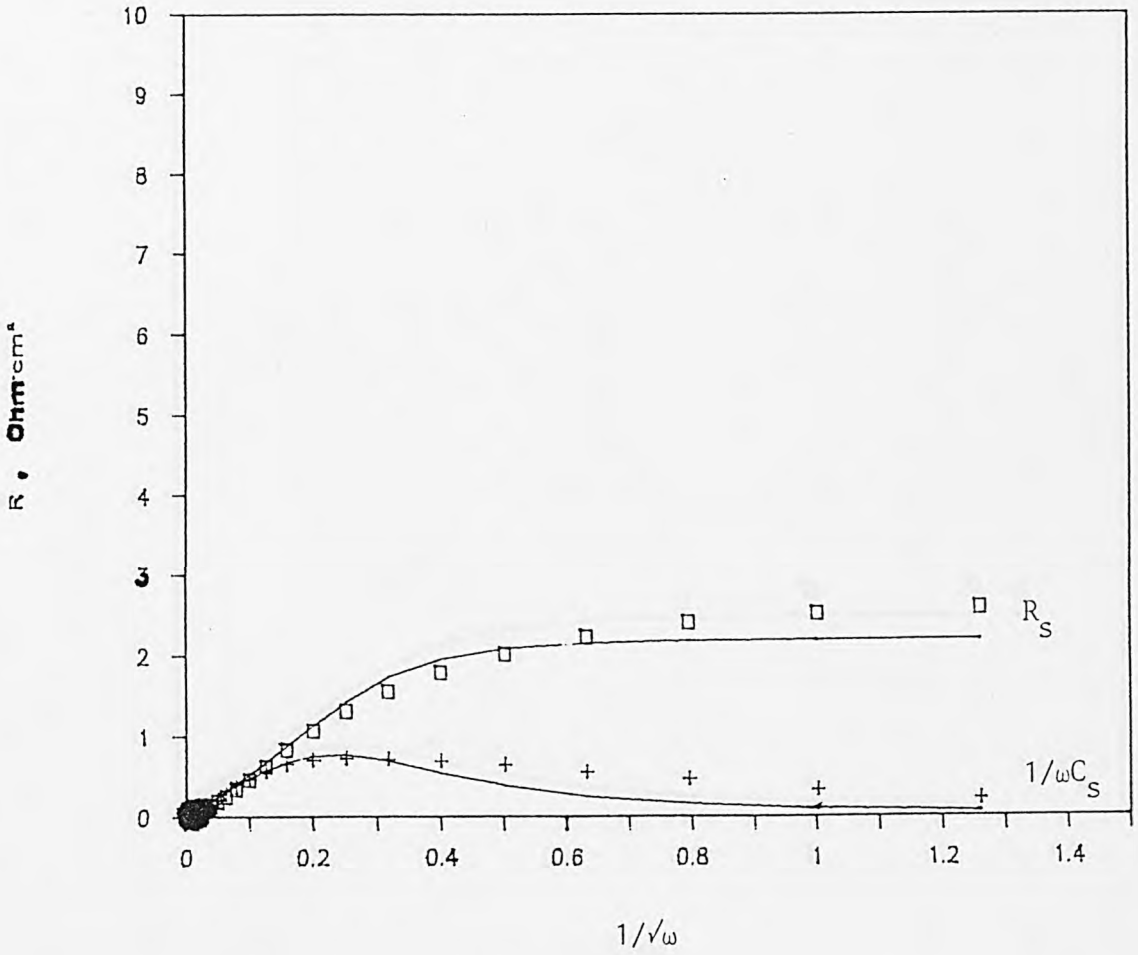

Fig. 7.11 Fitted Randles plots for electrode CG at 850 mV. 25°C, 5N KOH and using air as feed gas.

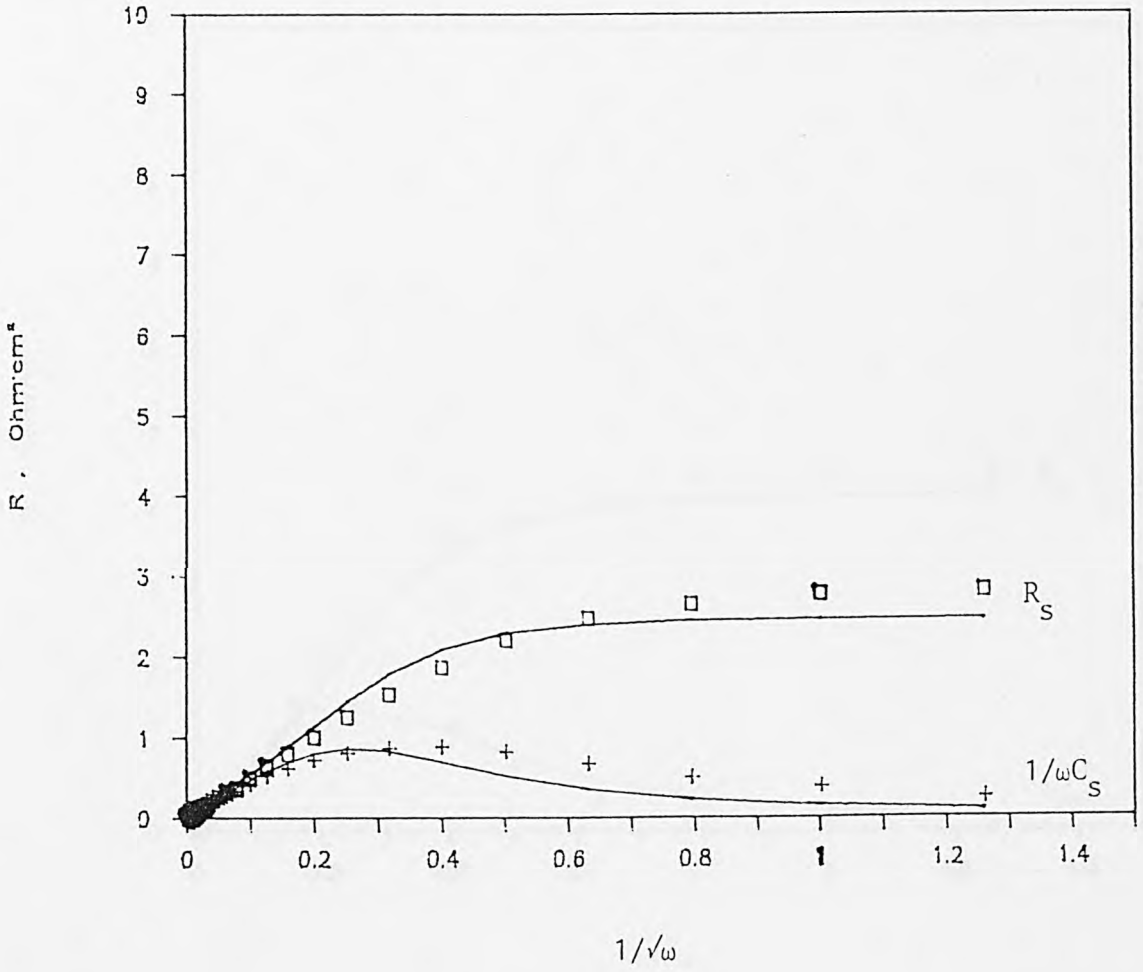

Fig. 7.12 Fitted Randles plots for electrode HASC2 at 850 mV. 25^{0}C, 5N KOH and using air as feed gas.

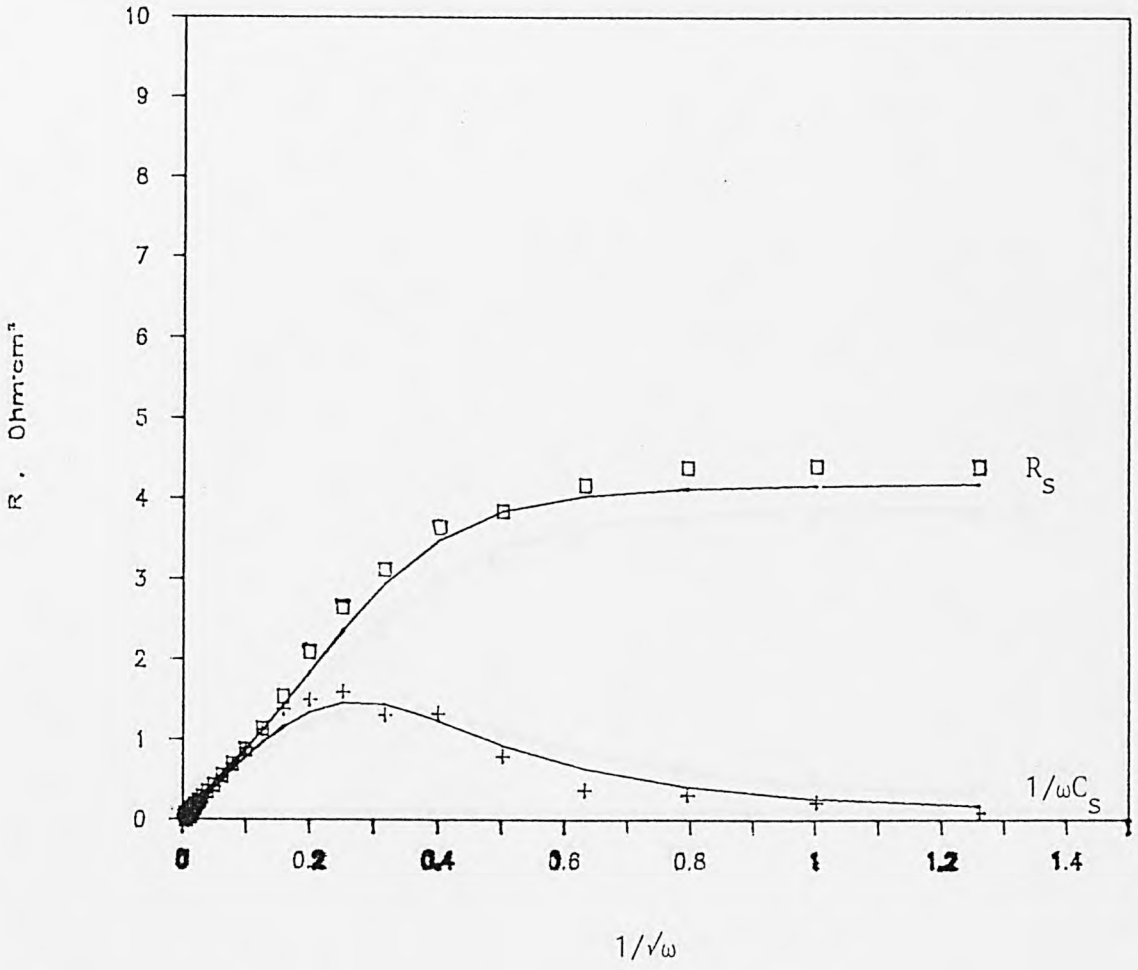

Fig. 7.13 Fitted Randles plots for electrode LDC2 at 850 mV. 25^{0}C, 5N KOH and using air as feed gas.

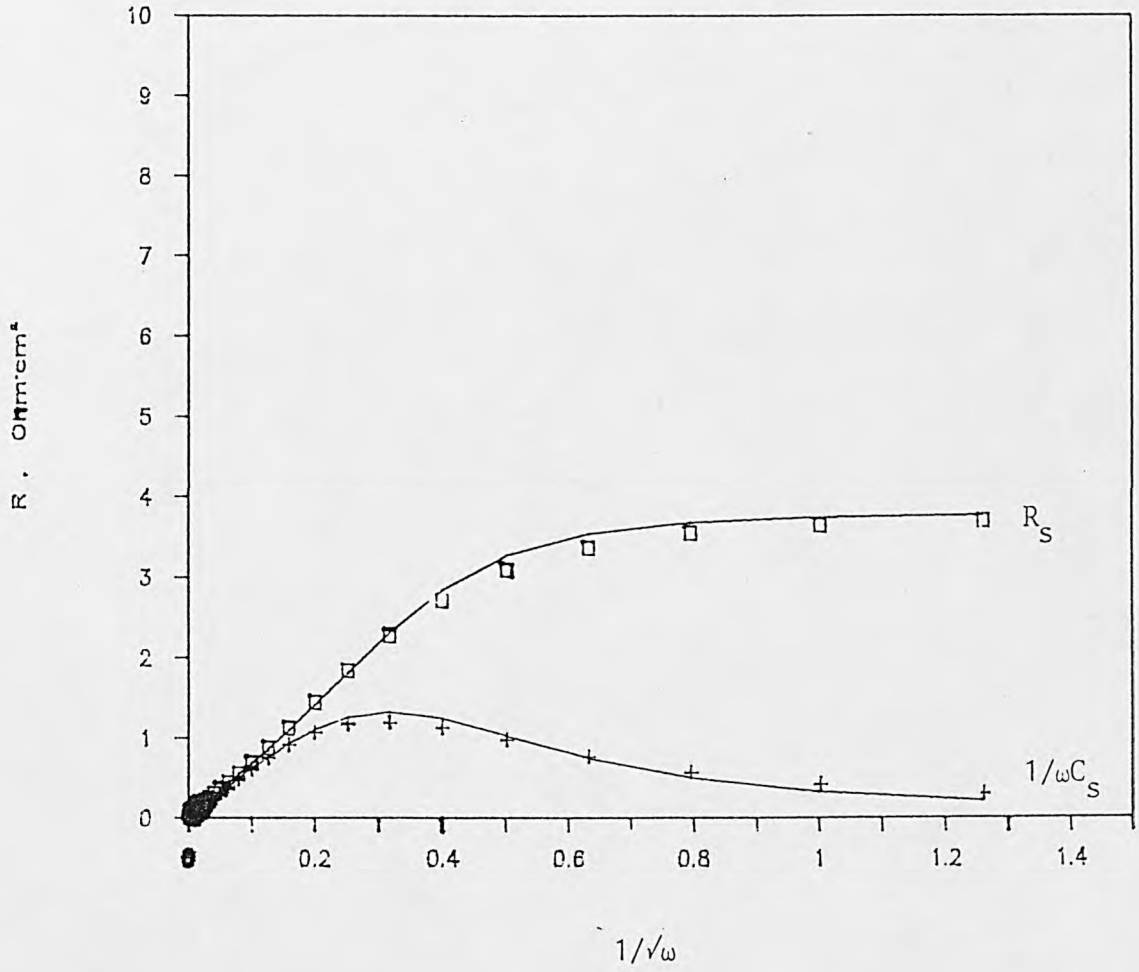

Fig. 7.14 Fitted Randles plots for electrode CP2 at 850 mV. 25^{0}C, 5N KOH and using air as feed gas.

Table 7.7

Theoretical impedance parameters of Teflon-bonded Co_3O_4/graphite electrodes. 25°C, 5N KOH, air and 850 mV.

Electrode Code	$C_{dl,app}$ mF/cm^2	f_s	R_{ct} ohm·cm^2	W ohm·cm^2/s$^{\frac{1}{2}}$	i_o' mA/cm^2	k_c 1/s	k_f*10^3 1/s
CG	1.200	120	0.009	4.950	11.889	10.20	1.60
HSAC2	0.828	83	0.022	4.897	7.049	8.05	1.11
LDC2	0.854	85	0.028	8.109	5.370	7.56	0.38
CP2	0.798	80	0.032	6.282	5.028	5.66	0.36

of the electrodes (e.g. i_o') is obvious. The magnitude of the k_c and i_o' values of electrode CG are, each, double those of electrode CP2. There is, however, no direct relationship between the chemical reaction constant k_f obtained from H_2O_2 decomposition and the electrochemical parameters shown in Table 7.7. It has been pointed out in Chapter 4 that homogeneous decomposition of hydrogen peroxide can occur in the presence of Co^{2+} in alkaline solutions and, that the decomposition reaction is initiated by the formation of free radicals. During O_2 reduction on the Co_3O_4/graphite electrodes the homogeneous catalysis of dissolved Co^{2+} could be seriously interrupted owing to the termination of free radicals on the Co^{3+} ions of the oxide spinel. Such decomposition mechanisms show that the homogeneous catalysis of Co^{2+} is active in the area near to the Co_3O_4 particles. With respect to the electrochemical activity of a porous Co_3O_4/graphite electrode, the value of k_c is an accumulative parameter of the catalytic activity of Co^{2+} ions inside the pores, and therefore represents the homogeneous catalysis activity of Co_3O_4 incorporated during the electroreduction of oxygen inside the pores.

The mechanisms of the localized homogeneous catalysis of dissolved Co^{2+} ions have been supported by the dependence of k_c on measured potential. Table 7.8 shows the k_c values calculated from observed impedance data at various potentials for O_2 reduction on electrodes CG and CP2. An example of the fitted Randles plots for both the measured and estimated impedance responses is shown in Fig. 7.15 for CG at 900 mV (DHE). It should be pointed out that the reliability of the k_c values obtained from measurements at ocv is doubtful because of the uncertainty of the complex reaction mechanisms at open-circuit. However, in general, the k_c values increase with increasing cathodic potential. From the

Table 7.8

Dependence of catalytic reaction parameter k_c on measured potentials.

$25^{o}C$, 5N KOH and using air as feed gas.

Potential mV (DHE)	k_c, 1/s Electrode CG	Electrode CP2
ocv	0.23	0.10
900	0.50	0.25
850	10.20	5.66
800	20.00	15.50

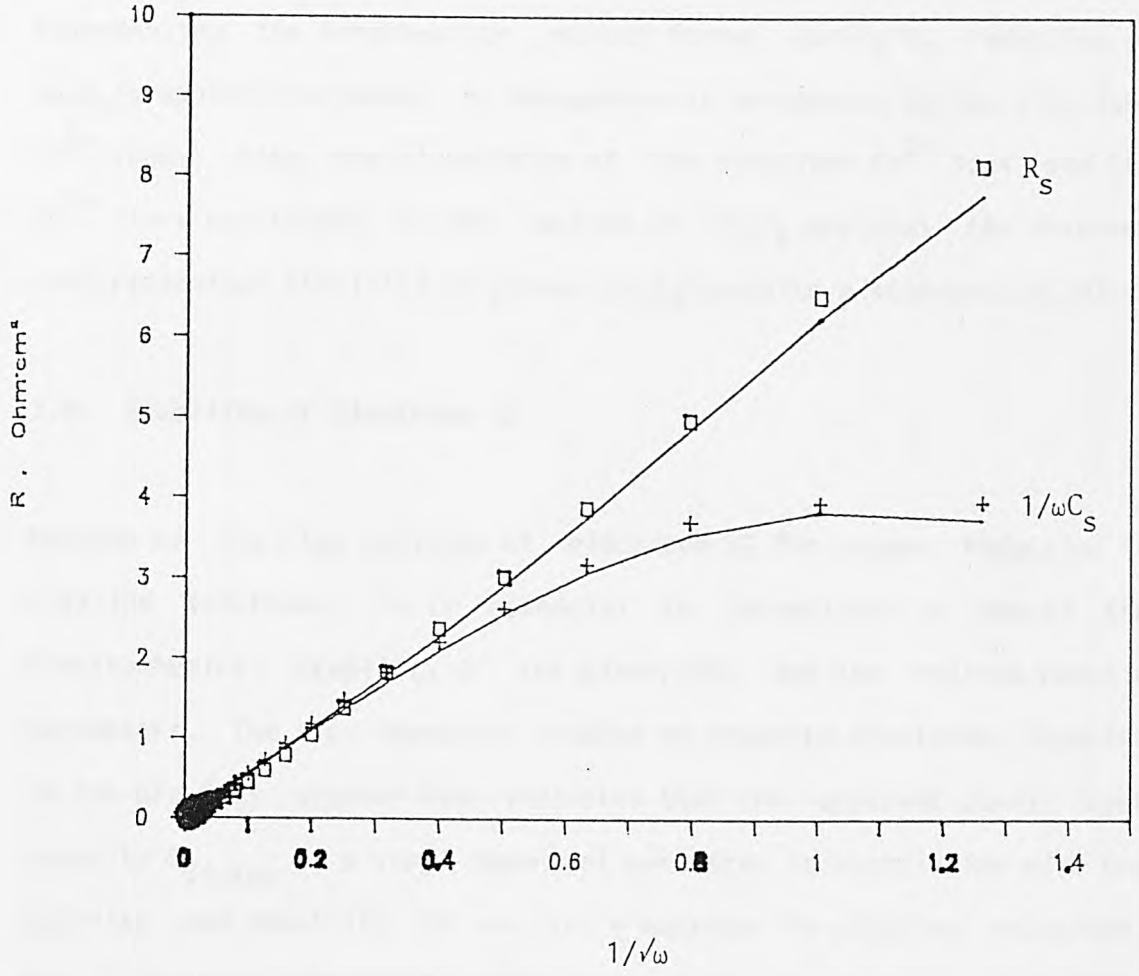

Fig. 7.15 Fitted Randles plots for electrode CG at 900 mV. 25^{0}C, 5N KOH and using air as feed gas.

chemical kinetic studies of H_2O_2 decomposition in the presence of 1 ppm Co^{2+} ions, it has been demonstrated that the first-order rate constant k_f is linearly proportional to the initial concentration of the peroxide. Consequently, it could be concluded that the HO_2^-, representing the intermediate product formed during O_2 reduction on Co_3O_4/graphite electrodes, is homogeneously decomposed by the dissolved Co^{2+} ions. Also, the circulation of the dissolved Co^{2+} ions and the Co^{3+} ions positioned in the lattice of Co_3O_4 explains the observed electrochemical stability of porous Co_3O_4/graphite electrodes[24,78].

7.4. Stability of Electrode CG

Because of the high activity of electrode CG for oxygen reduction in alkaline solutions, it is essential to investigate in detail the electrochemical stability of the electrodes and the related kinetic parameters. The a.c. impedance studies on graphite electrodes reported in the previous chapter have indicated that the apparent double layer capacity $C_{dl,app}$ is a very important parameter in association with the activity and stability of an air electrode in alkaline solutions. Fig. 7.16 shows the relationship between the $C_{dl,app}$ values and the cathodic polarization length of electrode CG, along with the results obtained for the graphite electrode. The $C_{dl,app}$ values were determined at ocv from a.c. impedance measurements. The cathodic current density was kept constant at 100 mA/cm^2. The experimental temperature was at 25^{o}C and air was used as the feed gas.

Compared with the graphite electrode, the $C_{dl,app}$ values for electrode CG are quite stable. The apparent double layer capacitance of the graphite electrode sharply decreases with increasing polarization time

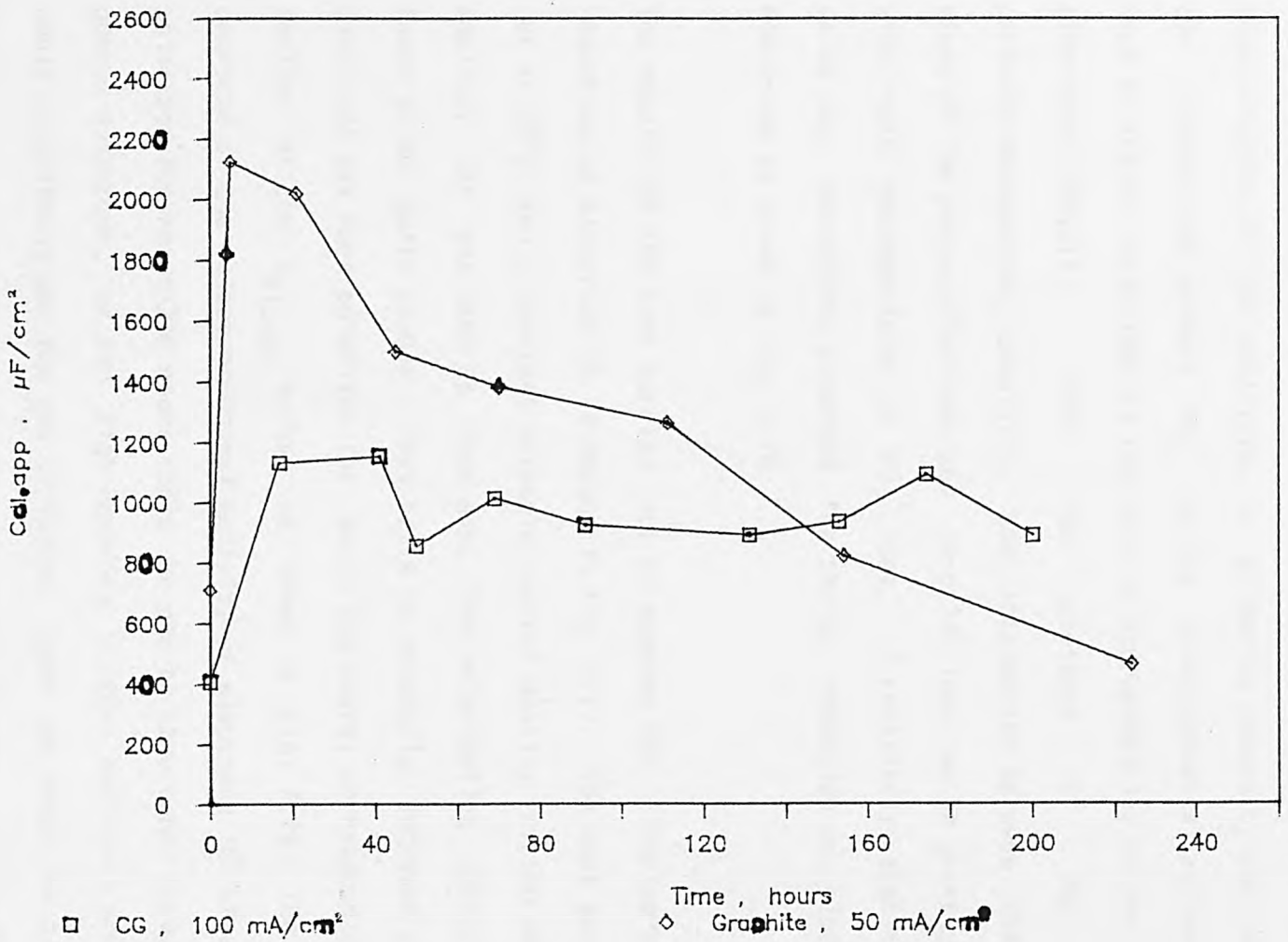

Fig. 7.16 Dependence of $C_{dl,app}$ value on polarization time for CG and graphite electrodes at constant current densities.

$25^{0}C$, 5N KOH and using air as feed gas.

and goes below that of CG after about 150 hours. It can be noted that the polarization current density for the graphite electrode is only half of that for the electrode CG. As demonstrated previously, the loss of active surface area of porous graphite electrodes, without the incorporation of the catalysts, is primarily caused by the attack of the intermediate product HO_2^- on the electrochemical active sites. Such an attack could lead to the loss of hydrophobicity of the graphite electrodes[209,211]. With the presence of the active peroxide-decomposing catalysts, the interaction between the active sites of the porous electrode and peroxide ions can be greatly reduced with rapid decomposition of HO_2^- ions. A relatively stable $C_{dl,app}$ value was, therefore, observed for the O_2 reduction on electrode CG electrode as shown in Fig. 7.16.

The result of the test carried out to examine the lifetime of oxygen reduction on electrode CG is shown in Fig. 7.17. The test was carried out at 25^oC and a constant cathodic current density of 100 mA/cm^2 was applied. Air was used as feed gas. The polarization potentials are found to be quite stable. They begin to gradually decrease after the electrode has been polarized for about 200 hours; corresponding to the decline of the $C_{dl,app}$ values as shown in Fig. 7.16. The gradual decrease of the electrochemical activity of electrode CG after having polarized for about 200 hours could be due to structural damage of the porous electrode, as the high humidity in the half-cell arrangement could unavoidably wet the gas diffusion layer and block the gas pores. Working on a rotating disk-ring electrode, Tanabe and Fukushima[229] reported that the H_2O_2 influences the stability and activity of the surface of glassy carbon electrodes, and with the introduction of Pt catalysts both the activity and stability of the glassy carbon

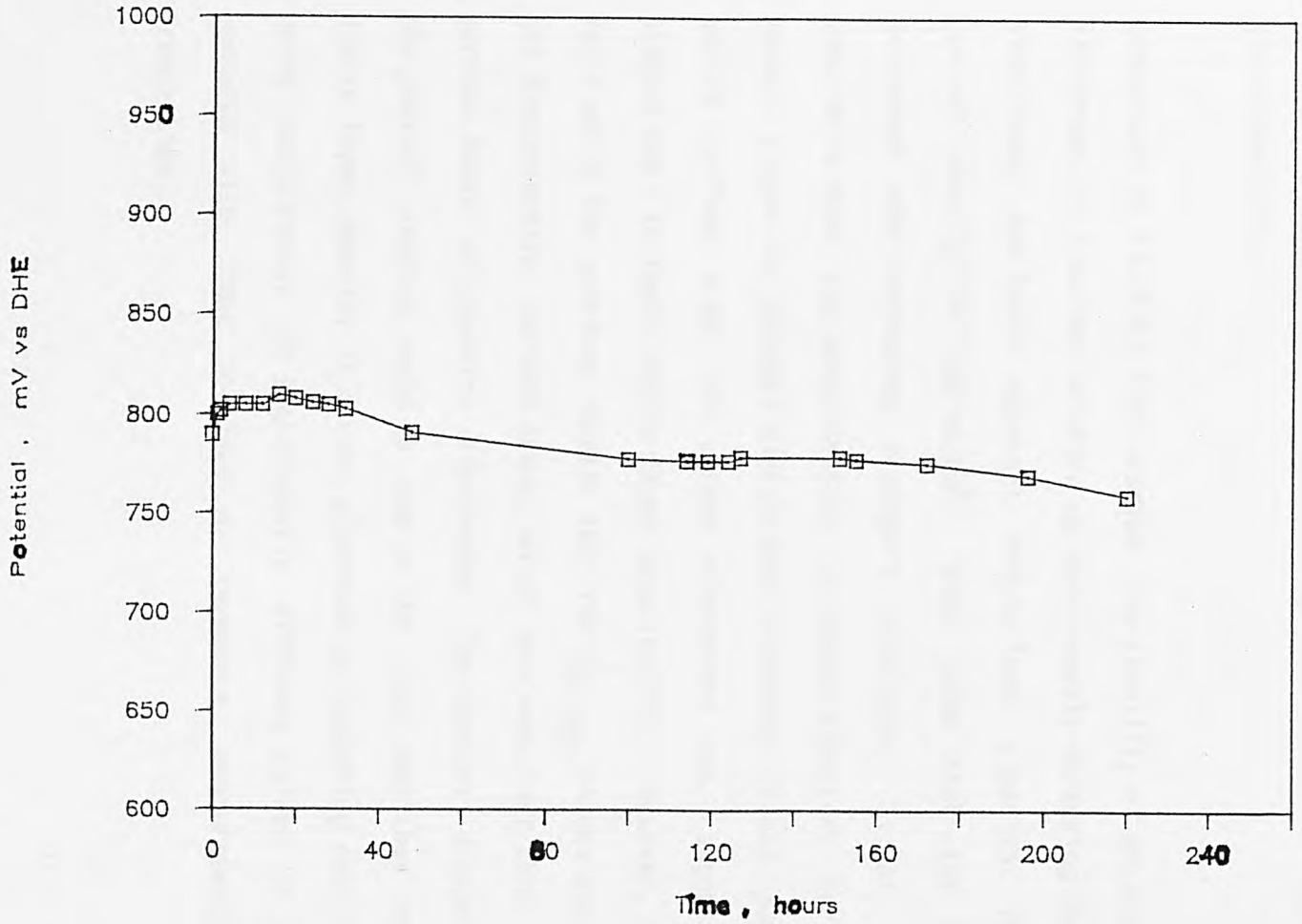

Fig. 7.17 Lifetime test for oxygen reduction on electrode CG at cathodic current density of 100 mA/cm^2.

25^0C, 5N KOH and using air as feed gas.

electrode are increased. The high i_o' value as well as the stable performances of CG, at room temperature, suggest the possibility of a very high efficiency of oxygen recycling in the active site regions; since a complete recycling of O_2 is possible for Pt/carbon electrodes[230].

Gamburtsev et al.[231] also studied the stability of wetproofed carbon electrodes in alkaline solution by continuously measuring the transport hindrances, and their apparent double layer capacity. At cathodic current density of 100 mA/cm^2, they found that the capacitance increased with increasing transport hindrance. It was, therefore, considered that the deterioration of carbon electrode performance is mainly caused by gradual electrolyte flooding of gas pores as the wetted surface area of carbon electrodes was suggested to be proportional to their double layer capacity[232]. However, it has been verified in the previous chapter that the $C_{dl,app}$ values are related to the electroactive surface areas, which are much less than the wetted surface areas of graphite electrodes. The obvious disagreement with the present studies could be due to the fact that they measured the double layer capacity of carbon electrode by recording charging curves, which could result in significantly different values of $C_{dl,app}$ as compared with that obtained by impedance measurements at high frequencies.

CHAPTER EIGHT

A.C. IMPEDANCE STUDY OF OXYGEN REDUCTION ON SEMICONDUCTING OXIDE ELECTRODES

8.1. Introduction

It is known that Co_3O_4 has a normal spinel structure in which magnetic cobaltous ions Co^{2+} occupy the tetrahedral sites and diamagnetic cobaltic ions Co^{3+} the octahedral sites[72,233]:

$$(Co^{2+})_{tetra}(Co^{3+})_{2,octa}O_4$$

Which means that Co^{2+} and Co^{3+} ions are localized in separated tetrahedral and octahedral sites respectively. The electronic conducting chain between cobalt ions is, thus, missing, resulting in a high resistance value for Co_3O_4. X-ray photoelectron spectroscopy (XPS) studies have confirmed that there are intrinsically different photoelectron spectral lines for Co^{2+} and Co^{3+} ions in Co_3O_4[234]. However, the electrical conductivity can be increased by introducing lithium ions into the spinel lattice of Co_3O_4. During lithiation, some of the tetrahedral Co^{2+} ions are displaced into neighbouring empty octahedral sites and incoming Li^+ ions occupy the remaining interstitial octahedra[235]. This results in an improved electrochemical activity for a Li-doped Co_3O_4[68,98], as compared to 'plain' Co_3O_4.

The electrochemical activity of semiconducting cobalt oxides for O_2 reduction in alkaline solutions has been most commonly studied by conventional steady state polarization[67,215] and rotating disk-ring electrode methods[63]. The data obtained by the rotating disk-ring method showed that the oxygen reduction reaction mainly proceeds to water on cobalt spinel oxides and to the formation of an intermediate peroxide on simple oxides[63,236]. A more detailed discussion of the

chemical and electrochemical properties of spinel cobalt oxides can be found in a review given by Tarasevich and Efremov[52]. One distinct feature of a semiconducting oxide electrode is that the current carrier concentration in a semiconducting oxide is far less than in a metal. According to Shub et al.[237], there appears to be a space-charge layer in a Co_3O_4 electrode at potentials less than 1.7 V (NHE). However, only a small number of the investigations concerned with the influence of the physical properties of semiconducting oxides on the kinetics of O_2 reduction can be found in literature. Impedance measurements have been used in studying electrochemical reactions on manganese dioxide electrodes[238] and on the electrodes constituted of some mixed conducting oxides[239]. Using the a.c. impedance method for the study of porous cobalt oxide electrode systems, very useful information about O_2 reduction in a semiconducting oxide/electrolyte interface, and the influence of porous structure and physical properties of the semiconducting oxides on O_2 reduction, can be obtained.

This study is concerned with the kinetics and mechanism of O_2 reduction on Co_3O_4 oxide electrodes in alkaline solutions, the influence of the characteristics of semiconducting oxides, and the influence of the porous structure of the electrodes. Oxygen reduction on high surface area Co_3O_4 (HSAC) and 3.1 at% Li-doped Co_3O_4 (LDC) will be investigated using steady state polarization and the a.c. impedance technique. The impedance analysis procedures are based on a simplified equivalent circuit which takes into account both the semiconducting properties and the porous nature of the cobalt oxide electrodes.

8.2. Steady State Polarization Performance

The electrochemical activities of Teflon-bonded HSAC and LDC electrodes, for oxygen reduction in 5N KOH, were determined, firstly, by the steady state polarization technique. The electrodes were fabricated using the rolling method. The catalyst loading was about 22 mg/cm^2. The measurement temperature was controlled at 25^oC and air and pure oxygen were used as feed gases.

Figs. 8.1 and 8.2 show the polarization curves of O_2 reduction on electrodes HSAC and LDC under air and pure oxygen respectively. In both cases electrode HSAC shows higher activity than electrode LDC at any given current density. This difference in electrode performance could be related directly to the significant difference in surface area. The specific surface area is 89.88 m^2/g for HSAC and 27.48 m^2/g for LDC. The Tafel plots for the electrodes corresponding to Fig. 8.1 were characterized by two distinct linear ranges, as shown in Figs. 8.3 and 8.4. The Tafel slopes obtained vary from 60 mV per decade, at low current density, to about 190 mV per decade, at high current density. Transport hindrance plots ($\Delta E/i$ plots) for electrodes HSAC and LDC are shown in Fig. 8.5. It can be seen that, at low current density, the transport hindrance of electrode LDC is considerably higher than that of electrode HSAC and vice versa as the current density increases. It was proposed by Trunov et al.[240] that the number of electrochemically active sites of semiconductor catalysts is a function of oxide conductivity. It is, however, indicated that the effect of electrical conductivity on the electroactivity of cobalt oxides is more manifested at relatively higher polarization; the measured electrical resistivity of HSAC is 1121.6 $\Omega \cdot cm$ and for LDC it is much smaller, 58.31 $\Omega \cdot cm$. The

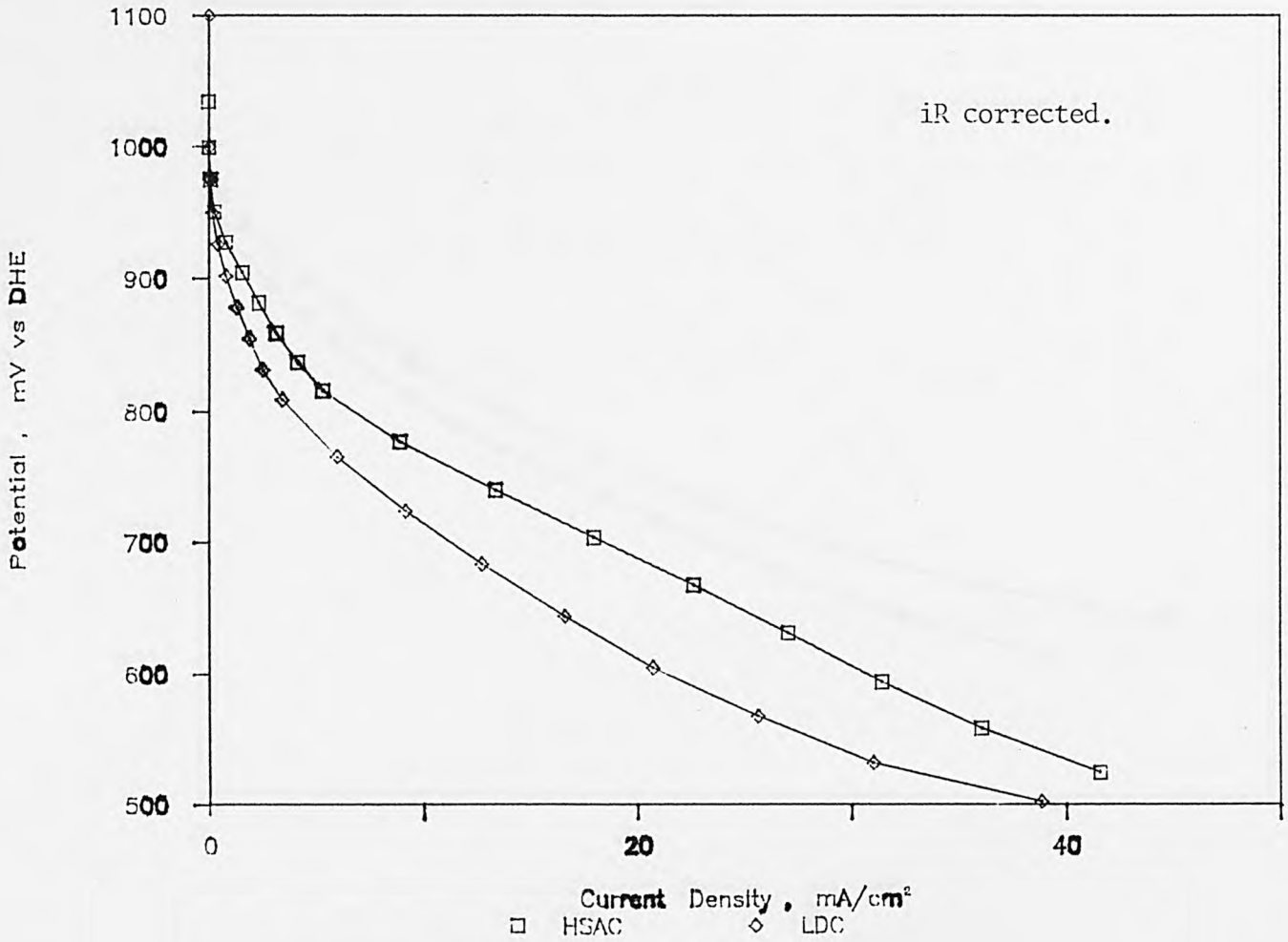

Fig. 8.1 Polarization curves of Teflon-bonded cobalt oxide electrodes. 25°C, 5N KOH and using air as feed gas.

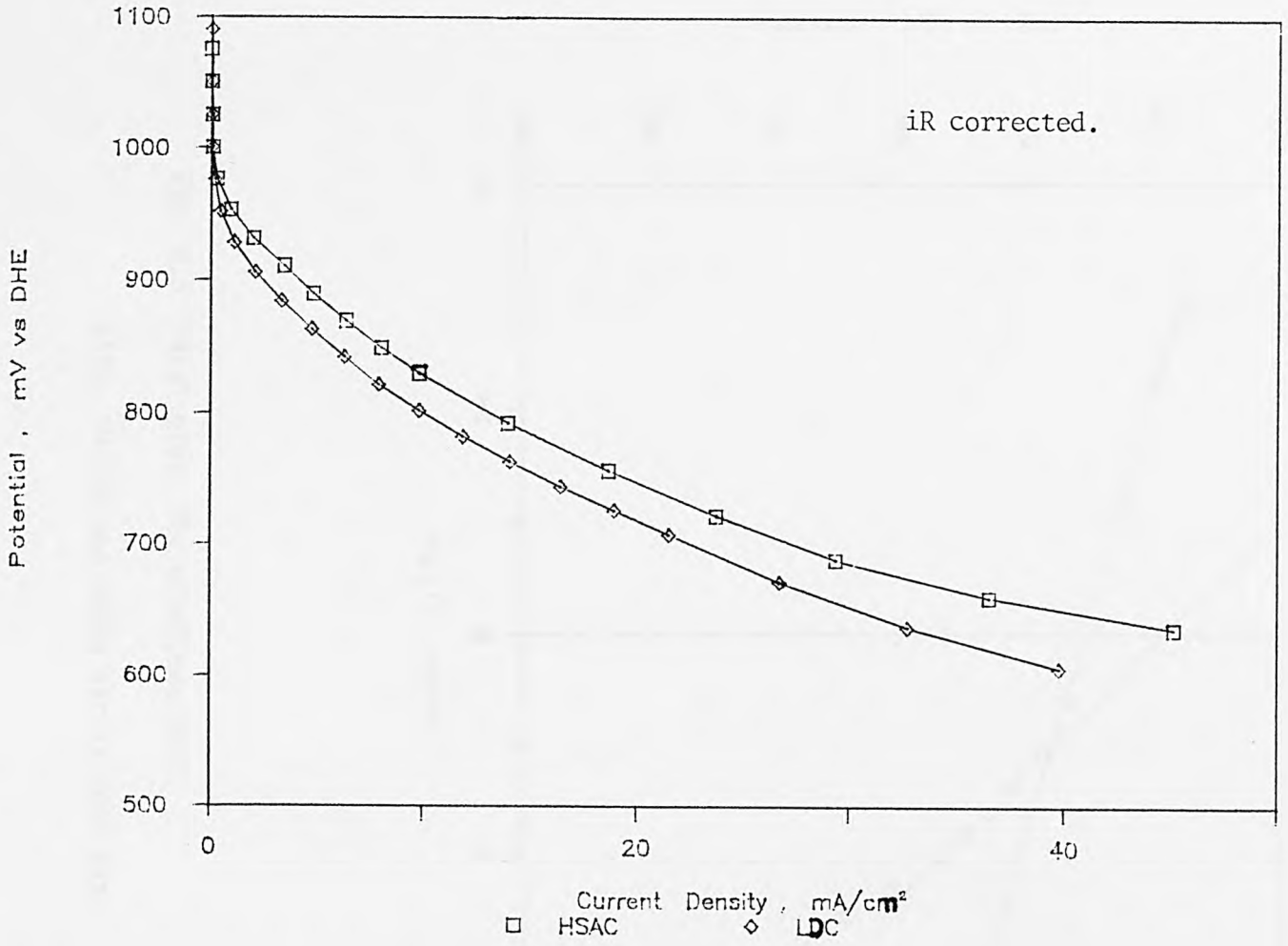

Fig. 8.2 Polarization curves of Teflon-bonded cobalt oxide electrodes.
25°C, 5N KOH and using oxygen as feed gas.

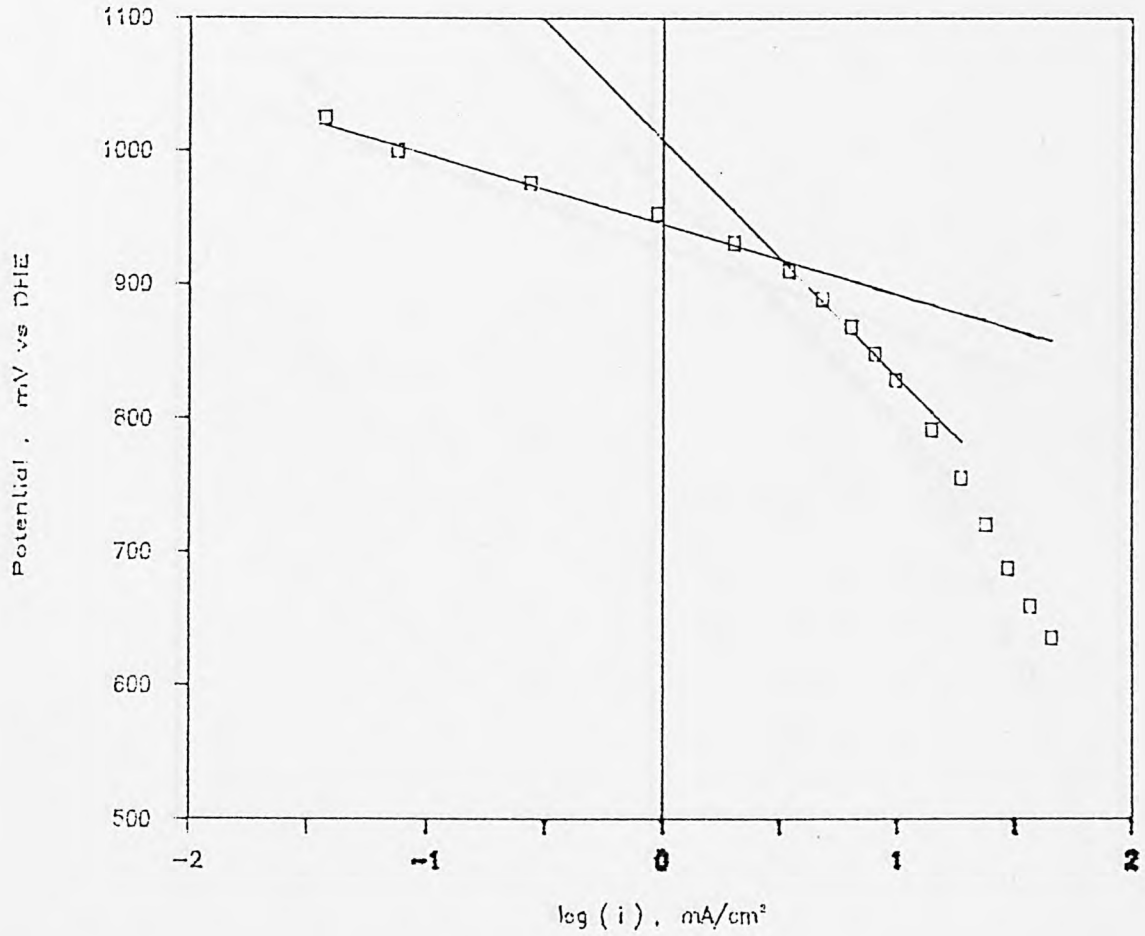

Fig. 8.3 Tafel plots for electrode HSAC.

25^{0}C, 5N KOH and using air as feed gas.

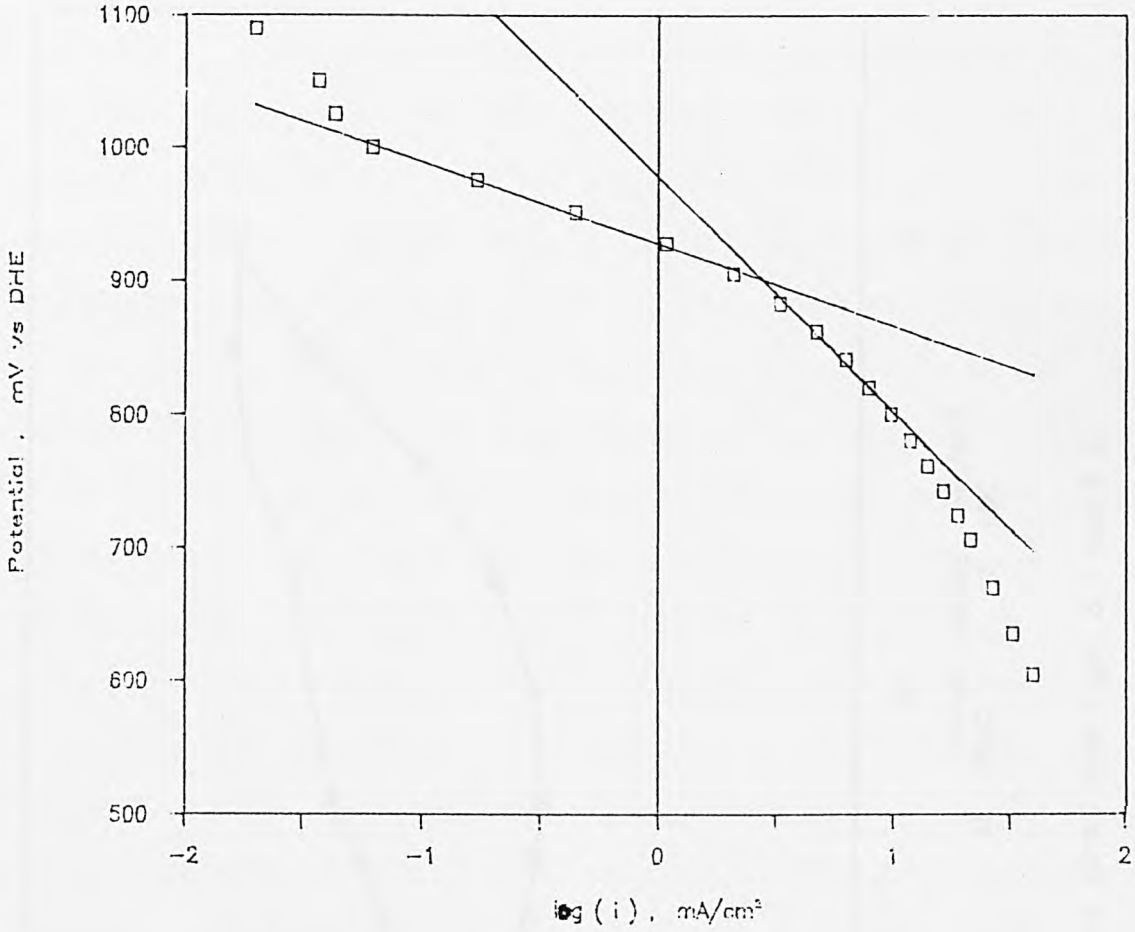

Fig. 8.4 Tafel plots for electrode LDC.

25°C, 5N KOH and using air as feed gas.

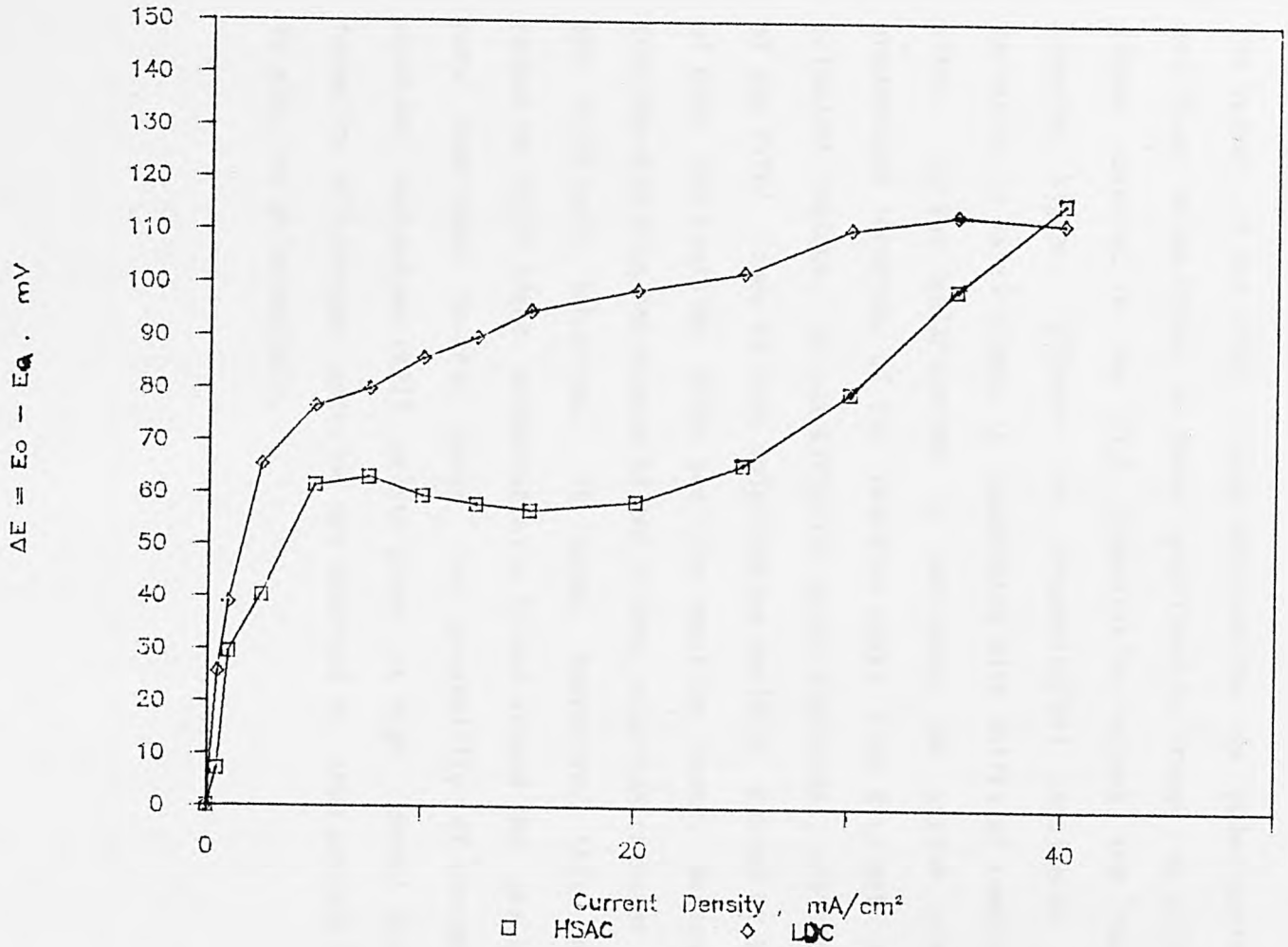

Fig. 8.5 Transport hindrance plots from Figs. 8.1 and 8.2.

kinetic parameters of oxygen reduction on electrodes HSAC and LDC are summarized in Table 8.1. The number of electrons n was calculated with the assumption that the transfer coefficient is 0.5.

The values of the Tafel slopes obtained for low polarization regions are found to be close to those published by Trunov et al[241]. The slopes obtained in the high polarization regions are found to be somewhat higher. Efremov and Tarasevich[64] considered that the variation in Tafel slopes is associated with shifts of reaction active sites. As the polarization is increased, the active site of the predominant location of the reaction moves from divalent cations to trivalent cations. On gas diffusion oxide electrodes, the steep ascent of the Tafel lines at high polarization could be caused by the shifts of both the reaction sites and the reaction zones. Because of the considerably high resistance of the oxides, electron transfer processes are relatively inhibited. It seems, therefore, that the oxygen reduction takes place preferentially in and around the gas and liquid pore interfaces in this case. The possibility of change in the reaction mechanisms still exists since at high current density the formation of hydrogen peroxide was observed on some perovskite oxides in alkaline solution[221].

Table 8.1

Polarization parameters of Teflon-bonded semiconducting cobalt oxide electrodes. 25°C and 5N KOH.

Electrode	Catalyst Loading	Tafel parameters			
		Low polarization ($i < 2$ mA/cm^2)		High polarization ($i > 2$ mA/cm^2)	
	mg/cm^2	mV/decade	n	mV/decade	n
Under air					
HSAC	21	59.44	2.0	188.74	0.6
LDC	21	63.84	1.9	187.66	0.6
Under oxygen					
HSAC	21	51.19	2.3	177.72	0.7
LDC	21	61.26	1.9	175.72	0.7

8.3. Equivalent Circuit Analysis

The preparation of the Teflon-bonded HSAC and LDC electrodes, the treatment of the electrodes before impedance measurement and the input impedance parameters are described in the previous chapter. The impedance measurements were carried out at $25^{o}C$ under air and pure oxygen.

A typical observed impedance response for O_2 reduction on a Teflon-bonded HSAC electrode is shown in Fig. 8.6 at ocv under oxygen. The impedance spectra for Teflon-bonded cobalt oxides in alkaline solution at ocv all consist of one depressed semicircle, in the high frequency region, and a diffusion tail with an angle less than 45^{o}, at low frequency region. In this case the angle between the tail and the real axis of the complex impedance, in Fig. 8.6, is about 30^{o}. The behaviour of the impedance responses is independent of the partial pressure of oxygen. As it will be shown later by the results of faradaic impedance analyses, the observed semicircles are mainly due to the charge transfer reactions.

One main difference between a cobalt oxide electrode and a graphite electrode is that the electrode resistance of the former is much higher. The R_{so} obtained at infinite frequency was 2.75 $\Omega \cdot cm^2$ for HSAC and 1.37 $\Omega \cdot cm^2$ for LDC in 5N KOH (the distance between the electrode and the tip of the Luggin capillary was about 0.5 mm). The resistance obtained from the impedance measurements is mainly due to the resistance of the oxides, in the presence of concentrated electrolyte. At a semiconductor/electrolyte interphase, the surface states can be represented by a network of resistors and capacitors in series[242] or

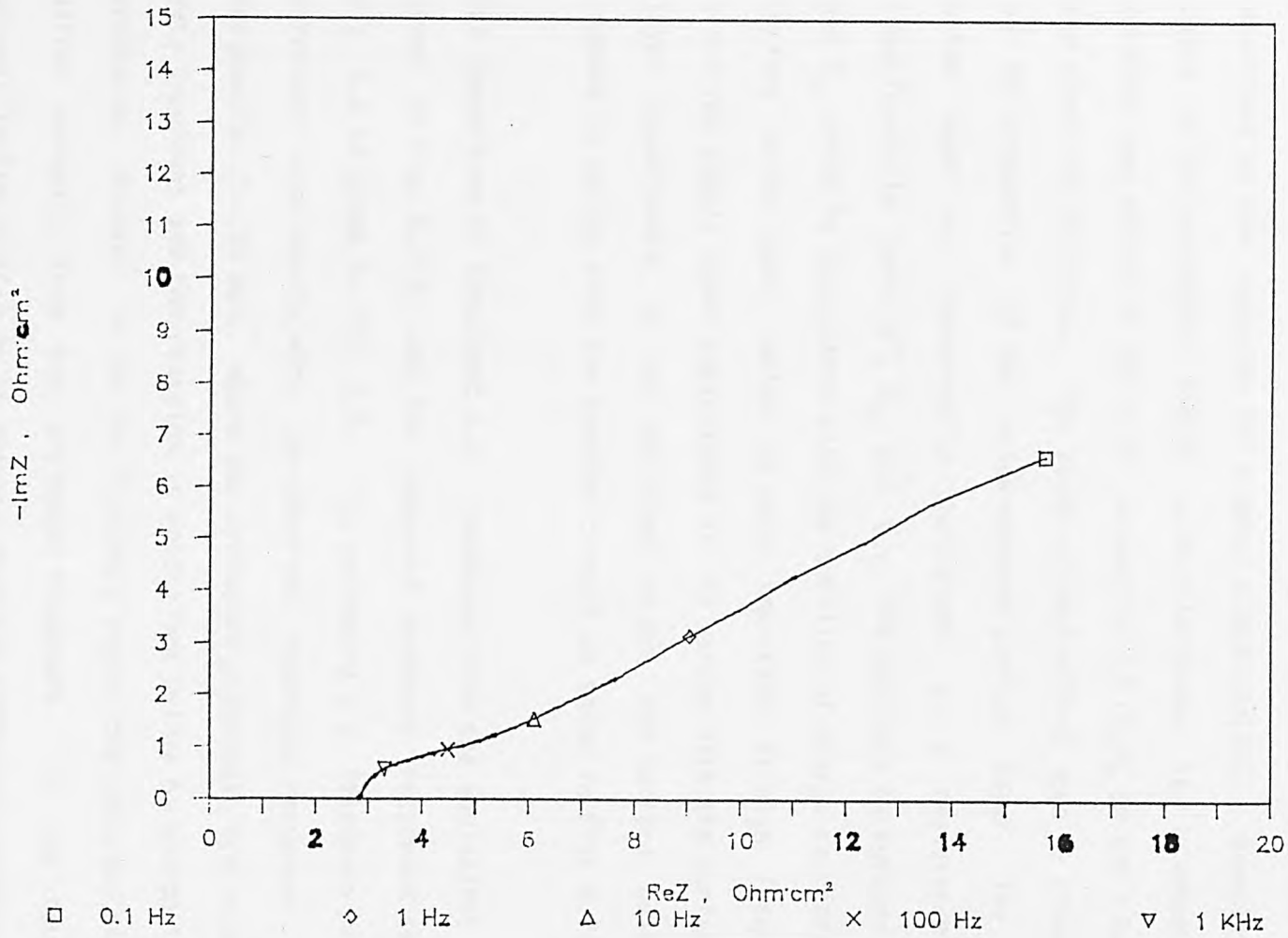

Fig. 8.6 Measured impedance response of electrode HSAC at ocv.

25^{0}C, 5N KOH and using oxygen as feed gas.

in parallel[89]. In the potential range studied in the oxygen reduction reaction, the semiconducting cobalt oxides most likely become degenerated at the surface[237]. For a thin film of Co_3O_4 prepared on cobalt alloy, the behaviour concerning cathodic polarization can be described by the equation for a metal electrode[68]. However, in the cases of Teflon-bonded cobalt oxide electrodes it is necessary to consider the effect of the bulk properties of Co_3O_4 on the kinetics of the electrode reaction. The study of such effect can be concentrated on the properties of the oxide-covered surface layer. The surface oxide layer was electrically analogized by a resistance and a capacitance in parallel, R_{sl} and C_{sl}. The physical background of R_{sl} and C_{sl} could be associated with the mobility of charge carriers in the surface oxide layer, which is more important at high frequencies. Since the double layer capacitance is in series with the surface oxide layer capacitance, it was justified to put the surface oxide layer segment in series with the Randles circuit as shown in Fig. 8.7(a).

The comparison of simulated a.c. impedance from the equivalent circuit shown in Fig. 8.7(a) and the measured impedance responses shown in Fig. 8.6 is given in Fig. 8.8. The estimated a.c. impedance responses correlate excellently with the observed impedance responses at high frequencies (> 100 Hz), where the diffusion processes are usually not very important and the reaction is controlled mainly by charge transfer processes. However, in the low frequency region the observed responses differ markedly from the estimated responses. In the equivalent circuit in Fig. 8.7(a) it is assumed that the diffusion impedance Z_W is the classical Warburg impedance in a semi-infinite medium on a planar electrode. The deviation of the observed impedance responses from an ideal Warburg diffusion process at low frequencies indicates, probably,

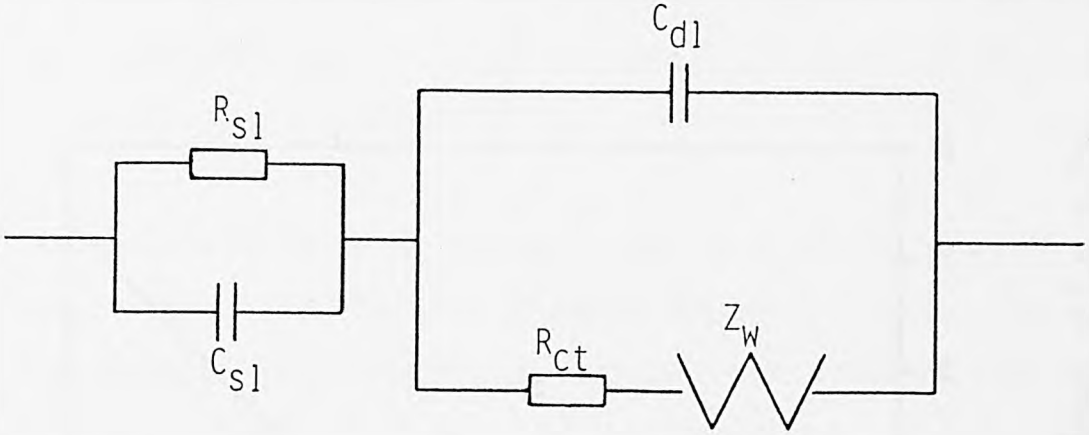

(a) Semiconducting oxide/electrolyte interphase.

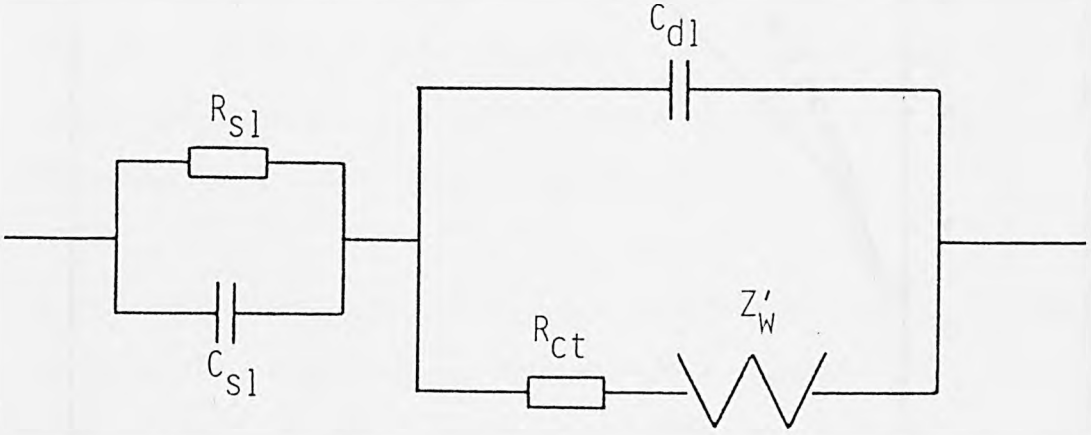

(b) Porous semiconducting oxide/electrolyte interphase.

Fig. 8.7 Equivalent circuits for oxygen reduction on semiconducting oxide electrode.

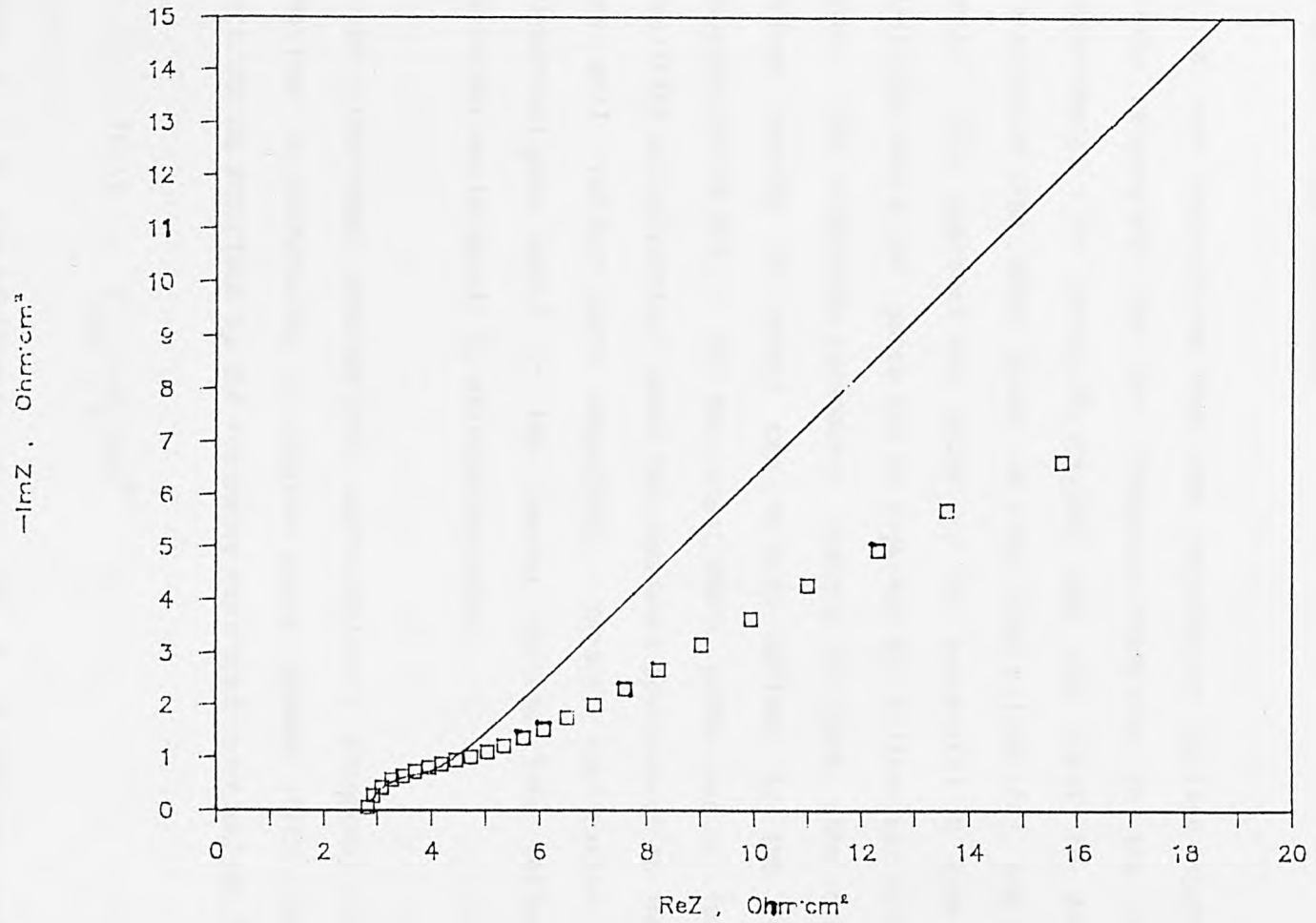

Fig. 8.8 Fitted impedance responses for Fig. 8.6 according to the circuit of Fig. 8.7(a).
R_{sl} = 0.14 Ω·cm^2; C_{sl} = 165 μF/cm^2; C_{dl} = 207 μF/cm^2; R_{ct} = 0.85 Ω·cm^2;
W = 16.25 Ω·cm^2/s$^{\frac{1}{2}}$; m = 0.5.

the dominant influence of the porous structure on the diffusion reactions inside the pores. Apparently, it is needed to further modify the equivalent circuit, taking into account the factor of the porous structure of the electrodes.

It has been established that the porosity or surface roughness is mainly responsible for the frequency dispersion in the impedance measurements. De Levie[178,179,243] was the first to develop a transmission line model based on simplified cylindrical and parallel pores. This approach was found to be successful in some porous electrodes where the pores can be regarded as cylindrical with finite depth. The electrode parameters (radius of pore, pore depth and surface density of pores) can be well defined by the impedance responses[87,88,244]. In the cases where pores can no longer be simplified as cylindrical pores the impedance spectrum of an individual pore will reflect pore shape[180]. Direct application of the cylindrical-pore model in the complex systems like Teflon-bonded electrodes would result in misinterpretation.

On the other hand Scheider[245] approached this frequency dispersive behaviour by introducing a constant phase element (CPE) impedance, which can be described by the following empirical relation[245,246]

$$Y_{cpe} = A_y(j\omega)^m \qquad (8.1)$$

where Y_{cpe} is the admittance of the CPE, A_y a constant and m the fractional power, $0 < m < 1$. With m=1 this element represents a capacitance and for m=0 a resistor. For m=0.5, the CPE resembles the classical Warburg impedance in the case of a semi-infinite medium:

$$(8.2) \qquad Y_W = 2^{-\frac{1}{2}} W^{-1} (j\omega)^{\frac{1}{2}}$$

where Y_W is the Warburg diffusion admittance. The presence of a CPE has been demonstrated in many diverse systems[86,246,247]. Generally, the CPE impedance is believed to originate from the coupling of solution resistance to the double layer capacitance as a result of surface inhomogeneity[245,247]. Brug et al.[248] pointed out that the CPE could be also related to the faradaic impedance in the non-ideally polarized electrode reactions.

Problems remain in characterizing O_2 reduction on porous semiconducting oxide electrodes using the a.c. impedance method. So far neither cylindrical-pore model nor a constant phase element is applicable for the interpretation of impedance response on porous Co_3O_4 electrodes. For Teflon-bonded Co_3O_4 electrodes, the electrodes are made of two or more materials with different particle shapes and sizes. A cylindrical pore model would be too rough to account for the influence of an assembly of shaped pores on the faradaic impedance. Furthermore, it was found that the angle of the observed diffusion tail is almost constant at a given potential, if measurements were done on the same electrodes. Hence, it is appreciable to introduce a modified factor for the Warburg diffusion impedance to account for the complex influence of pores and to avoid the detail of the porous structure. Analogous to the CPE[245,249], a modified Warburg impedance is expressed as

$$(8.3) \qquad Z'_W = 2^{\frac{1}{2}} W' (j\omega)^{-m}$$
$$= 2^{\frac{1}{2}} W' [\cos(m\pi/2) - j \sin(m\pi/2)] \omega^m$$

where W' is a constant with dimension ohm·cm^2/s^m and m the fraction power between 0 and 0.5. It must be emphasized that Z'_w has nothing to do with the concept of constant phase element. This empirical equation for the diffusion impedance reflects the assembly effects of porous structure on the electrochemical reaction, particularly on the diffusion processes inside the pores. It will be demonstrated later that the fraction power m is dependent only on the electrode materials at ocv. For the purpose of distinction from the CPE impedance, Z'_w will be called the porous diffusion impedance, which can be related to the corresponding Warburg diffusion impedance Z_w in a planar electrode by a porous coefficient function f(jω). This means

$$Z'_w = f(j\omega)Z_w \tag{8.4}$$

where

$$f(jw) = a(j\omega)^{(m - \frac{1}{2})} \tag{8.5}$$

in which 'a' is a dimensionless constant, W/W'. Then, for m=0.5 this so-called porous diffusion coefficient is equal to the Warburg diffusion coefficient. The modified equivalent circuit is schematically given in Fig. 8.7b. The electrode impedance can then be written as follows

$$Z = \frac{1}{j\omega C_{sl} + 1/R_{sl}} + \frac{1}{j\omega C_{dl} + \dfrac{1}{R_{ct} + Z'_w}} \tag{8.6}$$

At high frequencies the imaginary part of the electrode impedance reduces to the capacitive impedance of C_{sl} and C_{dl} in series. Evidently the experimental value of capacitance C_{ex} evaluated at the infinite frequency in admittance plane is

$$(8.7) \qquad 1/C_{ex} = 1/C_{sl} + 1/C_{dl}$$

which means that capacity, determined from the quadrature component of the impedance, does not equal to the double layer capacity of the electrodes. An example of the determination of C_{ex} from an admittance plane is shown in Fig. 8.9 for electrode HSAC at ocv under oxygen. The intercept on the imaginary admittance gives the total capacitance C_{ex} (C_{ex} = 101.86 $\mu F/cm^2$).

8.4. Application in Semiconducting Oxide/Electrolyte Systems

The equivalent circuit analysis developed above was applied to the measured impedance responses obtained on electrodes HSAC and LDC at 25°C under oxygen or air. The calculated and observed impedance responses were compared on the basis of a reliability factor F_r which is defined as

$$(8.8) \qquad F_r = \frac{[O(f_i) - E(f_i)]^2}{O(f_i)^2}$$

where $O(f_i)$ and $E(f_i)$ are the observed and estimated responses at the frequencies f_i (Hz). A good agreement between calculated and observed impedance data should be indicated by a low value of F_r plus a visual inspection of the graphical output produced by the fitting procedure.

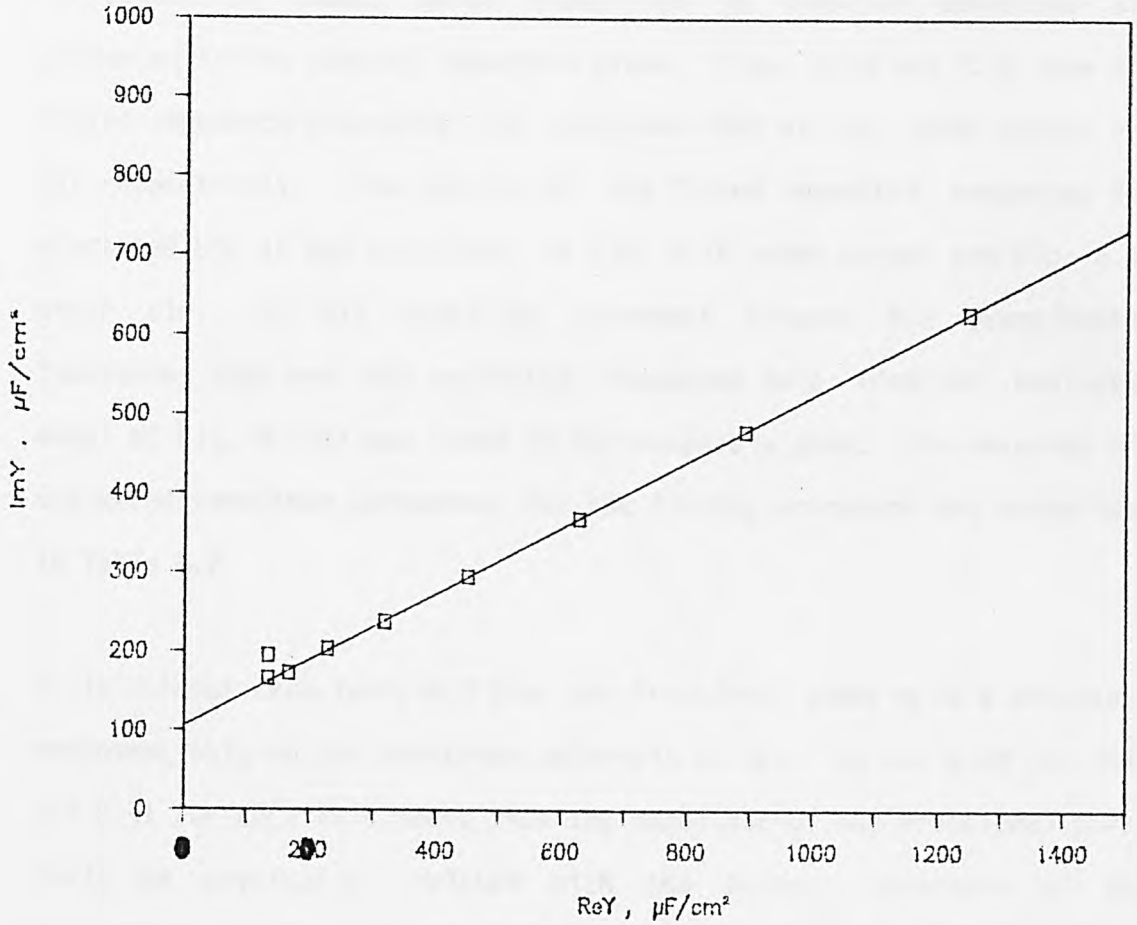

Fig. 8.9 Determination of total capacitance C_{ex} from admittance plane, Y_{el}/ω plane, on electrode HSAC at ocv.
25^0C, 5N KOH and using oxygen as feed gas.

8.4.1. Effect of the Partial Pressure of Oxygen

The observed and estimated impedance responses for oxygen reduction on semiconducting cobalt oxide electrodes in alkaline solutions are presented in the complex impedance plane. Figs. 8.10 and 8.11 show the fitted impedance responses for electrode HSAC at ocv under oxygen and air respectively. The results of the fitted impedance responses for electrode LDC at ocv are given in Fig. 8.12 under oxygen and Fig. 8.13 under air. In all cases the agreement between the experimental impedance data and the estimated impedance data from the evaluated model of Fig. 8.7(b) was found to be reasonably good. The measured and estimated impedance parameters for the fitting procedure are summarized in Table 8.2.

It is evident from Table 8.2 that the fractional power m is a constant, dependent only on the electrode materials at ocv. It was 0.34 for HSAC and 0.41 for LDC. This means that the magnitude of the fractional power could be physically related with the porous structure of the electrodes. The specific surface area of HSAC is about 3 times greater than that of LDC. If the porous structure of a Teflon-bonded electrode is dependent to a large extent on the surface area and particle size distribution of the oxides under the same fabrication conditions, the pores of electrode LDC would be expected to be relatively bigger than the pores of electrode HSAC. This point is supported by the smaller value of capacity C_{ex} evaluated from the admittance plane for Li-doped Co_3O_4, as shown in Table 8.2. Consequently, the diffusion processes of both the oxygen molecule and the possible intermediate peroxide inside pore channels are less affected by the porous structure, in the case of electrode LDC. Therefore, the value of m for LDC is expected to be more

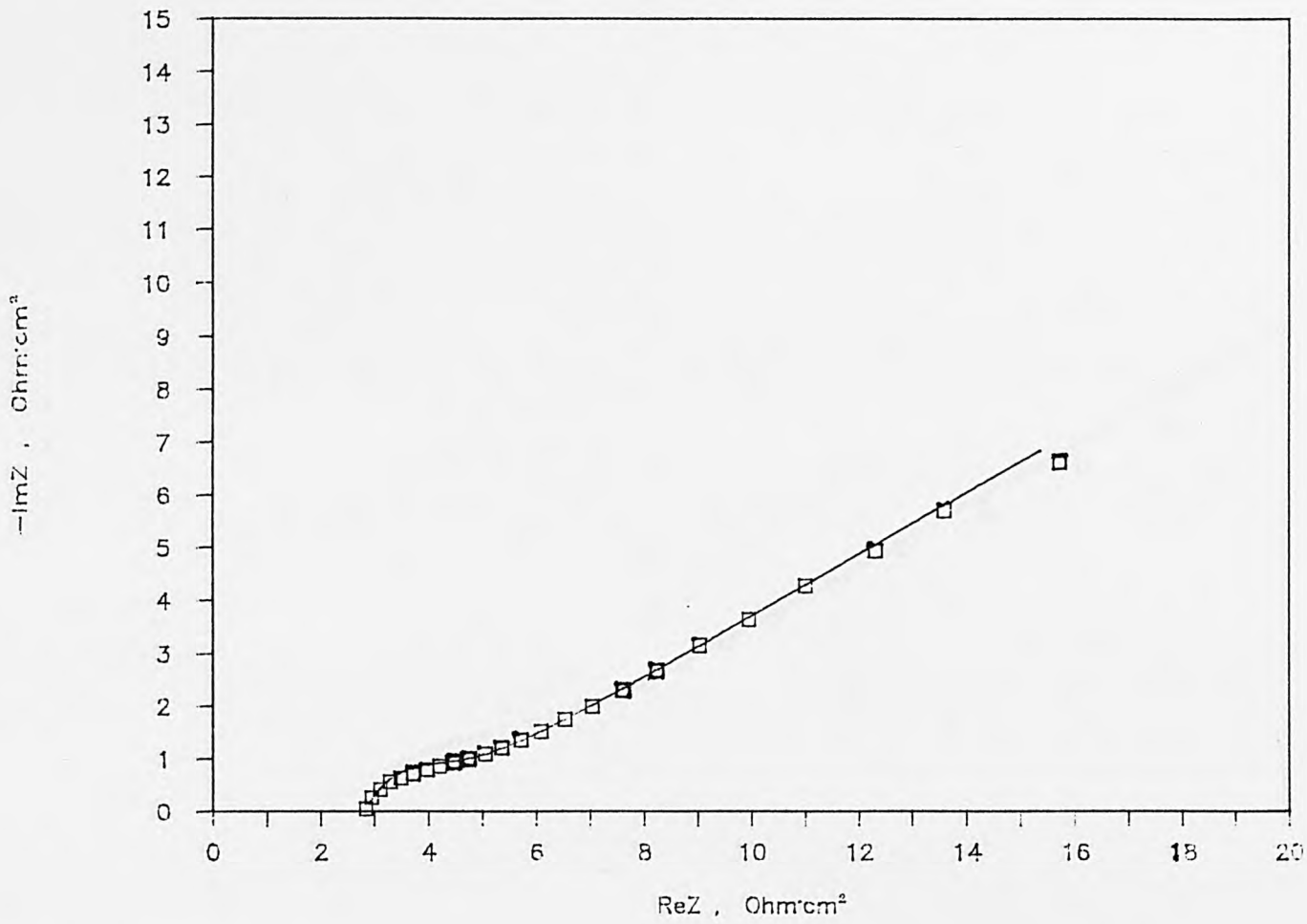

Fig. 8.10 Fitted impedance responses of electrode HSAC at ocv. 25°C, 5N KOH and using oxygen as feed gas.

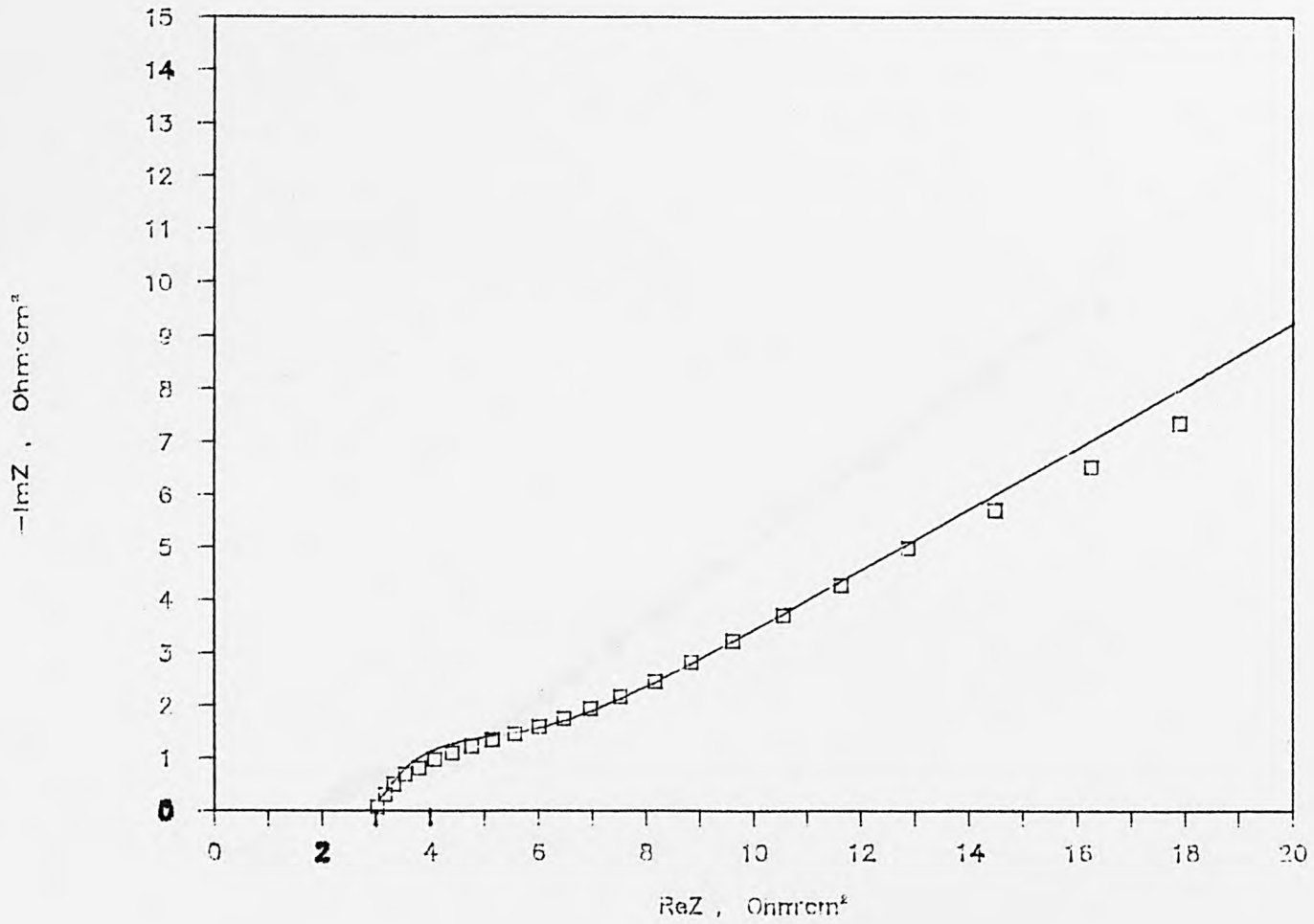

Fig. 8.11 Fitted impedance responses of electrode HSAC at ocv. 25°C, 5N KOH and using air as feed gas.

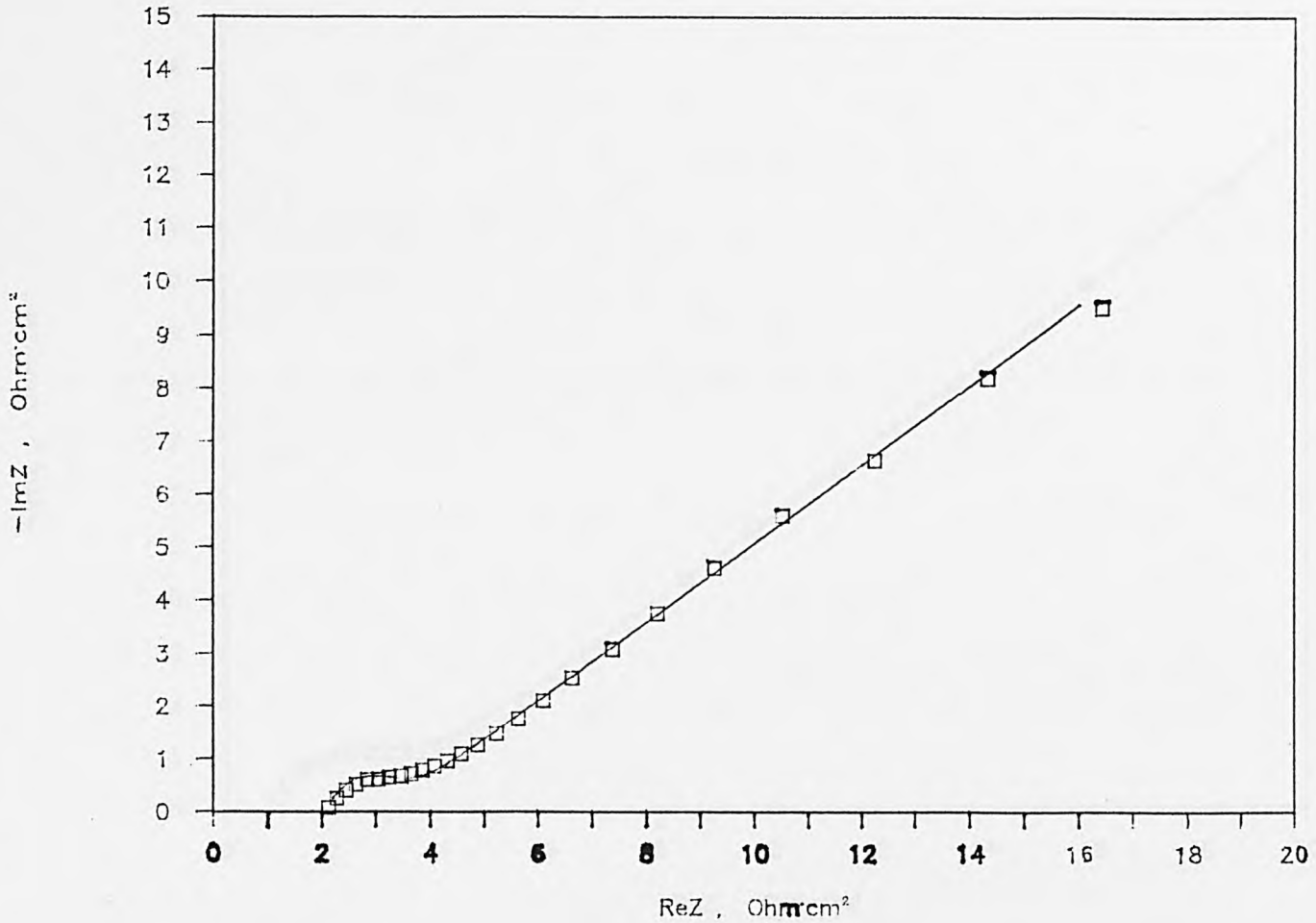

Fig. 8.12 Fitted impedance responses of electrode LDC at ocv. 25°C, 5N KOH and using oxygen as feed gas.

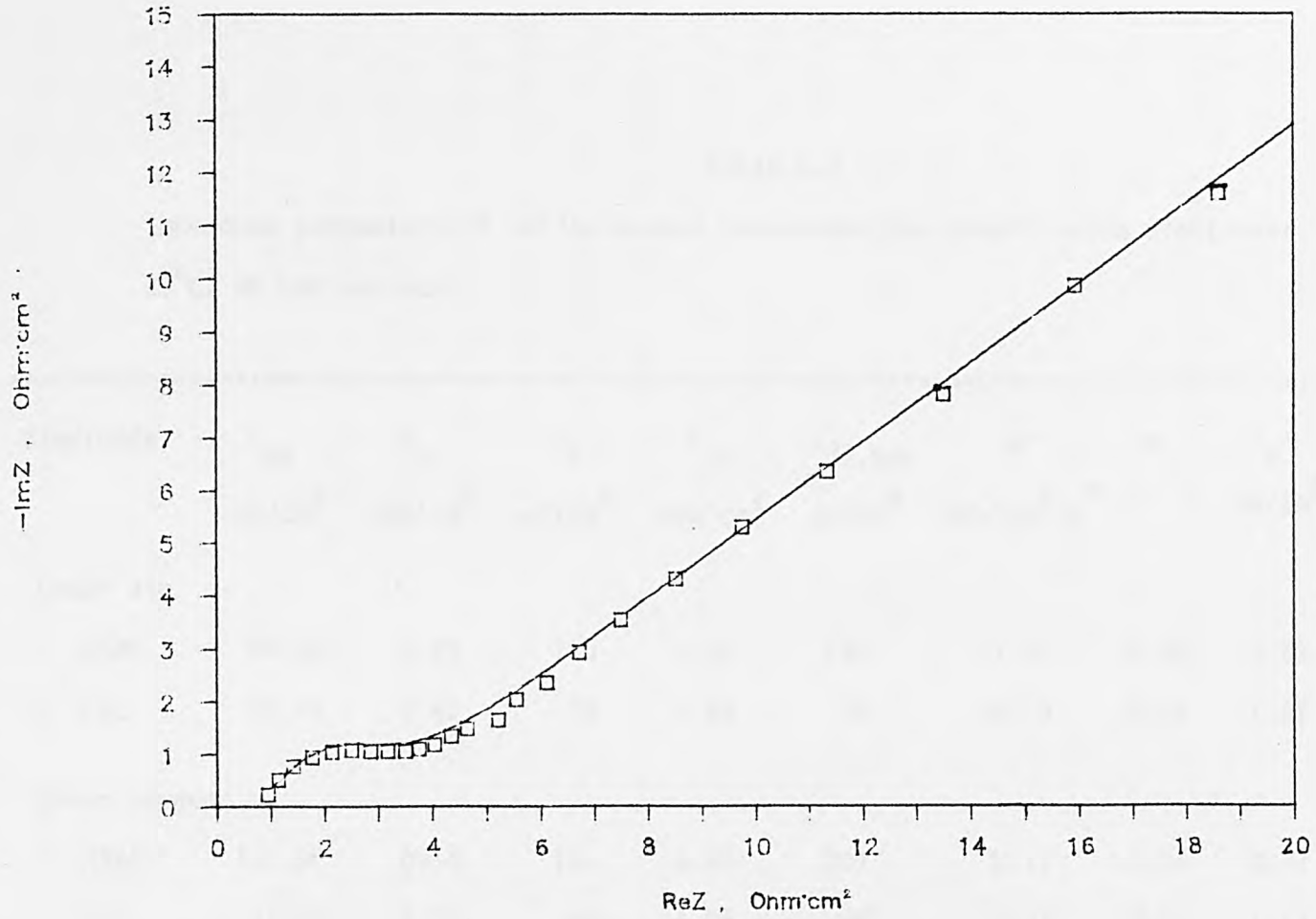

Fig. 8.13 Fitted impedance responses of electrode LDC at ocv.
25°C, 5N KOH and using air as feed gas.

Table 8.2

Impedance parameters of Teflon-bonded semiconducting cobalt oxide electrodes. 25°C, 5N KOH and ocv.

Electrode	C_{ex} $\mu F/cm^2$	R_{sl} $ohm \cdot cm^2$	C_{sl} $\mu F/cm^2$	R_{ct} $ohm \cdot cm^2$	$C_{dl,app}$ $\mu F/cm^2$	W' $ohm \cdot cm^2/s^m$	m	i_o' mA/cm^2	F_r $*10^3$
Under air									
HSAC	94.40	0.25	145	1.26	195	11.02	0.34	0.52	0.18
LDC	22.97	0.41	33	1.68	75	16.13	0.41	1.02	0.82
Under oxygen									
HSAC	101.86	0.14	165	0.85	207	8.11	0.34	0.73	0.06
LDC	27.88	0.20	42	1.04	84	9.32	0.41	1.47	0.54

close to 0.5, which is the Warburg diffusion process in the case of planar electrodes. However, direct comparison of the porous diffusion coefficient W' between different electrodes would be incorrect because of the difference in the true interfacial area.

Normally, in semiconductor/electrolyte systems the capacitances of the space charge layer and the surface state layer are relatively small compared with the capacitances of the Helmholtz double layer[250]. The capacity of the surface oxide layer was found to be less than the double layer capacity. But the C_{sl} value could not be, only, the capacitance of the space charge layer, because it is physically unreasonable for the cobalt oxide electrode systems under cathodic polarization. The capacitances of the surface layer in the model could be influenced by the electrochemical reactions in the surface region including the space charge layer, surface states as well as the surface adsorption processes. Also, the porous diffusion coefficient W' decreases with the increase of the partial pressure of oxygen, as indicated in Table 8.2. This dependence of W' on the partial pressure of oxygen demonstrates that there might exist a relationship between W' and the concentration of reactants similar to the classical Warburg diffusion processes[161]. However, the equivalent relationship between the Warburg diffusion resistance and capacitance can no longer hold in O_2 reduction on Teflon-bonded cobalt oxide electrodes.

Similarly, the characteristic exchange current densities i_o' were calculated from the values of R_{ct} on Teflon-bonded HSAC and LDC electrodes. The calculations were carried out according to equation (6.4), assuming the Helmholtz double layer thickness on a semiconductor resembles that of metals[251]. A value of 10 $\mu F/cm^2$ was used for the

double layer capacity per 1 cm^2 true surface area. At a first approximation, the number of electrons n participated was also 2, for the two-electron reaction. The i_o' values obtained for electrodes HSAC and LDC are lower than that for graphite, though they are still much higher than that for the corresponding four-electron reaction, which is about 10^{-7} mA/cm^2[64]. In conclusion, both the two-electron reaction (the formation of intermediate HO_2^-) and the four-electron reaction (the formation of water) simultaneously occur during O_2 reduction on Teflon-bonded HSAC and LDC electrodes. However, it seems that the reduction of oxygen on cobalt oxide electrodes is primarily dominated by the formation of peroxide particularly in the case of lithiated Co_3O_4. These results obtained from a.c. impedance measurements are in agreement with Savy[68], but in disagreement with Efremov and Tarasevich[64]. The difference could be attributed to the strong dependence of the kinetics of oxygen reduction on the surface states of semiconducting cobalt oxides prepared.

8.4.2. Effect of Polarization Potential

Studies of impedance responses as a function of the polarization potential in the same system gave more information about the kinetics and mechanism of oxygen reduction. Fig. 8.14 shows the complex impedance plots of HSAC at 25°C in 5N KOH solution using oxygen as a feed gas, measured at various potentials (vs. DHE). The calculated parameters are shown in Table 8.3. Two features are immediately observed, the appearance of a second semicircle at high polarization potentials and a change of the size of the first semicircle at high frequencies. The variation of the size of the semicircle in high frequency regions, with the applied potentials, can be explained by the

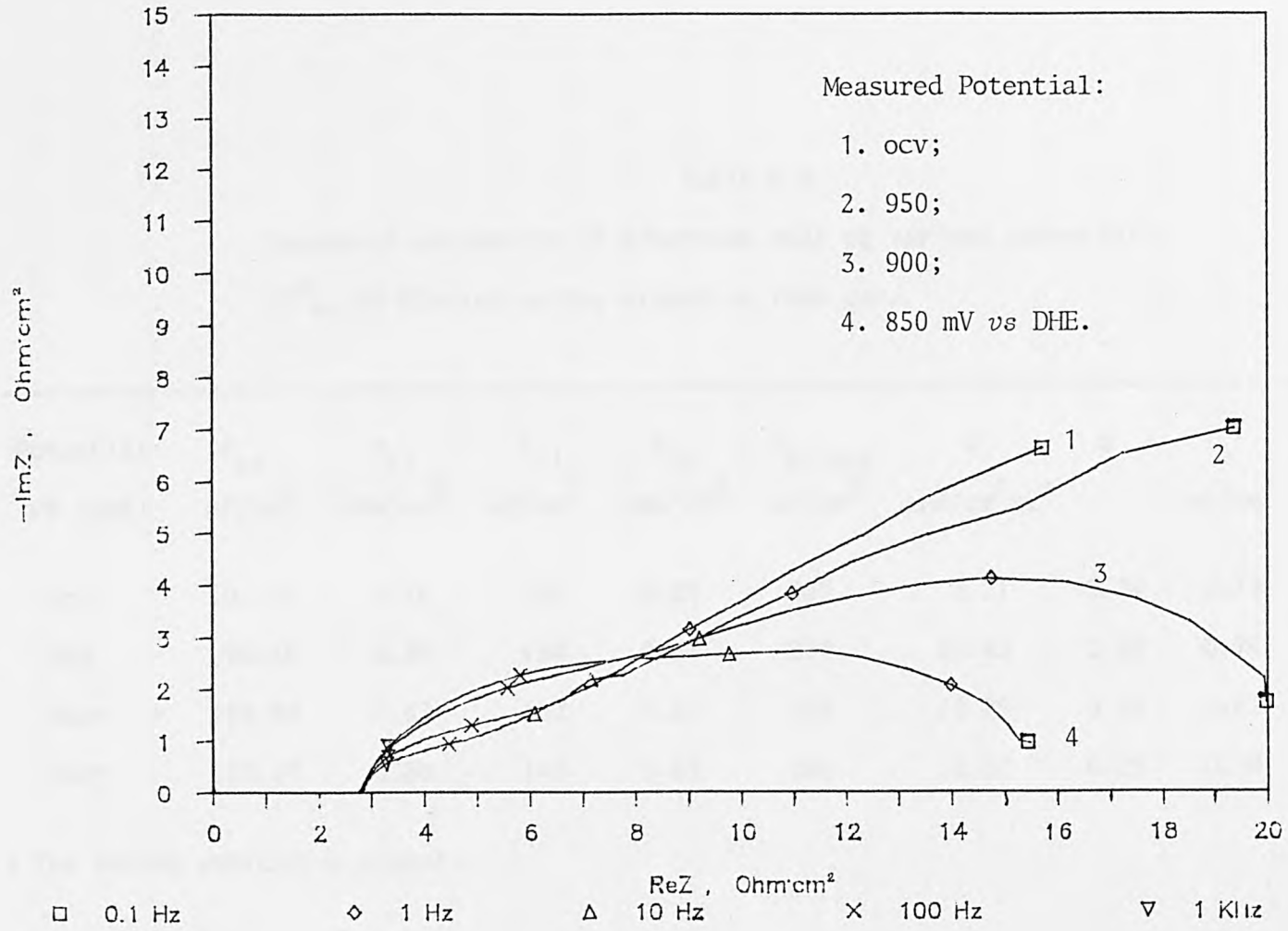

Fig. 8.14 Measured impedance responses of electrode HSAC at various potentials. 25°C, 5N KOH and using oxygen as feed gas.

Table 8.3

Impedance parameters of electrode HSAC at various potentials.

$25^{o}C$, 5N KOH and unsing oxygen as feed gas.

Potential mV (DHE)	C_{ex} $\mu F/cm^2$	R_{sl} $ohm \cdot cm^2$	C_{sl} $\mu F/cm^2$	R_{ct} $ohm \cdot cm^2$	$C_{dl,app}$ $\mu F/cm^2$	W' $ohm \cdot cm^2/s^m$	m	i_o' mA/cm^2	F_r $*10^3$
ocv	101.86	0.14	165	0.85	207	8.11	0.34	0.73	0.06
950	90.46	0.34	134	0.81	214	10.43	0.32	0.74	0.12
900*	105.83	0.53	132	0.81	235	13.25	0.28	0.67	3.66
850*	105.19	0.80	145	0.83	285	12.02	0.25	0.54	2.98

* The second semicircle appears.

possible variation of surface composition. For polarization near ocv, the divalent cobalt ions are present in the surface region mainly due to chemical dissolution. The determination of cobalt solubility shows that the concentration of Co^{2+} increases with the increase in KOH concentration. For oxygen reduction on a porous electrode the concentration of alkali inside the pores of the electrodes is increased with the polarization potentials. Consequently, the thickness of the surface layer is dependent on the polarization potential. For cobalt oxide having a fixed resistivity, the resistance R_{sl} should increase with the thickness of the surface oxide layer, and the capacitance should then decrease with thickness. In Table 8.3 this is just the case for oxygen reduction on electrode HSAC in alkaline solutions at different potentials. Moreover, it is improbable that increasing polarization would cause the increase of the charge transfer resistance R_{ct}. At this stage it is possible to describe, qualitatively, the structure of the surface oxide layer in the model: the adsorbed Co^{2+} ions or amorphous cobaltous oxides mainly attribute to the existence of the surface layer. The binding energies of Co $2p_{3/2}$ of Co_3O_4 are identical with that of CoO, which could mean that the surface region of Co_3O_4 contain very small amounts of cobaltic ions[252].

Similarly, the bending behaviour of the diffusion tail at a relatively high polarization could be explained by the same reason described for the oxygen reduction on graphite electrodes. The coupled surface adsorption processes and the further decomposition or transport of intermediate HO_2^- are responsible for the appearance of the second semicircle. This immediately indicates that oxygen reduction on semiconducting cobalt oxides proceeds mainly through the formation of intermediate HO_2^- ions at high polarization potentials. The change of

the reaction mechanism could be caused by the accumulation of CoO on the surface oxide layer. It was confirmed[63] that on simple cobalt oxide such as CoO oxygen reduction proceeds to HO_2^- in alkaline solution. It has been found that the proposed equivalent circuit, involving the surface oxide layer, cannot be used for the experimental impedance responses at low frequencies in these cases. Evidently, the reason for this is that the equivalent circuit does not in fact consider coupled catalytic reactions.

The Li-doped Co_3O_4 system shows quite similar impedance responses with respect to the variation of the applied potentials as shown in Fig. 8.15. The fitted impedance parameters are given in Table 8.4. It is noted that the characteristic exchange current density i_o' for LDC is higher than that for HSAC which seems inconsistent with their polarization performance for O_2 reduction in alkaline solution. However, as the i_o' values are characteristic of the electroactivity of the porous electrodes as pointed out previously, the higher i_o' values correspond to the larger number of active sites involved in the electrochemical reactions. This fact shows that the lithiation of Co_3O_4 enhances the electrical conductivity and electrochemical activity as well. The difference in the electrode performance for O_2 reduction can be said to be due to the difference of the interfacial active area of electrodes HSAC and LDC. However, the difference becomes smaller as the polarization increases, as indicated by the transport hindrance plots shown in Fig. 8.5.

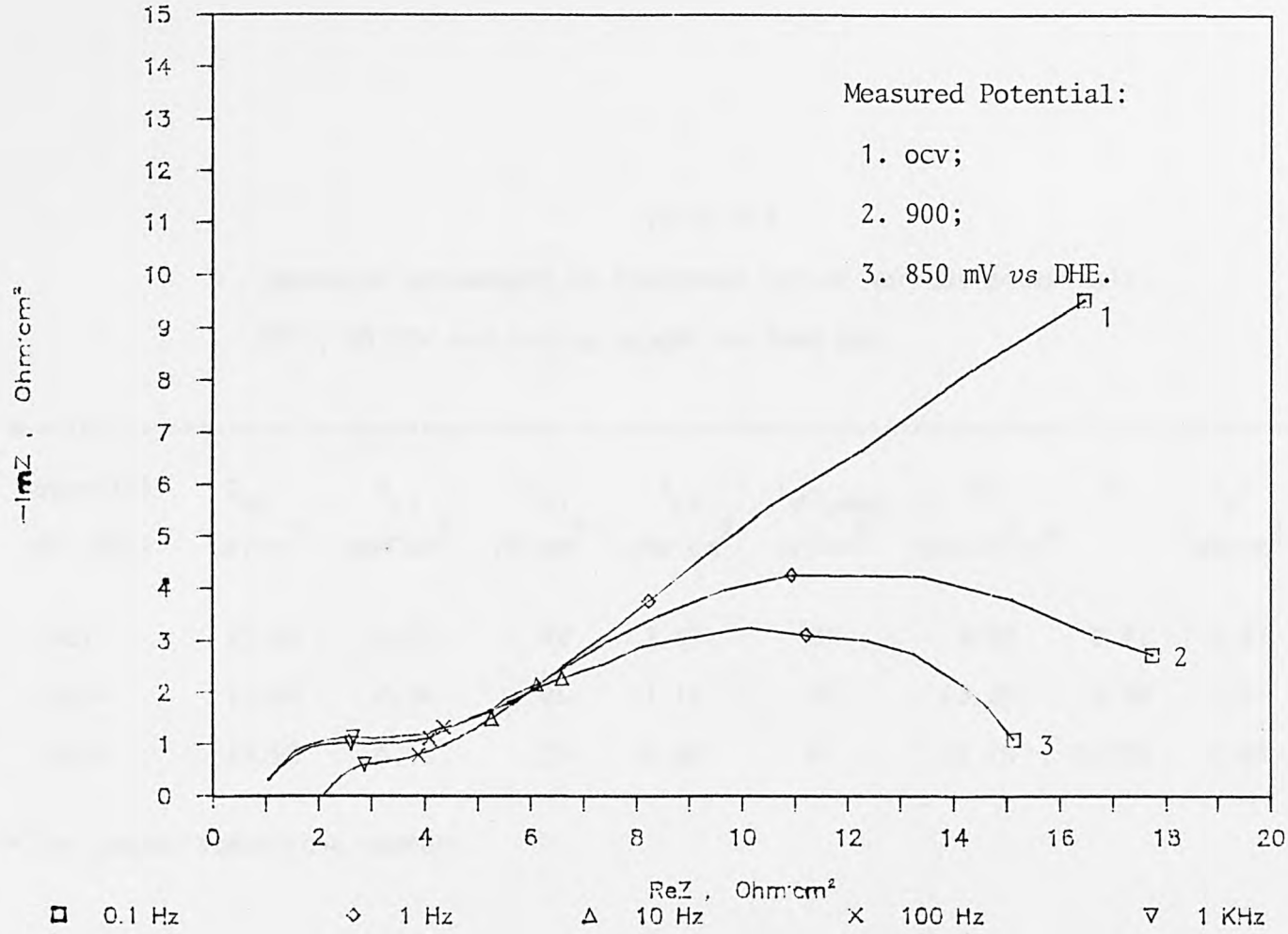

Fig. 8.15 Measured impedance responses of electrode LDC at various potentials. 25°C, 5N KOH and using oxygen as feed gas.

Table 8.4

Impedance parameters of electrode LDC at various potentials.

$25^{o}C$, 5N KOH and unsing oxygen as feed gas.

Potential mV (DHE)	C_{ex} $\mu F/cm^2$	R_{sl} $ohm \cdot cm^2$	C_{sl} $\mu F/cm^2$	R_{ct} $ohm \cdot cm^2$	$C_{dl,app}$ $\mu F/cm^2$	W' $ohm \cdot cm^2/s^m$	m	i_o' mA/cm^2	F_r $*10^3$
ocv	27.88	0.20	42	1.04	84	9.32	0.41	1.47	0.54
900*	17.63	0.34	25	1.14	59	13.30	0.34	1.91	3.96
850*	18.98	0.42	24	0.95	51	12.70	0.305	2.65	1.96

* The second semicircle appears.

CHAPTER NINE

PRELIMINARY STUDIES OF IN SITU REGENERATION OF AIR ELECTRODES AND OF REACTIVE DEPOSITION OF HIGHLY-POROUS COBALT ELECTRODES

9.1. In Situ Regeneration of Air Electrodes

One of the main reasons for the limited applications of air electrodes is the deterioration of their performance in long-term operation. For phosphoric acid fuel cells, the decay of the performance was found to be caused by the decrease in the surface area of platinum catalysts[253]. The use of air cathodes in the chlorine production industry is promising[4], but there exist consequent possibilities of deposition of catalyst poisons and leaching of active catalysts, owing to the higher current density of chloralkali cells and their continuous flow of electrolyte[254]. In cobalt oxide/graphite electrodes, it has been confirmed that intermediate peroxide formed during O_2 reduction is homogeneously decomposed by the dissolved Co^{2+} ions in alkaline solution. In the long-term operation of carbon-based electrodes, some of the dissolved Co^{2+} ions will go into the bulk solution. Consequently, the electrode performance will seriously deteriorate. It is quite clear, therefore, that the industrial applications of air electrodes, especially using semiconducting oxides as catalysts, in fuel cells, chloralkali cells and metal-air batteries are largely dependent on the possibility of the regeneration of the air electrodes in situ.

In principle the possibility of in situ regeneration of air electrodes has mainly relied on the efficient and convenient method of oxide catalyst deposition onto porous air electrodes. The electrodeposition of catalysts has been reported in a few cases; such as the electrodeposition of nickel onto carbon for the catalytic hydrogenation of organic molecules[255,256], and of Pb^{2+} onto titanium substrate in acidic $Pb(No_3)_2$ solution[257]. Few reports could be found in

literature about in situ electrodeposition of oxide catalysts on air electrodes. In first part of this chapter, the preliminary results of the electrodeposition of cobalt catalysts onto Teflon-bonded graphite electrode will be reported.

9.1.1. Experimental

In previous chapters, it has been demonstrated that the homogeneous catalysis activity of Co^{2+} ions is localized near the active sites inside pores, and therefore is largely affected by the distribution of Co_3O_4 catalysts on graphite electrodes, rather than the amount of catalyst. Consequently, it was thought that direct deposition of cobalt oxide catalysts from cobalt salt solutions onto porous graphite supports, could achieve uniform distribution of the catalysts, and enhance the homogeneous catalysis activity.

The Teflon-bonded graphite electrodes used were prepared by the rolling method. The electrode was in contact with 5 wt% $CoCl_2$ solution overnight to ensure that the pores were wetted. The graphite electrode was cathodically polarized in 5 wt% $CoCl_2$ solution at 2 mA/cm^2 for 30 minutes, using oxygen as the feed gas. The floating cell was assembled as shown in Fig. 2.3 (see section 2.2.1). After washing with distilled water, the electrode was polarized anodically at 1.4 V (DHE) under air, for 60 minutes, in 5N KOH solution. The electrode performance was tested at 25°C in 5N KOH solution, using air as the feed gas.

9.1.2. Results and Discussion

Fig. 9.1 shows the polarization curves for oxygen reduction on a graphite electrode before and after the electrodeposition treatments. The performance of the electrode, after deposition of cobalt catalysts, improved markedly; at 750 mV, the performance of the graphite air electrode only gave 40 mA/cm^2 but after the deposition of cobalt catalysts, the electrode gave 140 mA/cm^2. The amount of cobalt catalyst deposited was less than about 1 mg/cm^2; the graphite loading was 18 mg/cm^2. It was noticed that the performance of so treated electrodes for O_2 reduction was comparable with that of 20 wt% 3.1 at% Li-doped Co_3O_4/graphite electrode (electrode LDC2, see section 7.2.2).

Cobalt hydroxide $Co(OH)_2$ was considered to be formed as the intermediate product during the cathodic polarization processes, as the polarization potentials were determined to be in the range of -500 to -600 mV (vs. SCE) during deposition. At this cathodic potential, oxygen reduction could be very important in the case of Teflon-bonded graphite electrode. The OH^- thus generated inside the pores of the electrodes reacts immediately with Co^{2+} ions to form $Co(OH)_2$, which could be further reduced or deposited inside the pores of the electrodes.

It has been reported that at anodic potentials above 0.6 V (RHE), the cobaltous hydroxide is gradually converted to such Co^{3+}-containing species as Co_3O_4, Co_2O_3 and CoOOH in alkaline solutions[258]. At 1.25 V (NHE) along with $Co(OH)_2$, there appears an oxide of a spinel structure Co_3O_4 and as oxidation proceeds, the content of Co_3O_4 increases[63]. The following anodic treatment at 1.4 V first

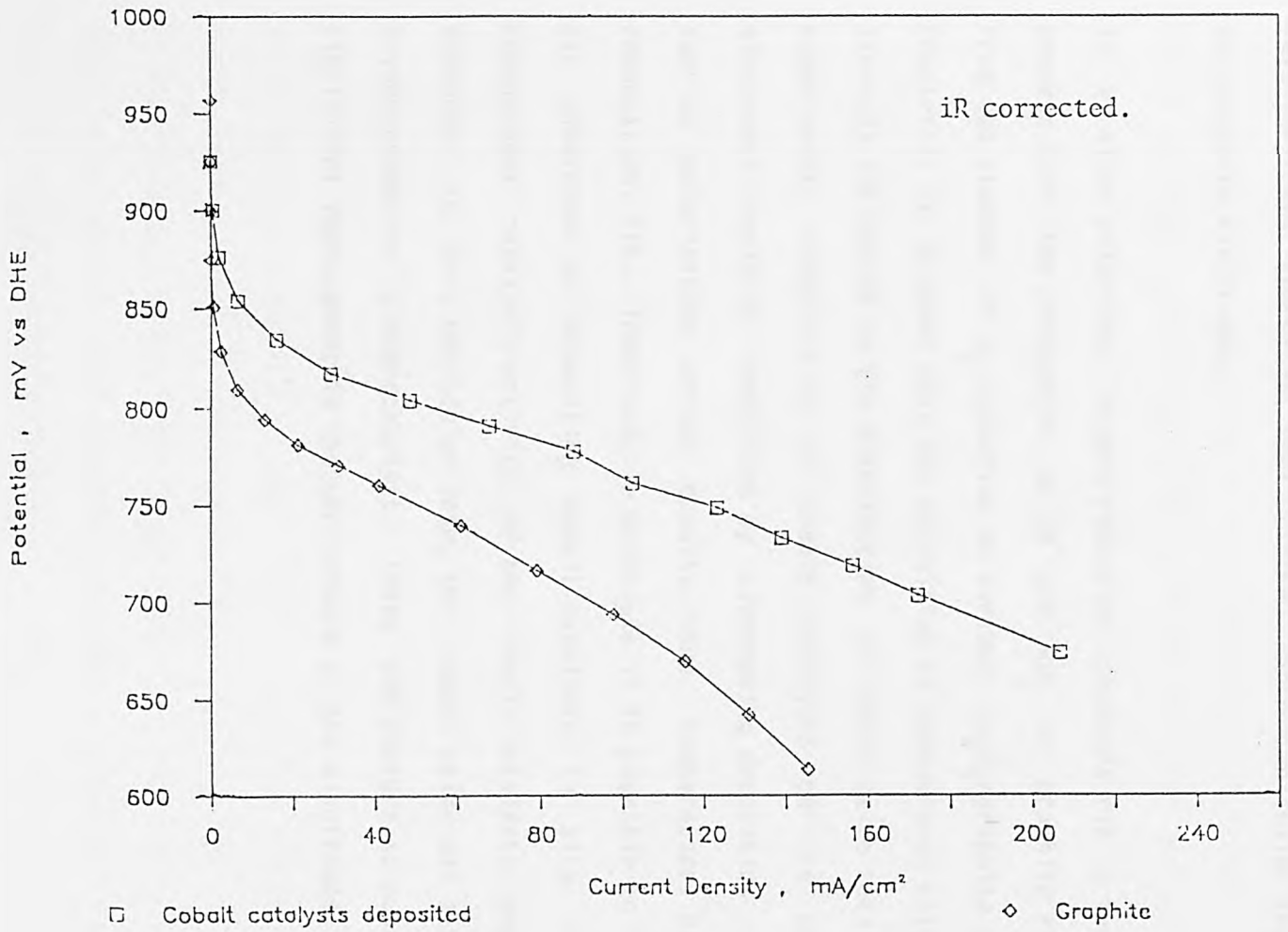

Fig. 9.1 Polarization curves of graphite electrode before and after the cobalt catalyst deposition treatments.

25^0C, 5N KOH and using air as feed gas.

discharges metallic cobalt deposits to $Co(OH)_2$, and then oxidises the $Co(OH)_2$ to cobalt oxide. The choice of 1.4 V ensured that the electrochemical oxidation of graphite was negligible. The cobalt catalysts were, therefore, very uniformly deposited inside the pores of the graphite electrodes.

In alkaline solutions, oxygen reduction proceeds via a two-electron process with the production of OH^- and HO_2^- on graphite electrodes. From the studies of O_2 reduction on various Co_3O_4/graphite systems in Chapter 7, it is shown that the activities of homogeneous catalysts are strongly influenced by the distribution of cobalt oxide catalysts. In experiments, distribution of cobalt catalysts on the porous air electrodes could be controlled by alternating deposition conditions such as polarization current density, time, temperature, electrolyte composition, etc. Therefore, in principle it is possible to regenerate air electrodes by depositing cobalt catalysts in situ. Also, the homogeneous catalysis activity of the cobalt catalysts was markedly enhanced. In this particular case, the cobalt oxide was also a good oxygen reduction electrocatalyst. These two factors account for the significant improvement in the performance of the electrodes.

9.2. Reactive Deposition of Highly-Porous Cobalt Electrodes

One of the most effect ways to intensify the electrode reaction, is to use porous electrodes. In general, there are two basic techniques used to manufacture porous electrodes: (1) sintering of powders (e.g., in metal ceramics technology)[259], and (2) leaching or the thermal decomposition of pore former such as $(NH_4)_2CO_3$ introduced into the powder[90,260]. It is, however, unavoidable to involve the treatments of high temperature or high pressure in preparation of porous electrodes using the techniques mentioned. The electrochemical activity of the porous reactant is rather low, and the pore distribution and the pore density are poor, mainly due to the physical nature of the treatments[90].

It was found that the method used for the deposition of cobalt catalysts on a graphite electrode could be employed to produce highly porous cobalt electrodes in $CoCl_2$ solution, under bubbling oxygen. The most attractive character of the cobalt electrode, as anode in rechargeable batteries[90,261], is its high specific capacity; the theoretical value is 0.909 Ah/g as compared to 0.477 Ah/g for cadmium. It is expected, however, that this novel deposition method could find applications not only in the fabrication of batteries, but also in high surface area electrocatalytic coatings. In brief, the preliminary experimental results and the characteristics of cobalt deposits are reported in the following sections.

9.2.1. Experimental

Titanium foil with thickness of 0.25 mm was used as the substrate. The foil was first polished with fine sand paper and washed in diluted sulphuric acid solution, and then rinsed with distilled and deionised water. The working surface area of the substrate was 1 cm^2. The remaining area was coated with lacomit seal (Canning, F65441) and allowed to air-dry for about 15 minutes.

The titanium substrate was assembled in a test cell, shown schematically in Fig. 9.2. The deposition processes were carried out galvanostatically at 25^{o}C in 5 wt% $CoCl_2$ solution. The substrate was immersed in the electrolyte and the working surface was faced directly to a nickel gauze counter electrode. For longer deposition, titanium or platinum foils were used as the counter electrodes in order to avoid contamination of the dissolved nickel. The operation potentials were measured against a standard saturated calomel electrode (SCE, 0.2444 V vs. NHE at 25^{o}C). During deposition, pure oxygen was bubbled through the tube sited below the substrate. Occasionally, pure nitrogen was also used for the purpose of comparison.

The influence of bubbling oxygen rates through the solution during the cobalt deposition was investigated by cyclic voltammetric technique. Cyclic voltammetry was carried out in 10 wt% $CoCl_2$ at 25^{o}C. The potential was measured against a SCE and the scan rate was set as 100 mV/sec. The rate of bubbling oxygen was controlled by a gas meter.

The cobalt deposited electrodes were examined by scanning electron microscopy (SEM), X-ray diffraction analysis and infrared spectroscopy

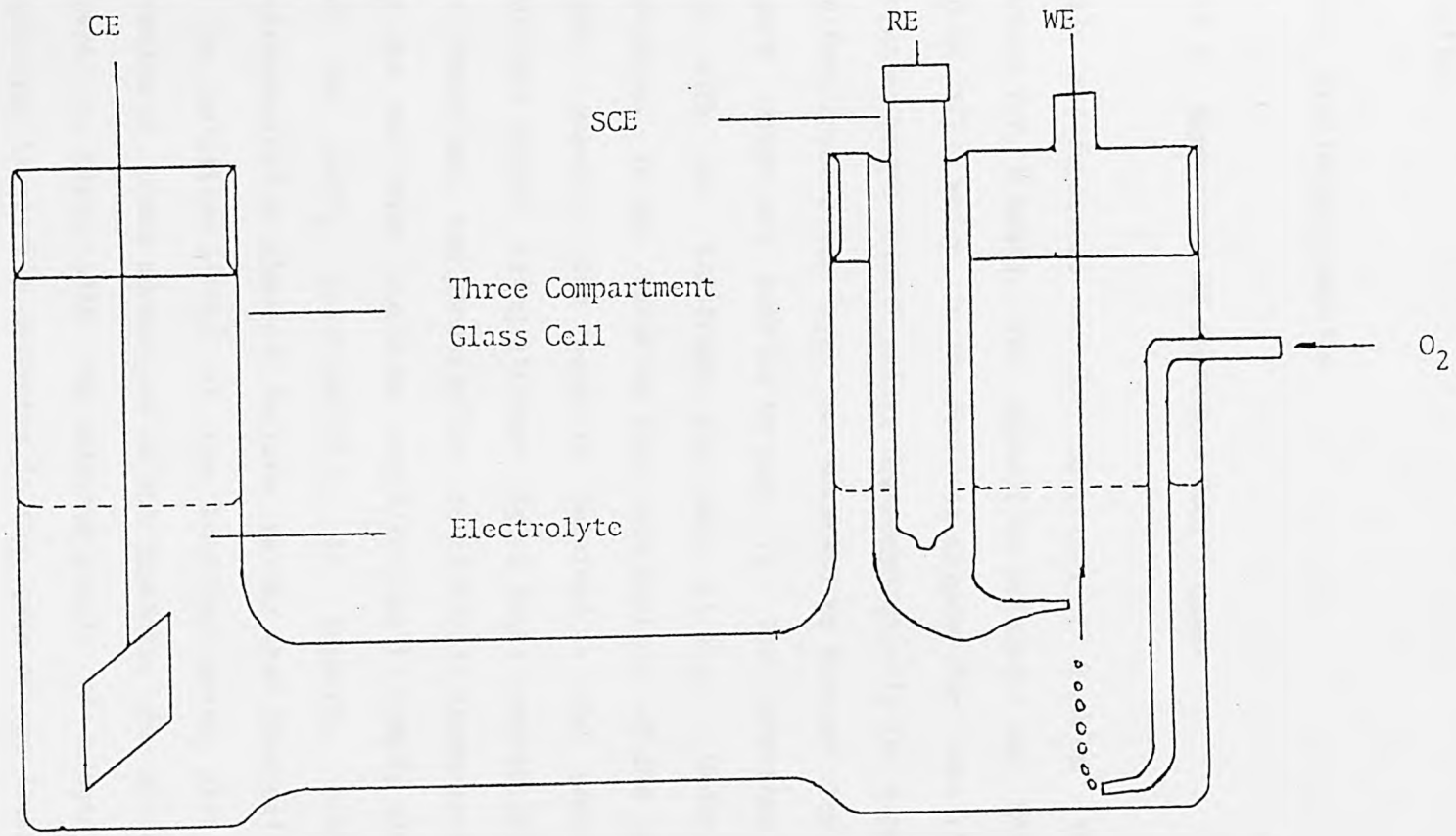

Fig. 9.2 Experimental setup for the cobalt deposition.

analysis.

9.2.2. Preliminary Results

9.2.2.1. Appearance of Deposited Cobalt Layer

Cobalt was deposited on Ti substrates at 2 mA/cm^2 in 5 wt% $CoCl_2$ solution for 2 hours. The deposition potential was determined below -700 mV (SCE), which in the Pourbaix diagram for cobalt[77] is inside the region where cobalt exists thermodynamically in a metallic state. A uniform brown-black layer was observed to form on the Ti substrate, if pure oxygen was bubbled through it. The adherence of this thin layer with the substrate was very strong. Under the optical microscope, it was observed that the surface of the film was very porous. However, the deposits obtained in the same experimental conditions except using nitrogen or no gases passed through at all, were simply mat, and were similar to silver in appearance. This shows that the mat layer could be metallic cobalt simply electrodeposited from the $CoCl_2$ solution[262]. It appears, therefore, that electrochemical or chemical factors rather than physical factors, such as the agitation effect of the bubbling gases, attribute to the formation of those porous and black deposits. An obvious difference between the cases with and without supply of oxygen is that the electrolyte is quickly deaerated in the case of the latter, and oxygen reduction in this case is essentially impossible.

9.2.2.2. Scanning Electron Microscopy Analysis

The surface morphology of cobalt deposits was examined by scanning electron microscopy[263]. The depositions were made under static conditions (no gases were passed through), bubbling nitrogen, and bubbling oxygen respectively. A cathodic current of 2 mA/cm^2 was passed for two hours in 5 wt% $CoCl_2$. The cobalt deposited electrodes were washed with distilled water and were air-dried. The samples were punched from the substrates to an appropriate size, and fixed onto the specimen holder using a silver glue. The measurements were carried out on a JEOL Analytical Electron Microscope (JEM 100B).

Fig. 9.3 shows the scanning electron micrographs of the cobalt deposits at a magnification of 3000. Significant differences of the microstructures of the deposits obtained in the absence and the presence of bubbling O_2 are obvious and striking. In static conditions, the cathodic reaction in cobalt chloride solution can be understood on the principles of basic electrodeposition processes[264]. At low current densities (and low cathodic overpotentials), the nuclei of electrodeposits will be apparently centred on some dislocations (e.g., kink sites and screw dislocations) emerging at the surface of metal substrates. The growth nuclei may take the form of spirals or pyramids. The growth pyramids were observed for cobalt deposited from $CoCl_2$ for 1 hour as shown in Fig. 9.3(a). As the deposition time increases, the crystallographic nature of electrodeposits becomes progressively less marked, and the density of growth nuclei also increases. Close-packed planes of the growth pyramids of cobalt with finer grain size, therefore, were resulted. This can be seen in Fig. 9.3(b). It was recognized from micrograph Fig. 9.3(c) that

(a) 2 mA/cm^2, 1 hr and bubbling no gas.

(b) 2 mA/cm^2, 2 hr and bubbling no gas.

Fig. 9.3 Scanning electron micrographs of cobalt deposits obtained under various bubbling gases.

Magnification: 3000 X.

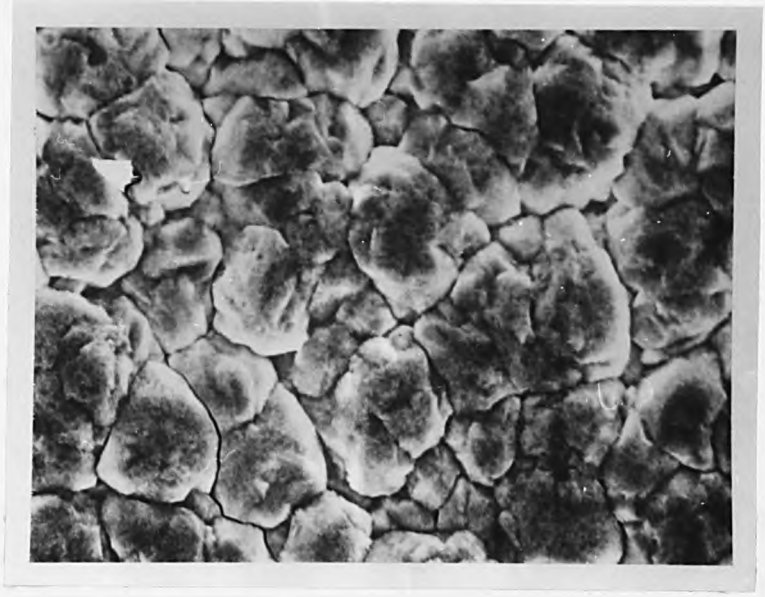

(c) 2 mA/cm^2, 2 hr and bubbling nitrogen.

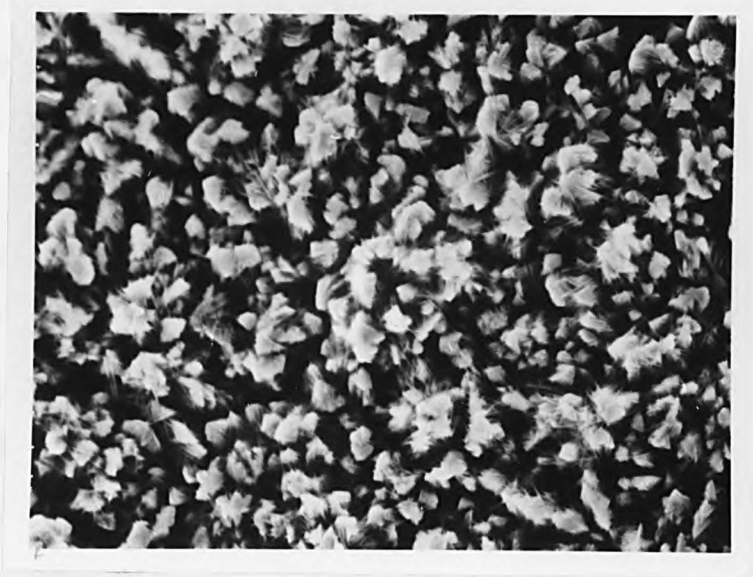

(d) 2 mA/cm^2, 2 hr and bubbling oxygen.

Fig. 9.3 continued.

bubbling nitrogen through the substrates during deposition did not significantly change the microstructure of the deposits. The relatively large crystals of the deposits could be due to the increase of the diffusion process of Co^{2+} ions.

However, a totally different morphology was observed for the black deposits obtained in the case of bubbling O_2 during deposition, as shown in Fig. 9.3(d). The microstructural feature of the black deposits appears as irregular particles, with fine whiskers. The size of the fine grains are almost identical, with an average diameter of about 1 micron. For cobalt anodes produced by powder metallurgical techniques (750^oC, hydrogen, 25 wt% $(NH_4)_2CO_3$ added), the cobalt particles are very much larger (typically about 10 to 20 microns), and the pores are nonuniform[90]. If the fine whiskers are taken into account, then the true reactive surface area available is even greater. It can be seen that the particles were interwoven to form uniformly distributed pores. It is considered that direct electrodeposition of cobalt could be seriously interrupted and the proper growth of the cobalt crystals becomes difficult, because oxygen reduction is unavoidable at such cathodic potentials in the presence of bubbling O_2. Another possibility could be the formation of cobalt hydroxide, $Co(OH)_2$, as the result of OH^- ions formed at the titanium surface by O_2 reduction. Further dehydration and reduction of intermediate $Co(OH)_2$ are most likely to follow. Highly-porous deposits of cobalt metal could, therefore, be formed as the density of metallic cobalt, 8.9 g/cm^3, is much high than that of $Co(OH)_2$, 3.597 g/cm^3 at 20^oC.

Fig. 9.4 demonstrates the influence of deposition current density on the crystallographies of the cobalt deposits. As the current density

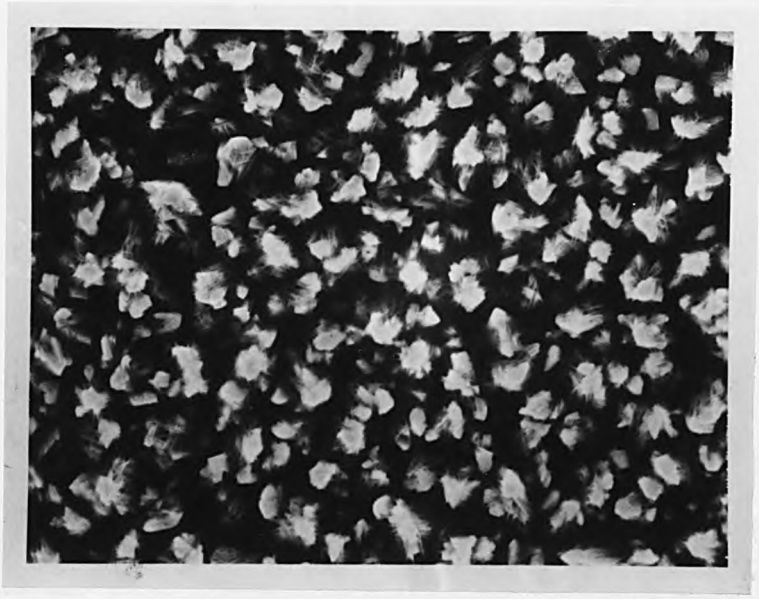

(a) 2 mA/cm^2, 1 hr and bubbling oxygen.

(b) 10 mA/cm^2, 1 hr and bubbling oxygen.

Fig. 9.4 Scanning electron micrographs of cobalt deposits obtained at various current densities.

Magnification: 3000 X.

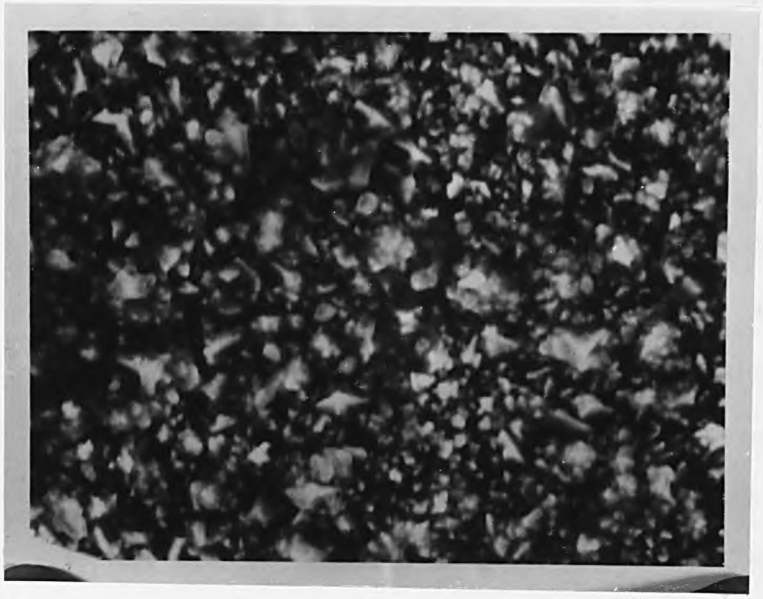

(c) 30 mA/cm^2, 1 hr and bubbling oxygen.

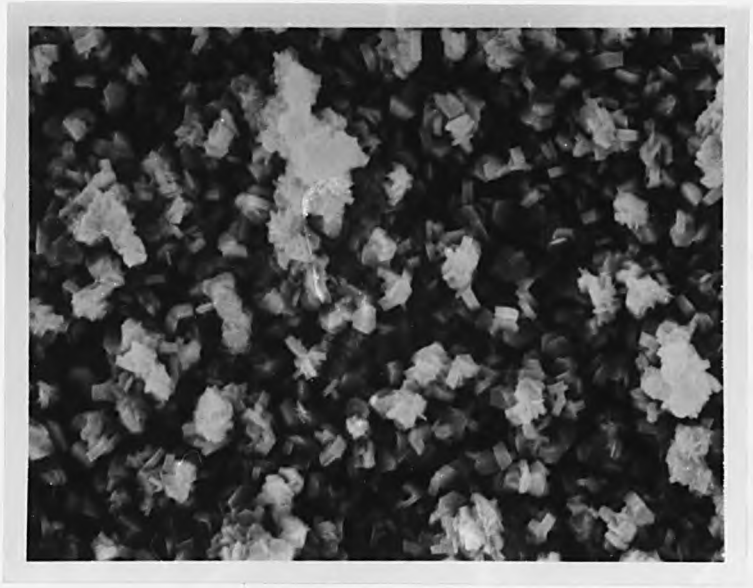

(d) Completely discharged sample (b).

Fig. 9.4 continued.

increases, the pores between the fine grains become smaller. It is interesting to note that at 10 mA/cm^2, the cobalt was deposited as needle-like crystals. These needle crystals were interlaced to form a highly porous structure. It would be expected that both the physical and electrochemical characters of these porous cobalt deposits are significantly different from that of the bulk cobalt metal. From the SEM studies of the cobalt deposited in the presence of bubbling oxygen, it seems that there is an intimate relationship between the porous structure of the deposits and the deposition current density. The reasons for the change of the crystal growth processes of cobalt deposits with the deposition current is not quite clear at this stage. Fig. 9.4(d) is the scanning electron micrograph of a completely discharged cobalt electrode. The electrode was also deposited at 10 mA/cm^2 for 1 hour, under bubbling oxygen. The hexagonal crystals of $Co(OH)_2$[129] were observed to be closely packed. The active $Co(OH)_2$ layers, however, still remained highly porous.

9.2.2.3. Infrared Spectroscopy and X-ray Diffraction Analyses

The infrared absorption spectra of cobalt deposits on the titanium substrate, in 5 wt% $CoCl_2$ solution, was studied in the region 4000 to 180 cm^{-1}, by KBr disc technique[109]. The samples were prepared at a deposition current density of 2 mA/cm^2 for 2 hours, and scraped off from the substrate. The result was compared with the spectrum of $Co(OH)_2$. $Co(OH)_2$ was prepared from $CoCl_2$ and KOH solutions. The precipitate was washed free of alkali and allowed to air dry.

Fig. 9.5 shows the spectra of $Co(OH)_2$ and cobalt deposits respectively. The infrared transmission of the cobalt deposit was, generally, very

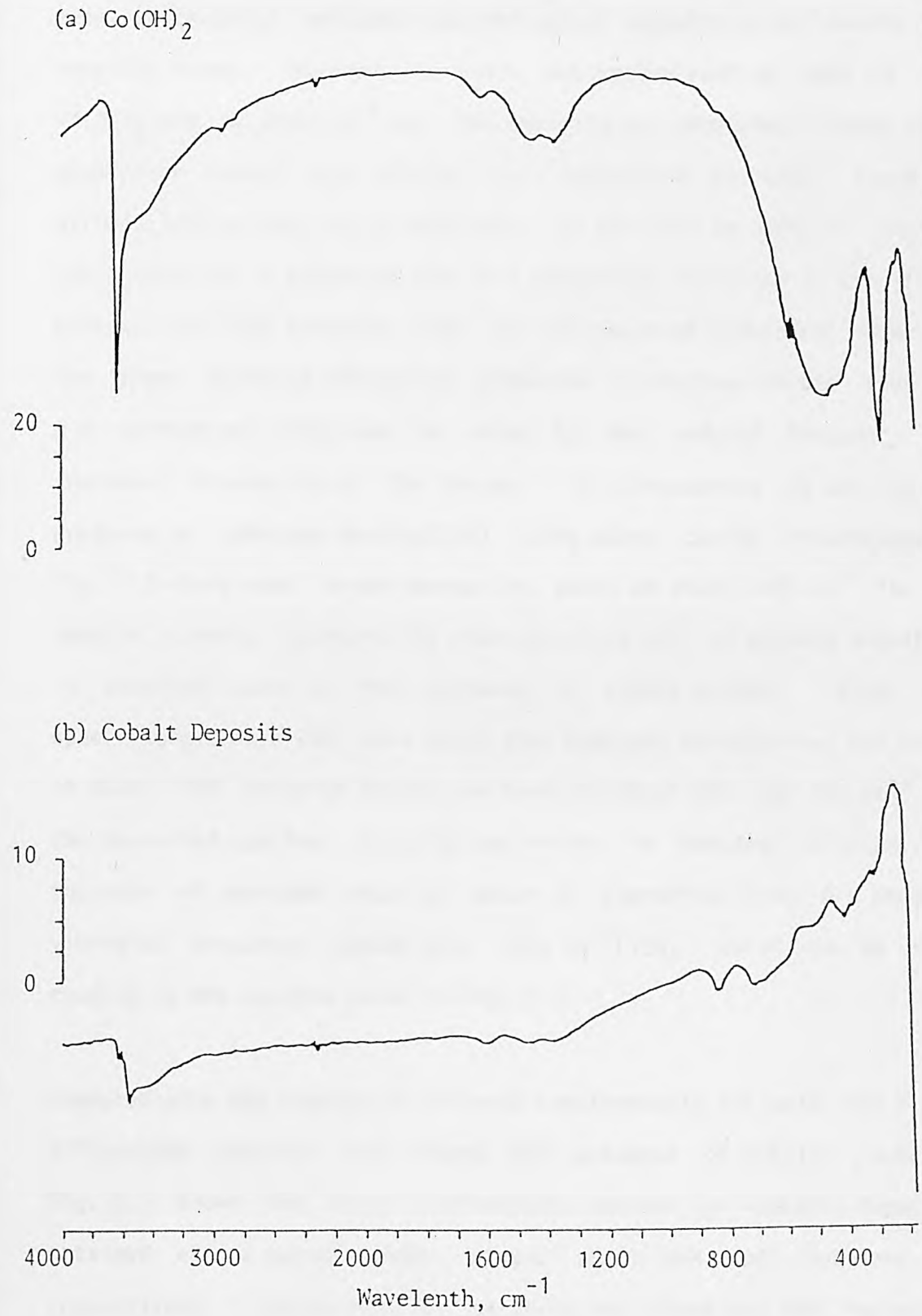

Fig. 9.5 Infrared spectra of $Co(OH)_2$ and cobalt deposits.

Matrix: KBr.

weak, which could indicate that the cobalt deposits exist mainly in a metallic state. However, the sharp absorption band at 3626 cm^{-1} for $Co(OH)_2$ and at 3548 cm^{-1} for the deposits was detected. These sharp absorption bands are similar in appearance to that found in $Ni(OH)_2$[133] as well as in NaOH[265]. In the 3700 to 3500 cm^{-1} region, the absorption is caused by the O-H stretching vibration in the 'free' hydroxyl and both adsorbed water and the water of hydration. However, the 'free' hydroxyl stretching vibration is distinguishable from the O-H stretching vibration in water by the reduced frequency and increased broadening of the latter. This broadening is due to the presence of hydrogen bonding[134] (This point can be illustrated in Fig. 3.3 where small broad absorption bands at about 3435 cm^{-1} for all samples, clearly indicate the characteristic O-H stretching vibration in adsorbed water on the surfaces of cobalt oxides). Also, the spectroscopic data[265] have shown that hydrogen bonding does not occur in NaOH. The infrared absorption bands at about 840 and 720 cm^{-1} for the deposited specimen could be due to the O-H bending vibration. In the case of absorbed water or water of hydration, this O-H bending vibration frequency occurs near 1600 cm^{-1}[134], which can be seen roughly in the spectra shown in Fig. 3.3.

Compared with the results of infrared spectroscopic analysis, the X-ray diffraction analysis only showed the presence of metallic cobalt. Fig. 9.6 shows the X-ray diffraction spectra of cobalt deposits obtained at 2 mA/cm^2 under static conditions and bubbling O_2 respectively. The diffraction patterns are identical and represent that of cobalt metal[135]. It is, thus, confirmed that the deposits, obtained in the presence of bubbling O_2, are still metallic cobalt as that obtained by normal electrodeposition process, though the surface

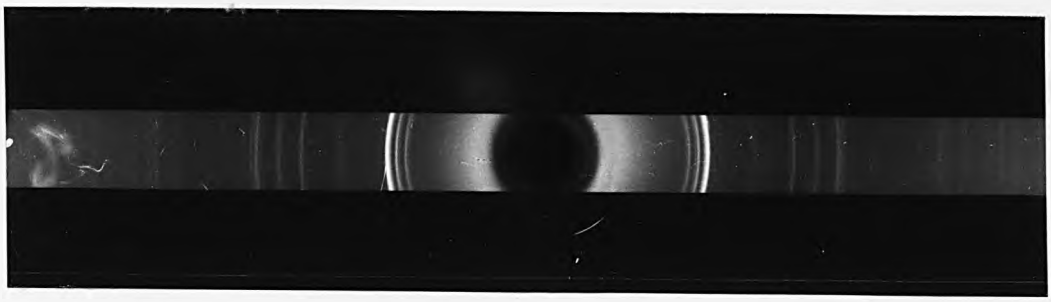

(a) 2 mA/cm^2, 2 hr and bubbling no gas.

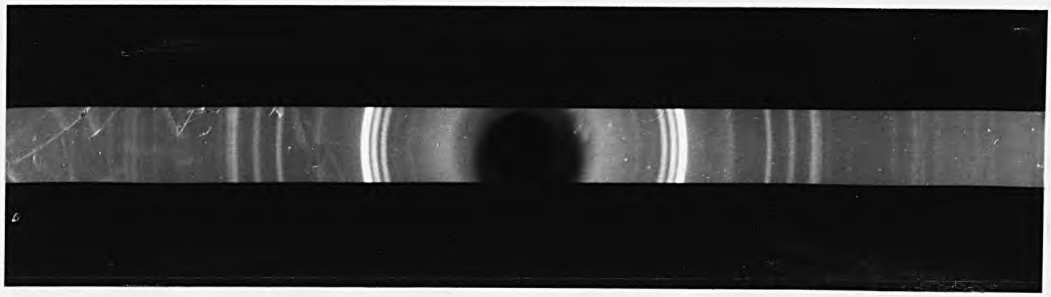

(b) 2 mA/cm^2, 2 hr and bubbling oxygen.

Fig. 9.6 X-ray diffraction patterns of cobalt deposits obtained with and without bubbling oxygen.

crystallography of the deposits is completely changed. However, the discrepancy between the X-ray diffraction and infrared spectroscopic data demonstrate that cobaltous hydroxide is the intermediate product during the deposition in the case of bubbling O_2. The very small amount of $Co(OH)_2$ remaining at the end of the deposition process is possibly an amorphous form.

9.2.2.4. Cyclic Voltammetric Analysis

The influence of the rate of bubbling oxygen in the cobalt deposition processes was investigated by the cyclic voltammetry technique. Fig. 9.7 shows the stable votammetric curves of cobalt deposition reaction on Ti substrate in 10 wt% $CoCl_2$. The bubbling rates, ml/min, are indicated as numbers in the figure and the scan rate was 100 mV/sec. An obvious trend is that the anodic peak current values were inevitably reduced as the rate of bubbling oxygen increases. The cathodic peak current, however, remained almost unchanged. The voltammetric behaviour of cobalt deposition under bubbling O_2 demonstrates again the participation of O_2 reduction. The OH^- ions produced by O_2 reduction could be either adsorbed on the electrode surface or diffuse into the bulk of the solution. They either chemically react with Co^{2+} to form $Co(OH)_2$, or are neutralized. It must be pointed out that only adsorbed $Co(OH)_2$, preferentially in the sites of the adsorbed OH^- ions, could be further electrochemically reduced to metallic cobalt. Increasing O_2 supply rate corresponds to the increase of interfacial contact area between the substrate and O_2 gas, leading to the formation of more OH^- ions. However, the $Co(OH)_2$ formed on the electrode surface could hardly be increased due to the limitation of reactive sites. The net result is, therefore, to

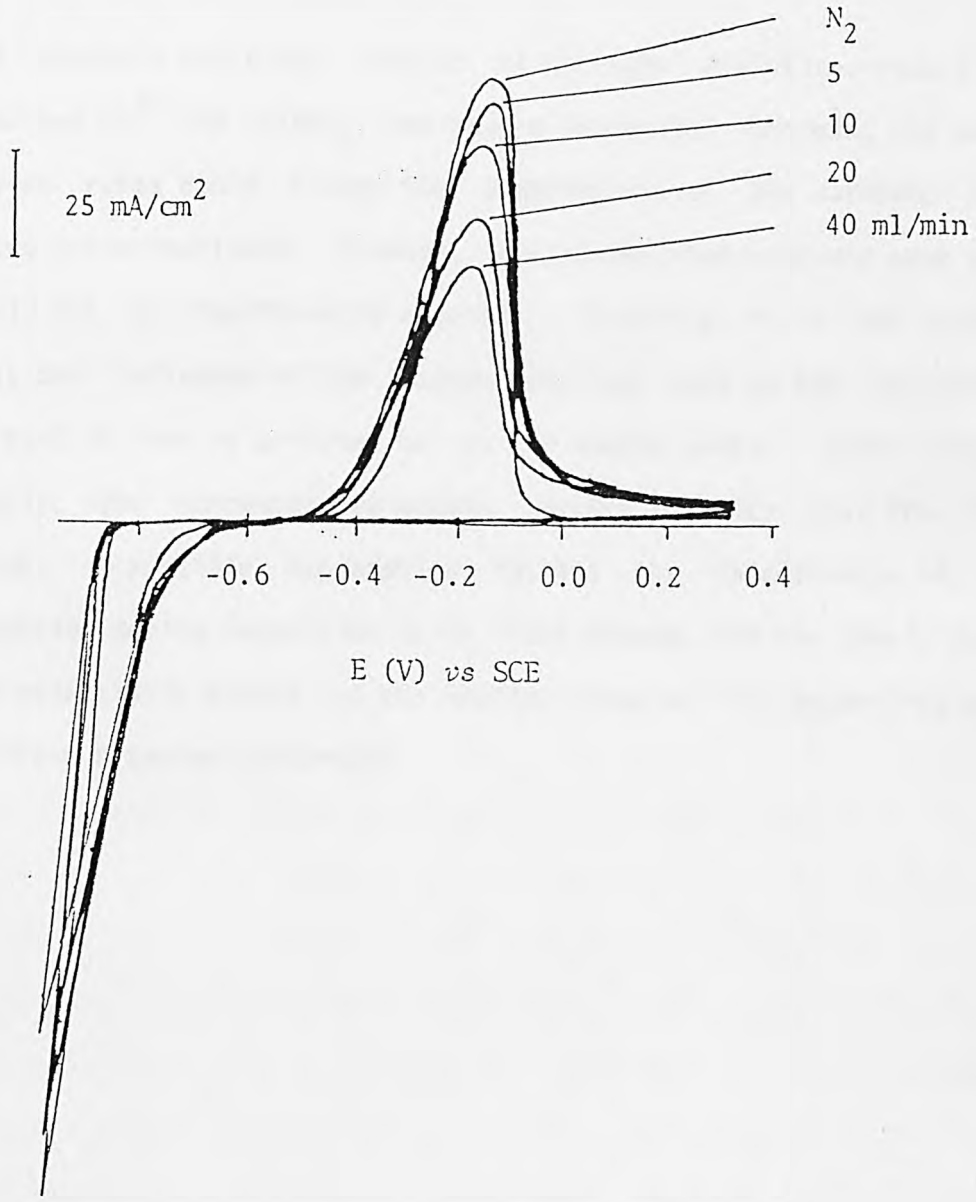

Fig. 9.7 Voltammetric curves recorded during cobalt deposition on a Ti substrate in 10 wt% $CoCl_2$ at various oxygen supplying rates. The sweep rate was 100 mV/sec.

diminish the amount of the cobalt deposited, either through direction deposition of Co^{2+} or indirect reduction of $Co(OH)_2$.

The cathodic reactions consist of hydrogen evolution, reduction of adsorbed Co^{2+} and $Co(OH)_2$, and oxygen reduction. Changing the bubbling oxygen rates could change the distribution of the cathodic current among these reactions. However, the accumulated cathodic peak current could not be significantly altered. Therefore, it is not surprising that the influence of the oxygen bubbling rate on the cathodic peak current is not so profound as on the anodic parts. Under a nitrogen supply, the corresponding anodic current density gave the highest value. A possible explanation is that the interference of oxygen reduction during deposition is in fact absent, and the cobalt deposits are essentially porous at the initial stage of the deposition process on fresh titanium substrates.

9.2.3. Characteristics of Porous Cobalt Deposits

9.2.3.1. Discharge Performance

The discharge performances of the cobalt deposited electrodes were studied at various deposition conditions. The electrodes were discharged at a constant current drain rate of 25 mA/cm^2, in 5N KOH solution. The measurements were carried out at 25^oC and the potential was measured against a DHE. The maximum admissible discharge capacities were estimated by the time required for a complete discharge and the discharge current density. The loading of the cobalt deposits was calculated by the weight difference of the substrate before and after the deposition. The specific discharge capacity was obtained by dividing maximum admissible discharge capacity with the loading.

Fig. 9.8 shows the discharge curves of the cobalt deposited electrode. The electrodes were prepared by cathodic deposition in 5 wt% $CoCl_2$ at 10 mA/cm^2, for 1, 2 and 5 hours respectively. The loadings of the cobalt deposits were also indicated on the curve. The discharge potentials were observed to gradually increase with the discharge time, as more cobalt reactants were anodically oxidized to $Co(OH)_2$. However, for the cobalt electrodes with lower loadings obtained after a relatively shorter deposition time, the discharge curves were quite sharp. As the deposition times increased, the discharge curves became flattened and stable. An important feature could be observed from the discharge curves. It is measurable from the curves that the maximum discharge capacity increases proportionally with the cobalt loading, i.e., the deposition time. This could indicate that under bubbling oxygen, the cobalt, through the intermediate $Co(OH)_2$ formation, is

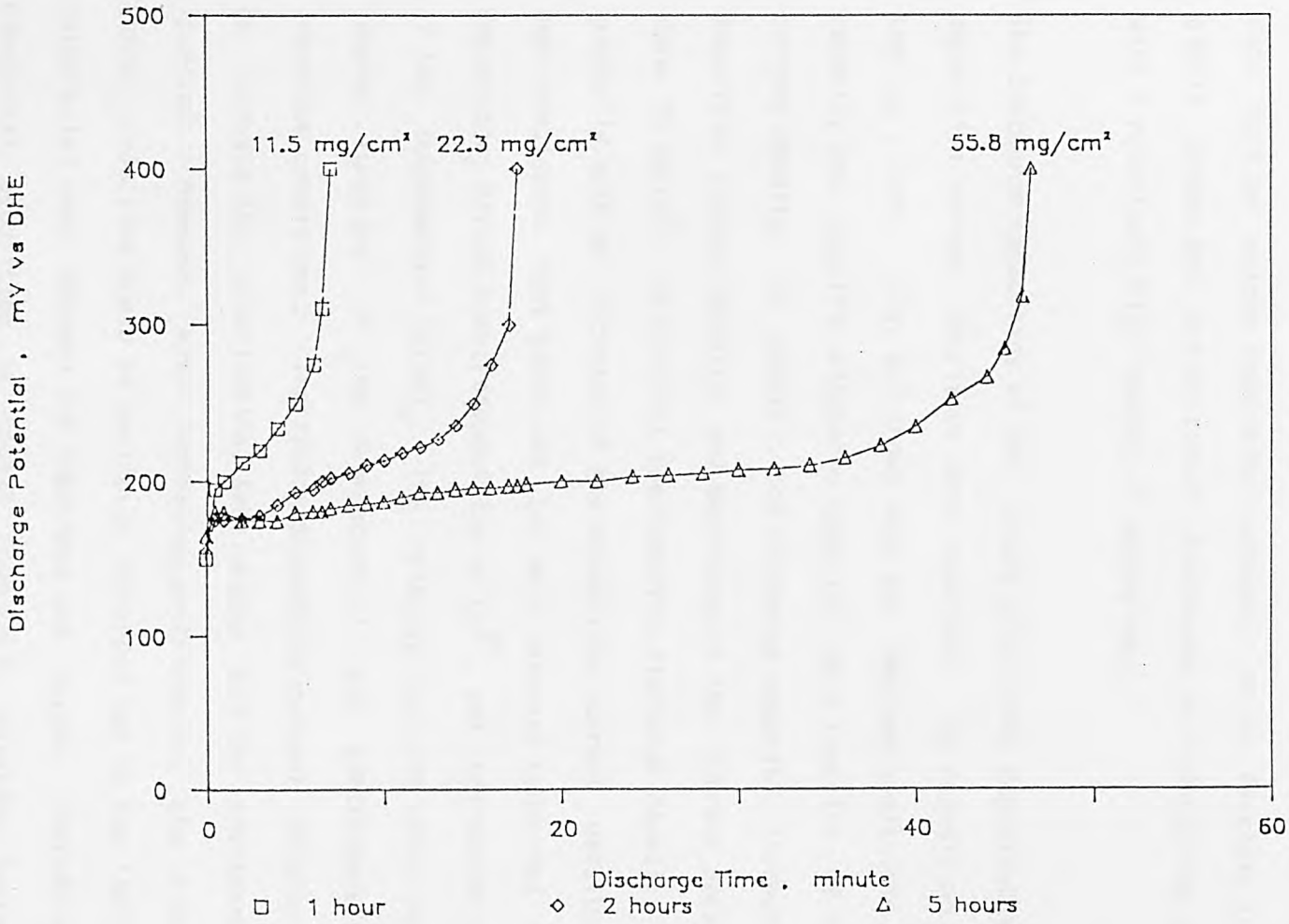

Fig. 9.8 Discharge curves of cobalt electrodes deposited at 10 mA/cm^2 for various times. 25°C and 5N KOH.

deposited above the porous layer formed to grow another porous layer, rather than to fill the inside of the pores. Increasing deposition time results in a superimposing of the porous cobalt layer, and a multi-porous-layer structure of cobalt could be formed. Therefore, with such an unique deposition process, it is feasible to produce highly porous and active cobalt electrodes on conducting substrates with a relatively high loading of active mass.

The discharge capacities of the cobalt electrodes deposited at various deposition current densities were examined. The deposition time was kept as 1 hour. Fig. 9.9 shows both the maximum admissible discharge capacity and specific discharge capacity as a function of deposition current density. In general, the discharge capacity increases at low deposition current density and decreases as the current density rises above 30 mA/cm^2. In contrast the specific discharge capacity decreases gradually with an increase of the deposition current density. It has been considered that there are two main pathways concerned in cobalt deposition; direct electrodeposition of Co^{2+}, and indirection reduction of the intermediate $Co(OH)_2$. The relative reaction rates could be a complex function of the overpotential and electrode/electrolyte interface conditions. Increasing deposition current density (leading to increase the polarization) accelerates all the electroreductions involved. However, with increasing polarization, the kinetics of $Co(OH)_2$ reduction could be seriously retarded due to the limitation of interfacial area between the substrate and oxygen. Therefore, direct electrical deposition of cobalt from $CoCl_2$ solution becomes more predominant, forming dense and less active cobalt deposits. This, especially, leads to a diminishing specific discharge capacity, and discharge capacity as well.

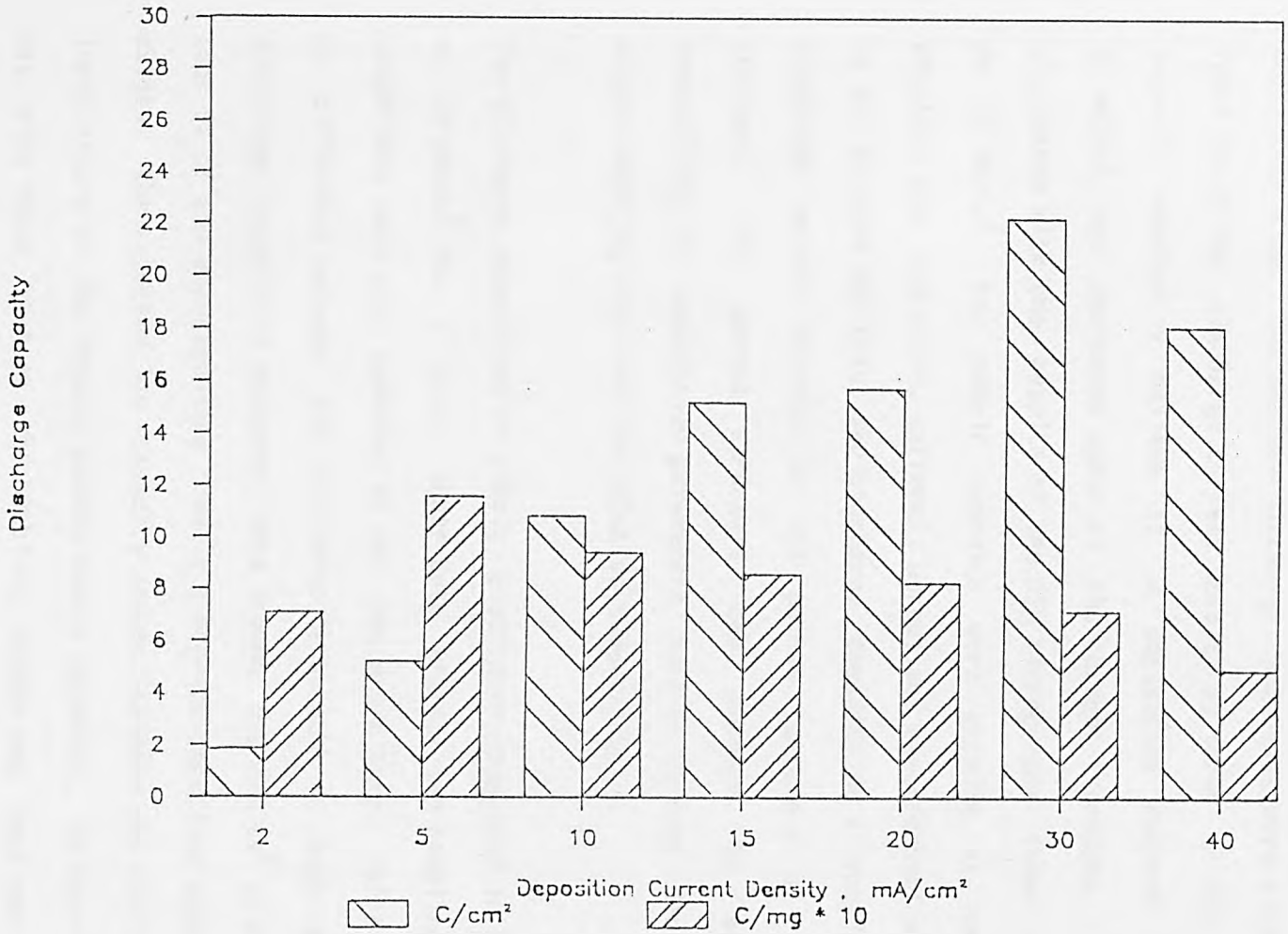

Fig. 9.9 Discharge capacities of cobalt electrodes deposited at various deposition currents for 1 hr. 25°C and 5N KOH.

The points argued above were supported by the results of another experiment. In this experiment, the deposition capacity was kept constant at 20 $mA \cdot h/cm^2$ (or 72 C/cm^2), i.e., increasing the deposition current density corresponded to the proportional decrease of the deposition time. The maximum discharge capacities were also plotted as function of the discharge current density as shown in Fig. 9.10. The capacity reaches a maximum at a deposition current density of 10 mA/cm^2, and decreases again as the current increases. This is in accordance with the results of the SEM micrographs shown in Fig. 9.4. At 10 mA/cm^2, the cobalt deposits were growing as needle-shaped crystals and, therefore, extremely porous and electrochemically active. It is pointed out that the discharge capacity of a cobalt deposited electrode mainly depends on the porous component of the cobalt reactant. The porous structure can, however, be adjusted by controlling the deposition parameters such as current density, time, oxygen bubbling rate and the solution composition.

The discharge capacities of cobalt electrodes deposited in 5 wt% $CoCl_2$ at 10 mA/cm^2 for 1 hour, under both static and bubbling nitrogen conditions were also examined at the same drain rate. There was almost no difference between the discharge behaviour in both cases. The discharge capacities measured were around 0.2 mAh/cm^2 which is less than 6% of the corresponding cobalt electrode deposited under bubbling oxygen. The expected low capacity values indicate the electrochemical inert nature of the densely-packed cobalt deposits. In experiments, it was also found that if the bubbling oxygen was kept away from the surface of the substrate, only part of the electrode was covered by the black porous cobalt deposits, and the performance of the deposited electrode was poor and was not reproducible. It is, therefore,

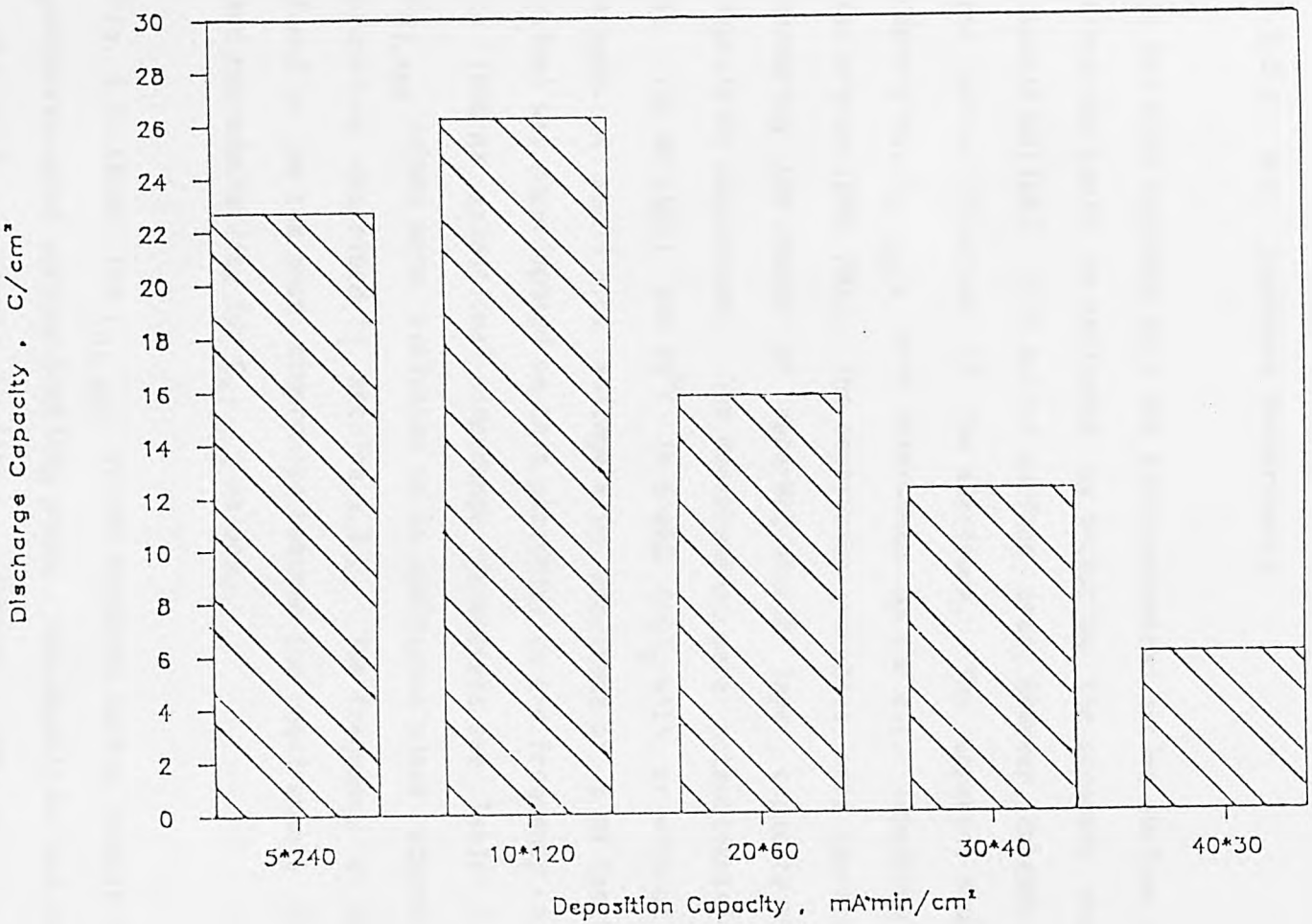

Fig. 9.10 Discharge capacities of cobalt electrodes deposited at deposition capacity 20 mA·hr/cm^2. 25^{0}C and 5N KOH.

considered that oxygen reduction may predominantly proceed in the interfacial area, where the O_2 gas bubbles are in contact with the substrate surface.

9.2.3.2. A.C. Impedance Measurements

It has been realized that the electrochemical active surface area of an electrode could be evaluated by measuring the apparent double layer capacities[188]. This active surface area, however, depends mainly on the porous structure of the electrode. The apparent double layer capacities, $C_{dl,app}$, were determined by the a.c. impedance technique (Solartron 1250 FRA). The deposition processes were characterized by measuring the change of apparent double layer capacity at various deposition conditions. The measurements were potentiostatically made at -750 mV (SCE) and 25°C in 5 wt% $CoCl_2$ with or without bubbling oxygen. A small a.c. voltage with amplitude of 5 mV (peak to peak value) was superimposed on this potential in the frequency range of 100 to 1000 Hz (additional impedance parameters see Table 2.1). The $C_{dl,app}$ values were evaluated on an admittance plane according to the procedure described in section 5.3.2. The frequency of 600 Hz was found to be the best compromise between the requirements of accuracy and reproducibility for $C_{dl,app}$ values.

Fig. 9.11 shows the $C_{dl,app}$ values measured during cobalt deposition processes under various bubbling gases. The deposition was carried out continuously in static conditions, bubbling nitrogen, and bubbling oxygen respectively. The influence of bubbling different gases on the formation of the porous deposits is clearly reflected by the change of shape in the curves. In the first hour of deposition, the solution was

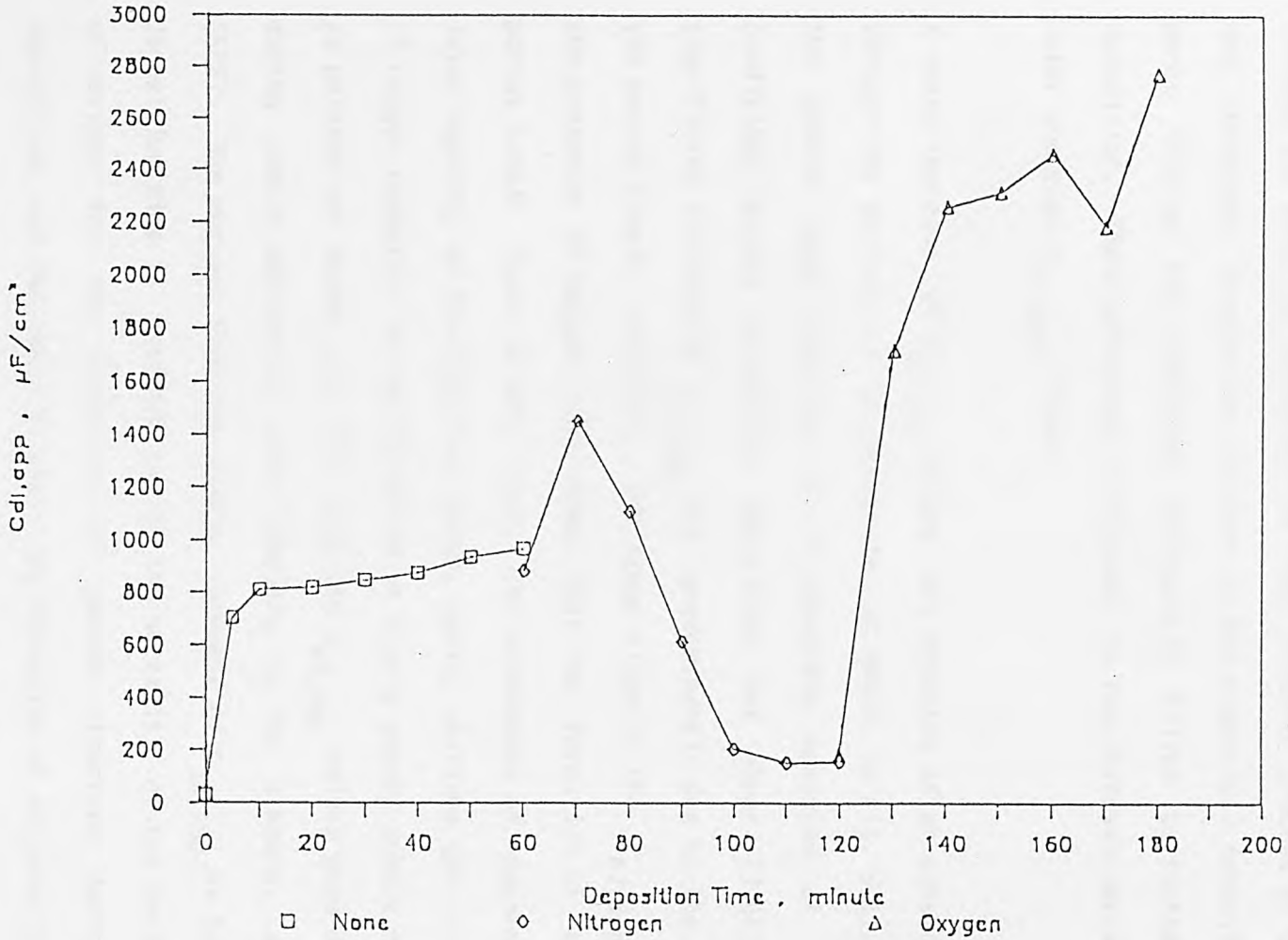

Fig. 9.11 Dependence of $C_{dl,app}$ values on the bubbling gases during cobalt deposition. 25°C and 5 wt% $CoCl_2$.

not stirred and cobalt was in fact directly deposited. The cobalt pyramids grow individually on the substrate and the cobalt deposits in this initial stage, are still porous in nature. Bubbling nitrogen through the solution increases the mass transfer process of Co^{2+} ions, and, therefore, accelerates the rate of the electrical deposition. The pores left on the substrate are quickly filled by further cobalt deposition. These processes correspond to the observed decreasing and later constant $C_{dl,app}$ values.

A sharp increase of $C_{dl,app}$ values was detected after passing O_2 gas through the surface of the substrate, as shown in Fig. 9.11. Because the double layer capacity of Ti substrate measured at the same conditions before proceeding deposition was about 23 $\mu F/cm^2$, the significant increase of $C_{dl,app}$ was predominantly due to the growth of the porous cobalt structure. The steep slope of the $C_{dl,app}$ curve in the presence of oxygen also shows that the formation of an initial porous cobalt layer is very fast. The dependence of apparent double layer capacity on the bubbling gases, again, confirms the crucial role of oxygen reduction in the formation of highly-porous cobalt electrodes as pointed out above. In Fig. 9.12 the $C_{dl,app}$ values were determined during cobalt deposition under bubbling O_2 for 3 hours, at -750 mV (SCE). The message from the stable increase of $C_{dl,app}$ as function of deposition time is twofold: one is the necessity of the participation of oxygen for the formation of porous structure during cobalt deposition; and the other is that the formation of adsorbed $Co(OH)_2$ is preferentially taking place on the surface of the porous layer formed. The latter means that the porous structures formed are less affected as the deposition reaction proceeds. Therefore, the apparent double layer capacities are stably increasing with the deposition time.

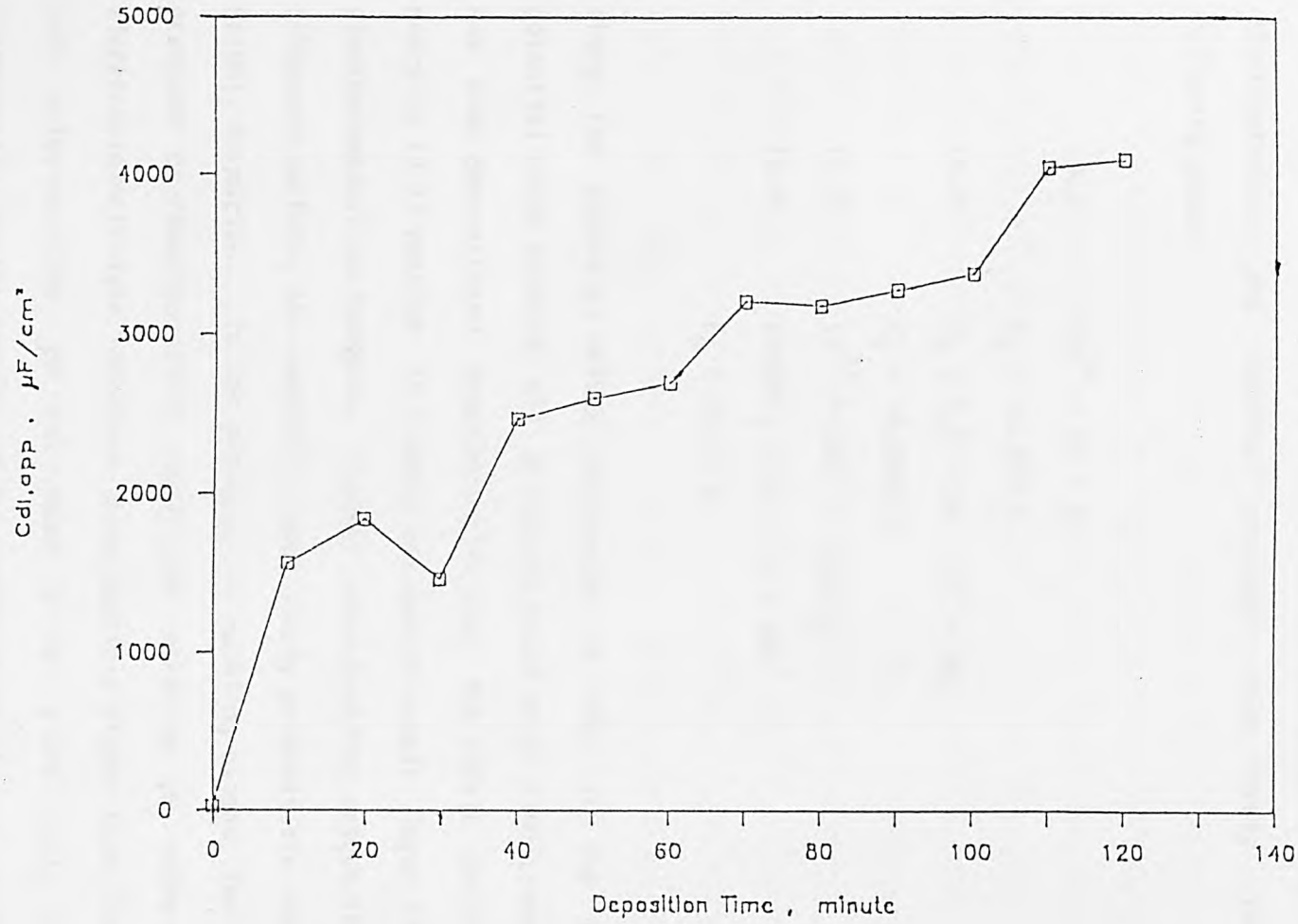

Fig. 9.12 Dependence of $C_{dl,app}$ values on the deposition time under bubbling oxygen. 25°C and 5 wt% $CoCl_2$.

9.3. Discussions of Deposition Mechanism

The deposition processes of cobalt on Ti substrates in the presence of bubbling O_2 to form highly-porous deposits are complicated. The basic electrochemical and chemical processes most likely involve the following steps:

(9.1) $Co^{2+} + 2e = Co$

$E_o = -0.277$ V

(9.2) $O_2 + H_2O + 2e = OH^- + HO_2^-$

$E_o = -0.0649$ V

(9.3) $Co^{2+} + 2OH^- = Co(OH)_2$

(9.4) $Co(OH)_2 + 2e = Co + 2OH^-$

$E_o = -0.73$ V

where the potential values correspond to NHE. In the deposition potential range studied, all processes could occur simultaneously. It has been demonstrated experimentally that the cobalt deposition via reaction (9.1) results in a dense and smooth cobalt layer with a poor electrochemical performance. However, when bubbling oxygen through the substrate surface, the deposition most likely proceeds via intermediate $Co(OH)_2$ formation. In the presence of bubbling oxygen, the OH^- ions produced by reaction (9.2) could also make the pH value near the electrode/electrolyte interface area possibly higher than that in the bulk solution (the pH was about 3 in 5 wt% $CoCl_2$ solution). Consequently, as the results of the modification of local pH value, the direct deposition of cobalt would become disadvantage.

The discharge capacity and apparent double layer capacity measurements

implied the continuous growth of the multi-porous-layers on the Ti substrates, if oxygen was bubbled through the electrode. In order to describe the growth processes of the porous cobalt layers during the deposition, a sandwich-type model was proposed. In this model the $Co(OH)_2$ formed near the substrate surface was considered to be adsorbed on the inner porous cobalt layer to form a thin outer $Co(OH)_{2(ads)}$ layer. This outer $Co(OH)_{2(ads)}$ layer and the inner porous cobalt layer yield a sandwich-type structure. The intermediate change between layers may be complicated, involving possibly the adsorption and formation of $Co(OH)^-_{ads}$, or a $Co(OH)_{ads}$ monolayer[266], further dehydration and reduction to metallic cobalt. A highly porous cobalt layer was formed due to the obvious volume shrinkage of the final products. Also, the direct deposition of cobalt from $CoCl_2$ solution can be strongly inhibited by the formation of such sandwich-type structures. Both the formation and destruction of the $Co_{porous}/Co(OH)_{2(ads)}$ structures can almost simultaneously proceed to build up a multi-porous-layer structure.

According to the model proposed, it seems that the amount of OH^- ions produced on the electrode surface by oxygen reduction is a crucial factor for building up such multi-porous-layer structure. The product of OH^- ions is mainly dependent on the interfacial contact area between the substrate and oxygen gas, and the deposition current density. At a certain rate of bubbling oxygen, the formation of OH^- ions increases with increasing deposition current density, and reaches a constant value. This is due to the limiting contact area. It is thought that, at this point, there exists an optimizing deposition current value i_{opt}, at which the production of OH^- is high enough to form an outer $Co(OH)_{2(ads)}$ layer. The direct deposition of cobalt is, therefore,

minimized. Below i_{opt} only part of the electrode surface could be covered by the intermediate $Co(OH)_{2(ads)}$ layer. Consequently, the deposition of cobalt via the intermediate formation as well as direct electrodeposition of cobalt proceeds with less interference. The pores formed could be continuously filled by the direct cobalt deposition. This was supported by the experimental observation that at low deposition current densities (e.g., 2 mA/cm^2), the porous cobalt deposits were observed only at the surface layer. In the situation where the deposition current density was far beyond i_{opt}, increasing current density simply enhances the direct electrodeposition process. The discharge capacity was, consequently, reduced. This was clearly demonstrated by the discharge characteristics of the cobalt electrodes deposited at various current densities.

The sandwich-type growth processes could be very sensitive to the ionic composition of the deposition solutions. It was found that the electrochemical activities of cobalt electrodes deposited in $CoSO_4$, $Co(NO_3)_2$ or $(CH_3COO)_2Co$ solutions, other factors being identical, were relatively poor, compared with those deposited in $CoCl_2$ solution. One of the possibilities is that Cl^- ions with higher polarizability could replace part of the H_2O molecules inside the hydration sheath of Co^{2+} cations. This could evidently affect the polarizability of cobalt cations, as Cl^- anions are more deformable[264]. At this stage the role of Cl^- anions during cobalt deposition in the presence of bubbling oxygen is still not quite clear.

CHAPTER TEN

CONCLUDING REMARKS AND SUGGESTIONS FOR FURTHER WORK

10.1. Homogeneous Catalysis Mechanism of Cobalt Oxides

This is the first time that the catalytic activity of Co^{2+} ions in alkaline solution has been comprehensively studied for the decomposition of hydrogen peroxide. Cobaltous ions, in very low concentration (e.g. 1 ppm), show very high activity for peroxide decomposition. The Co^{2+}-catalysed decomposition of H_2O_2 is a first-order reaction, and the first-order rate k_f is linearly proportional to the initial concentration of peroxide, in the cases of presence or absence of high surface area graphite.

A reaction mechanism invoking the chain reactions[152] was proposed for the homogeneous decomposition of H_2O_2 by Co^{2+} ions. It was considered that peroxide decomposition was initiated by the free radicals (e.g. $OH^{\cdot}$) formed by collisions between Co^{2+} and H_2O_2. The steady-state approximation analysis indicated that the formation of the free radicals is proportional to the initial concentration of peroxide. This, in turn, suggests that in the Co^{2+}-catalysed decomposition of H_2O_2, the rate determining step is the formation of the free radicals. However, in the case of Co_3O_4 catalysts, the Co^{3+} ions in the spinel lattice act as inhibitors in the chain reaction. Such a termination process could be responsible for the heterogeneous behaviour of cobalt oxide catalysts, during the catalytic decomposition of H_2O_2 in alkaline solutions, as reported in literature[23,222]. This characteristic of the decomposition mechanism also indicates that the homogeneous catalysis activity of cobalt oxide was localized and strongly influenced by the state of oxide distribution on the graphite support.

Further a.c. impedance studies on various Co_3O_4/graphite electrodes confirmed, electrochemically, the homogeneous catalysis role of Co^{2+} for the decomposition of intermediate HO_2^-, during oxygen reduction. It was observed that there was a close correlation between the catalytic parameter k_c evaluated from impedance measurements and the electroactivity of the electrode (e.g. i_o' values). The k_c values increased with increasing polarization, indicating that during oxygen reduction, the decomposition of the intermediate HO_2^- formed could also be initiated by the formation of the free radicals. In conclusion the intermediate HO_2^- formed during oxygen reduction, in alkaline solution, is predominantly homogeneously decomposed by dissolved Co^{2+} ions: Co_3O_4 is capable of being dissolved in concentrated alkaline solutions. However, in this case, the subsequent chain reactions could be seriously interrupted due to the termination of the free radicals on Co^{3+} ions. The observed stability of Co_3O_4/graphite electrodes in alkaline solutions was attributed to the effective circulation between the dissolved Co^{2+} ions and the lattice Co^{3+} ions.

There is a need to study the homogeneous catalysis mechanism of cobalt oxide catalysts in various cobaltite oxides/graphite systems. Further studies in this area will result in a deeper understanding of the catalytic role of oxide catalysts in oxygen electrochemistry, and stimulate the research and development of efficient homogeneous oxide catalysts. It is recommended that e.s.r. spectroscopy should be used to obtain the direct evidence of the participation of free radicals in the peroxide decomposition by cobalt oxide catalysts and Co^{2+} ions in alkaline solution.

10.2. A.C. Impedance Studies of Oxygen Reduction on Air Electrodes

The a.c. impedance technique was employed for the studies of the kinetics and mechanism of oxygen reduction on Teflon-bonded graphite and Co_3O_4/graphite electrodes, in alkaline solutions. The impedance responses in such complex systems can be, to some extent, theoretically analysed by the adsorption equivalent circuit method (for electrode reaction coupled with an adsorption process) and the analytical method (for electrode reaction coupled with a catalytic reaction) in the cases of low polarization potentials. The advantage of impedance technique is that both the kinetic parameters of the reactions concerned and the electroactivity of the electrodes can be evaluated from faradaic impedance analysis. It should, however, be pointed out that the detail of the porous structure of the electrodes cannot be obtained on the basis of the methods used.

The kinetic study of oxygen reduction on pyrographite has shown that the rate determining step is the first-electron adsorption process of oxygen[58,60]. It is, therefore, appreciable to use the adsorption equivalent circuit for the impedance analyses on Teflon-bonded graphite electrodes. The observed impedance responses show a semicircle at high frequencies and a diffusion tail at low frequencies. However, it was found that the observed semicircle is caused by the adsorption and desorption interfacial reactions, as the evaluated adsorption resistance R_a is much higher than the charge transfer resistance R_{ct}. This fact also confirms that the kinetics of O_2 reduction in this case are determined by the surface adsorption processes, which are probably diffusion controlled. The introduced characteristic exchange current density i_o' value, calculated from R_{ct} was 2.02 mA/cm^2, which is in

good agreement with that obtained on the pyrolytic graphite[58]. The evidence obtained from a.c. impedance measurements verifies again that the oxygen reduction on Teflon-bonded graphite electrodes proceeds predominantly by the two-electron pathway.

It has been emphasized that the promoting effects of Co_3O_4 catalysts incorporated into graphite electrodes are mainly catalytic, the decomposing intermediate HO_2^- being formed. This will result in the recycling of some of the oxygen and also prevent interaction between the HO_2^- ions and the active graphite particles. It has been demonstrated that the analytical method can be used for impedance analysis in oxygen reduction on Co_3O_4/graphite electrodes. The measurements were carried out at 850 mV (DHE) in order to avoid the interference of other interfacial reactions. Significantly, the higher the catalytic activity of the cobalt oxides, the higher the i_o' values, showing that the electrochemical activity of an air electrode is largely determined by the activity of the H_2O_2-decomposing catalysts. It was also considered that the catalytic parameter k_c evaluated, is an accumulated parameter of the homogeneous catalytic activity of the dissolved Co^{2+} inside the pores of the electrode during oxygen reduction. The increase of i_o' values after incorporation of Co_3O_4 catalysts is most likely due to the increase in the recycling efficiency of the oxygen molecules inside the pores.

The factors determining the stability of Co_3O_4/graphite electrodes were found to be the attack of intermediate HO_2^- on the active sites inside pores, at the initial stage of polarization (e.g. about 200 hours), in alkaline solution. Cobalt oxide catalysts incorporated into graphite electrodes decompose the HO_2^- formed, and, thus, improve both the

activity and the stability of the electrodes. It is suggested that stability of air electrodes can be conveniently investigated by measuring the relative change of the $C_{dl,app}$ values. The physical significance of $C_{dl,app}$ values obtained on such complex porous systems is not quite understood. Further work should be directed to the studies on the relationship between the $C_{dl,app}$ values, the catalyst loading, the BET and the active surface area of the catalyst layer, and the porous structure parameters.

It was found by experimentation that the impedance responses estimated from the theoretical analysis methods, deviated significantly from the observed one of Teflon-bonded electrodes, at high polarization potentials. This could indicate the limitation of the use of a.c. techniques on porous electrodes. If the polarization is increased, the reaction can be localized to the interfacial area between gas and electrolyte. In this case, particularly at high frequencies, the penetration depth becomes so small that the signal can not reach the three-phase reaction zone. However, using Teflon-bonded thin-film electrodes, it is possible to overcome this barrier. It is hopeful that a breakthrough in this important area could make the a.c. impedance measurements powerful technique in studying electrochemical processes in porous system, in the future. It is also suggested that further work should be carried out to establish more realistic porous impedance models. The combination of the transmission line method[178], the random network model[267] and the probability model[268] is worth considering.

10.3. Mechanism of Oxygen Reduction on Cobalt Oxide Electrodes

Steady state polarization and a.c. impedance methods were used for the investigation of the reaction mechanism of oxygen reduction on Teflon-bonded high surface area Co_3O_4 (HSAC) and 3.1 at% Li-doped Co_3O_4 (LDC) electrodes. Taking into account the porous structure of the electrodes and the physical properties of cobalt oxides, an empirical impedance model was proposed and developed. In this model, it was considered that the O_2 reduction takes place mainly on the oxide-covered surface layer, while the porous structure of the electrode has a more profound effect on diffusion processes inside the pores.

Based on results obtained from steady state polarizations and a.c. impedance measurements, it seems that oxygen reduction on cobalt oxides, prepared by low temperature decomposition, does not simply go through the formation of the HO_2^- intermediate[68], neither does it directly take place via a four-electron process[63]. However, the accuracy of the characteristic exchange current density i_o', calculated from R_{ct}, is doubtful because the double layer capacitance of true electroactive component in a porous cobalt oxide electrode is, usually, unknown. On complex impedance plots, at low polarization potentials, only one depressed semicircle was observed in the high frequency region, this was primarily caused by the charge transfer process through the surface oxide layer, but as polarization increased the second semicircle appeared in the low frequency region. This shows that the rate of the formation of the HO_2^- intermediate sped up with increasing polarization, particularly on LDC. It was explained that on cobalt oxide electrodes, the oxygen molecules could be chemisorbed

'side-on' (the main requirement for direct four-electron process[36]), and 'end-on' (the splitting process of which leads to the formation of HO_2^- as well as OH^-[269]). However, the kinetics of both chemisorption processes depend to a greater extent on the surface states of the oxides. In the case of cobalt oxides, it seems that the 'end-on' adsorption of oxygen is more important[67].

10.4. Reactive Deposition Method

10.4.1. Potential Applications

10.4.1.1. Regenerative Air Electrodes

High surface area Co_3O_4 catalyst (HSAC), prepared by oxidizing and precipitating $HCoO_2^-$ ions in alkaline solution, was found to be highly active for both H_2O_2 decomposition and oxygen reduction. TEM analysis illustrated the peculiar needle-shaped crystallographic structure formed, which contributes, mainly, to the high activity of HSAC catalysts. When HSAC was coprecipitated with graphite to form a composite catalyst (electrode CG), a polarization potential of about 825 mV (DHE) at 200 mA/cm^2 under air was realised. Moreover, the polarization performance of the electrode was quite stable at 100 mA/cm^2 in 5N KOH.

The high performance of HSAC shows an encouraging prospect of substitution for the expensive platinum catalysts, widely used in metal-air batteries and fuel cells, with cheaper and equally active ones. A major problem that may be encountered in utilizing HSAC catalysts in air cathodes is the gradual loss of the cobalt oxide

catalysts over long periods of time, under various operation conditions. The preliminary studies on in situ deposition of cobalt catalysts on graphite supports showed that, in principle, it is feasible to regenerate the air electrodes. Also, because there are no thermal treatments and drying processes involved in the deposition method, the oxide catalysts can be uniformly distributed inside the porous supports.

It is suggested that further work should be carried out to research the deposition processes of cobalt catalysts inside the pores, and to optimize the electrochemical parameters for the deposition and oxidation conditions. Long-term testing of graphite air electrodes using HSAC catalysts in alkaline solution, and in situ regeneration of such air cathodes used in Al-air alkaline cells, are also suggested. It is expected that the cost of metal-air batteries and fuel cells could be substantially reduced as a result of using cheaper and easily available cobalt oxide catalysts.

10.4.1.2. Nickel-Cobalt Storage Cell

The studies of Tang[90] and Yon Hin[114] on porous cobalt electrodes in alkaline solutions have shown that the cobalt electrode can be anodically discharged in electrode systems with high specific capacity (theoretical 0.909 Ah/g). However, it was found[90] that the grains of the porous electrodes prepared by the powder metallurgical method (750^{o}C, hydrogen, 25% $(NH_4)_2CO_3$ added) were about 10 to 20 microns, and the distribution of pores with large openings is poor. Using the novel reactive deposition method, it is feasible to produce highly porous cobalt electrodes with uniform pore distribution and fine grains (about

1 micron). The cobalt deposited electrodes have showed very high electrical performance. The requirement for the batteries with higher energy density is increasing in fields like portable communication systems, portable computers and electrical vehicles. Nickel-cobalt cells with a higher energy density (which was projected to be about 60 Wh/Kg[90]) show promise in the replacement of part of the conventional types of nickel-cadmiun cells (energy density is about 20 to 30 Wh/Kg[270]). However, it is necessary to industrialize the reactive deposition methods in order to make such nickel-cobalt cells commercially competitive.

10.4.1.3. Silver-Cobalt Storage Cell

The promising physical and electrical characteristics of the porous cobalt electrodes, prepared by the deposition method, open up very exciting prospects in the battery industry. The deposited cobalt electrodes could be combined with silver electrodes to produce a high performance silver-cobalt storage cell. The total current-producing reaction in the cell, in general, could be described by the following equation:

$$(10.1) \qquad Co + AgO + H_2O = Co(OH)_2 + Ag$$

where the theoretical cell voltage is 1.318 V and the theoretical energy density is 386 Wh/Kg. Based on the structural parameters for a D-size nickel-cadmium (NiCd) cell (RS, 4.0 Ah capacity)[90], the specific capacity and energy density for silver-cobalt cells were estimated. The nickel positive electrode and cadmium negative electrode were supplanted by a silver electrode and a cobalt electrode

respectively (based on 80% utilization). The results are listed in Table 10.1.

As shown in the table an energy density as high as 120 Wh/Kg was projected for the silver-cobalt cell. Unlike zinc in silver-zinc storage cells, the cobalt electrode of the silver-cobalt cells is quite stable, and the growth of zinc dendrites as well as the displacement of the active materials, with cycling, can largely be eliminated. It seems that the main cause limiting the cycle and service life may be the deterioration of the separator, due to the oxidation of the organic material by the dissolved silver ions[270]. The relatively high costs of such alkaline silver-cobalt storage cells can, however, be compensated by their high performance and long cycle and service life, especially for some specific applications.

10.4.2. Further Work

As a suggestion for further work, the deposition kinetics and mechanism should be fully investigated under various deposition conditions, such as the contact area between the substrate and the oxygen gas bubbled, the ionic composition of the electrolyte, the deposition current density and the electrochemical properties of the deposited metal ions. Further studies can also be carried out to apply this reactive deposition method to other metals like iron and cadmium. It is suggested that the interfacial reactions during deposition in the presence of bubbling oxygen can be studied by in situ electrochemical techniques such as infrared spectroscopy, and the surface composition and surface configuration can be examined by ESCA techniques. Further work in these areas will be very rewarding.

Table 10.1

Projected energy density of silver-cobalt cell.

Component	Weight of Component, g	
	Nickel-Cadmium	Silver-Cobalt
Casing	21.9	21.9
Top	12.4	12.4
Separator + Electrolyte	6.4	6.4
Spacer	0.7	0.7
Leads	0.7	0.7
Positive Material	44.3	25.4
Negative Material	42.8	10.3
Total Weight	129.2	77.8
Cell Voltage, V (at C/10)	1.15	1.16
Specific Capacity (Amp·hr/Kg)	31.0	102.3
Energy Density (Watt·hr/Kg)	35.7	118.7

Appendix A

Calculation of the impedance for a simple electron transfer and planar diffusion reaction[177].

Consider a simple electrode reaction with both activation and diffusion controls

$$(A.1) \qquad O + ne \underset{k_2}{\overset{k_1}{\rightleftharpoons}} R$$

where k_1 and k_2 are the rate constants of reduction and oxidation respectively. An impedance of the electrode system can be frequently determined by imposing an a.c. current and measuring the potential response. The concentration perturbations of reactant and product, c^2_o and c^2_r, obey the Fick's second diffusion law.

$$(A.2) \qquad \frac{\partial c^2_o}{\partial t} = D_o \frac{\partial^2 c^2_o}{\partial x^2}$$

$$(A.3) \qquad \frac{\partial c^2_r}{\partial t} = D_r \frac{\partial^2 c^2_r}{\partial x^2}$$

The boundary conditions can thus be established under conditions where the electrochemical system is activated by a sinusoidal current $i=i_m \sin\omega t$ with a small amplitude.

$$(A.4) \qquad D\left(\frac{\partial c^2(x,t)}{\partial x}\right)_{x=0} = \pm \frac{i}{nF}$$

$$(A.5) \qquad c^2(x=\infty, t) = 0$$

where in equation (A.4), '+' is applicable for reactant and '-' for

product.

The impedance is usually measured after the system is allowed to reach a steady state. Therefore, the pertubation of concentration is also sinusoidal with the same frequency of the applied signal.

$$c^{2}_{o}(x,t) = Ae^{ux + j\omega t} \qquad (A.6)$$

Substituting equation (A.6) into differential equations (A.2) and (A.4), it is obtained

$$j\omega = D_o u^2 \qquad (A.7)$$

and

$$D_o uA = i_m/nF \qquad (A.8)$$

With the boundary condition (A.5), combination of equations (A.7) and (A.8) results in

$$u = -(j\omega/D_o)^{\frac{1}{2}} = -(\omega/2D_o)^{\frac{1}{2}}(1 + j) \qquad (A.9)$$

$$A = - \frac{i_m}{2F(2D_o\omega)^{\frac{1}{2}}} (1 - j) \qquad (A.10)$$

From equation (A.6) the pertubation of concentration of reactant O can thus be expressed as

$$c^{2}_{o}(x,t) = - \frac{i_m}{nF(D_o\omega)^{\frac{1}{2}}} \exp\left[- \frac{x}{(2D_o/\omega)^{\frac{1}{2}}} + j\left(\omega t - \frac{x}{(2D_o/\omega)^{\frac{1}{2}}} - \frac{\pi}{4}\right)\right] \qquad (A.11)$$

Similarly

$$(A.12) \qquad c^2_r(x,t) = + \frac{i_m}{nF(D_r\omega)^{\frac{1}{2}}} \exp\left[- \frac{x}{(2D_r/\omega)^{\frac{1}{2}}} + j\left(\omega t - \frac{x}{(2D_r/\omega)^{\frac{1}{2}}} - \frac{\pi}{4}\right)\right]$$

The magnitudes of concentration perturbations are exponentially declined with the increase of distance x as shown in equations (A.11) and (A.12). At x=0, the perturbation at the electrode surface is directly written as in following form.

$$(A.13) \qquad c^2_s = \pm \frac{i_m}{nF(D\omega)^{\frac{1}{2}}} \exp\left[j\left(\omega t - \frac{\pi}{4}\right)\right]$$

$$= \pm \frac{i_m}{nF(D\omega)^{\frac{1}{2}}} \exp(1 - j)$$

which is the fundamental equation for the calculation of faradaic impedance of an electrochemical system and the meaning of symble '±' is the same as defined before.

In order to derive the faradaic impedance, it is necessary to come back to the Butler-Volmer equation which is expressed as

$$(A.14) \qquad I = I_1 - I_2$$

$$= nF\left[k_1 c_{so} \exp\left(- \frac{\alpha nF}{RT} E\right) - k_2 c_{sr} \exp\left(- \frac{\beta nF}{RT} E\right)\right]$$

Where c_{so} and c_{sr} are the surface concentrations of species O and R respectively. Differentiating above equation and considering only the sinusoidal components, it is obtained

$$(A.15)\qquad \frac{di}{dt} = \frac{i_1}{c_{so}} \cdot \frac{dc^2_{so}}{dt} - \frac{i_2}{c_{sr}} \cdot \frac{dc^2_{sr}}{dt} - \frac{nF}{RT}(\alpha i_1+\beta i_2)\frac{dE^2}{dt}$$

Again this differentiation may be simplified considerably becouse all the perturbation parameters, i.e. i, E^2, c^2_{so} and c^2_{sr} have the same sinusoidal dependence on the angular frequency and the differentiations are in fact equal to themself multiplied by a factor $j\omega$. Consequently, the solution of equation (A.15) is

$$(A.16)\qquad i = \frac{i_1}{c_{so}} c^2_{so} - \frac{i_2}{c_{sr}} c^2_{sr} - \frac{nF}{RT}(\alpha i_1+\beta i_2)E^2$$

According to the definition of faradaic impedance, $Z=-E^2/i$, one have the faradaic impedance at quasi reversible potential

$$(A.17)\qquad Z_f = Z_{ct} + Z_o + Z_r$$

where
$$(A.18)\qquad Z_{ct} = RT/nF*1/(\alpha i_1+\beta i_2) = R_{ct}$$

$$(A.19)\qquad Z_o = \frac{RT}{nFc_{so}} \cdot \frac{i_1}{\alpha i_1+\beta i_2} \cdot \frac{c^2_{so}}{i}$$

$$(A.20)\qquad Z_r = \frac{RT}{nFc_{sr}} \cdot \frac{i_2}{\alpha i_1+\beta i_2} \cdot \frac{c^2_{sr}}{i}$$

Therefore equations (A.17) to (A.20) are general expressions of the faradaic impedance for electrode reaction (A.1). By application of equation (A.13), the faradaic impedances of reactant and product due to diffusion are equal to

$$(A.21)\qquad Z_o = \frac{g}{c_{so}(2D_o\omega)^{\frac{1}{2}}} \cdot \frac{i_1}{\alpha i_1+\beta i_2}(1 - j)$$

$$= R_{wo} - j\ 1/\omega C_{wo}$$

$$(A.22) \qquad Z_r = \frac{g}{c_{sr}(2D_r\omega)^{\frac{1}{2}}} \cdot \frac{i_2}{\alpha i_1 + \beta i_2}(1 - j)$$

$$= R_{wr} - j\, 1/\omega C_{wr}$$

where $g = RT/n^2F^2$. R_{wi} and C_{wi} represent as the resistance and capacitance of the Warburg impedance for species i alternatively. For reversible reaction where $i_1 = i_2 = i$ and $\alpha + \beta = 1$, the corresponding relations are directly obtained.

$$(A.23) \qquad Z_{ct} = R_{ct} = RT/nF * 1/i_o$$

$$(A.24) \qquad Z_o = \frac{g}{c_{so}(2D_o\omega)^{\frac{1}{2}}}(1 - j) = R_{wo} - j\,\frac{1}{\omega C_{wo}}$$

$$(A.25) \qquad Z_r = \frac{g}{c_{sr}(2D_r\omega)^{\frac{1}{2}}}(1 - j) = R_{wr} - j\,\frac{1}{\omega C_{wr}}$$

where $$(A.26) \qquad R_{wi} = \frac{1}{\omega C_{wi}} = \frac{g}{c_{si}(2D_i\omega)^{\frac{1}{2}}}$$

And for the irreversible reaction where $i_2 = 0$ and $i = i_1$, it follows that

$$(A.27) \qquad Z_{ct} = R_{ct} = RT/nF * 1/\alpha i$$

$$(A.28) \qquad Z_o = \frac{g}{c_{so}(2D_o\omega)^{\frac{1}{2}}} \cdot \frac{1}{\alpha}(1 - j)$$

$$(A.29) \qquad Z_r = 0$$

It is important to mention that both diffusion resistance and capacitance, C_{wi} and R_{wi}, are dependent on frequency, which is distinct from the normal concept of capacitance and resistance. Therefore it is more convenient to introduce a Warburg coeffient W which is defined as

$$(A.30) \qquad W = W_o + W_r$$

where W_i is the Warburg diffusion coeffient of species i expressed as

$$W_o = g/c_{so}(2D_o)^{\frac{1}{2}} \qquad (A.31)$$

and

$$W_r = g/c_{sr}(2D_r)^{\frac{1}{2}} \qquad (A.32)$$

Finally, according to equation (A.17) the faradaic impedance for a simple electrode reaction coupled with both diffusion process and charge transfer reaction can be simply expressed by

$$Z_f = R_{ct} + W\omega^{-\frac{1}{2}}(1 - j) \qquad (A.33)$$

Appendix B

The proportional dependence of first-order rate constant k_f on the initial concentration of peroxide, which has been confirmed in Chapter 4 suggests that the homogeneous decomposition reaction of H_2O_2 in the presence of Co^{2+} ions cannot be described by the first-order reaction rate law. In order to establish the actual order of the reaction, the initial reaction rates were determined at 30^oC but using different concentrations of peroxide. From the slope of log-log plot of initial rate k_i vs initial concentration of H_2O_2, the order of the decomposition reaction was obtained. Fig. B.1 shows the logarithmic plots of peroxide decomposition in the presence and absence of graphite. In the absence of graphite, the order of the reaction was found to be 1.2. When high surface area graphite was added, the reaction order was found to be slightly higher, about 1.3. By considering the reaction order to be 1.2, the kinetics of H_2O_2 decomposition could be described by the 1.2-order reaction rate law.

$$dx/dt = k\,(a - x)^{1.2} \qquad \text{(B.1)}$$

where k is the 1.2-order rate constant. Using the initial conditions, the integration yields

$$5\left(\frac{1}{(a - x)^{0.2}} - \frac{1}{a^{0.2}}\right) = k\,t \qquad \text{(B.2)}$$

where x can be calculated by the evolved O_2 volume measured at time t by

$$x = V * a / V_{max} \qquad \text{(B.3)}$$

Fig. B.2 shows the typical 1.2-order reaction rate plots corresponding to the peroxide decomposition reactions in Fig. 4.3. In Fig. B.3 the rate constants were determined at various initial concentration of peroxide in the presence of 1 ppm Co^{2+} ions. In both cases where graphite was present or absent in the reaction media, the value of the reaction rate was virtually independent of the initial concentration of peroxide. This confirmed the existence of the fractional order reaction kinetics for homogeneous decomposition of H_2O_2 in the presence of Co^{2+} ions in alkaline solution.

The Arrhenius plots for peroxide decomposition was also obtained in the temperature range of 20 to $50^{o}C$, using 1.2-order rate constants as shown in Fig. B.4. The apparent activation energy E_a was calculated from the slopes by the Arrhenius equation. The results are given in Table B.1.

Table B.1

Activation energy of the 1.2-order peroxide decomposition reaction in the presence of 1 ppm Co^{2+} ions.

50ml 5N KOH and 5ml 1.15M H_2O_2

	E_a, KJ/mol	A
In absence of graphite	73.35	$5.2*10^9$
In presence of graphite, 50mg	68.77	$1.6*10^9$

During the peroxide decomposition by Co^{2+} ions, particularly in the case of cobalt oxide catalysts, the Co^{2+} ions are first dissolved from cobalt oxides in alkaline media, and then the Co^{2+} ions in solution are themselves oxidized to Co^{3+} ions. Co^{3+} ions are most probably located at the surface lattice sites of the oxides. The Co^{3+} ions in the lattice sites could also be reduced to Co^{2+} due to the termination reaction of free radicals. However, the rate of the redox reaction between the Co^{2+} and Co^{3+} could be relatively slow as the slow dehydration and diffusion processes are involved in the electron transfer processes. It should be noted that such electron transfer process between the Co^{2+} in the liquid state and the Co^{3+} in the lattice solid state is a heterogeneous reaction. Consequently, the concentration of Co^{2+} ions in solution could not be constant during the peroxide decomposition. This implies that the peroxide reaction could be controlled by more than one step. It seems that the fractional reaction order shows the multistep mechanisms for the homogeneous decomposition of H_2O_2 in the presence of cobalt oxide catalysts. One possible explanation could be the participation of the free radicals in the Co^{2+}-catalysed decomposition of H_2O_2. In the OsO_4-catalysed reaction, the formation of superoxide radicals was reported to be 0.6-order of peroxide concentration[147].

In the decomposition of peroxide on various MnO_2 catalysts, the order of the reaction was observed to vary between 1 and 1.5 by Kanungo et al[158]. However, no consideration was given to the participation of transition metal ions in alkaline solutions and this led to the erroneous conclusion in the mechanism of hydrogen peroxide decomposition reaction. Therefore, it is unjustified to simply use the first-order reaction law to establish and evaluate the reaction

mechanism and to compare the kinetic parameters. In conclusion, the peroxide decomposition in the presence of cobalt oxides is a combined process of the homogeneous reaction of dissolved Co^{2+} ions and the heterogeneous reactions involving the redox reaction between Co^{2+} and Co^{3+} ions. Detailed elucidation of such homogeneous-heterogeneous reaction mechanism for the H_2O_2 decomposition reaction would need more experimental work. One possible solution is to use direct electron spin resonance technique to determine the reaction order of the formation of free radicals for peroxide reaction in the presence of cobalt oxides.

List of Figures

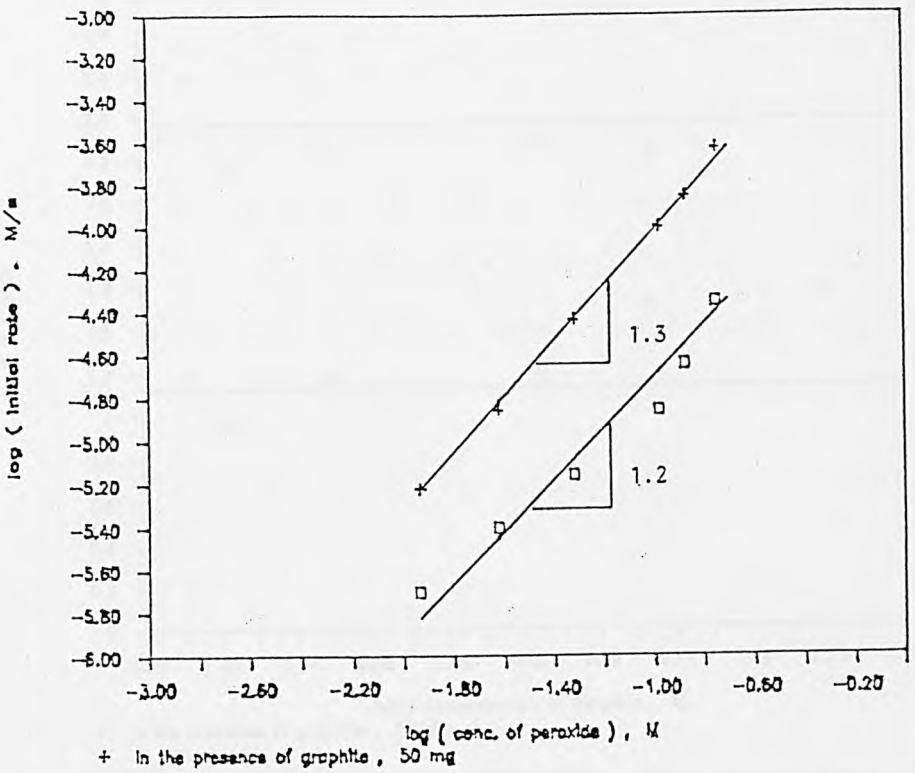
log (initial rate) , M/s
-3.00
-3.20
-3.40
-3.60
-3.80
-4.00
-4.20
-4.40
-4.60
-4.80
-5.00
-5.20
-5.40
-5.60
-5.80
-6.00
1.3
1.2
-3.00
-2.60
-2.20
-1.80
-1.40
-1.00
-0.60
-0.20
log (conc. of peroxide) , M
+ In the presence of graphite , 50 mg

Fig. B.1

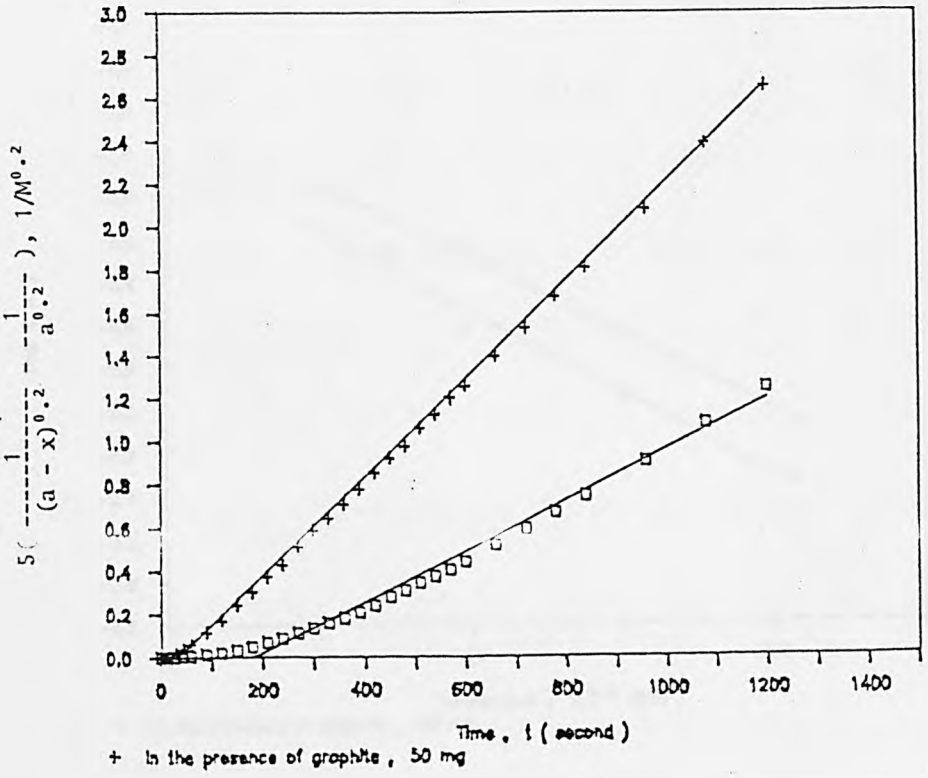
5(1/(a - x)^0.2 - 1/a^0.2), 1/M^0.2
3.0
2.8
2.6
2.4
2.2
2.0
1.8
1.6
1.4
1.2
1.0
0.8
0.6
0.4
0.2
0.0
0
200
400
600
800
1000
1200
1400
Time , t (second)
+ In the presence of graphite , 50 mg

Fig. B.2

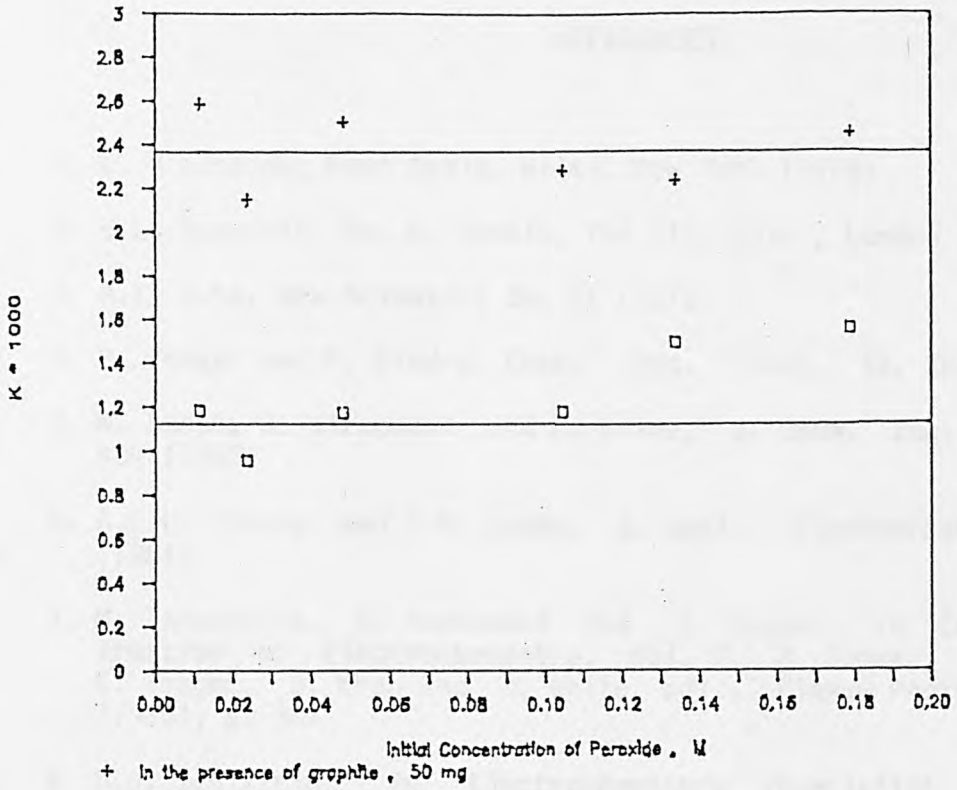
K * 1000
3
2.8
2.6
2.4
2.2
2
1.8
1.6
1.4
1.2
1
0.8
0.6
0.4
0.2
0
0.00
0.02
0.04
0.06
0.08
0.10
0.12
0.14
0.16
0.18
0.20
Initial Concentration of Peroxide , M
+ In the presence of graphite , 50 mg

Fig. B.3

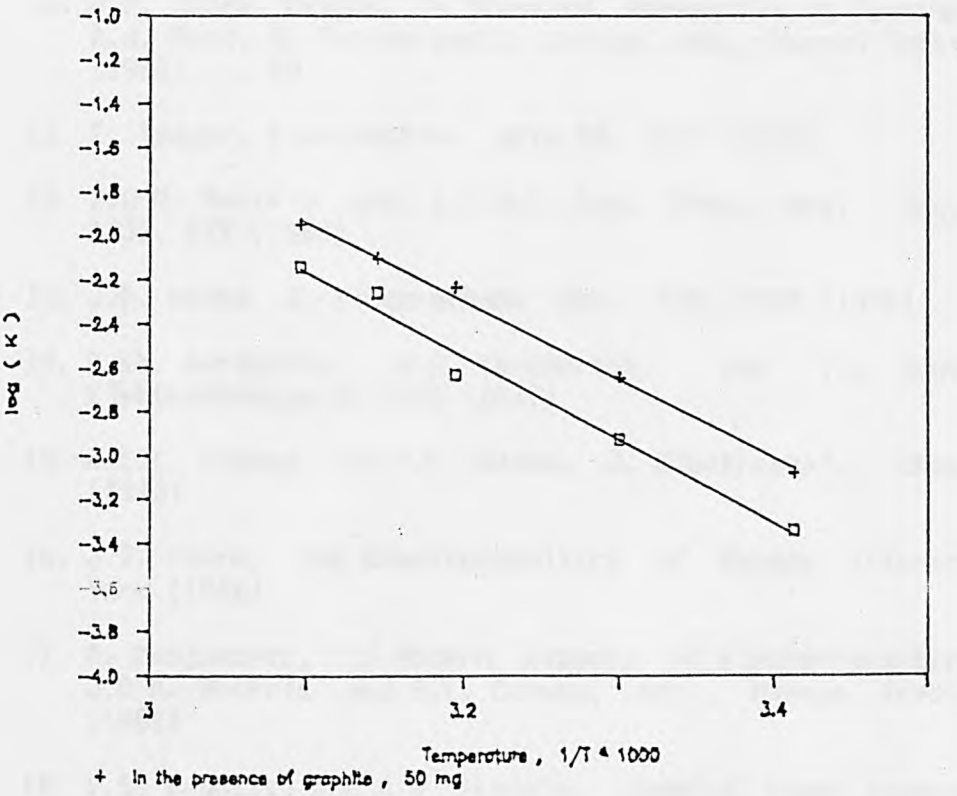
log (K)
-1.0
-1.2
-1.4
-1.6
-1.8
-2.0
-2.2
-2.4
-2.6
-2.8
-3.0
-3.2
-3.4
-3.6
-3.8
-4.0
3
3.2
3.4
Temperature , 1/T * 1000
+ In the presence of graphite , 50 mg

Fig. B.4

REFERENCES

1. W. Vielstich, **Fuel Cells**, Wiley, New York (1970)

2. R.L. Quarshie, **Ph. D. Thesis**, The City Univ., London (1985)

3. A.T. Kuhn, **New Scientist 36**, 21 (1971)

4. E. Yeager and P. Bindra, **Chem. -Ing. -Tech. 52**, 384 (1980)

5. M. Sudoh, H. Kitaguchi and K. Koide, **J. Chem. Eng. Japan 18**, 409 (1985)

6. A.C.C. Tseung and S.M. Jasem, **J. Appl. Electrochem. 11**, 209 (1981)

7. M. Tarasevich, A. Sadkowski and E. Yeager, in **Comprehensive Treatise of Electrochemistry**, Vol. 7, B. Conway, J. Bockris, E. Yeager, S. Khan and R. White, eds., Plenum Press, New York (1983), p. 301

8. D.J. Schiffrin, in **Electrochemistry (Specialist Periodical Reports)**, Vol. 8, D. Pletcher, ed., The Royal Society of Chemistry, London (1983), p. 126

9. J.P. Hoare, in **The Encyclopedia of Electrochemistry of the Elements**, Vol. 2, A.J. Bard, ed., Marcel Dekker, New York (1974), p. 220

10. J.P. Hoare, **Oxygen**, in **Standard Potentials in Aqueous Solutions**, A.J. Bard, R. Parson and J. Jordan, eds., Marcel Dekker, New York (1985), p. 49

11. E. Yeager, **Electrochim. Acta 29**, 1527 (1984)

12. J.O'M. Bockris and A.K.M.S. Hug, **Proc. Roy. Soc. (London) A237**, 277 (1956)

13. J.P. Hoare, **J. Electrochem. Soc. 126**, 1502 (1979)

14. R.Kh. Burshtein, M.R. Tarasevich, and V.A. Bogdsanovskaya, **Elektrokhimiya 8**, 1542 (1972)

15. A.C.C. Tseung and H.L. Bevan, **J. Electroanal. Chem. 45**, 429 (1973)

16. J.P. Hoare, **The Electrochemistry of Oxygen**, Interscience, New York (1968)

17. A. Damjanovic, in **Modern Aspects of Electrochemistry**, Vol. 5, J.O'M. Bockris and B.E. Conway, eds., Plenum Press, New York (1969)

18. V.S. Bagotzky and A.M. Skundin, **Chemical Power Sources**, Academic Press, London (1980)

19. S.A. Elbeik and A.C.C. Tseung, in **Advances in Battery Materials and Processes**, J. McBreen, R.S. Yeo, D.T. Chin and A.C.C. Tseung, eds., The Electrochem. Soc., (1984), p. 240

20. G.V. Shteinberg, A.V. Dribinsky, I.A. Kukushkina, L.N. Mokorousov and V.S. Bagotzky, **J. Electroanal. Chem. 180**, 619 (1984)

21. W.G. Berl, **Trans. Electrochem. Soc. 83**, 253 (1943)

22. P. Fischer and J. Heitbaum, **J. Electroanal. Chem. 112**, R31 (1980)

23. J.R. Goldstein, **Ph. D. Thesis**, The City Univ., London (1970)

24. Y.H. Chou, A.C.C. Tseung and P. Rasiyah, **Extended Abstracts**, Vol. **81-2**, The Electrochem. Soc., Colorado (1981), p. 276

25. T. Kenjo and K. Kawatsu, **Electrochim. Acta 30**, 229 (1985)

26. R. Manoharan and A.K. Shukla, **Electrochim. Acta 30**, 205 (1985)

27. R.J. Taylor and A.A. Humffray, **J. Electroanal. Chem. 64**, 85 (1975)

28. Lj.M. Vracar, D.B. Sepa and A. Damjanovic, **J. Electrochem. Soc. 133**, 1835 (1986)

29. K. Juttner, **Electrochim. Acta 29**, 1597 (1984)

30. J.C. Huang, R.K. Sen and E. Yeager, **J. Electrochem. Soc. 126**, 736 (1979)

31. J.P. Hoare, **J. Electrochem. Soc. 112**, 849 (1965)

32. V.S. Bagotskii and M.R. Tarasevich, **J. Electroanal. Chem. 101**, 1 (1979)

33. D.B. Sepa, M.V. Vojnovic and A. Damjanovic, **Electrochim. Acta 25**, 1491 (1980)

34. D.B. Sepa, M.V. Vojnovic and A. Damjanovic, **Electrochim. Acta 26**, 781 (1980)

35. H.L. Bevan and A.C.C. Tseung, **Electrochim. Acta 19**, 201 (1974)

36. A.C.C. Tseung, **J. Electrochem. Soc. 125**, 1662 (1978)

37. I. Iliev, S. Gamburzev and A. Kaisheva, **J. Power Sources 17**, 345 (1986)

38. E. Yeager, D. Scherson and B. Simic-Glauaski, in **Proc. Electrochem. Soc.**, Vol. **84-12** (Chem. Phys. Electrocatal.), (1984), p. 247

39. M.R. Tarasevich and K.A. Radyushkina, **Russ. Chem. Rev. 49**, 718 (1980)

40. J. Zagal, P. Bindra and E. Yeager, **J. Electrochem. Soc. 127**, 1506 (1980)

41. J.P. Collman, P. Denisevich, Y. Konai, M. Marrocco, C. Koval and F.C. Anson, **J. Am. Chem. Soc. 102**, 6027 (1980)

42. M.R. Tarasevich, K.A. Radyushkina and S.I. Andrusyova, **Bioelectrochemistry and Bioenergetics 4**, 18 (1977)

43. H.Y. Liu, I. Abdalmuhdi, C.K. Chang and F.C. Anson, **J. Phys. Chem. 89**, 665 (1985)

44. K. Wiesener and G. Grunig, **J. Electroanal. Chem. 180**, 639 (1984)

45. T. Hirai, J.I. Yamaki and A. Yamaji, **J. Appl. Electrochem. 15**, 77 (1985)

46. H.P. Dhar, R. Darby, V.Y. Young and R.E. White, **Electrochim. Acta 30**, 423 (1985)

47. D.A. Scherson, S.L. Gupta, C. Fierro, E.B. Yeager, M.E. Kordesch, J. Eldridge and R.W. Hoffman, **J. Electrochem. Soc. 28**, 1205 (1983)

48. A. Karasheva, S. Gamburtzev and I. Iliev, **Elektrokhimiya 18**, 127 (1982)

49. A.Van Der Putten, A. Elzing, W. Visscher and E. Barendrecht, **J. Electroanal. Chem. 205**, 233 (1986)

50. J. Kelly, D.B. Hibbert and A.C.C. Tseung, **J. Mater. Sci. 13**, 1053 (1978)

51. D.B. Meadowcroft, **Nature 226**, 847 (1970)

52. M.R. Tarasevich and B.N. Efremov, in **Electrodes of Conductive Metallic Oxides**, Vol. **11A**, S. Trasatti, ed., Elsevier, Amsterdam (1980), p. 221

53. P.F. Carcia, R.D. Shannon, P.E. Bierstedt and R.B. Flippen, **J. Electrochem. Soc. 127**, 1974 (1980)

54. H.S. Horowitz, J.M. Longo and H.H. Horowitz, **J. Electrochem. Soc. 130**, 1851(1983)

55. D.T. Sawyer and E.T. Seo, **Inorganic Chemistry 16**, 499 (1977)

56. J. Divisek and B. Kastening, **J. Electroanal. Chem. 65**, 603 (1975)

57. R.K. Sen, J. Zagel, and E. Yeager, **Inorganic Chemistry 16**, 3379 (1977)

58. I. Morcos and E. Yeager, **Electrochim. Acta 15**, 953 (1970)

59. N.M. Zagudaeva, V.S. Vilinskaya and G.V. Shteinberg, **Elektrokhimiya 18**, 541 (1982)

60. E. Yeager, P. Krouse and K.V. Rao, **Electrochim. Acta 9**, 1057 (1964)

61. M.O. Davies, M. Clark, E. Yeager and F. Hovorka, **J. Electrochem. Soc. 106**, 56 (1959)

62. R.J. Taylor and A.A. Humffray, **J. Electroanal. Chem. 64**, 63 (1975)

63. V.S. Bagotzky, N.A. Shumilova and E.I. Khrusheva, **Electrochim. Acta 21**, 919 (1976)

64. B.N. Efremov and M.R. Tarasevich, **Elektrokhimiya 17**, 1672 (1981)

65. L. Pauling, **Nature 203**, 182 (1964)

66. D.B. Hibbert and A.C.C. Tseung, **Extended Abstracts**, Vol. **77-1**, The Electrochem. Soc., Princeton (1977), p. 751

67. N.P. Rasiyah, **Ph. D. Thesis**, The City Univ., London (1982)

68. M. Savy, **Electrochim. Acta 13**, 1359 (1968)

69. C. Pirovano and S. Trasatti, **J. Electroanal. Chem. 180**, 171 (1984)

70. Z.G. Lin and A.C.C. Tseung, **Extended Abstracts**, Int. Soc. Electrochem. 35th Meeting, Berkely (1984), p. 63

71. R.Kh. Burshtein, M.R. Tarasevich, A.M. Khutornoi, V.S. Vilinskaya, F.Z. Sabirov, I.I. Astakhov and G.G. Teplitskaya, **Elektrokhimiya 11**, 1064 (1975)

72. W.L. Roth, **J. Phys. Chem. Solids 25**, 1 (1964)

73. J. Weiss, **Faraday Soc. Trans. 31**, 1547 (1935)

74. C.B. Roy, **J. Catal. 12**, 129 (1968)

75. J.R. Goldstein and A.C.C. Tseung, **J. Catal. 32**, 452 (1974)

76. G.M. Schwab and Kraut, **Anorg. allgem. Chem. 295**, 36 (1958)

77. M. Pourbaix, **Atlas of Electrochemical Equilibria in Aqueous Solutions**, Pergamon Press, Oxford (1966), p. 325

78. A.C.C. Tseung and K.L.K. Yeung, **J. Electrochem. Soc. 125**, 1003 (1978)

79. B.N. Efremov, M.R. Tarasevich, G.I. Zakharkin, and S.R. Zhukov, **Elektrokhimiya 14**, 1504 (1978)

80. B.N. Efremov, G.I. Zakharkin, M.R. Tarasevich, and S.R. Zhukov, **Zh. Fiz. Khim. 52**, 1671 (1978)

81. Z.G. Lin, S.P. Jiang and A.C.C. Tseung, **Extended Abstracts**, in **Power Sources 11**, L.J. Pearce, ed., Inter. Power Sources Symposium Committee, (1986), p. 542

82. R.Kh. Burshtein, F.Z. Sabirov and M.R. Tarasevich, **Kinet. Katal. 17**, 1333 (1976)

83. J.E.B. Randles, **Faraday Disc. Soc. 1**, 11 (1941)

84. R.D. Armstrong, R.E. Firman and H.R. Thirsk, **Faraday Disc. Soc. 56**, 244 (1973)

85. R.D. Armstrong and K. Edmondson, **J. Electroanal. Chem. 53**, 371 (1974)

86. R.L. Zeller III and R.F. Savinell, **Corrosion Science 26**, 389 (1986)

87. J.P. Candy and P. Fouilloux, **Electrochim. Acta 26**, 1029 (1981)

88. J.P. Candy and P. Fouilloux, **J. Chem. Soc., Faraday Trans. 1 79**, 823 (1983)

89. J.F. McCann and S.P.S. Badwal, **J. Electrochem. Soc. 29**, 551 (1982)

90. T.S.K. Tang, **Ph. D. Thesis**, The City Univ., London (1985)

91. M.R. Suchanski, **J. Electrochem. Soc. 132**, 2059 (1985)

92. P. Drossbach, **Electrochim. Acta 11**, 667 (1966)

93. S. Iseki, K. Ohashi and S. Nagaura, **Electrochim. Acta 17**, 2239 (1972)

94. H. Willems, M. Moers, G.H.J. Broers and J.H.W. de Wit, **J. Electroanal. Chem. 194**, 305 (1985)

95. R. de Levie, in **Advances in Electrochemistry and Electrochemical Engineering**, Vol. 6, P. Delahay, ed., John Wiley, New York (1967), p. 329

96. M. Sluyters-Rehbach and J.H. Sluyters, in **Electroanalytical Chemistry**, Vol. 4, A.J. Bard, ed., Marcel Dekker, New York (1970), p. 1

97. M. Sluyters-Rehbach and J.H. Sluyters, in **Comprehensive Treatise of Electrochemistry**, Vol. 9, E. Yeager, J.O'M. Bockris, B.E. Conway and S. Sarangapani, eds., Plenum Press, New York (1984), p. 177

98. P. Rasiyah and A.C.C. Tseung, **J. Electrochem. Soc. 130**, 2384 (1983)

99. R. Parsons, **Trans. Faraday Soc. 47**, 1332 (1951)

100. S. Jasem and A.C.C. Tseung, **J. Electrochem. Soc. 126**, 1353 (1979)

101. J. Haenen, W. Visscher and E. Barendrecht, **J. Electroanal. Chem. 208**, 273 (1986)

102. S. Iseki, K. Ohashi and S. Nagaura, **Electrochim. Acta 17**, 2249 (1972)

103. M.M.J. Pieterse, M. Sluyters-Rehbach and J.H. Sluyters, **J. Electroanal. Chem. 107**, 247 (1980)

104. R. Holze and W. Vielstich, **J. Electrochem. Soc. 131**, 2298 (1984)

105. V.S. Bogatskii, M.R. Tarasevich and V.Yu. Filinovskii, **Elektrokhimiya 5**, 1218 (1969)

106. V.S. Bogatskii, M.R. Tarasevich and V.Yu. Filinovskii, **Elektrokhimiya 8**, 84 (1972)

107. H.M. Cota, T. Katan, M. Chim and F.J. Schoenweis, **Nature (London) 203**, 1281 (1964)

108. S. Siggia, **Survey of Analytical Chemistry**, McGraw-Hill, New York (1968), p. 56, 98

109. M.J. de Faubert Maunder, **Practical Hints on Infrared Spectrometry**, Adam Hilger, London (1971), p. 5

110. K.L.K. Yeung, **Ph. D. Thesis**, The City Univ., London (1978)

111. H.L. Bevan, **Ph. D. Thesis**, The City Univ., London (1970)

112. J. Giner, **J. Electrochem. Soc. 111**, 376 (1964)

113. E. Gileadi, E. Kirowa-Eisner and J. Penciner, **Interfacial Electrochemistry**, Addison-Welsley, London (1975), p. 368

114. F.Y.Y. Yon Hin, **Ph. D. Thesis**, The City Univ., London (1984)

115. B.B. Damaskin, **The Principles of Current Methods for the Study of Electrochemical Reactions**, McGraw-Hill, New York (1967), Chap. 3

116. R.D. Armstrong and W.P. Race, **J. Electroanal. Chem. 33**, 285 (1971)

117. H. Gohr, M. Mirnik and C.A. Schiller, **J. Electroanal. Chem. 180**, 273 (1984)

118. A.C.C. Tseung, S. Jasem, and M.N. Mahmood, in **Hydrogen Energy Systems**, Vol. 1, T.N. Viziroglu and W. Zeifriz, eds., Pergamon Press, (1978), p. 214

119. K. Kordesch, S. Jahangir and M. Schautz, **Electrochim. Acta 29**, 1589 (1984)

120. M. Watanabe, M. Tomikawa and S. Motoo, **J. Electroanal. Chem. 182**, 193 (1985)

121. A.C.C. Tseung and J.R. Goldstein, **J. Mater. Sci. 7**, 1383 (1972)

122. A.C.C. Tseung, J.C. Botejue and P. Rasiyah, **Optimization of Teflon Bonded Gas Evolving Electrodes**, Progress Report No.3, EEC Contact No. EH/B/09/006/80 UK(H), (1981)

123. M.V. Uminskii, N.N. Verenikina, A.M. Trunov and V.A. Presnov, **Elektrokhimiya 7**, 554 (1971)

124. A.C.C. Tseung and H.L. Bevan, **J. Mater. Sci. 5**, 604 (1970)

125. A.A. Domnikov, G.L. Reznikov and F.R. Yuppets, **Elektrokhimiya 12**, 1868 (1976)

126. A.D.S. Tantram and A.C.C. Tseung, **Nature 221**, 167 (1967)

127. A.C.C. Tseung and L. Wang, **J. Appl. Electrochem. 3**, 211 (1972)

128. S.J. Teichner, **Adv. Catalysis 20**, 167 (1969)

129. J.C. Botejue, **Ph. D. Thesis**, The City Univ., London (1984)

130. S. Gordon and J.M. Schreyer, **Chemist-Analyst 44**, 95 (1955)

131. S. Brunauer, P.H. Emmett and E. Teller, **J. Amer. Chem. Soc. 60**, 309 (1938)

132. P. Cossee, **J. Inor. Nucl. Chem. 8**, 483 (1958)

133. R.A. Nyquist and R.O. Kagel, **Infrared Spectra of Inorganic Compounds**, Academic Press, New York (1971)

134. J.A. Gadsden, **Infrared Spectra of Minerals and Related Inorganic Compounds**, Butterworths (1975), p. 16, 56

135. ASTMA, **Powder Diffraction File, Alphabetical Index of Inorganic Compounds**, TCPDS International Centre for Diffraction Data, Pennsylvania, U.S.A. (1978)

136. M. Ardon, **Oxygen: Elementary Forms and Hydrogen Peroxide**, Publ. Banjamin, New York (1965), p. 68

137. D.W. McKee, **J. Catal. 14**, 355 (1969)

138. M.R. Tarasevich, G.I. Zakharkin and R.M. Smirnova, **Sov. Electrochem. 9**, 620 (1973)

139. S.B. Kanungo, **J. Catal. 58**, 419 (1979)

140. N. Uri, **Chem. Revs. 50**, 375 (1952).

141. A.I. Onuchukwu and A.B. Zuru, **Mater. Chem. Phys. 15**, 131 (1986)

142. W.J. Moore, **Physical Chemistry**, Longman, London (1972), p. 333

143. B.N. Efremov, G.I. Zakharkin, S.R. Zhukov and M.R. Tarasevich, **Elektrokhimiya 14**, 937 (1978)

144. L.J. Csanyi, Z.M. Galbacs and L. Nagy, **J. Chem. Soc. Dalton Trans. 1982**, 237 (1982)

145. K.E. Gubbins and R.D. Walker, **J. Electrochem. Soc. 112**, 469 (1965)

146. F. Wikinson, **Chemical Kinetics and Reaction Mechanism**, Van Nostrand Reinhold Company, New York (1980), p. 95,137.

147. L. Nagy, Z.M. Galbacs, L.J. Csanyi and L. Horvath, **J. Chem. Soc. Dalton Trans.**, 859 (1982)

148. R.N. Ram, **Kinet. Katal 25**, 1105 (1984)

149. J.A. Plambeck, **Electroanalytical Chemistry: Basic Principles and Applications**, John Wiley & Sons, New York (1982), p. 315

150. V.G. Prabhu, L.R. Zarapkar and R.G. Dhaneshwar, **Electrochim. Acta 26**, 725 (1981)

151. A.G. Kicheev and V.M. Sheblovinskii, **Elektrokhimiya 22**, 671 (1986)

152. F. Haber and J. Weiss, **Proc. Roy. Soc. (London) A147**, 332 (1934)

153. R. Gerischer and H. Gerischer, **Z. Physik. Chem. (N.F.) 6**, 1978 (1966)

154. M. Setaka, Y. Kirino, T. Ozawa and T. Kwan, **J. Catal. 15**, 209 (1969)

155. Y. Shimizu, T. Shiga and K. Kuwata, **J. Phys. Chem. 74**, 2929 (1974)

156. Y. Ono, T. Matsumura, N. Kitajima and S. Fukuzumi, **J. Phys. Chem. 81**, 1307 (1977)

157. N. Kitajima, S. Fukuzumi and Y. Ono, **J. Phys. Chem. 82**, 1505 (1978)

158. S.B. Kanungo, K.M. Parida and B.R. Sant, **Electrochim. Acta 26**, 1157 (1981)

159. F.E.R. Gimblett, **Introduction to Kinetics of Chemical and Chain Reactions**, McGraw-Hill, London (1970)

160. Southampton Electrochemistry Group, **Instrumental Methods in Electrochemistry**, Ellis Horwood, New York (1985), Chap. 8

161. J.H. Sluyters, **Reacl. Trav. Chim. 79**, 1092 (1960)

162. M. Rehbach and J.H. Sluyters, **Reacl. Trav. Chim. 80**, 469 (1961)

163. M. Sluyters-Rehbach and J.H. Sluyters, **Reacl. Trav. Chim. 82**, 525 (1963)

164. P. Delahay, **J. Phys. Chem.** 70, 2373 (1966)

165. K. Holub, G. Tessari and P. Delahay, **J. Phys. Chem.** 71, 2612 (1967)

166. I. Epelboin and M. Keddam, **J. Electroanal. Chem.** 117, 1052 (1970)

167. R. de Levie, **Electrochim. Acta** 10, 395 (1965)

168. A.J. Bard and L.A. Faulkner, **Electrochemical Methods Fundamentals and Applications**, John Wiley & Sons, New York (1980), p. 348

169. I. Epelboin, M. Keddam and J.C. Lestrade, **Faraday Disc. Soc.** 56, 264 (1973).

170. R.D. Armstrong and R.E. Firman, **J. Electrochem. Chem.** 45, 3 (1973)

171. H.A. Laitinen and J.E. Randles, **Trans. Faraday Soc.** 51, 54 (1955)

172. B. Timmer, M. Sluyters-Rehbach and J.H. Sluyters, **J. Electroanal. Chem.** 18, 93 (1968)

173. R. Parsons, in **Advances in Electrochemistry and Electrochemical Engineering**, Vol. 7, P. Delahay and C.W. Tobias, eds., John Wiley, New York (1970), p. 177

174. M. Senda and P. Delahay, **J. Phys. Chem.** 65, 1580 (1961)

175. D.E. Smith, in **Electroanalytical Chemistry**, Vol. 1, A.J. Bard, ed., Marcel Dekker, New York (1966), Chap. 1

176. H. Gerischer, **Z. Physik. Chem. (Leipzig)** 198, 286 (1951)

177. C.W. Tien, **The Electrochemical Research Methods**, Science Press, Beijing, China (1984), Chap. 8 (in Chinese)

178. R. de Levie, **Electrochim. Acta** 9, 1231 (1964)

179. R. de Levie, **Electrochim. Acta** 8, 751 (1963)

180. H. Keiser, K.D. Beccu and M.A. Gutjahr, **Electrochim. Acta** 21, 539 (1976)

181. R.D. Armstrong, K. Edmondson and J.A. Lee, **J. Electroanal. Chem.** 63, 287 (1975)

182. R. Darby, **J. Electrochem. Soc.** 113, 392 (1966)

183. B.V. Tilak, R.S. Yeo and S. Srinivasan, in **Comprehensive Treatise of Electrochemistry**, Vol. 3, J.O'M. Bockris, B.E. Conway, E. Yeager and R.E. White, eds., Plenum Press, New York (1981), p. 39

184. P. Drossbach and J. Schulz, **Electrochim. Acta** 9, 1391 (1964)

185. M.R. Tarasevich, F.Z. Sabirov and R.Kh. Burshtein, **Sov. Electrochem. 7**, 387 (1971)

186. A.J. Appleby and J. Marie, **Electrochim. Acta 24**, 195 (1979)

187. P. Drossbach and P. Schmittinger, **Electrochim. Acta 11**, 687 (1966)

188. J. McHardy, J.M. Baris and P. Stonehart, **J. Appl. Electrochem. 6**, 371 (1976)

189. R. Holze and W. Vielstich, **Electrochim. Acta 29**, 607 (1984)

190. J.D. Voorhies, **in Proc. 22nd Annu. Power Sources Conf.**, Red Bank, New York (1968), p. 124

191. K.V. Kordesch, **in Fuel Cells**, W. Mitchell, ed., Academic Press, New York (1963), p. 329

192. I. Iliev, S. Gamburzev, A. Kaisheva and J. Mrha, **J. Appl. Electrochem. 5**, 291 (1975)

193. P. Bjornbom, **Electrochim. Acta 32**, 115 (1987)

194. R.Kh. Burshtein, A.V. Dribinskii, M.R. Tarasevich, Yu.A. Chizmadzhev and Yu.G. Chirkov, **Elektrokhimiya 7**, 1826 (1971)

195. J.O'M. Bockris and S. Srinivasan, **Fuel Cells: Their Electrochemistry**, McGraw-Hill Book Company, New York (1969), Chap. 5

196. A. Damjanovic, M.A. Genshaw and J.O'M. Bockris, **J. Electrochem. Soc. 114**, 1107 (1967)

197. E.G. Gagnon, **J. Electrochem. Soc. 122**, 521 (1975)

198. Y. Oren and A. Soffer, **J. Electrochem. Soc. 125**, 869 (1978)

199. K. Kinoshita and J.A.S. Bett, **Carbon 11**, 403 (1973)

200. J.P. Randin and E. Yeager, **J. Electrochem. Soc. 118**, 711 (1971)

201. H.H. Bauer, M.S. Spritzer and P.J. Elving, **J. Electroanal. Chem. 17**, 299 (1968)

202. R.J. Taylor and A.A. Humffray, **J. Electroanal. Chem. 42**, 347 (1973)

203. R. McIntyre, D. Scherson, W. Storck and H. Gerischer, **Electrochim. Acta 32**, 51 (1987)

204. L.H. Cross, H.L. Roberts, P. Goggin and L.A. Woodward, **Trans. Faraday Soc. 56**, 945 (1960)

205. J.P. Candy, P. Fouiloux, M. Keddam and H. Takenouti, **Electrochim. Acta 26**, 1029 (1981)

206. R. Holze and W. Vielstich, in **Advances in Battery Materials and Processes**, J. McBreen, R.S. Yee, P. Chin and A.C.C. Tseung, eds., The Electrochem. Soc., (1984), p. 230

207. R.E. White, M.A. Nicholson, L.G. Kleine, J. Van Zee and R. Darby, **J. Electrochem. Soc. 131**, 268 (1984)

208. A.G. Pshenichnikov, Yu.I. Kryukov, R.Kh. Burshtein, I.I. Astakhov and V.V. Surikov, **Elektrokhimiya 12**, 1292 (1976)

209. S. Gamburtsev, **Elektrokhimiya 18**, 134 (1982)

210. Y. Rotenberg, S. Srinvasan, E.I. Vargha-Butler and A.W. Neumann, **J. Electroanal. Chem. 213**, 43 (1986)

211. I.A. Kukushkina, G.V. Shteinberg and A.V. Dribinskii, **Elektrokhimiya 21**, 1384(1985)

212. B.R. Puri, in **Chemistry and Physics of Carbon**, Vol. 6, P.L.Walker, ed., Marcel Dekker, New York (1970), p. 242

213. K. Matsuki and H. Kamada, **Electrochim. Acta 31**, 13 (1986)

214. V.I. Marshneva and G.K. Boreskov, **Reaction Kinetics and Catalysis Letters 1**, 15 (1974)

215. W.J. King and A.C.C. Tseung, **Electrochim. Acta 19**, 493 (1974)

216. R.Kh. Burshtein, V.S. Vilinskaya, N.G. Bulavina and V.Ya. Shepelev, **Elektrokhimiya 14**, 907 (1978)

217. M.R. Tarasevich, V.S. Vilinskaya, A.M. Khutornoi, R.Kh. Burshtein, F.V. Makordei and Yu.A. Tkach, **Elektrokhimiya 12**, 504 (1976)

218. D.B. Hibbert and A.C.C. Tseung, **J. Electrochem. Soc. 125**, 74 (1978)

219. K.L.K. Yeung and A.C.C. Tseung, **J. Electrochem. Soc. 125**, 1660 (1978)

220. K.V. Kordesh, in **Hydrocarbon Fuel-cell Technology**, B.S. Baker, ed., Academic Press, New York (1965), p. 17

221. I.A. Raj, K.V. Rao and V.K. Venkatesan, **Bull. Electrochem. 2**, 157 (1986)

222. J.R. Goldstein and A.C.C. Tseung, **J. Phys. Chem. 76**, 3646 (1972)

223. N.P. Rasiyah and A.C.C. Tseung, **Extended Abstracts**, Vol. **81-2**, The Electrochem. Soc., Colorado (1981), p. 273

224. J.D.E. McIntyre, **J. Phys. Chem. 71**, 1196 (1967)

225. W.M. Vogel and J.T. Lundquist, **J. Electrochem. Soc. 117**, 1512 (1970)

226. F. Barz, R. Holze and J. Willsau, in **Proc. 2nd Int. Workshop on Reactive Metal-Air Batteries**, Belgrade (1982), p. 339

227. P. Bjornbom, **J. Electrochem. Soc. 133**, 1874 (1986)

228. M. Sluyters-Rehbach and J. Sluyters, **J. Electroanal. Chem. 23**, 457 (1969)

229. H. Tanabe and S. Fukushima, **Nippon Kagaku Kaishi (6)**, 745 (1986)

230. L.G. Edwards and S. Sarangapani, in **Electrochem. Soc. Proc.**, Vol. **84-11** (1984), p. 254

231. S. Gamburtsev, I. Iliev, A. Kaisheva, G.V. Shteinberg and L.N. Mokrousov, **Elektrokhimiya 16**, 1069 (1980)

232. A.V. Dribinskii, L.N. Mokrousov, I.G. Abidor, G.V. Shteinberg, M.R. Tarasevich and V.S. Bagotskii, **Elektrokhimiya 13**, 284 (1977)

233. K. Miyatani, K. Kohn, H. Kakimura and S. Iida, **J. Phys. Soc. Japan 21**, 464 (1966)

234. M. Oku and K. Hirokawa, **J. Electron Spectrosc. Relat. Phenom. 8**, 475 (1976)

235. M.M. Thackeray, S.D. Baker, K.T. Adendorff and J.B. Goodenough, **Solid State Ionics 17**, 175 (1985)

236. E.I. Khrusheva, O.V. Moravskaya, V.V. Karonik, L.V. Eremina, N.A. Shumilova and V.S. Bagotskii, **Elektrokhimiya 11**, 620 (1975)

237. D.M. Shub, A.N. Chemodanov and V.V. Shalaginov, **Elektrokhimiya 14**, 595 (1978)

238. A.V. Vosekalns and G.Ya. Slaidin, **Elektrokhimiya 14**, 787 (1978)

239. M.P. Van Dijk, K.J. De Varies and A.J. Burggraaf, **Solid State Ionics 21**, 83 (1986)

240. A.M. Trunov and N.N. Verenikina, **Elektrokhimiya 17**, 135 (1981)

241. A.M. Trunov, V.P. Presnov, M.V. Uminskii, O.F. Rakityanskaya, T.S. Bakutina and A.I. Kotseruba, **Elektrokhimiya 11**, 552 (1975)

242. P.J. Boddy, **J. Electroanal. Chem. 10**, 199 (1965)

243. R. de Levie, **Electrochim. Acta 10**, 113 (1965)

244. C. Cachet and R. Wiart, **Electrochim. Acta 29**, 145 (1984)

245. W. Scheider, **J. Phys. Chem. 79**, 127 (1975)

246. M.G.S.R. Thomas, P.G. Bruce and J.B. Goodenough, **Solid State Ionics 18-19**, 794 (1986)

247. L. Nyikos and T. Pajkossy, **Electrochim. Acta 30**, 1533 (1985)

248. G.J. Brug, A.L.G. Van Den Eeden, M. Sluyters-Rehbach and J.H. Sluyters, **J. Electroanal. Chem. 176**, 275 (1984)

249. M.G.S.R. Thomas, P.G. Bruce and J.B. Goodenough, **J. Electrochem. Soc. 132**, 1521 (1985)

250. H. Gerischer, in **Physical Chemistry An Advanced Treatise**, Vol. **IXA**, H. Eyring, D. Henderson and W. Jost, eds., Academic Press, New York (1970), Chap. 5

251. S.R. Morrison, **Electrochemistry at Semiconductor and Oxidized Metal Electrodes**, Plenum Press, New York (1980), Chap. 2

252. W. Dianis and J.E. Lester, **Surface Sci. 43**, 602 (1974)

253. H. Olender, W.E.O' Grady, H.S. Isaacs, S. Srinivasan and A.C.C. Tseung, **J. Appl. Electrochem. 12**, 135 (1982)

254. D.L. Caldwell, in **Comprehensive Treatise of Electrochemistry**, Vol. **2**, J.O'M. Bockris, B.E. Conway, E. Yeager and R.E. White, eds., Plenum Press, New York (1981), p. 105

255. M.J. Lain and D. Pletcher, **Electrochim. Acta 32**, 99 (1987)

256. M.J. Lain and D. Pletcher, **Electrochim. Acta 32**, 109 (1987)

257. J.C.G. Thanos and D.W. Wabner, **J. Electroanal. Chem. 182**, 25 (1985)

258. L.D. Burke, M.E. Lyons and O.J. Murphy, **J. Electroanal. Chem. 132**, 247 (1982)

259. V.A. Tracey, **Mod. Dev. Powder Metall. 12**, 423 (1981)

260. D.J. Gordy, E. Luksha and C.J. Menard, **J. Electrochem. Soc. 120**, 1447 (1973)

261. E.W. Justi and H.H. Ewe, **Porous Cobalt Electrodes for Alkaline Accumulators and Hybrid Cell Therewith and Air Electrode**, US Patent No. 3986892 (1976)

262. Cobalt and Cobalt Alloys, in **Kirk-Othmer Encyclopedia of Chemical Technology**, Third Edition, Vol. 6, John Wiley, New York (1979), p. 481

263. J.W.S. Hearle, J.T. Sparrow and P.M. Cross, **The Use of the Scanning Electron Microscope**, Pergamon Press, Oxford (1972), p. 124

264. J.M. West, **Electrodeposition and Corrosion Processes**, Van Nostrand, London (1965), p. 100, 113

265. W.R. Busing, **J. Chem. Phys. 23**, 933 (1955)

266. H. Gomez Meier, J.R. Vilche and A.J. Arvia, **J. Electroanal. Chem. 134**, 251 (1982)

267. M. Kramer and M. Tomkiewicz, **J. Electrochem. Soc. 131**, 1283 (1984)

268. K.M. Mehata and V.K. Venkatesan, **Trans. SAEST 11**, 411 (1976)

269. J.R. Goldstein and A.C.C. Tseung, **Nature 222**, 869 (1969)

270. Ref. 18, p. 224, 260